Broad interests, better scientists *pp. 22 & 24*

No rules of the road for driverless cars? *p. 36*

Multiple origins of domesticated goats *p. 85*

Science

$15
6 JULY 2018
sciencemag.org

AAAS

HIDDEN CONFLICTS?

Investigative report: How pharma money could bias FDA drug approvals

p. 16

CONTENTS

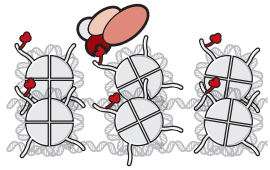

33 Inheriting histone modifications

6 JULY 2018 • VOLUME 361 • ISSUE 6397

16

NEWS

IN BRIEF

IN DEPTH

FEATURES

INSIGHTS

BOOKS *ET AL.*

LETTERS

PERSPECTIVES

Published by AAAS

CONTENTS

30 & 64
Watching a breakup

6 JULY 2018 • VOLUME 361 • ISSUE 6397

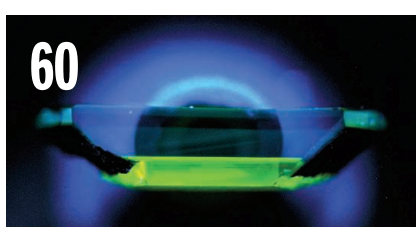

ON THE COVER

An analysis of pharmaceutical payments to physicians after they voted on drug approval recommendations suggests that the Food and Drug Administration (FDA) needs to consider whether prospects of future rewards could influence its advisory panels. The investigation also indicates that the FDA may have missed more traditional conflicts of interest for those advisers. Another story looks at revolving-door concerns for FDA staff. See page 16. *Illustration: Stephan Schmitz*

SCIENCE (ISSN 0036-8075) is published weekly on Friday, except last week in December, by the American Association for the Advancement of Science, 1200 New York Avenue, NW, Washington, DC 20005. Periodicals mail postage (publication No. 484460) paid at Washington, DC, and additional mailing offices. Domestic individual membership, including subscription (12 months): $165 ($74 allocated to subscription). Domestic institutional subscription (51 issues): $1808; Foreign postage extra: Mexico, Caribbean (surface mail) $55; other countries (air assist delivery): $89. First class, airmail, student, and emeritus rates on request. Canadian rates with GST available upon request, GST #125488122. Publications Mail Agreement Number 1069624. **Printed in the U.S.A.**
Change of address: Allow 4 weeks, giving old and new addresses and 8-digit account number. **Postmaster:** Send change of address to AAAS, P.O. Box 96178, Washington, DC 20090–6178. **Single-copy sales:** $15 each plus shipping and handling; bulk rate on request. **Authorization to reproduce** material for internal or personal use under circumstances not falling within the fair use provisions of the Copyright Act is granted by AAAS to libraries and others who use Copyright Clearance Center (CCC) Pay-Per-Use services provided that $35.00 per article is paid directly to CCC, 222 Rosewood Drive, Danvers, MA 01923. The identification code for *Science* is 0036-8075. *Science* is indexed in the *Reader's Guide to Periodical Literature* and in several specialized indexes.

CREDITS: (CLOCKWISE FROM TOP): J. YANG *ET AL.*; ROBERT NEUBECKER; BRENDON ROSE

Science
AAAS
1200 New York Avenue, NW, Washington, DC 20005
Clarendon House, Clarendon Road, Cambridge, UK CB2 8FH

SUBSCRIPTION SERVICES For change of address, missing issues, new orders and renewals, and payment questions: 866-434-AAAS (2227) or 202-326-6417, FAX 202-842-1065. Mailing addresses: AAAS, P.O. Box 96178, Washington, DC 20090-6178 or AAAS Member Services, 1200 New York Avenue, NW, Washington, DC 20005

INSTITUTIONAL SITE LICENSES 202-326-6730 **REPRINTS:** Author Inquiries 800-635-7181 **COMMERCIAL INQUIRIES** 803-359-4578 **PERMISSIONS** 202-326-6765, permissions@aaas.org **AAAS Member Central Support** 866-434-2227 www.aaas.org/membercentral.

INFORMATION FOR AUTHORS See www.sciencemag.org/authors/science-information-authors

Corrected 5 July 2018. See full text

EDITORIAL

Science Advances advancing

Editor-in-Chief, Science *Journals.*
jberg@aaas.org

In February 2014, the American Association for the Advancement of Science (AAAS) announced the decision to launch *Science Advances* as a way to "expand the…content of *Science*" (science.sciencemag.org/content/343/6172/709.full). The new publication was envisioned as a multidisciplinary, open-access, digital-only journal, edited by a team of scientists actively engaged in research. The first *Science Advances* papers were published within a year. Now, nearly three-and-a-half years later, *Science Advances* is soon to publish its 2000th paper—a good time to examine how the journal is fulfilling its founding vision.

These 2000 papers have been selected from over 15,000 manuscripts submitted to *Science Advances*. They have been handled by a dedicated board of deputy editors working with an outstanding group of associate editors (advances.sciencemag.org/content/editorial-board). The current 11 deputy editors have expertise in chemistry, materials science and engineering, physics, molecular biology and genetics, biomedical sciences, biophysics, cognitive and molecular neuroscience, Earth and environmental sciences, space sciences, and social sciences and interdisciplinary research. The board of associate editors currently includes 134 individuals with expertise focused within subdisciplines in these areas. The editors work to foster fast and fair expert peer review with the goal of yielding a selection of research that reflects the boundaries of new knowledge, while aligned with the standards of *Science*.

Science Advances was envisioned to cover research areas as broad as, or even broader than, those covered by *Science*. This breadth can be examined by using previously described methods based on natural language processing analysis of abstracts (blogs.sciencemag.org/sciencehound/2017/01/05/science-family-journal-content-analysis/). Analysis of Research Articles and Reviews published in *Science Advances* through May 2018, and *Science*'s Reports, Research Articles, and Reviews published over the same period, confirms that both journals span similar areas of science. Of the papers published in *Science*, ~25% are in physical sciences and engineering; 50% in life sciences; 20% in Earth, environmental, and space sciences; and 5% in social sciences and interdisciplinary research. Interestingly, ~45% of *Science Advances* content is in physical sciences and engineering; 25% in life sciences; 25% in Earth, environmental, and space sciences; and 5% in social sciences and interdisciplinary research. It is satisfying to see broad representation of research areas in both journals, and such analyses are guiding continued growth to cover areas of strength and to enhance coverage of other areas.

"Despite its relatively recent launch, it is ranked among the top multidisciplinary journals…"

Science Advances has been well received by the scientific community and the public. More than 20% of the papers published in its first 2 years have garnered more than 25 citations. Despite its relatively recent launch, it is ranked among the top multidisciplinary journals based on the distributions of such citation data. Many papers have also received considerable attention in the popular press, including those covering environmental and social sciences. The gold open-access publishing model enhances exposure of the complete papers to the public at the time of publication.

As *Science Advances* moves into its next phase, Ali Shilatifard transitions from his position as one the founding deputy editors to the position of editor. Dr. Shilatifard is chair of the Department of Biochemistry and Molecular Genetics at the Feinberg School of Medicine at Northwestern University. The editorial team has also expanded its deputy editor and associate editor rosters in response to steady growth in the number of submissions. We anticipate increasing the number of papers that are published in *Science Advances* while maintaining the goal of high quality, speed, and attention to the editorial guidelines and requirements common to the *Science* family of journals. In so doing, we support AAAS's mission as a global participant in, and advocate for, the communication and use of science to benefit humankind.

–Jeremy Berg

10.1126/science.aau6038

NEWS

> "It's true! Science was my first passion."
>
> **Alexandria Ocasio-Cortez**, the 28-year-old who won the Democratic primary for a House seat in New York's 14th district, in a tweet confirming an asteroid was named for her after she placed second in the Intel International Science and Engineering Fair's microbiology contest as a teenager.

IN BRIEF

Edited by **Kelly Servick**

WORKPLACE

#Metoo complaints fell noted geneticist

Francisco Ayala's name will be removed from the University of California, Irvine, science library.

Francisco Ayala, an eminent evolutionary geneticist, has resigned from the University of California, Irvine (UCI), effective 1 July, on the heels of a sexual harassment investigation driven by complaints from two faculty members, an administrator, and a graduate student. UCI Chancellor Howard Gillman announced on 28 June that the 84-year-old Ayala would resign without emeritus status and "abstain" from future campus activities. His name will be removed from the biological sciences building and UCI's science library. Ayala, a former Dominican priest, is also a vintner who donated $10 million to the university's School of Biological Sciences in 2011. An attorney representing three of the four complainants accused the university of failing to respond to an actionable complaint against Ayala 3 years ago. Ayala made groundbreaking discoveries in parasitology and received the $1.5 million Templeton Prize in 2010. He is a member of the National Academy of Sciences and a past president of AAAS, the publisher of *Science*.

More delays for Webb telescope

ASTRONOMY | NASA is delaying the launch of its flagship astrophysics mission, the James Webb Space Telescope (JWST), to 30 March 2021—the third schedule slip in less than a year. In a 27 June press briefing, NASA responded to a report from an Independent Review Board (IRB), which found that the previous launch date of May 2020 was unrealistic, in part because of delays caused by human error in the testing and integration of the spacecraft and its sunshield. The agency also revealed that the development cost of the telescope would rise from $8 billion to $8.8 billion. That means Congress, which set an $8 billion cap in 2011, must reauthorize it. The total cost of the JWST, including operations, is expected to be $9.66 billion. IRB head Thomas Young maintained the mission was still worth completing because of its "awesome scientific potential."

Japan's asteroid probe arrives

SPACE EXPLORATION | After 3.5 years traveling 3.2 billion kilometers, Japan's Hayabusa2 spacecraft officially arrived at the asteroid it will land on later this year to pick up soil and rock samples and—hopefully—return them to Earth. On 27 June, Japan's Aerospace Exploration Agency announced the craft had reached a position 20 kilometers away from Ryugu, an asteroid in orbit between Earth and Mars. It will spend the next 18 months maneuvering around the asteroid to map its mass, density, and gravity; determine its mineral and elemental composition; and scout out landing sites. The first of a series of touchdowns is scheduled for October. Hayabusa2's findings could lend support to the theory that asteroids and comets are one source of Earth's water and its amino acids—the building blocks of life.

Concern over transparency rule

ENVIRONMENT | The 44-member Scientific Advisory Board to the U.S. Environmental Protection Agency (EPA) wants a chance to weigh in on a controversial proposed data transparency rule before EPA Administrator Scott Pruitt finalizes it.

PHOTO: IAN PARKER

Advocates of the proposal, unveiled in April, say it would make the scientific basis for regulations stronger by requiring that all underlying data be disclosed. Critics call it a thinly veiled effort to keep regulators from tapping influential air pollution research and other studies that rely on confidential health records or hard-to-replicate designs. A 28 June letter to Pruitt, signed by the advisory board's chair, says the proposal was designed without a process for seeking scientific input and raises thorny issues the board wants to examine, including the cost of implementing the rule and how it might "infringe on legitimate confidentiality and privacy interests." It is not clear whether Pruitt needs to wait for the board's advice before moving forward. The agency will hold a public hearing on the plan on 17 July, ahead of the 16 August deadline for public comment.

First glimpse of a planet's birth

ASTRONOMY | In the first convincing observation of its kind, astronomers have directly imaged a newborn planet still forming around its star. The planet, hotter than any in our solar system, supports the theory that such bodies are born from disks of gas and dust that coalesce around young stars. A team at the Max Planck Institute for Astronomy in Heidelberg, Germany, used images from an instrument known as SPHERE (Spectro-Polarimetric High-contrast Exoplanet Research), attached to the European Southern Observatory's Very Large Telescope atop Cerro Paranal in Chile's Atacama Desert, to identify a bright point of light close to a 10-million-year-old dwarf star called PDS 70, about 370 light-years from Earth. The team reported its finding last week in *Astronomy & Astrophysics*.

Fusion effort breaks record

ENERGY | An experimental nuclear fusion reactor in Germany known as Wendelstein 7-X has broken the world record for fusion performance in a device known as a stellarator, its operators announced last week. The reactor was designed by computer algorithm to optimize the shape of the magnetic cage that holds in superhot ionized gas as it heats to temperatures sufficient to fuse atomic nucleii. But the optimal design turned out to be a bizarrely twisted shape that took 2 decades and €1 billion to build (*Science*, 23 October 2015, p. 369). The gamble seems to be paying off. After a refit last year, the reactor achieved temperatures of 40 million degrees C which, along with improved plasma density and energy confinement, make it the world's best performing stellarator—and bring it a step closer to conditions that generate net energy. Wendelstein 7-X will power up again this month with new instruments and increased heating power.

Mexican scientist elected mayor

POLITICS | Environmental engineer Claudia Sheinbaum Pardo won Mexico City's mayoral election by a landslide on 1 July, earning nearly 50% of the vote. She is the first woman elected to the post. Her fellow National Regeneration Movement member Andrés Manuel López Obrador swept the presidential race with a similar margin. "A new era is beginning," Sheinbaum Pardo said in a speech on election night. She has promised to use scientific evidence, including her own research at the National Autonomous University of Mexico, to improve transportation and mitigate a worsening water crisis (*Science*, 8 June, p. 1052).

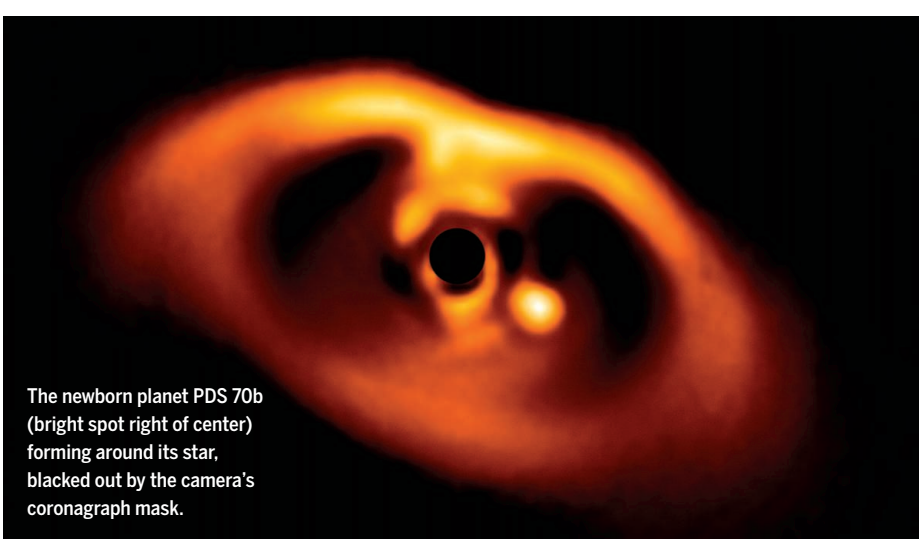

The newborn planet PDS 70b (bright spot right of center) forming around its star, blacked out by the camera's coronagraph mask.

IMAGE: ESO/A. MÜLLER *ET AL.*

THREE QS

Could crime scene DNA reveal too much?

When forensic scientists use DNA from blood and other biological samples found at crime scenes to help identify suspects, their analysis is normally restricted to parts of the genome not involved in creating proteins to protect a suspect's privacy. But a new approach examines just the chemical tags on DNA that regulate gene expression, added through a process called methylation. It could soon be used to determine a suspect's age—but could inadvertently reveal much more, raising legal and ethical issues. Bram Bekaert of the University of Leuven in Belgium, co-author of a new commentary on those issues in *Trends in Genetics*, told *Science* about the emerging technique. (A longer version of this interview is available at https://scim.ag/CrimeSceneDNA.)

Q: Besides age, what kind of personal data could methylation patterns reveal?
A: There was one paper ... where forensic scientists who had developed an age-prediction assay were actually showing they could determine whether individuals had chronic lymphocytic leukemia. ... Methylation has also been associated with risk of mortality and all kinds of other pathologies.

Q: In many countries, regulations prevent using DNA samples to predict traits like hair or skin color. Why don't those apply here?
A: We are not actually looking at DNA sequences, so the law does not apply to this type of technology. We're looking at the chemical compounds on top of the DNA sequence. ... Right now, I can just look at all of these markers, without breaking the law, and determine whether somebody has cancer or not. So [the technology] has to be regulated or controlled in some kind of way.

Q: What could that regulation look like?
A: [One] approach could be to restrict the information that [a forensic scientist can give] to the police and to the magistrates, so you only provide the predicted age, based on a sample's methylation values. In my opinion, that would probably be the best solution.

SCIENCEMAG.ORG/NEWS
Read more news from *Science* online.

IN DEPTH

The weakened virus in polio vaccine drops can, on rare occasions, regain virulence, sparking outbreaks.

PUBLIC HEALTH

Polio outbreaks in the DRC threaten eradication effort

Vaccine-derived virus spreads despite emergency response

By **Leslie Roberts**

Overshadowed by the Ebola outbreak in the Democratic Republic of the Congo (DRC), another frightening virus is on the loose in that vast, chaotic country: polio. Public health experts have worked for months to stamp out the virus, but it keeps spreading. It has already paralyzed 29 children, and on 21 June a case was reported on the border with Uganda, far outside the known outbreak zone, heightening fears that the virus will sweep across Africa. The DRC is "absolutely" the most worrisome polio outbreak today, says Michel Zaffran, who heads the Global Polio Eradication Initiative (GPEI) at the World Health Organization (WHO) in Geneva, Switzerland.

The outbreak also underscores the latest complication on the bumpy road toward polio eradication. It is caused not by the wild virus hanging on by a thread in Afghanistan, Pakistan, and perhaps Nigeria, but by a rare mutant variant derived from the weakened live virus in the oral polio vaccine (OPV) that has regained its neurovirulence and ability to spread. As OPV campaigns have driven the wild virus to near-extinction, these circulating vaccine-derived polioviruses (cVDPVs) have emerged as the greatest threat to polio eradication. If the outbreaks are not stopped quickly, polio scientists warn, they could spiral out of control, setting eradication efforts back years.

"There is an urgency" to stopping these vaccine-derived outbreaks, says epidemiologist Nicholas Grassly of Imperial College London. "It is so much more important than controlling the wild virus."

Safe and effective, OPV has long been the workhorse of the eradication effort. But a feature that makes the vaccine so powerful can also be a serious downside. For a short time after vaccination, the weakened live virus can spread from person to person, boosting immunity even in those who didn't receive the polio drops. But in rare instances, in poor countries such as the DRC where many children have not been vaccinated, the virus can continue circulating for years, accumulating mutations until it reverts to its dangerous form. The vast majority of cVDPVs are caused by serotype 2, one of three variants of the virus.

Almost as soon as cVDPVs were discovered in 2000, the World Health Assembly in Geneva declared that all use of OPV must stop when the wild virus was gone. In 2016, with the threat of cVDPVs looming larger—they now cause more cases of paralysis than the wild virus—GPEI decided waiting was no longer an option. By then, poliovirus type 2 had been eradicated in the wild, which meant that every type 2 virus originated from the vaccine itself. In April of that year, the 155 countries still using the trivalent vaccine, which targets all three polio variants, replaced it with a bivalent vaccine with the type 2 component removed. No one knew exactly how this experiment would play out. It was clear, however, that for a few years some type 2 outbreaks would still occur—either those that had started before "the switch," as it is called, but had not been detected or those caused by the last use of trivalent OPV.

In a virological catch 22, the only way to stop type 2 outbreaks is with a version of the same vaccine that gave rise to them in the first place—somehow without seeding another one. The virus in the inactivated polio vaccine cannot revert, but it simply does not pack enough punch to stop an outbreak.

To fight these outbreaks, GPEI created a closely guarded stockpile of a new monovalent OPV type 2 (mOPV2), which can only be released with the approval of the WHO director-general. If mOPV2 is used judiciously and sparingly, it can stop an outbreak without starting a future one, Zaffran says. Speed is essential, because population immunity to the type 2 virus is waning now that it has been removed from the vaccine, setting the stage for an explosive outbreak.

A virus on the march

In the past year, multiple vaccine-derived polioviruses have paralyzed children across the Democratic Republic of the Congo (DRC).

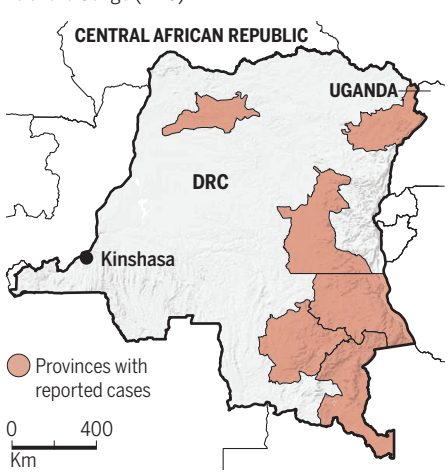

CREDITS: (PHOTO) WORLD HEALTH ORGANIZATION; (MAP) A. CUADRA/*SCIENCE*; (DATA) WORLD HEALTH ORGANIZATION

Since 2016, the type 2 vaccine has been released to fight outbreaks in 10 countries, and so far the strategy seems to be working, although a type 2 outbreak in Syria paralyzed 74 children before coming under control last year. The outlier is the DRC.

The outbreak was first detected in June 2017 in Maniema province in the middle of the country. Within days, another case was reported about 900 kilometers away in Haut-Lomami province in the southeast. Genetic analysis revealed it wasn't the same strain as in Maniema, but a distinct type 2 cVDPV that had emerged independently. Even worse, the sequences indicated both had been circulating undetected for at least 2 years.

The country and its international partners targeted mOPV2 campaigns to eight health districts deemed at highest risk—the minimum, experts thought, to get the maximum effect. But vaccination campaigns in the DRC, with its remote villages, crumbling infrastructure, and weak health system, are tough, and they failed to reach enough children. The Haut-Lomami virus broke through, spreading south to Tanganyika and then Haut-Katanga.

Then in the first week of June this year, officials confirmed another case on the other side of the country, not far from the Ebola outbreak, where health workers are already stretched thin. This strain, too, emerged independently, an indication of just how weak surveillance is in the country. More alarming still, about 2 weeks later a polio case was reported in the northeast, close to the Uganda border. The Haut-Lomami virus had made the big jump northward, to an area where no mOPV2 campaigns were underway. "This really increases the risk of international spread," says Oliver Rosenbauer, a spokesperson for polio eradication at WHO. And insecurity in parts of the province "makes everything more dangerous and more complicated."

In the worst case—if type 2 explodes across Africa, or if case numbers shoot up exponentially—the only option would be to reintroduce OPV2 into routine immunization, says Mark Pallansch, a molecular virologist at the U.S. Centers for Disease Control and Prevention in Atlanta. The switch will have failed, turning back the eradication clock years and ratcheting up costs, which now run about $1 billion a year, to the dismay of tapped-out funders.

But that scenario is years away, Zaffran says. Pallansch agrees. "At present, I truly believe type 2 cVDPVs can be managed. The only question is for how much longer," he says. "I have yet to see anything that makes me think eradication is not possible. But the endgame is proving to be much more complicated than eradicating the wild virus." ■

RESEARCH FUNDING

Lawmakers ask NIH and CDC charities for more on donors

Congressional panel seeks greater transparency on private donations to foundations that aid federal research

By **Jeffrey Mervis**

A key congressional spending panel has fired a shot across the bow of two federally chartered medical foundations, warning that the way they disclose information about donors may not pass muster. It's the latest controversy involving the traditionally low-profile foundations, which over the past quarter-century have funneled nearly $2 billion for research, clinical trials, training, and educational programs to the National Institutes of Health (NIH) and the Centers for Disease Control and Prevention (CDC).

Congress created the Foundation for the National Institutes of Health (FNIH) and the CDC Foundation in the early 1990s to raise private funds to support federal biomedical and health research. (The private donations amount to a tiny fraction of the annual NIH and CDC budgets.) In a bid to encourage transparency and prevent potential conflicts of interest, Congress specified that the foundations had to report "the source and amount of all gifts" they receive, as well as any restrictions on how the donations could be used.

> ***"We know who [our donors] are, and we're not taking their money if it's from a source that's a problem."***
>
> **David Wholley**, Foundation for the National Institutes of Health

But last month, legislators on the House of Representatives appropriations subcommittee that oversees NIH and CDC expressed concern that the foundations may not be following those disclosure rules, which are spelled out in the Public Health Service Act. A report accompanying a 2019 spending bill moving through Congress reminds the foundations to abide by the act when writing their annual reports. The lawmakers also say it's not OK to hide the identity of donors who have attached strings to their gift by labeling them as "anonymous."

The language "is a marker that we want more transparency," says one House appropriations staffer, speaking anonymously because of committee rules on who can speak to the press. "We'd like to see [the foundations] go further, and this language is meant to start a conversation."

The foundations, located near the agencies they serve in Rockville, Maryland, and Atlanta, respectively, appeared on the committee's radar this spring as a result of media coverage of projects partly funded by industry gifts that went awry. Last month, NIH Director Francis Collins canceled a $100 million study on the effects of moderate alcohol drinking that was largely funded by the spirits industry after an investigation found NIH staff had improperly solicited gifts and shaped the study to satisfy industry interests (*Science,* 22 June, p. 1286). In April, Collins killed a plan to partner with drug companies on a $400-million study of opioid dependency, after an outside panel warned of potential conflicts. The CDC Foundation has also come under fire in recent years for how it has handled corporate donations, and has severed connections with some donors.

Officials at both foundations insist they are following the spirit and letter of their founding legislation. "We have the responsibility … to do these partnerships that support the NIH mission to advance public health, and we do that," says David Wholley, FNIH's senior vice president of research partnerships. "And we have always complied with the law."

CDC Foundation officials declined to be interviewed, but asserted in an email that their public reports adhere to the law.

It's not hard to see why legislators might think the foundations aren't being sufficiently transparent. For example, both list anonymous donors without specifying the size of their gifts. Their annual reports also group donors by the approximate size of their donations, without listing exact amounts.

As a result, those gift-size groups can be misleading. In 2016, for example, FNIH listed eight donors who each gave more than $2.5 million, its top category. But a

separate report FNIH filed with the Internal Revenue Service reveals that one of those donors gave $19.1 million. (The filing does not name the donor, but FNIH told *Science* it was the Bill & Melinda Gates Foundation in Seattle, Washington.)

Julie Wolf-Rodda, the head of FNIH's development office, says there's nothing untoward or unusual about listing some donors as anonymous and grouping gifts by approximate size. "The lion's share of anonymous gifts are from a relative of someone who was treated at the NIH Clinical Center and wants to make a memorial gift and doesn't want their name listed in the annual report," Wolf-Rodda said. "We've assumed that Congress was comfortable with us doing that, just as every other nonprofit does."

FNIH does not accept contributions from the tobacco industry, Wholley says, and it has procedures for screening potential donations that raise red flags. "We know who [our donors] are, and we're not taking their money if it's from a source that's a problem," he says.

The House report also highlights legislators' concern about how the foundations report gifts that come with strings attached. FNIH negotiates with each donor "an exhaustive letter of agreement" governing the use of each gift, Wolf-Rodda says. "We seek [donations] for a specific purpose, and the money is restricted to that purpose."

FNIH's annual report, however, makes no mention of donor directives, although it might mention a donor's "essential role" in a specific initiative. The CDC Foundation's annual report is a bit more descriptive, listing "funding partners" for specific programs. Foundation officials say it's standard practice among charitable foundations not to link gifts to specific projects in annual reports, and the move is not intended to reduce transparency.

U.S. foundations are obliged to respect donor wishes to remain anonymous, and don't typically publicize gift restrictions, says Art Taylor, the CEO of the Wise Giving Alliance for the Better Business Bureau in Arlington, Virginia. But he says when donations eventually lead to a publicly available study or report, failing to identify donors and amounts could raise questions about the nature of the relationship between the donor and the foundation. In particular, he says, listing a donation in a category without a ceiling (such as $5 million or more) "means they are not doing a good job of communicating with the public."

The House report language is partly the result of lobbying by the exercise company CrossFit, Inc. Its founder, Greg Glassman, became concerned several years ago about allegations that The Coca-Cola Company and other soft drink makers had used donations to the CDC Foundation to influence the charity's work. This past spring, after company staff "looked at [the CDC Foundation's] disclosures and found they weren't even close to following the law," they brought their concerns to appropriations committee staff, says Russ Greene, CrossFit's director of government relations in Washington, D.C.

Wholley notes that legislators have, so far, expressed their concerns only in report language, which is not legally binding. But he says FNIH would certainly obey a directive from Congress to revise its reporting practices. ■

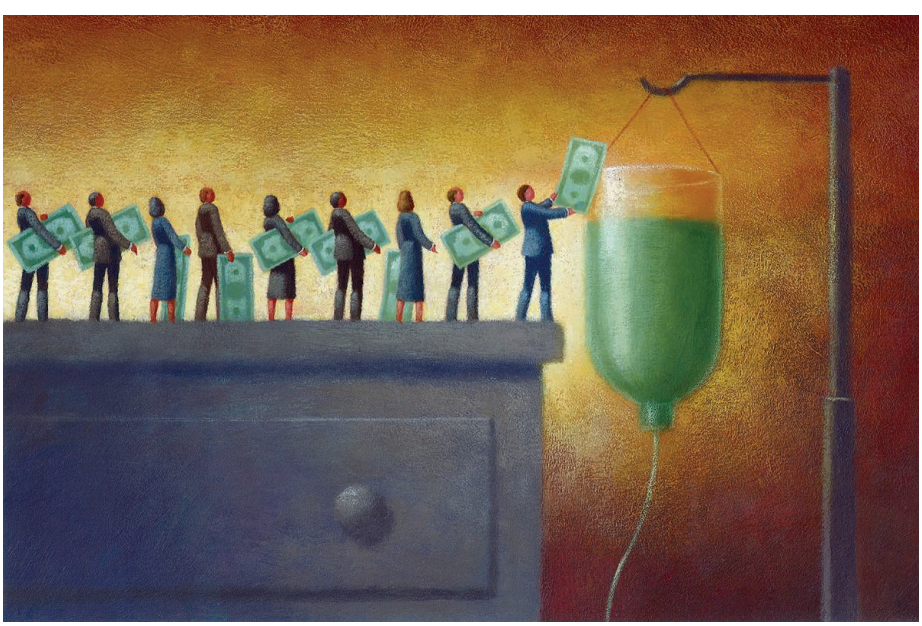

ILLUSTRATION: IMAGEZOO/ALAMY STOCK PHOTO

ASTRONOMY

Optical interferometers sharpen views of the sky

In New Mexico, a renewed attempt to build an optical array could bring spy satellites into focus

By **Adam Mann**

At a time when astronomers are building billion-dollar telescopes with mirrors 30 meters across, the 1.4-meter instrument being installed this month atop South Baldy Mountain in New Mexico may seem like a bit player. But over the next few years, nine more identical telescopes will join it on the grassy, 3200-meter summit, forming a Y-shaped array that will surpass any other optical telescope in its eye for detail. When it's complete around 2025, the $200 million Magdalena Ridge Observatory Interferometer (MROI) will have the equivalent resolution of an gigantic telescope 347 meters across.

MROI's small telescopes can't match the light-gathering power of its giant cousins, so it will be limited to bright targets. But by combining light from the spread-out telescopes, it is expected to make out small structures on stellar surfaces, image dust around newborn stars, and peer at supermassive black holes at the center of some galaxies. It will even be able to make out details as small as a centimeter across on satellites in geosynchronous orbit, 36,000 kilometers above Earth, enabling it to spy on spy satellites.

That's one reason why the U.S. Air Force, which wants to monitor its own orbital assets and presumably those of others, is funding MROI. "They want to know: Did the boom break or did some part of the photovoltaic panels collapse?" says Michelle Creech-Eakman, an astronomer at the New Mexico Institute of Mining and Technology in Socorro and project scientist on MROI. But if the facility succeeds, its biggest impact could be on the field of astronomy, by drawing new attention to the promise of optical interferometry, a powerful but challenging strategy for extracting exquisitely sharp images from relatively small, cheap telescopes.

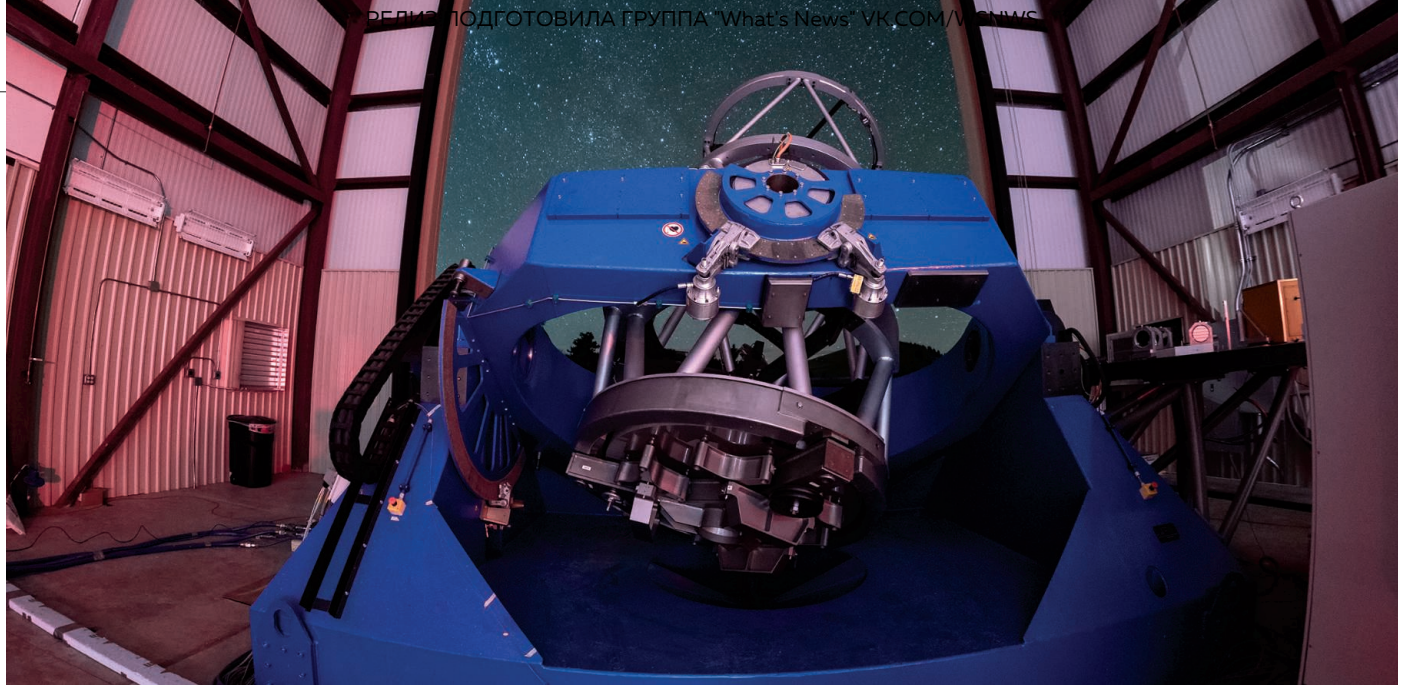

This month, a dome will be slipped over the first of 10 1.4-meter telescopes in an optical interferometer.

MROI, like optical interferometry itself, has made slow progress. The U.S. Navy began funding the facility in 2000, but lost interest and pulled out in 2011. Air Force support is not assured beyond the array's first three telescopes. "If for some horrible reason they failed, it would be a disaster for us all," says Theo ten Brummelaar, associate director of the Center for High Angular Resolution Astronomy (CHARA), an array of six 1-meter optical telescopes on Mount Wilson in Los Angeles, California.

Radio astronomers have had it easier. The long radio wavelengths mean data from separated dishes can be recorded, digitized, time-stamped by an atomic clock, and combined later for analysis. But optical interferometry is far trickier: The short wavelengths of visible light, running at terahertz frequencies, cannot yet be digitized by any electrical system. So the light must be merged in real time, with nanometer precision.

In the 1990s, advances in fiber optics, lasers, and computers developed to the point where the Keck Observatory's twin 10-meter telescopes, separated by 85 meters atop Mauna Kea in Hawaii, could be made to work as an optical interferometer. But the system needed at least four additional NASA-funded "outrigger" telescopes to reach its full potential—and the outriggers were canceled in 2006 after protests from native Hawaiians, who consider the summit of Mauna Kea sacred. "Interferometry is still something of a dirty word around NASA," says Gerard van Belle, chief scientist at the Navy Precision Optical Interferometer (NPOI) near Flagstaff, Arizona.

Many astronomers have overlooked optical interferometry's recent achievements, says Tabetha Boyajian, an astronomer at Louisiana State University in Baton Rouge, who used CHARA to perform a survey of stellar sizes. She says astronomers are sometimes surprised to learn about the technique's capabilities. "You hear, '"Oh wow, how can I use that for my science?"' she says.

CHARA and other optical arrays have imaged the squashed shapes of rapidly rotating stars, captured roving sunspots on stellar surfaces, filmed binary companion stars swapping material, and witnessed objects whipping around the Milky Way's central black hole in real time. After linking up the four 8.2-meter telescopes of the Very Large Telescope in the Atacama Desert of Chile, researchers with the European Southern Observatory last year were able to discern boiling convective cells on the face of a star 530 light-years away. A new infrared instrument should enable that interferometer to image the warm dusty disks where planets are forming around other stars.

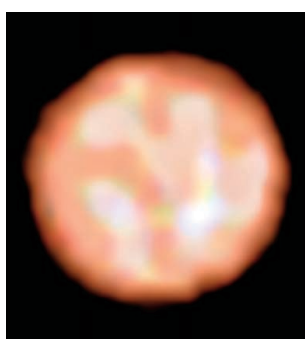

Boiling cells of plasma were seen on a distant red giant star using an optical interferometer in Chile.

And despite its previous setbacks, NASA is supporting interferometry on the twin 8.4-meter instruments at the Large Binocular Telescope Observatory atop Mount Graham in Arizona. This year, scientists there announced they had used an interferometric technique to show that many young solar systems contain less dust than expected—good news for astronomers hoping to image exoplanets directly.

Once complete, MROI's telescopes will be more widely separated than any other interferometer, enabling its superior resolution. It will also test new technologies for combining starlight from multiple telescopes that could simplify the process. If it lives up to expectations, the observatory could give optical interferometry a boost in future decadal reviews, community exercises that set budget priorities for NASA and the National Science Foundation. By the time of the 2030 decadal survey, John Monnier, a physicist at the University of Michigan in Ann Arbor and a CHARA member, wants solid support for the Planet Formation Imager, a 12-telescope, 1-kilometer-baseline optical interferometer that would be able to resolve dusty disks not just around young stars but newborn planets—the grist for moons and rings.

By then, NASA could be ready to put an optical interferometer in space, too. In 2007, the agency abandoned plans for the Terrestrial Planet Finder, an orbiting array of four telescopes designed to image planets around other stars. But it may now be more receptive to space interferometers, as giant space telescopes like the 6.5-meter James Webb Space Telescope, due to launch in 2021, strain the limits of rocket cargo loads.

"At some point [interferometry is] the only way we can address questions that are burning on the frontiers of astronomy," Van Belle says. ■

Adam Mann is a science journalist based in Oakland, California.

IMAGES (TOP TO BOTTOM): MAGDALENA RIDGE OBSERVATORY INTERFEROMETER/M. COLLEEN GINO, PHOTOGRAPHER; ESO

India's neem tree, which has fungicidal properties, has been the subject of a battle over biopiracy.

BIODIVERSITY

Biologists raise alarm over changes to biopiracy rules

Plan would bring genetic sequences under Nagoya Protocol

By **Kai Kupferschmidt**

European scientists are warning that a push to include "digital sequence information" in an international agreement against biopiracy could stifle research, hamper the fight against disease outbreaks, and even jeopardize food safety. Under proposed changes to the Nagoya Protocol, researchers might have to ask a country's government for permission before using publicly available gene sequences obtained from plants or animals originating there. Just how that would work is unclear, but some biologists are alarmed.

"If this comes to pass the regulatory burden will be enormous," says Andreas Graner, head of the Leibniz Institute of Plant Genetics and Crop Plant Research in Gatersleben, Germany. "A lot of research could stop in its tracks."

The European Plant Science Organisation (EPSO) warned in a 26 June statement that the plan "would smother research activities worldwide." The United States, however, has not ratified the 1992 Convention on Biological Diversity (CBD), to which the 2010 Nagoya Protocol is a supplementary agreement, and would not be bound by changes to the protocol.

Biopiracy—in which scientists or companies profit from the biological resources they find elsewhere in the world—has long been a concern of developing nations with a rich biodiversity. Under the Nagoya Protocol, countries can ask foreign researchers what they plan to study during a visit, and require a plan to share the benefits of any useful organisms they find. Many researchers say it has already added a huge burden of regulation to work.

But in recent decades, scientists have assembled massive amounts of genetic information from organisms collected around the world and stored them in publicly available databases for others to study or use. The fight now brewing is whether the protocol applies not just to actual biological samples, but also to this type of information.

As *Science* went to press this week, a CBD advisory body was meeting in Montreal, Canada, to try to come up with a recommendation. But any decisions can only be made at the next conference of the parties to the convention, in Egypt in November. Some insiders expected this week's meeting to focus not so much on whether "digital sequence information" should be included in Nagoya, but on how exactly to define that term. Does it include only gene sequences, for instance, or also data on an organism's gene transcription and its metabolites?

Either way, developed countries are likely to try to delay a decision, says Edward Hammond, who directs Prickly Research, a small consultancy in Austin, Texas; developing countries will likely push for treating digital information much the same way as biological materials. "It's going to be a big collision. … It will be the biggest issue [at the meeting] in Egypt," Hammond says.

Alice Jamieson, a policy officer at the Wellcome Trust, a London-based biomedical research charity, notes that rapid sequencing of the Ebola virus in the West African epidemic a few years ago helped stop its spread. Including sequence information in Nagoya would "do more harm than good," the trust says in a statement submitted to the CBD panel. And taxonomist Chris Lyal of the Natural History Museum in London calls the idea of negotiating with dozens of countries to build a phylogenetic tree from sequence data "nightmarishly extreme." EPSO says the plan would also "seriously impact the improvement of germplasm and thus put food safety in jeopardy."

Hammond calls that "low-class scaremongering." It's not yet clear what the new system would look like, he says. "To claim, before efforts to define the system are earnestly underway, that it will jeopardize food safety is irresponsible and likely reflects attempt to cloak self-interest in more palatable clothing."

Having a mechanism for benefit sharing is important, says Cassandra Quave, an ethnobotanist at Emory University in Atlanta who works with indigenous people to identify plants with medicinal properties. "On the other hand, overextension of the Nagoya Protocol to encompass sequence information on organisms could seriously compromise efforts aimed at the very conservation of the species in question," Quave says, because genetic information also allows tracking of illicitly traded plants.

Manuel Ruiz, a lawyer with the Peruvian Society for Environmental Law in Lima, says the researchers' concerns are valid, but predicts that the extension of Nagoya is inevitable because it's genetic information that is ultimately important for biotechnology—not a physical sample. "Digital sequence information should not only be included in the Nagoya protocol," Ruiz says, "it's what it should all be about." To avoid hampering research, Ruiz says the Nagoya Protocol system should be changed from its current form, based on bilateral contracts drawn up before research is done, to a multilateral system focused on sharing benefits later.

Despite worries about his own research, Lyal sympathizes with the developing countries. He says scientists have an obligation to "make this work so that everyone actually benefits. That's the way we need to go." ■

PHOTO: STEVE SPELLER/ALAMY STOCK PHOTO

NUCLEAR ENERGY

Proposed DOE test reactor sparks controversy

Congress favors the Versatile Fast Neutron Source but some scientists see little need

By **Adrian Cho**

Plans for a controversial multibillion-dollar U.S. nuclear research reactor are coming together at lightning speed—much too fast, say some nuclear policy experts. With a push from Congress, the Department of Energy (DOE) has begun designing the Versatile Fast Neutron Source, which would be the first DOE-built reactor since the 1970s. It would generate high-energy neutrons for testing materials and fuels for so-called fast reactors. But U.S. utilities have no plans to deploy such reactors, which some nuclear proliferation analysts say pose a risk because they use plutonium, the stuff of atomic bombs.

Researchers are divided on whether the reactor, which would likely be built at Idaho National Laboratory (INL) near Idaho Falls, is badly needed or a boondoggle. "Definitely, there is a lack of capability in the U.S. and a shortage of such facilities worldwide," says Massimiliano Fratoni, a nuclear engineer at the University of California, Berkeley. But Frank von Hippel, a nuclear physicist at Princeton University, says, "It's a pork-barrel project."

The reactor does enjoy extraordinary congressional support. In March, Congress gave the project $35 million for this year, although DOE only requested $10 million. The House of Representatives and the Senate have passed separate bills that call for completing the facility by 2025, with the House bill authorizing DOE to spend $2 billion. Von Hippel speculates that the cost could end up reaching $10 billion.

Nuclear reactors come in two broad types: thermal and fast. A thermal reactor "burns" a fuel typically containing a few percent of the isotope uranium-235, which releases energy and neutrons in a chain reaction. To maximize the chances that each neutron will split another atom in the dilute fuel, a "moderator" must slow them. It is often the same cooling water that conveys heat energy out of the core. Nearly all commercial power reactors are water-cooled thermal reactors.

In contrast, fast reactors split atoms with the raw high-energy neutrons. They must burn fuels that are enriched with more uranium-235 or that contain plutonium-239, and their coolant, often molten sodium or molten lead, does not slow the neutrons. They also come with a bonus: The fast neutrons can efficiently transmute inert uranium-238 into plutonium-239 to breed more fuel. That was attractive decades ago, when experts expected nuclear energy to supply all the world's electricity and feared running out of uranium. Today, with no shortage of uranium, the more complex fast reactors can't compete economically with thermal reactors—although some nuclear experts say breeders will one day be needed.

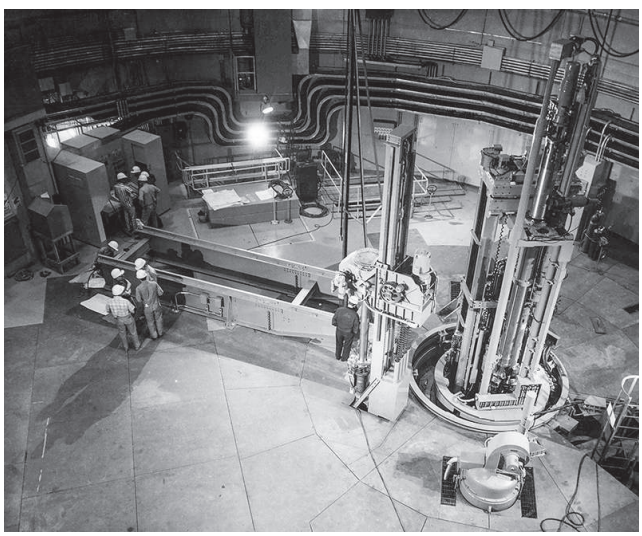

A new "fast" nuclear reactor would work a bit like the Experimental Breeder Reactor-II, which ran until 1994 at what is now Idaho National Laboratory.

PHOTO: IDAHO NATIONAL LABORATORY

In April, INL invited industry to help design a modest 300 megawatt sodium-cooled fast reactor that would burn a plutonium-based fuel made from retired nuclear weapons. The need for a research fast reactor to study materials and fuels emerged in 2015, when DOE's Office of Nuclear Energy reviewed its facilities, says Kemal Pasamehmetoglu, a nuclear engineer at INL who leads the project. "The one glaring gap was a lack of access to fast neutrons." Russia has the world's only fast-neutron test reactor.

Others are skeptical. "I don't see a compelling need for this facility," says Jacopo Buongiorno, a nuclear engineer at the Massachusetts Institute of Technology in Cambridge. He says the test reactor would come online too late to help companies now developing novel fast-reactor designs, such as Oklo Inc., of Sunnyvale, California. Oklo Co-Founder Caroline Cochran agrees that the reactor won't be ready in time to help the company, but says, "It will be a national resource in the decade to come."

Edwin Lyman, a physicist with the Union of Concerned Scientists in Washington, D.C., argues that INL's real goal is reviving its fast-reactor program. INL's sodium-cooled Experimental Breeder Reactor-II shut down in 1994. Pasamehmetoglu acknowledges that one reason to build the neutron source is to maintain expertise.

The debate over the test reactor mirrors a larger one over the future of nuclear energy, says Mark Hibbs, policy analyst with the Carnegie Institution for International Peace in Berlin. If nuclear energy provides a bridge to other carbon-free sources such as wind and solar, fast reactors won't be needed, he says. But if nuclear energy will be needed for centuries—as China anticipates—then utilities must eventually switch to fuel-breeding fast reactors, Hibbs says. The debate, he says, "is dominated by theology and lobbyists."

In Congress, the reactor has bipartisan support, especially from the House science committee, where Representatives Randy Weber (R–TX) and Eddie Bernice Johnson (D–TX) both sponsored the House bill. "We felt that there is a very clear need and it's timely," says one committee aide. "If we wait too long, all these companies will go to Russia."

The project is already taking an usual trajectory at DOE. According to agency rules, a major project must pass a review that certifies the need for the facility before moving on to designs. But in this case, Pasamehmetoglu says his team will develop the design and costing first, and present it to DOE for a yes or no decision in 2020.

That is a problem, Lyman says. "Clearly, they haven't done their due diligence to show that this facility is needed," he says. Before going further, Von Hippel says, DOE should ask the National Academies of Sciences, Engineering, and Medicine to study the need for the reactor. ■

FEATURES

HIDDEN CONFLICTS?

An investigation finds a pattern of after-the-fact compensation by pharma to those advising the U.S. government on drug approvals

By **Charles Piller**; *Data analysis by* **Charles Piller** *and* **Jia You**

On a sweltering July day in 2010, seven medical researchers and one patient advocate gathered in a plush Marriott hotel in College Park, Maryland, to review a promising drug designed to prevent heart attacks and strokes by limiting blood clotting. The panel is one of dozens of advisory committees that vote each year on whether the Food and Drug Administration (FDA) should approve a therapy for the U.S. market. That day, panel members heard presentations on the drug's preclinical and clinical data from agency staff and AstraZeneca in Cambridge, U.K., its maker and one of the world's largest pharmaceutical companies. The occasion sparked little drama. In the cool refuge of the conference room, advisers politely questioned company scientists and complimented their work. By day's end, the panel voted seven to one to approve. FDA, as usual, later signed off. The drug, ticagrelor, marketed under the name Brilinta, sold rapidly, emerging as a billion-dollar blockbuster. It cuts risk of death from vascular causes, heart attacks, and strokes modestly more than its chief competitor—and currently costs 25 times as much.

FDA, headquartered in Silver Spring, Maryland, uses a well-established system to identify possible conflicts of interest before such advisory panels meet. Before the Brilinta vote, the agency mentioned no financial conflicts among the voting panelists, who included four physicians. As Brilinta's sales took off later, however, AstraZeneca and firms selling or developing similar cardiovascular therapies showered the four with money for travel and advice. For example, those companies paid or reimbursed cardiologist Jonathan Halperin of the Icahn School of Medicine at Mount Sinai in New York City more than $200,000 for accommodations, honoraria, and consulting from 2013 to 2016. During that period, Halperin got $7500 from AstraZeneca to study Brilinta, and the company separately declared nearly $2 million in "associated research" payments tied to him.

Brilinta fits a pattern of what might be called pay-later conflicts of interest, which have gone largely unnoticed—and entirely unpoliced. In examining compensation records from drug companies to physicians who advised FDA on whether to approve 28 psychopharmacologic, arthritis, and cardiac or renal drugs between 2008 and 2014, *Science* found widespread after-the-fact payments or research support to panel members. The agency's safeguards against potential conflicts of interest are not designed to prevent such future financial ties.

Other apparent conflicts may have also slipped by: *Science* found that at the time of or in the year leading up to the advisory meetings, many of those panel members—including Halperin—received payments or other financial support from the drugmaker or key competitors for consulting, travel, lectures, or research. FDA did not publicly note those financial ties.

The analysis, which used physician disclosures in freely available publications and Centers for Medicare & Medicaid Services records for 2013 to 2016 on the federal Open Payments website, examined direct payments to physicians from firms whose drugs were voted on. It also considered payments from competitors selling or researching drugs of the same class or intended for the same condition—because competing drugs might be affected positively or negatively by the market entry of a new contender or by restrictions or warnings placed on a new drug's label. *Science* further looked at research funding from a company to an FDA adviser, directly or through their institution. Such money—including "associated research" funding that nearly always supports principal investigators—affects a scientist's career advancement, compensation, or professional influence.

Among the investigation's key findings:

- Of 107 physician advisers who voted on the committees *Science* examined, 40 over a nearly 4-year period received more than $10,000 in post hoc earnings or research support from the makers of drugs that the panels voted to approve, or from competing firms; 26 of those gained more than $100,000; and seven more than $1 million.
- Of the more than $26 million in personal payments or research support from industry to the 17 top-earning advisers—who received more than $300,000 each—94% came from the makers of drugs those advisers previously reviewed or from competitors.
- Most of those top earners—and many others—received other funds from those same companies, concurrent with or in the year before their advisory service. Those payments were disclosed in scholarly journals but not by FDA.

Varying sums

An analysis of pharma payments to 107 physicians who advised FDA on 28 drugs approved from 2008 to 2014 found that a majority later got money for travel or consulting, or received research subsidies, from the makers of the drugs on which they voted or from competing firms.

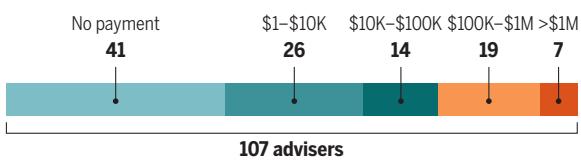

CREDITS: (ILLUSTRATION, OPPOSITE PAGE) STEPHAN SCHMITZ; (GRAPHIC) J. YOU/*SCIENCE*; (DATA) CENTERS FOR MEDICARE & MEDICAID SERVICES/OPEN PAYMENTS

Corporate payments and other support given to advisers before a drug review are widely acknowledged as troubling. When "a voting member of a committee demonstrably had financial associations with the company or the competitor prior to the meeting, and the FDA doesn't flag it, then somebody's dropping the ball on due diligence," says Yale University physician Robert Steinbrook, editor at large for *JAMA Internal Medicine*.

Yet benefits that come later, even years after a drug approval vote—jobs, money, professional prestige, and influence—are also fraught, ethicists say. They are a way of "postponing your reward," says Carl Elliott, a medical ethicist at the University of Minnesota in Minneapolis who has persistently criticized the financial inducements pharma gives to researchers (*Science*, 23 May 2014, p. 793). "You do something positive for a company that you feel confident is going to pay you back for it later on. And they do."

Vinay Prasad, a hematologist-oncologist at Oregon Health & Science University in Portland who has studied financial conflicts in drug approvals, is similarly troubled. "The people who are asked to weigh this evidence impartially often stand to gain tremendously in their further professional careers from a positive relationship with the company," he says. It might not be a "quid pro quo," according to Prasad, "but you don't have to evoke that to be very concerned. It's in their best interest to play nice with these companies."

FDA declined interview requests about *Science*'s findings. A spokesperson provided a statement saying people serving on drug approval advisory panels must disclose any "prospective employer," but not anticipated payments. The statement further notes that "FDA also screens potential participants for relationships and situations that do not create a financial conflict of interest but that may create the appearance that a committee member lacks impartiality."

AstraZeneca spokesperson Karen Birmingham says "we are not aware" of any effort to support advisers after they serve on FDA panels reviewing the company's drugs, "other than the routine involvement in clinical trials or expert panels for which that [adviser] may have been sought independently because of their expertise."

Halperin says a direct payment from a drug company for a lecture or consulting "isn't really very much different than having an insurance company giving you a check for seeing a patient one day. It's the same thing." He adds that he did not personally benefit from more than $1.9 million in research funds that AstraZeneca declared. He says the funds were paid to Duke University in Durham, North Carolina, to support a major study of Brilinta and that his role was to chair its data monitoring committee. His 2009 recommendation for Brilinta's approval, he says, was not influenced by anticipation of large payments or research funding from AstraZeneca or its competitors. And Halperin argues that such relationships may be the price of expertise. "It's probably better to have someone who has some experience in [the specialized topics considered] than a bunch of unconflicted high school students," he says.

But the cardiologist agrees that expectations of future rewards can promote bias. "I share [the] concern that this could lead to people acting in ways that you would not want them to do," Halperin says. "We don't want incentives that are not serving the public interest. In my case, it's the patient's interest." And he notes that some medical organizations have begun to address delayed incentives. They ask members who write clinical practice guidelines to avoid financial relationships with affected companies for a period afterward—a tougher standard than what FDA requires for its advisers.

That solution and others should be up for debate, say ethicists and regulatory experts, including one prominent former FDA employee. "The idea of banning future payments is likely to have a lot of thorny aspects, but it's worth discussing," even at the risk of losing some experts to government service, says David Kessler, FDA commissioner under former Presidents George H. W. Bush and Bill Clinton. "It's a balancing act, but public trust is paramount."

JACOB SITKO ENLISTED in the U.S. Army in January 2008 and gave his heart and soul to it for more than 3 years—for a time serving in Iraq as a Humvee gunner in the infantry. In 2011, the private died in bed at his barracks at Fort Carson in Colorado, where he was being treated for posttraumatic stress disorder (PTSD). Months later, the Army finally gave Sitko's heart back to his mom.

Lois Vinall cries softly as she recounts her son's story. Right after his death, the Army told her that Sitko, who was 21 and in good health other than his PTSD, had been killed by "mixed-drug intoxication." Army doctors had been giving him a cocktail of medicines that included quetiapine,

After the Brilinta vote

In 2010, FDA advisers voted to recommend approval for Brilinta, which helps prevent blood clots in heart-disease patients. Four physicians who voted later received funds from AstraZeneca, its maker, and competing firms for consulting and travel, or worked on research underwritten by those companies.

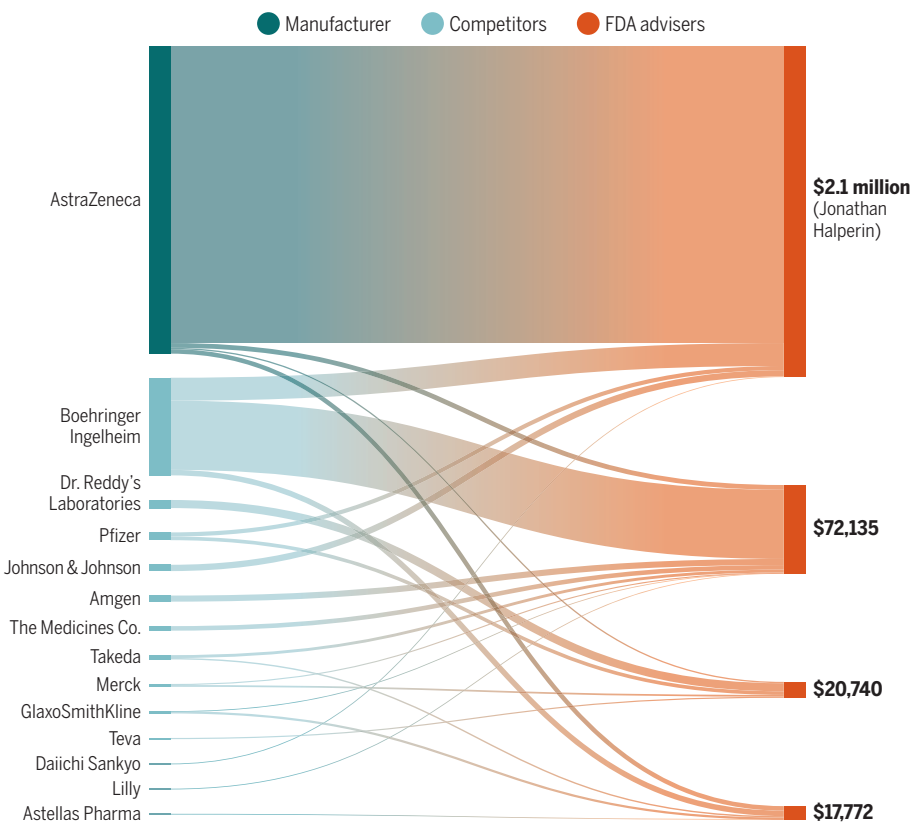

CREDITS: (GRAPHIC) J. YOU/*SCIENCE*; (DATA) CENTERS FOR MEDICARE & MEDICAID SERVICES/OPEN PAYMENTS

a top-selling antipsychotic from AstraZeneca sold under the name Seroquel. The particular mixture had been linked for years to sudden cardiac death, though no evidence has been made public that Sitko was told that.

"They sent his body home without his heart" and didn't say why, Vinall says. "They returned it in a baby coffin to me 3 months later, wrapped in green felt." Vinall recently learned that after removing her son's heart, the Army decided not to examine it further. She says a military medical examiner told her Sitko's autopsy hadn't been correctly "certified" and that her son might have suffered cardiac death. Vinall had cremated his body but buried his heart in a veterans' cemetery in Redding, California, close to family.

Two years earlier, two panels of FDA advisers had considered whether to approve Seroquel for new conditions—schizophrenia and bipolar disorder in children, and depression in adults who are taking other medicines. Seroquel was then known to be associated with sudden cardiac death when used with certain drugs, and several antipsychotics similar to Seroquel also had a record of cardiac fatalities. But AstraZeneca presented results from its clinical studies, which company representatives said showed, at worst, minimal risks (see sidebar, p. 21).

In 2009, both panels voted by wide margins to approve Seroquel for the additional conditions. In the years afterward, several FDA advisers received significant financial support from AstraZeneca and the makers of competing drugs. The biggest payments went to Duke cardiologist Christopher Granger, who sat on one of the two groups. From 2013 to 2016, the period recorded by Open Payments, he or Duke on his behalf received more than $63,000 from AstraZeneca and $1.3 million from competitors. According to conflict-of-interest disclosures in journal articles on which Granger was an author, he received additional, unspecified amounts from those companies between 2010 and 2012.

Granger says the industry funds solely underwrote research on cardiovascular topics and did not augment his salary. But according to the federal data, more than $400,000—including all of AstraZeneca's portion—went to him for travel, consulting, and honoraria.

"I fully realize that when I'm paid by somebody, like every other human being, that may affect the way that I think about things. So I'm not naïve," Granger says. But the expectation of future support from the makers of antipsychotics, he adds, did not influence his assessments of Seroquel or similar drugs. Granger says he recommended the drug's conditional approval after becoming convinced—as were nearly all others on his panel—that Seroquel's value outweighed its risks for some people with severe psychiatric disabilities.

The next year, in 2010, AstraZeneca paid the government $520 million to settle lawsuits involving alleged improprieties in the company's clinical trials and improper marketing of Seroquel for unapproved conditions. The company, which denied wrongdoing, pulled in more than $5 billion in revenues from the drug that year. In 2011, after mounting evidence of sudden cardiac deaths, FDA forced AstraZeneca to add a warning to Seroquel's label that the drug posed risks of fatal cardiac events when combined with certain other drugs. Sitko died 3 weeks later.

In recent years, FDA has fielded thousands of complaints about cardiac problems, including many deaths, tied to Seroquel. Granger calls the drug's widespread use for unapproved conditions, such as insomnia, a "public health tragedy." Sitko and many others were given the drug, in part, to treat insomnia. The company has said repeatedly that Seroquel is acceptably safe and effective to treat conditions for which FDA approved it.

> ***"I share [the] concern that this could lead to people acting in ways that you would not want them to do."***
>
> **Jonathan Halperin**, Icahn School of Medicine at Mount Sinai

POLICING FUTURE DRUG INDUSTRY payments received by FDA advisory committee members would be challenging even for an agency adept at limiting conflicts of interest. Yet *Science*'s investigation raises questions about how well FDA enforces more traditional conflict rules.

FDA asks panel members who vote on recommending drug approvals to disclose in advance details of investments, contracts, or other payments from drugmakers. The agency uses those disclosures to determine whether pharma backing during or before a meeting should disqualify an adviser. Each adviser must "certify to the truth and completeness of any information provided," according to the FDA statement to *Science*. The agency can issue a waiver to permit participation despite an active conflict or one that ended during the 12 months preceding a meeting if special expertise cannot readily be obtained otherwise. That system helps secure researchers with "deep scientific and medical expertise," Kessler, a pediatrician and lawyer now at the University of California, San Francisco, says.

But the agency's financial review process is primarily an honor system and seems to miss obvious conflicts. For the 17 physicians receiving the most compensation after a drug advisory vote, *Science* examined whether they also received industry compensation concurrent with or shortly before their FDA service. Evidence of such payments came from conflict-of-interest statements in journal articles that those authors published near the time of their advisory role. Eleven physicians acknowledged support from competing companies on one or more drugs they reviewed. Five of those also received such funding from the makers of one or more of the drugs. Yet FDA publicly noted none of those apparent conflicts and issued no conflict waivers.

Science found that AstraZeneca and makers of rival drugs made payments to, or funded research by, several FDA advisers—including Granger—in the year leading up to the 2009 meetings on Seroquel. Granger calls full financial disclosure "crucially important" in order for FDA to assemble the best committee. "I certainly hope that I disclosed everything," he says. "If I hadn't, I would be horrified because that's antithetical to everything I believe in." After initially offering to share his disclosure forms, Granger did not respond to repeated requests for copies. In response to a Freedom of Information Act (FOIA) request, FDA says it could not locate his documents.

Halperin has a similar history. In addition to receiving funds from AstraZeneca and its competitors after he voted to approve the anticlotting drug Brilinta, Halperin was receiving unspecified payments or research support from rival firms during the 12 months before the meeting. He says he disclosed the payments to FDA and that it did not flag them as conflicts. *Science* requested copies of his disclosure materials, but Halperin did not provide them. Again, FDA says it could not locate Halperin's disclosures.

"The system is dependent on the truthfulness of the self-reporting of disclosures," says Genevieve Kanter, a University of Pennsylvania economist who has studied conflicts of interest in FDA drug evaluations. She calls *Science*'s findings of payments to advisers during the year before a committee meeting "significant." And she added that such payments would be "stunning" if consistently large.

The journal disclosures don't specify payment amounts, and the Open Payments data cover only a few years, making such a pattern impossible to show. But an FDA advisory committee that in 2016 voted unanimously to recommend approval of adalimumab-atto (Amjevita), Amgen's immune-altering drug for rheumatoid arthritis, serves as one striking example. Amjevita, which FDA then greenlighted, is similar to AbbVie's

blockbuster adalimumab (Humira), and experts believe Amjevita will be a big seller.

Rheumatologist Daniel Solomon of Harvard Medical School in Boston chaired the Amjevita panel. Neither FDA nor Solomon disclosed publicly that about 3 months before that meeting, Amgen provided $232,000 for his study of etanercept (Enbrel), another arthritis drug made by Amgen, and 1 month before the meeting AbbVie provided $819,000 for a Solomon study of Humira.

That support was for "in-kind donations" of drugs "evaluated as part of a NIH-funded research study for which I am one of the principal investigators," Solomon wrote in an email. He does not regard them as a conflict with Amjevita's approval. Drug donations, a common practice, benefit both parties. Donated drugs help ensure that leading academic specialists will prioritize a company's product in major studies that also enhance the researcher's professional standing and influence. Solomon says he described the payments in an FDA disclosure, but he hadn't kept a copy. The agency rejected a FOIA request for the document, calling its release "a clearly unwarranted invasion of personal privacy."

From such responses, it's not clear whether the agency knew about those potential conflicts and, if so, whether officials decided they didn't warrant a waiver. FDA would not discuss any individual adviser or detail what, if anything, the agency does to validate advisers' disclosures.

Kanter says she favors more research to learn how commonly payments are not disclosed by advisers, or by FDA, to "give us a sense of whether the agency should do some independent verification."

Kessler suggests that greater FDA transparency also could help. "Maybe we need to think about whether the process for reviewing conflicts of interest should be done in a more open, independent manner than the current black box the agency uses," he says. But the former agency head warns that FDA still must find and retain the relatively few specialists "who really can contribute to the issues at hand with exquisite, detailed experience." When so many of them take pharma money, Kessler adds, the agency has to be flexible.

Halperin—one of the 17 top earners and a national leader in cardiology research and practice—puts it bluntly: "The key is disclosure, not squeaky cleanness."

Yet some ethicists say such arguments are unconvincing, if not self-serving. The 107 advisers that *Science* reviewed, combined with 11 federal scientists who served on at least one of the 28 review panels and remain with the government, suggest that potential conflicts can be avoided and often are. Among that group, 47 took less than $800 from pharma after their service on the advisory panel. Thirty-four took no money at all. (Regular federal employees can almost never accept outside compensation.) Elliott argues that the prestige and importance of serving on an FDA advisory committee would outweigh the lure of industry financial favors for many more discipline experts if FDA forced them to choose.

The European Medicines Agency in London, the closest analog to FDA, does force such choices. It has no policy on payments to advisers after serving on a drug advisory panel. However, it bars advisers who have concurrent financial ties to drug companies whose products are under consideration, and it prohibits or strictly limits the participation of advisers whose connections to a company go back at least 3 years before an advisory meeting. Disqualifying factors can include speaking fees, consulting contracts, and research grants—both for scientists conducting industry-sponsored studies and for those, like Halperin, who work on data monitoring committees. The agency investigates financial disclosures on its own initiative or after tips from whistleblowers.

Given the apparent gaps *Science* found, Kanter says the FDA system for evaluating possible conflicts of interest—hidden from the public and based primarily or completely on adviser disclosures—might be strengthened to guard against the clearest causes of potential bias. For example, she found that advisory committee members are more likely to vote for a drug's approval if their financial ties were exclusively to that drug's maker rather than to several companies.

Elliott suggests a more radical solution. "Even in the best of circumstances, disclosure is a remarkably weak way of controlling conflicts of interest," he says. "A better way would simply be for the FDA to say, 'We are not taking anybody with any kind of conflict on an advisory committee.'" ■

After the Seroquel vote

In 2009, FDA advisers voted to recommend approval of the antipsychotic Seroquel for new indications, despite data linking the drug and similar offerings to sudden cardiac death. Four physicians who voted later received funds for consulting, travel, or research from AstraZeneca, Seroquel's maker, and its competitors.

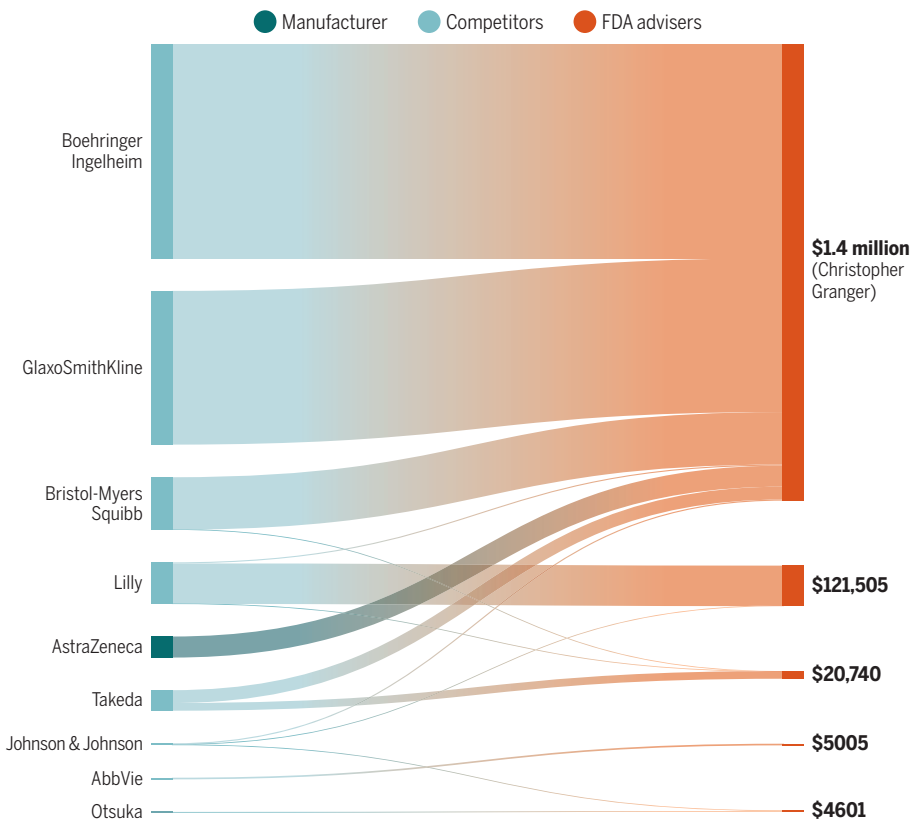

The methodology and data for this story are online at https://scim.ag/FDAanalysis. Meagan Weiland and Katie Langin contributed reporting. The story was supported by the Science *Fund for Investigative Reporting.*

CREDITS: (GRAPHIC) J. YOU/*SCIENCE*; (DATA) CENTERS FOR MEDICARE & MEDICAID SERVICES/OPEN PAYMENTS

Is FDA's revolving door open too wide?

By **Charles Piller**

The Food and Drug Administration (FDA) says its rules, along with federal laws, stop employees from improperly cashing in on their government service. But how adequate are those revolving door controls? *Science* has found that much like outside advisers (see main story, p. 16), regular employees at the agency, headquartered in Silver Spring, Maryland, often reap later rewards—jobs or consulting work—from the makers of the drugs they previously regulated.

FDA staffers play a pivotal role in drug approvals, presenting evidence to the agency's advisory panels and influencing or making approval decisions. They are free to move to jobs in pharma, and many do; in a 2016 study in *The BMJ,* researchers examined the job histories of 55 FDA staff who had conducted drug reviews over a 9-year period in the hematology-oncology field. They found that 15 of the 26 employees who left the agency later worked or consulted for the biopharmaceutical industry.

FDA's safeguards are supposed to keep the prospect of industry employment from affecting employees' decisions while at the agency, and to discourage them from exploiting relationships with former colleagues after they depart. For example, former high-level employees can't appear before the agency on the precise issues they regulated—sometimes permanently, in other cases for a year or two.

Through web searches and online services such as LinkedIn, however, *Science* has discovered that 11 of 16 FDA medical examiners who worked on 28 drug approvals and then left the agency for new jobs are now employed by or consult for the companies they recently regulated. This can create at least the appearance of conflicts of interest.

In 2009, for example, an FDA panel weighed whether the agency should approve AstraZeneca's widely prescribed antipsychotic drug quetiapine (Seroquel) for a wider range of conditions. The panel heard from health policy expert Wayne Ray of Vanderbilt University in Nashville, who described his research linking the drug to sudden cardiac death when used with certain other medications. Ray recalls "an FDA staff member who gave a very negative presentation on our paper." That staffer, according to a meeting transcript, was the agency's then-Director of Psychiatric Products Thomas Laughren, who was instrumental in shepherding Seroquel and similar drugs through the review process and personally signed their FDA approvals.

At the meeting, Laughren defended AstraZeneca's clinical trial findings. The company's "analysis should have been able to pick up a difference in sudden cardiac death, and they didn't find any difference between drug and placebo," he said.

Ray told Laughren and the panel that AstraZeneca had pooled data from all its trials as though the data were one data set, causing a well-known statistical error called Simpson's paradox. To take the company's conclusion "as definitive" would be "very

dangerous," Ray said, according to the transcript. Laughren responded by calling sudden death "a pretty definitive event."

Ultimately, the committee voted overwhelmingly to advise approval of the drug for new indications and made no recommendation on labeling it to warn about sudden cardiac death. Later evidence showed that the cardiac problems Ray described are real, and in 2011, FDA required adding a warning on Seroquel's label.

Soon after, Laughren left the agency and formed a consultancy to help psychiatric drug makers, including AstraZeneca, navigate FDA approvals. He did not respond to repeated requests for comment.

In 2012 and 2013, data expert Joan Buenconsejo led FDA's analysis of medical statistics in drug reviews, including offerings from AstraZeneca. In 2014, she joined the company as a director and biometrics team leader. By 2015, Buenconsejo had already represented AstraZeneca before her former FDA colleagues as the company sought a drug's approval. In an email, Buenconsejo wrote that she strictly adhered to FDA's recusal rules "when considering employment with AstraZeneca." She added, "I do not believe there was any conflict of interest around my transition."

Former FDA employees, AstraZeneca spokesperson Karen Birmingham wrote in an email, "bring the perspective of seasoned regulators" who can assist current regulators with the "challenging decisions in approving innovative medicines to meet unmet medical needs."

Jeffrey Siegel, who was an FDA staff member specializing in reviews for arthritis drugs, oversaw the 2010 approval of Genentech's arthritis drug tocilizumab (Actemra). Months later, he left the agency to join the company and its parent, Roche, as director of the division that includes Actemra and related offerings. Siegel represented Roche before his former FDA colleagues when the company sought approval to promote Actemra for new conditions. Last year, he told *STAT* that the timing of his decision to join Roche and Genentech was coincidental.

Laughren, Buenconsejo, and Siegel apparently complied with existing federal laws and FDA requirements. And David Kessler, who led FDA under former Presidents George H. W. Bush and Bill Clinton, says such moves to industry by former FDA experts, steeped in "a culture of drug regulation," can benefit the public if they improve pharma practices. But "revolving door" rules need a fresh look, he adds, to ensure that "the tipping point, where that balance is," serves the public interest.

Vinay Prasad, a hematologist-oncologist at Oregon Health & Science University in Portland who co-wrote the 2016 study in *The BMJ*, contends that weak federal restrictions, plus an expectation of future employment, inevitably bias how FDA staffers conduct drug reviews.

"When your No. 1, major employer after you leave your job is sitting across the table from you, you're not going to be a hard-ass when you regulate. That's just human nature."

ILLUSTRATION: STEPHAN SCHMITZ

Corrected 6 July 2018. See full text

INSIGHTS

BOOKS *et al.*

SCIENCE & THE ARTS

STEMM education should get "HACD"

Incorporating humanities, arts, crafts, and design into curricula makes better scientists

By **Robert Root-Bernstein**

If you've ever had a medical procedure, chances are you benefited from the arts. The stethoscope was invented by a French flautist/physician named René Laennec who recorded his first observations of heart sounds in musical notation. The suturing techniques used for organ transplants were adapted from lacemaking by another Frenchman, Nobel laureate Alexis Carrel. The methods (and some of the tools) required to perform the first open-heart surgeries were invented by an African-American innovator named Vivien Thomas, whose formal training was as a master carpenter.

But perhaps you're more of a technology lover. The idea of instantaneous electronic communication was the invention of one of America's most famous artists, Samuel Morse, who built his first telegraph on a canvas stretcher. Actress Hedy Lamarr collaborated with the avant-garde composer George Antheil to invent modern encryption of electronic messages. Even the electronic chips that run our phones and computers are fabricated using artistic inventions: etching, silk-screen printing, and photolithography.

On 7 May 2018, the Board on Higher Education and Workforce of the U.S. National Academies of Sciences, Engineering, and Medicine (NASEM) released a report recommending that humanities, arts, crafts, and design (HACD) practices be integrated with science, technology, engineering, mathematics, and medicine (STEMM) in college and post-graduate curricula (*1*). The motivation for the study is the growing divide in American educational systems between traditional liberal arts curricula and job-related specialization. "Ironically," the report notes, "as this movement toward narrower, disciplinary education has progressed inexorably, many employers—even, and, in fact, especially in 'high tech' areas—have emphasized that learning outcomes associated with integrated education, such as critical thinking, communication, teamwork, and abilities for lifelong learning, are more, not less, desirable."

Because the ecology of education is so complex, the report concludes that there is no one, or best, way to integrate arts and humanities with STEMM learning, nor any single type of pedagogical experiment or set of data that proves incontrovertibly that integration is the definitive answer to improved job preparedness. Nonetheless, a preponderance of evidence converges on the conclusion that incorporating HACD into STEMM pedagogies can improve STEMM performance.

Large-scale statistical studies have demonstrated significant correlations between the persistent practice of HACD with vari-

The author is a MacArthur Fellow at the Department of Physiology, Michigan State University, East Lansing, MI 48824, USA, and the author of a forthcoming book tentatively titled Modern Leonardos: Artists, Musicians, and Performers as Scientists and Inventors. *Email: rootbern@msu.edu*

PHOTO: IMAGEBROKER/ALAMY STOCK PHOTO

Art, science, and music converge in a graffiti portrait of Mozart and Einstein in Duisburg, Germany.

PHOTO: MONDADORI PORTFOLIO/CONTRIBUTOR/GETTY IMAGES

ous measures of STEMM achievement. Niemi reports, for example, that individuals who practice the arts are more likely to file patents (*2*). My colleagues and I, meanwhile, have found that STEMM professionals with avocations such as wood- and metalworking, printmaking, painting, and music composition are more likely to file and license patents and to found companies than those who lack such experience (*3*). Likewise, authors that publish high-impact papers are more likely to paint, sculpt, act, engage in wood- or metalworking, or pursue creative writing (*4*). Members of the U.S. National Academies of Sciences and Engineering are about three to five times more likely to have a lifelong avocation involving arts, crafts, theater, or some type of creative writing than are average scientists, and Nobel Prize winners engage in such activities at 15 to 25 times the rate of average scientists (*5*).

Every scientist knows that correlation is not causation, but many STEMM professionals report that they actively integrate their HACD and STEMM practices. In 2013, my colleagues and I conducted a survey of 225 scientists and engineers and found that more than 60% could cite a direct impact of their HACD activities on their STEMM work, and over 80% recommended that HACD be a required part of STEMM education (*6*).

"I spent vast hours in a woodworking shop [my father] maintained in the basement of our house, building gadgets," wrote Richard Smalley, winner of the 1996 Nobel Prize in Chemistry, in his Nobel autobiography. "My mother taught me mechanical drawing so that I could be more systematic in my design work, and I continued in drafting classes throughout my 4 years in high school. This … was a wonderful preparation for my later career as an experimentalist working on the frontiers of chemistry and physics."

Nobel laureate Dorothy Crowfoot Hodgkin attributed her success in crystallography, in part, to learning symmetry operations as a teenager while illustrating floor tilings for her parent's archaeological papers. "I began to think of the restraints imposed by two-dimensional order in a plane," she reveals in Georgina Ferry's 1998 biography (*7*).

Artistic innovations can even drive sciences and technologies. In 1990, for example, the National Endowment for the Arts funded a collaboration between conceptual artist Mel Chin and botanist Rufus Chaney to create an environmental art experiment called *Revival Field*. The piece provided the first proof of concept that plants can take harmful compounds such as lead, arsenic, and cobalt out of contaminated soil. Chin and Chaney's collaboration opened up a phytoremediation market currently estimated to be worth $36 billion to $54 billion in the United States and Europe. Not a bad return on an investment of $70,000.

Analyses of hundreds of individual case studies reveal that STEMM professionals often link HACD with STEMM practices by means of 13 mental "tools for thinking": observing (using any or all senses); imaging; abstracting; pattern recognition; pattern forming; dimensional thinking; analogizing; proprioceptive (or body) thinking; empathizing or play-acting (Nobel laureate Barbara McClintock reported having "a

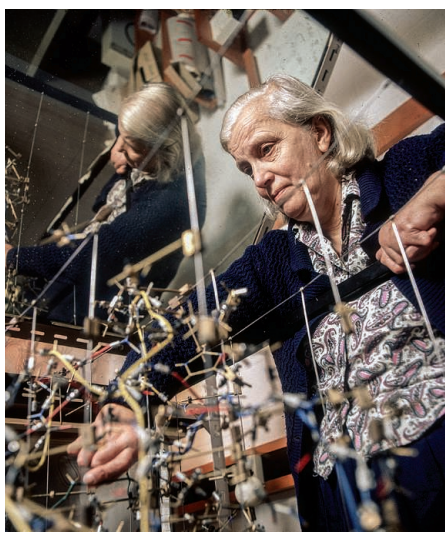

Nobel laureate Dorothy Hodgkin applied lessons learned from drawing to crystallography.

feeling for the organism" and Jonas Salk of "becoming the virus"); modeling; playing; transforming between these various ways of thinking; and synthesizing (*8*).

Such tools have also proven to be useful for successfully integrating HACD-STEMM pedagogies in K—12, college, and postgraduate classrooms [reviewed in (*9*)]. Drawing, for example, develops observational and visual thinking skills that facilitate STEMM learning (*10*–*12*). Tailored musical or artistic pedagogical interventions improve visual and aural observational skills among STEMM students (*13*). And developing transformational and synthetic thinking skills by inventing and producing one's own scientific game or model has greater pedagogical effectiveness for STEMM students than passively playing with one (*14*, *15*).

HACD and STEMM disciplines are valuable to each other only to the extent to which they are understood to contribute complementary principles, methods, ideas, and content that have emerged from their characteristic approaches. One set of disciplines cannot become the handmaid of the other without losing their mutual benefits.

Integration occurs best through the building of conceptual or methodological "bridges" between disciplines for the purpose of addressing well-defined multi- or transdisciplinary problems. Integration is not a goal in and of itself, but rather a skill that needs to be developed in order to respond to the connectedness of the real world.

The NASEM report on STEMM-HACD integration repeatedly emphasizes that every real-world problem spans disciplinary boundaries. To quote the embryologist, dancer, and artist Conrad Hal Waddington, "The acute problems of the world can be solved only by whole men, not by people who refuse to be, publicly, anything more than a technologist, or a pure scientist, or an artist (*8*)." The late Charles M. Vest, president emeritus of the National Academy of Engineering and president emeritus of the Massachusetts Institute of Technology, concurred: "[Engineering] systems cannot be wisely envisioned, designed, or deployed without an understanding of society, culture, politics, economics, and communications—in other words, the very stuff of the liberal arts and also of the social sciences (*16*)." ■

REFERENCES

1. National Academies of Sciences, Engineering, and Medicine, *The Integration of the Humanities and Arts with Sciences, Engineering, and Medicine in Higher Education: Branches from the Same Tree* (National Academies Press, Washington, DC, 2018).
2. R. Lamore *et al.*, *Econ. Develop. Q.* **27**, 3 (2013).
3. L. Niemi, The Arts & Economic Vitality: Relationships Between the Arts, Entrepreneurship & Innovation in the Workplace (2015); https://www.arts.gov/sites/default/files/Research-Art-Works-BostonCollege.pdf
4. R. S. Root-Bernstein, M. Bernstein, H. Garnier, *Creativity Res. J.* **8**, 2 (1995).
5. R. Root-Bernstein *et al.*, *J. Psychol. Sci. Tech.* **1**, 2 (2008).
6. R. Root-Bernstein *et al.*, in *Creative Communities: Art Works in Economic Development* (National Endowment for the Arts and The Brookings Institution, Washington, DC, 2012), pp. 97–117 .
7. G. Ferry, *Dorothy Hodgkin: A Life* (Cold Spring Harbor Laboratory Press, Cold Spring Harbor, NY, 1998).
8. R. Root-Bernstein, M. Root-Bernstein, *Sparks of Genius. The Thirteen Thinking Tools of the World's Most Creative People* (Houghton Mifflin, New York, 1999).
9. R. Root-Bernstein, A. Pathak, M. Root-Bernstein, *Leonardo* **2017**, 10.1162/LEON_a_01581 (2017).
10. S. Ainsworth, V. Prain, R. Tytler, *Science* **333**, 6046 (2011).
11. J. C. Dolev, L. K. Friedlaender, I. M. Braverman, *J. Am. Med. Assoc.* **286**, 9 (2001).
12. D. H. Uttal, C. A. Cohen, *Psychol. Learning Motivation* **57**, 147 (2012).
13. J. C. Dolev, L. K. Friedlaender, I. M. Braverman, *J. Am. Med. Assoc.* **286**, 9 (2001).
14. D. Gurnon, J. Voss-Andreae, J. Stanley, *PLOS Biol.* **11**, 2 (2013).
15. M. K. Jarvinen, L. Z. Jarvinen, *J. Undergrad. Neurosci. Educ.* **11**, 1 (2012).
16. Union College Office of Communications and Marketing, "Top engineer calls integration of liberal arts and engineering essential" (3 June 2012); www.union.edu/news/stories/2012/06/top-engineer-calls-integration-of-liberal-arts-and-engineering-essential.php.

10.1126/science.aat8566

NEXTGEN VOICES

Broad interests reap benefits for science

We asked young scientists this question: **How do broad interests benefit your science?** Scientists with a variety of hobbies responded that their extracurricular activities have enhanced a wide range of skills, from creativity to communication to resilience. Many also mentioned the value of clearing their minds and relaxing. Follow NextGen and share your own hobbies on Twitter with #NextGenSci. —**Jennifer Sills**

As a rock climber, you have to risk falling in order to become better; the same principle applies in science. Realizing this has made me look at research failures in a more positive light—less as a demonstration of incompetence, and more of an opportunity to learn something and build resilience. I've learned that reminding yourself of your own competence (on the wall or in the lab) is a useful way to build up the courage to take more risks.

Beth M. Adamowicz
Biotechnology Institute, University of Minnesota, St. Paul, MN 55108, USA. Email: adamo010@umn.edu

As a biotechnologist, I manipulate experimental variables under the most precise conditions. Gardening, in contrast, is much less controlled. Not everything will go the way that I want it to go, but that's okay. I can try to eliminate slugs from my garden, and I can also restart an experiment while considering the previous trials. Gardening teaches me patience and reminds me that it is natural for things to go unexpectedly.

Derrick Ho Yan Chong
Department of Microbiology and Immunology, University of British Columbia, Vancouver, BC V6T 1Z4, Canada. Email: derrick.chong@alumni.ubc.ca

My experience as a cartoonist/comic artist has taught me how to take a complex visual image (such as a human face) and boil it down to key facial signatures that capture the essence of the person, and how to tell a story visually without text. These skills have helped me to express complex physics processes through simple schematics and to produce scientific figures that tell a visual "story" about the research topic.

Christopher Gutiérrez
Stewart Blusson Quantum Matter Institute, The University of British Columbia, Vancouver, BC V6T 1Z4, Canada. Email: christopher.gutierrez@ubc.ca

In sewing, you turn a flat pattern into a three-dimensional object. You need a good imagination and excellent spatial reasoning skills to do this effectively. As an entomologist, I try to discern subtle differences between closely related species. The skills I've developed while sewing have helped me to dissect and understand the intricate shapes of butterfly anatomy.

Jess Matz
La Vergne, TN 37086, USA.
Email: jessofthebugs@gmail.com

I have applied the lessons of aikido, a martial art of self-defense, to my science career: Avoid unnecessary arguments by understanding the opposite side, stop comparing myself with others, and focus only on my own path.

Evrim Fer
Department of Bioinformatics, Middle East Technical University, Ankara, 6800, Turkey.
Email: evrimfer@gmail.com

As an experimental physicist, I build semiconductor devices. My model aircraft building hobby helped prepare me for this work. When implementing a complex design, I always imagine how I would put together the base, interior, and outer armory of a model aircraft. Assembling models has provided me with a sense of smart design.

Emre Ozan Polat
ICFO-The Institute of Photonic Sciences, Mediterranean Technology Park, Castelldefels (Barcelona), 8860, Spain.
Email: emre-ozan.polat@icfo.eu

Woodworking engages a mode of thinking that differs from the mental process I use in the lab. Developing my mind through building has made me better at planning solutions several steps in advance and more willing to try to formulate my own problem-solving strategies. These skills have informed my bioinformatics work.

Harry MacKay
Department of Pediatrics, Baylor College of Medicine, Houston, TX 77030, USA.
Email: harry.m@gmail.com

Painting has opened my eyes to the hidden details of the world. Playing with colors stretches my creativity and helps me to see things in a different light. For a scientist, these are important skills.

Ruwansha Galagedara
Department of Anthropology, Binghamton University, Binghamton, NY 13902, USA.
Email: ruwansha89@gmail.com

Cooking has taught me that reproducing a recipe is not always an easy task, especially if crucial details are missing. I've learned that I should not spare any detail if I want others to be able to reproduce my experience,

PHOTO: ISTOCK.COM/TEMPURA

whether I'm making dinner or documenting experimental materials and methods.

Alexandre Coste
EuroMov, University of Montpellier, Montpellier, 34090, France.
Email: alexandre.coste1@umontpellier.fr

In collaborative role-playing games such as Dungeons & Dragons, a group of people work together to tell stories. These games require creative problem solving, communication, collaboration, and conflict-resolution skills. By playing a character, participants see problems from a different point of view. I apply the skills I've developed by playing role-playing games when working in multidisciplinary research projects, which require coordinating many collaborators and understanding the perspectives of scientists from different fields and different cultures.

Justina Pupkaite
University of Ottawa Heart Institute, Ottawa, ON K1Y4W7, Canada. Email: jpupk094@uottawa.ca

Chess has improved my analytical thinking, composure, and persistence. I have developed a habit of constantly evaluating research projects and looking for the right "move." In chess, I frequently have to make decisions under time pressure; this has helped me stay composed and think clearly even when deadlines are close. In chess, as in research, you do not always win, but you learn more from your losses than you do from winning, and learning from losses is the only way to improve.

Amir M. Farnoud
Department of Chemical and Biomolecular Engineering, Ohio University, Athens, OH 45701, USA. Email: farnoud@ohio.edu

In today's political, partisan and information-dense world, being right is not enough; you have to convince your audience to listen. As a Renaissance Faire performer, I practice reading the audience, following their cues, and timing jokes for maximum impact. These skills allow me to stand in front of a professional audience, regulatory panel, or commission and deliver a message that not only conveys information but also holds my audience's attention.

Colin W. Murphy
Nextgen Policy Center, San Francisco, CA 94104, USA. Email: persuasivescience@gmail.com

Learning Spanish and American Sign Language has made me a better science communicator. American Sign Language is partly the signs themselves, but also partly facial expressions. This has tricked my brain into being more expressive when I speak English. Of course, not everything translates directly from English to other languages. Thus, I have become more aware of my word choices. Like any new skill, learning languages reminds me how it feels to be a novice. Because I struggle to learn languages, I am more empathetic when communicating science.

Easton R. White
Center for Population Biology, University of California, Davis, Davis, CA 95616, USA.
Email: eastonrwhite@gmail.com

By playing the guitar, I have learned how to improvise and think outside the box, which is vital for working in Croatia. After the war, we sometimes could not find sufficient grants for all of our needs, so we had to use our resources creatively.

Iva Rezic
Faculty of Textile Technology, University of Zagreb, Zagreb, 10000, Croatia. Email: iva.rezic@ttf.hr

Every time I bake a loaf of bread, I am reminded of my research. Because gravity on asteroids is very weak, the cohesive forces between grains are relatively strong. Cohesion is also responsible for the steep cliffs that form in baking flour. Just as flour sticks to your hands, grains on an asteroid could stick to astronaut gloves. Baking is my field work. It gives me an intuitive understanding of the near-surface asteroid environment.

Christine Hartzell
Department of Aerospace Engineering, University of Maryland, College Park, MD 20742, USA. Email: hartzell@umd.edu

The amount of originality that comedy requires makes performing stand-up an incredibly vulnerable craft; an audience's silence in response to an act you've invested so much into can feel like a personal defeat. Science requires a similar intimacy with our work. With countless weekends and holidays spent in the lab, our work can become an integral part of our identity, and scientific setbacks can feel like personal failures. Every day, I come to the lab with the persistence that I learned performing stand-up, and I am a better researcher because of it.

Allison Matia
Psychology Department, Rutgers University, Piscataway, NJ 08854, USA.
Email: acm263@scarletmail.rutgers.edu

As a scientist, I am increasingly focused on specific skills and subjects of study, and I may miss the big picture. Contemporary dance allows me to think in an unstructured and unpredictable way, different from the controlled scientific environment. Dancing connects my body with my mind and with what surrounds me; it challenges me to question established truths, overcome my limitations, and be creative.

Marcela Viviana Nicola
Instituto de Botánica Darwinion, B1642HYD San Isidro, Buenos Aires, Argentina.
Email: mnicola@darwin.edu.ar

I seek out the history of nearby towns. Many of my weekends are filled with road trips to these obscure locations, and I am consistently filled with awe at the step-by-step progress of long-forgotten persons who helped make the world a better place. These historical ventures provide me a moment to reflect on the immediate task at hand. Analogous to the building of cities, scientific advances are made one spilled chemical after another. This perspective guides my work each day.

Kyle J. Isaacson
Department of Bioengineering, University of Utah, Salt Lake City, UT 84112, USA.
Email: kyle.isaacson@utah.edu

I have engaged with my community, as a Humanity in Action fellow and departmental representative for equity and diversity, to bring about positive social change. I strive to be radically kind and to seek justice for voices that have been silenced. I bring this urgency for social activism to my science. I must be socially responsible in the questions I ask, my methodological processes, and the conclusions that I draw from the data. The pursuit of knowledge must be inclusive and equitable, or else it's not worth doing.

Mehrgol Tiv
Department of Psychology, McGill University, Montreal, QC H3A 1G1, Canada.
Email: mehrgol.tiv@mail.mcgill.ca

It can be easy in science to get caught up in the frustration of an experiment not working or the disappointment of negative

reviewer comments on a manuscript. Yoga has helped me realize that these external forces do not define me, and it's up to me how I handle stressors when they arise. Yoga allows me to step back and be less stressed, which makes me more present and focused when I am in the lab.

Aliyah M. Weinstein
Carter Immunology Center, University of Virginia, Charlottesville, VA 22908, USA.
Email: aliyahweinstein@gmail.com

The highly technical demands and progressive nature of Olympic weightlifting make it a slow, laborious, and often frustrating endeavor. Like science, progress is nonlinear. The process of mastering the lifts is a daily grind and not always glamorous, but the outcome is highly rewarding. This sport has instilled in me a deep patience, persistence, and resilience—qualities that have carried over into my research.

Sarah Ch'ng
Florey Institute of Neuroscience and Mental Health, Parkville, VIC 3052, Australia.
Email: sarah.chng@florey.edu.au

Playing the saxophone builds my confidence and enhances my creativity—both skills I need in my work. Just like science, music requires precision, teamwork, and an ability to think about what you're creating and what you want to show.

Melissa Sweeney
Department of Biochemistry, Monash University, Clayton, VIC 3800, Australia.
Email: melissa.sweeney@monash.edu

The slow but steady nature of progress in ballet has prepared me for the similar pace of experiments. Ballet has also helped me understand how to be creative in science. Both science and ballet provide a structure within which to explore, anchored by technique or technology. In ballet class, I use the space inside the choreography to make it my own. Understanding this has taught me that creativity in science can look similar: I can find places where other people haven't looked and adjust them to create my own style.

Anna Lipkin
University of California, San Francisco, CA 94122, USA. Email: anna.lipkin@ucsf.edu

As a crisis counselor with the Crisis Text Line, I've learned how to support people in crisis through active listening and collaborative problem-solving. Scientific research involves a multitude of experimental, cultural, and personal setbacks, which can substantially affect mental health. Being a scientist means not only executing experiments but also maintaining a healthy lab atmosphere. My counseling skills help me to promote a lab environment that supports mental health and nurtures curious minds.

Sayantan Chakraborty
National Institute on Aging, NIH, Baltimore, MD 21224, USA. Email: sayantan.chakraborty@nih.gov

I use creative writing as a form of escapism, especially when I'm struggling in my research or in desperate need of a fresh perspective. Creating characters, plots, and conflicts mirrors research framing and design.

Edmond Sanganyado
Marine Biology Institute, Shantou University, Shantou, Guangdong, 515063, China. Email: esang001@ucr.edu

Joining a progressive Christian church community was by far the non-science interest of mine that most improved my ability to be a scientist. Open-minded religious communities have a broad cross-section of society with diversity in age, ethnicity, sexual orientation, income, interests, and backgrounds personally, professionally, and geographically. Being part of a diverse community opened my mind and helped me see the world from different (and dare I say, nonscientific) perspectives. Learning to discuss, deliberate, disagree, and listen together was the heart of this religious community, where we wrestled with questions about life, morality, ethics, society, and justice all in the face of current events. Engaging with this community enriched me by requiring me to think in different ways and from different perspectives, which has made me not just a better scientist but also a better human being.

Sarah Marie Anderson
Washington, DC 20018, USA.
Email: sarah.m.anderson.10@gmail.com

When writing fiction you must present your world such that the reader wants to enter it. This applies science writing as well. You must entice readers with a good premise, introduce them to the background of your field, bring them through the journey of what you have done, and finish with a climax of what you have learned. Research is just data, but writing makes that data into a story.

Neilson Nguyen
Brainwave Phantom, Mississauga, ON L4Z 2J1, Canada. Email: neilson.nguyen.phd@gmail.com

In ground fighting, chokes and joint locks are applied to submit your opponent. The sport has given me the mental strength to deal with the stressful situations that I, as a female scientist, face every day. We all have our battles, whether they are on the mat, in the office, or in our heads. Thanks to my hobby, I now know that no matter the outcome, I either win or I learn.

Triin Laisk
Department of Obstetrics and Gynecology, University of Tartu, Tartu, 51014, Estonia.
Email: triin.laisk@ut.ee

Conservation science is a never-ending grind punctuated by rare victories. While other disciplines unlock innovations and achievements, ours is focused on the cessation of loss. And conservation scientists often face abuse by people who feel the discipline infringes on economic progress. Competitive swimming helped prepare me for these challenges. Victory in the pool means a total commitment to training, mostly in the wee hours of the morning when no one is watching. It means racing with everything you have, and not giving an inch until the race is won. When you do win, the cycle begins all over again. Swimming has taught me to remain committed to goals that others may not understand.

Brett Favaro
School of Fisheries, Fisheries and Marine Institute of Memorial University of Newfoundland, St. John's, NL A1C5R3, Canada.
Email: brett.favaro@mi.mun.ca

10.1126/science.aau3978

Ceramic figure is of an ancient American dog from western Mexico (300 BC to 300 AD).

PHOTO: ALERT SEATED CANINE EFFIGY VESSEL, 300 BC TO 300 AD (EARTHENWARE WITH SLIP), COLIMA CULTURE/ MUSEUM OF FINE ARTS, HOUSTON, TEXAS, USA/MUSEUM PURCHASE FUNDED BY MEREDITH J. LONG IN HONOR OF FAYEZ SAROFIM AND ALFRED C. GLASSELL JR. AT "ONE GREAT NIGHT IN NOVEMBER, 1994"/BRIDGEMAN IMAGES

GENOMICS

America's lost dogs

The dogs that arrived in the Americas with human settlers ~10,000 years ago left almost no genetic traces

By **Linda Goodman**[1,2] *and* **Elinor K. Karlsson**[1,3]

Few traces remain of the domesticated dogs that populated the Americas before the arrival of Europeans in the 15th century. On page 81 of this issue, Ní Leathlobhair *et al.* (*1*) shed light on the origins of the elusive precontact dog population through genetic analysis of ancient and modern dogs. Building on earlier work, they show that American dogs alive today have almost no ancestry from precontact dogs, a monophyletic lineage descended from Arctic dogs that accompanied human migrations from Asia. Instead, the authors found that their closest remaining relative is a global transmissible cancer carrying the DNA of a long-deceased dog. It remains unclear why precontact dogs survived and thrived for thousands of years in the Americas only to swiftly and almost completely disappear with the arrival of Europeans.

Paleontologists unearthed the first evidence of precontact dogs in the 1930s. Since then, dog burial sites and artistic representations dating as far back as 10,000 years have been found throughout the Americas (*2*, *3*) (see the figure). In recent years, scientists have started to apply powerful new genomic approaches to study these ancient dogs. Ní Leathlobhair *et al.* combine archaeology with the genomic analysis of ancient and modern DNA to investigate the origins of the precontact American dog in unprecedented detail.

The first humans to cross the Bering Land Bridge 16,000 years ago (*4*, *5*) may have done so without dogs. The earliest human archaeological sites have no dogs, as the oldest dog remains are only 10,000 years old (*2*). Ní Leathlobhair *et al.* affirm these archaeological data points with a genetic analysis of a much larger cohort of dogs. They analyzed hundreds of complete mitochondrial genomes from living dogs and dog remains around the world, including 71 from archaeological remains in Siberia and North America. On the basis of this analysis, they date

Published by AAAS

the arrival of precontact dogs to 6500 years after the first human lineages. These ancient dogs form a distinct clade that is most closely related to ancient sled dogs from Eastern Siberia, where the first human settlements appeared about 9000 years ago.

Once they arrived in the Americas, dogs flourished. Early European colonists described native dogs as pervasive throughout the continent and diverse in color and size (*6*). Dogs may have assisted with hunting, guarding camps, and carrying or pulling heavy packs when the tribes needed to move (*2*, *7*). Given their prevalence, it would be reasonable to assume that the descendants of these dogs must persist today, and American breeds such as the Carolina dog and the Chihuahua are claimed to have ancient American heritage.

However, as with earlier work (*8*, *9*), Ní Leathlobhair *et al.* find almost no genetic traces of precontact dog ancestry in modern dogs, whether purebred or American village dog. Modern Arctic dogs are not descended from precontact dogs, but instead are part of a sister clade brought into the Americas within the last 1000 years (see the figure). None of the village dogs, Carolina dogs, or Chihuahuas could be confidently shown to have precontact dog ancestry of more than 2 to 4%.

It is unclear why there is so little evidence today of this thriving precontact dog population. Early European colonists may have discouraged the sale and breeding of native dogs, or even actively persecuted them (*10*). Yet, cultural preferences alone seem insufficient to explain their rapid decline. Most dogs worldwide are free-breeding scavengers, with minimal human control and high reproductive rates (*11*); native American dogs were likely similar.

Instead, American dogs may have suffered the same fate as the human populations. Infectious diseases brought by European colonists, such as tuberculosis, scarlet fever, and bubonic plague, led to millions of human deaths. Diseases carried by European dogs may have inflicted a similar fate on native American dogs and may explain how a continent-scale dog population declined so quickly that it left few traces behind. The loss of precontact dog lineages echoes the substantial loss of ancient lineages seen in modern humans (*5*).

There is, however, at least one remaining representative of this ancient dog lineage: a sexually transmitted cancer that affects dogs on every inhabitable continent. First documented by veterinarians hundreds of years ago, canine transmissible venereal tumor (CTVT) may actually be far older. Ní Leathlobhair *et al.* estimate that the founder lived up to 8200 years ago and find that CTVT is more closely related to American precontact dogs than to modern dogs, wolves, or coyotes.

However, CTVT probably did not evolve in the Americas. Instead, CTVT may have evolved in an Asian dog related to the precontact dogs sometime after the land bridge to the Americas flooded (see the figure) (*12*). This timing raises an intriguing new possibility: CTVT arrived in the Americas with European dogs in the 15th century, where it infected, for the first time in thousands of years, dogs that were genetically similar to its founder. The severity of CTVT in such closely related dogs is unknown, because no dogs of this lineage are known to survive in the modern world.

The story of the precontact American dog is just starting to be told. Ní Leathlobhair *et al.* combined data collected with a variety of approaches, each with its own limitations. Mitochondrial sequencing captures just a tiny portion (1/140,000) of the genome from the maternal lineage only, and conclusions based on mitochondrial data alone can prove deceptive (*4*). The dog genotyping array is biased toward genetic variation found in modern breeds and may miss important differences between nonbreed populations. Finally, the seven precontact nuclear genomes were sequenced to an average depth of just 0.005 to 2×, far lower than the 30× standard for modern DNA, making it difficult to accurately and comprehensively type variants. More complete genomes, both nuclear and mitochondrial, from both ancient and modern dogs will reveal new details about the precontact dog populations that were an integral part of native American life. ■

[1]Broad Institute of MIT and Harvard, Cambridge, MA 02142, USA. [2]Stanford University, Stanford, CA 94305, USA. [3]University of Massachusetts Medical School, Worcester, MA 01655, USA. Email: elinor.karlsson@umassmed.edu

REFERENCES

1. M. Ní Leathlobhair *et al.*, *Science* **361**, 81 (2018).
2. A. Perri *et al.*, bioRxiv 343574 [Preprint] (11 June 2018).
3. E. C. Galbreath, *Post-Glacial Fossil Vertebrates from East-Central Illinois* (Field Museum of Natural History, Chicago, IL, 1938).
4. P. Skoglund, D. Reich, *Curr. Opin. Genet. Dev.* **41**, 27 (2016).
5. B. Llamas *et al.*, *Sci. Adv.* **2**, e1501385 (2016).
6. L. M. Snyder, J. A. Leonard, in *Handbook of North American Indians: Environments, Origins, and Populations*, D. H. Ubelaker, W. C. Sturtevant, Eds. (Smithsonian Institution, Washington, DC, 2006), vol. 3, pp. 452–462.
7. V. V. Pitulko, A. K. Kasparov, *J. Archaeol. Sci. Rep.* **13**, 491 (2017).
8. S. Castroviejo-Fisher, P. Skoglund, R. Valadez, C. Vilà, J. A. Leonard, *BMC Evol. Biol.* **11**, 73 (2011).
9. K. E. Witt *et al.*, *J. Hum. Evol.* **79**, 105 (2015).
10. A. W. Crosby, *The Columbian Exchange: Biological and Cultural Consequences of 1492* (Greenwood Publishing Group, 2003).
11. R. Coppinger, L. Coppinger, A. Beck, *What Is a Dog?* (Univ. of Chicago Press, 2016).
12. M. Jakobsson *et al.*, *Clim. Past.* **13**, 991 (2017).

10.1126/science.aau1306

Dog migrations into the Americas

1 Archaeological and genetic data suggest that dogs accompanied the later human migrations over the Bering Land Bridge. After the bridge flooded, they were isolated for ~9000years, until Arctic and European dogs arrived.

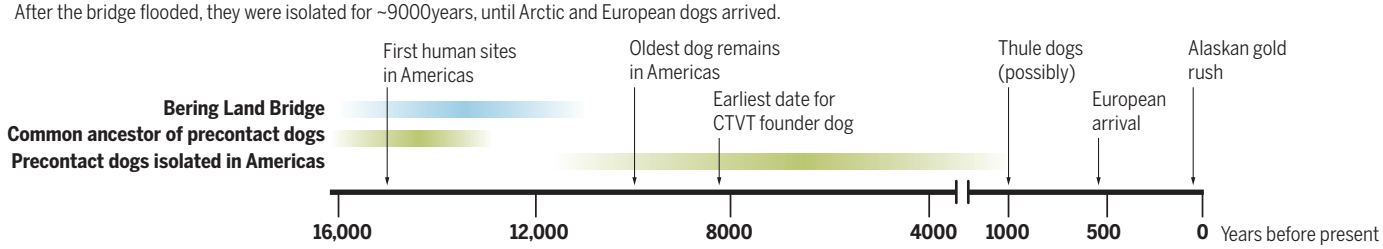

2 The four independent dog introductions into America (thick green bars) proposed by Ní Leathlobhair *et al.* include more closely related precontact and Arctic dogs and more distantly related European dogs (black lines). The CTVT founder dog, although likely from Asia, is most closely related to precontact dogs.

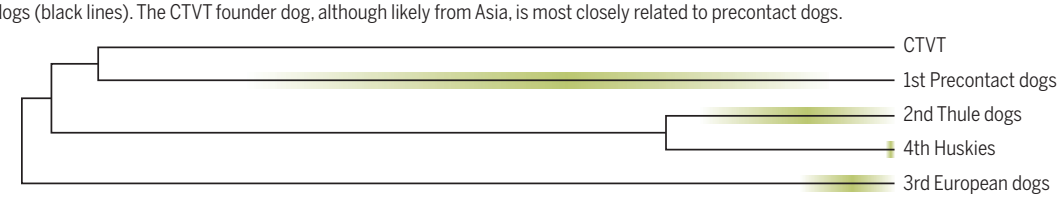

GRAPHIC: N. DESAI/*SCIENCE*

BEHAVIOR

A new brain circuit in feeding control

Components of a neural circuit that regulates body weight are found

By **Sabrina Diano**[1,2]

The discovery of the anorexigenic (loss of feeding) adipose-derived hormone leptin (*1*) and its action on part of the brain, the central melanocortin system (*2*), confirmed earlier predictions of a crucial role of peptides produced by the neurons in this system, neuropeptide Y (NPY) and proopiomelanocortin (POMC), in the control of appetite and feeding (*3*). Further studies reaffirmed the relevance of these circuits in metabolism regulation by the use of increasingly sophisticated methods (*4*, *5*). On page 76 of this issue, Luo *et al.* (*6*) reveal the unsuspected role of another hypothalamic neuronal population in control of feeding, consisting of cells that express the neuropeptide somatostatin (SST), in the nucleus tuberalis lateralis (NTL). This finding adds to the neurological components that regulate food intake and thus body weight.

Luo *et al.* observed that after overnight food deprivation or the administration of the hunger hormone ghrelin in mice, SST-expressing neurons in the hypothalamic NTL expressed the immediate early gene *Fos*, a marker of neuronal activation. This suggested a potential role for these neurons in feeding regulation. To investigate this possibility, Luo *et al.* used selective activation of NTL SST$^+$ neurons either by means of DREADD (designer receptor exclusively activated by designer drug) or optogenetics. Either approach increased cumulative eating time and frequency. Conversely, inhibition of SST$^+$ neurons by use of DREADD or optogenetics significantly reduced feeding. To assess their long-term effect on metabolism, elimination of SST$^+$ neurons in mice resulted in decreased daily food intake and decreased body weight gain over time. To explore the efferent signaling involved in this process, they traced SST$^+$ collateral neuronal projections to several brain areas, including the hypothalamic paraventricular nucleus (PVN), the bed nucleus of the stria terminalis (BNST), the central amygdala, and the periaqueductal gray. The PVN and the BNST were found to be the main projection sites of the NTL SST$^+$ neurons, and only their axonal stimulation from optogenetics increased food intake (see the figure). This effect on food intake was blunted by local administration of the γ-aminobutyric acid ($GABA_A$) receptor antagonist bicuculline, indicating that GABAergic inhibitory signaling of the NTL SST$^+$ neurons is important. In line with this, both enzymes involved in GABA production, glutamate decarboxylase 1 (GAD1) and GAD2, were found to be expressed in these neurons.

These findings add another player to the increasing number of nodes in the brain that affect homeostatic feeding. To date, the efforts to modulate feeding and aberrant feeding behavior—for example, in association with obesity or anorexia nervosa—have proven futile to control body weight and related impairments in physiology. Because food intake is a crucial aspect of survival, and because the neurological control of executions of complex, goal-oriented behaviors assures survival, it is not surprising that many brain regions are involved in the control of feeding. Indeed, multiple brain areas, from "lower" to "higher" function–related brain regions, have been shown to affect various aspects of eating. These include multiple hypothalamic nuclei, the BNST in the basal forebrain, the parabrachial nucleus in the hindbrain, the amygdala, the hippocampus, as well as the prefrontal cortex (*7*).

However, there are several caveats with all these observations, including the one by Luo *et al.* Regardless of the increasing sophistication of the experimental tools, such as optogenetics and chemogenetics, activation or inactivation of cells are both arbitrary from the perspective of the size of the cell population, the timing, and type and amounts of interference with neuronal activity. For example, what are the physiological triggers for the activation of these cells? What are the intracellular and extracellular adaptations that enable firing of these cells at a time of declining glucose and increasing fatty acid availability? Could lipid utilization as well as mitochondrial and synaptic adaptations drive the activation of SST$^+$ cells under hunger conditions, similar to what was found for hypothalamic NPY$^+$ neurons that also produce Agouti-related peptide (AgRP) (*8*–*10*)?

Another interesting question is whether these NTL SST$^+$ neurons that are involved in feeding control may also affect other complex behaviors. For example, hypothalamic NPY$^+$AgRP$^+$ neurons drive complex behaviors beyond feeding, such as reward seeking (*11*), anxiety, locomotion, and repetitive

Neurological circuits in appetite

Hypothalamic neuronal populations (POMC$^+$, NPY$^+$AgRP$^+$, and SST$^+$) regulate appetite and food intake through multiple neurological circuits. Activation of NTL SST$^+$ neurons increases feeding time and frequency. Modulating this circuit may help overcome the aberrant feeding behavior of obesity and anorexia nervosa.

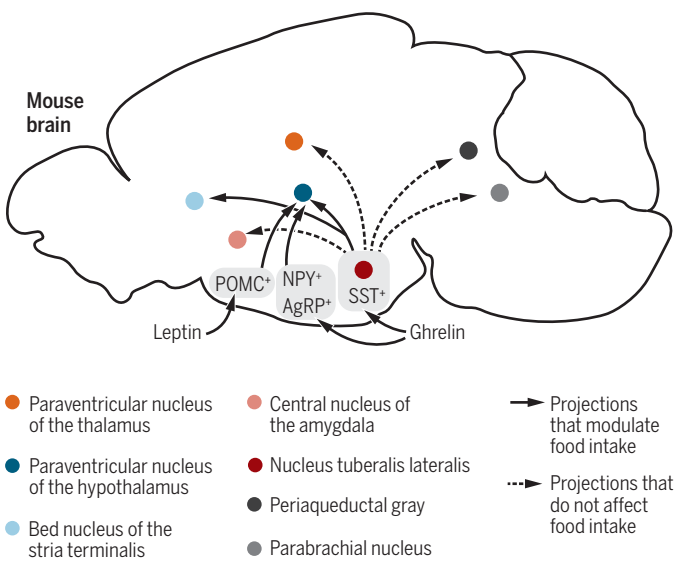

GRAPHIC: V. ALTOUNIAN/*SCIENCE*

[1]*Department of Obstetrics, Gynecology and Reproductive Sciences, Section of Comparative Medicine, and Department of Neuroscience, Yale University School of Medicine, 310 Cedar Street FMB302A, New Haven, CT 06520, USA.* [2]*Department of Clinical Medicine and Surgery, University of Naples "Federico II," Via Pansini 5, Naples 80131, Italy. Email: sabrina.diano@yale.edu*

behavior (*12*, *13*). Because hunger evokes multiple well-coordinated efferent outputs in the brain, it is likely that NTL SST$^+$ neurons will affect multiple behavioral outputs as well. In this regard, it is notable that the NTL has been less defined in rodents. Intriguingly, and arguing for a potential role for these neurons in complex behaviors, neuronal loss in the NTL has been shown to occur in Huntington's disease (*14*), whereas SST production in NTL neurons is reduced in Alzheimer's disease (*15*).

The physiological and pathophysiological implications of the study by Luo *et al.* need future investigations to confirm the role of these circuits in humans. This is further confounded by the fact that our understanding of the homology between mouse and human circuits affecting feeding behavior is currently limited. Nevertheless, because most discoveries on neurological control of human feeding behavior originated in animal studies, the current finding of a role for NTL SST$^+$ neurons in feeding regulation in mice warrants investigations in human subjects as well. The human studies that followed the discovery of leptin and melanocortin signaling in mice were a notable success of these comparative approaches. Whether such endeavors pursuing the NTL SST$^+$ circuit will deliver insights and potential therapies for metabolic disorders in humans is yet to be seen.

"This finding adds to the neurological components that regulate food intake and thus body weight."

Luo *et al.* have introduced a new player in the sandbox of neuronal nodes that affect feeding. Their observations open up a new vista in the control of eating and other goal-oriented complex behaviors and peripheral tissue functions. ■

REFERENCES

1. Y. Zhang *et al.*, *Nature* **372**, 425 (1994).
2. M. A. Cowley *et al.*, *Nature* **411**, 480 (2001).
3. T. L. Horvath *et al.*, *Endocrinology* **131**, 2461 (1992).
4. S. Luquet *et al.*, *Science* **310**, 683 (2005).
5. M. L. Andermann, B. B. Lowell, *Neuron* **95**, 757 (2017).
6. S. X. Luo *et al.*, *Science* **361**, 76 (2018).
7. M. J. Waterson, T. L. Horvath, *Cell Metab.* **22**, 962 (2015).
8. Z. B. Andrews *et al.*, *Nature* **454**, 846 (2008).
9. M. O. Dietrich *et al.*, *Cell* **155**, 188 (2013).
10. S. Pinto *et al.*, *Science* **304**, 110 (2004).
11. L. S. Zweifel *et al.*, *Nat. Neurosci.* **14**, 620 (2011).
12. M. O. Dietrich *et al.*, *Cell* **160**, 1222 (2015).
13. S. L. Padilla *et al.*, *Nat. Neurosci.* **19**, 734 (2016).
14. H. P. Kremer, *Prog. Brain Res.* **93**, 249 (1992).
15. H. J. L. M. Timmers *et al.*, *Brain Res.* **728**, 141 (1996).

10.1126/science.aau1419

CHEMICAL PHYSICS

Molecular movies filmed at conical intersections

Electron diffraction maps atomic motions that result from photoexcitation of CF_3I molecules

By **Helen H. Fielding**

How molecules respond to ultraviolet (UV) light is not only a fundamental issue but has relevance in nature (such as in photosynthesis) and technology (such as with solar cells). Many spectroscopic methods have been developed for the study of photoexcited molecules in the gas phase, free from interactions with any environment, because these conditions allow the intrinsic properties of the molecule to be studied in exquisite detail and to be compared directly with theory. Many spectroscopic methods rely on measuring observables from which it is possible to infer the positions of the individual atoms of the molecule but do not directly measure molecular structure. On page 64 of this issue, Yang *et al.* (*1*) report the use of ultrafast gas-phase electron diffraction (GED) and high-level calculations to probe the movements of individual atoms in the prototypical molecule CF_3I after the absorption of UV light.

When a molecule absorbs UV light, it is promoted to an electronically excited state in which the individual atoms are no longer in their equilibrium positions. Their resulting excess potential energy can be redistributed in a variety of ways. For example, a molecular bond may break, or the atoms may rearrange to form a new molecular structure in which the excited electronic state and another electronic state become degenerate (a conical intersection between potential energy surfaces). Such conical intersections provide particularly efficient "funnels" for transferring molecules from an electronically excited state to a lower-lying excited electronic state or back to the ground state.

A molecular bond typically breaks or relaxes through a conical intersection in a few tens of femtoseconds. Spectroscopic measurements on these time scales became possible in the late 1980s with the advent of femtosecond lasers. Zewail and co-workers carried out the first pioneering experiments, using femtosecond laser pulses to record spectroscopic signatures of molecular bonds breaking and rearranging (*2*). After the pump pulse, a series of precisely timed probe pulses interrogate the electronic or molecular structure of the excited molecule. One approach is femtosecond time-resolved photoelectron spectroscopy, which has proved to be a powerful detection technique for probing ultrafast electronic relaxation processes in neutral molecules (*3*, *4*) and molecular anions (*5*–*7*) in the gas phase. The related techniques of femtosecond pump-probe velocity-map ion imaging (*8*) and time-resolved photoelectron-photoion imaging (*9*) have also proved valuable for monitoring the fragments of dissociation reactions. However, these techniques probe the evolution of the electronic wave function or the products of dissociation reactions and rely on complementary quantum chemistry calculations to deduce the corresponding molecular geometries after the absorption of the photon or after dissociation.

Time-resolved x-ray and electron diffraction techniques, on the other hand, are now emerging as exciting new methods for real-time measurement of molecular structure after absorption of UV light (molecular movies) (*10*, *11*). Yang *et al.* used the ultrafast GED setup at the SLAC National Accelerator Laboratory to record a molecular movie of photoexcited CF_3I molecules. A femtosecond UV pump pulse promoted the molecules to electronically excited states. Ultrashort pulses of electrons were then fired at the photoexcited molecules at a series of precisely timed intervals after the UV pump pulse. The resulting interference patterns arising from electron waves being scattered from the nuclei and electron clouds of the molecule were recorded at each time interval. Each diffraction pattern effectively provides a snapshot of the movie of molecular structures at the time each was recorded.

Yang *et al.* used a single UV photon to initiate C–I bond dissociation on an excited electronic state. This process has been the subject of several femtosecond pump-probe experiments, and the electronic states involved and time scale for dissociation are well characterized (*12*). The velocity and angular distributions provide information on the multiphoton pathways and the potential

Department of Chemistry, University College London, 20 Gordon Street, London WC1H 0AJ, UK. Email: h.h.fielding@ucl.ac.uk

energy surfaces involved. However, the ultrafast GED measurements could also follow the molecular motions of the CF_3 fragment after dissociation (see the figure). This fragment underwent a repeated opening and closing of the F–C–F bond angle (an umbrella motion). This motion was accompanied by an elongation of the C–F bonds, and there was a delay between the initial F–C–F bond opening and the C–F bond elongation.

If the CF_3I molecules absorbed two UV photons, they were excited to a different set of higher-lying excited electronic states. Ultrafast GED measurements revealed that the nuclei rearranged in the first 100 fs to the molecular structure associated with a conical intersection between this high-lying electronic state and an ion-pair state lying below it. The population of molecules was observed to bifurcate at the conical intersection (see the figure, top). Some of the population was transferred through the conical intersection to the ion-pair state. The remaining population underwent a C–I stretching motion with a period of ~200 fs on the higher-lying excited electronic state, but each time the nuclei returned to the geometry corresponding to the conical intersection, more of the population was transferred down to the ion-pair state. Some of the population on the ion-pair state was transferred through another conical intersection to another electronic state lying between the one initially populated and the ion-pair state, and the nuclei returned to their initial geometry (before photoexcitation) after ~500 fs. This process resulted in quantum mechanical interference patterns on this electronically excited state. Thus, the molecular structure of a molecule has been measured directly as it passed through a conical intersection.

The results of Yang *et al.* show that ultrafast GED can measure molecular structure after photoexcitation of molecules in exquisite detail. Combining the information obtained about the nuclear coordinates with that obtained about the electronic wave function from femtosecond pump-probe spectroscopies and time-averaged experiments has the potential to provide the most stringent tests for theory. ■

REFERENCES

1. J. Yang *et al.*, *Science* **361**, 64 (2018).
2. A. H. Zewail, *Angew. Chem. Int. Ed.* **39**, 2586 (2000).
3. V. Blanchet, M. Z. Zgierski, T. Seideman, A. Stolow, *Nature* **401**, 52 (1999).
4. R. Spesyvtsev, O. M. Kirkby, M. Vacher, H. H. Fielding, *Phys. Chem. Chem. Phys.* **14**, 9942 (2012).
5. T. Horio *et al.*, *J. Chem. Phys.* **145**, 044306 (2016).
6. C. R. S. Mooney *et al.*, *Chem. Sci.* **4**, 921 (2013).
7. M. A. Yandell, S. B. King, D. M. Neumark, *J. Am. Chem. Soc.* **135**, 2128 (2013).
8. G. M. Roberts *et al.*, *J. Am. Chem. Soc.* **134**, 12578 (2012).
9. O. Geßner *et al.*, *Science* **311**, 219 (2006).
10. M. P. Minitti *et al.*, *Phys. Rev. Lett.* **114**, 255501 (2015).
11. A. A. Ischenko, P. M. Weber, R. J. D. Miller, *Chem. Rev.* **117**, 11066 (2017).
12. W. G. Roeterdink, M. H. M. Janssen, *Phys. Chem. Chem. Phys.* **4**, 601 (2002).

10.1126/science.aat6002

Coming apart

The structures during the photodissociation of CF_3I were followed by Yang *et al*. with electron diffraction. Wave packets are shown moving along the potential energy surfaces after absorption of one and two UV photons. Atoms are shown in gray for carbon, green for fluorine, and purple for iodine.

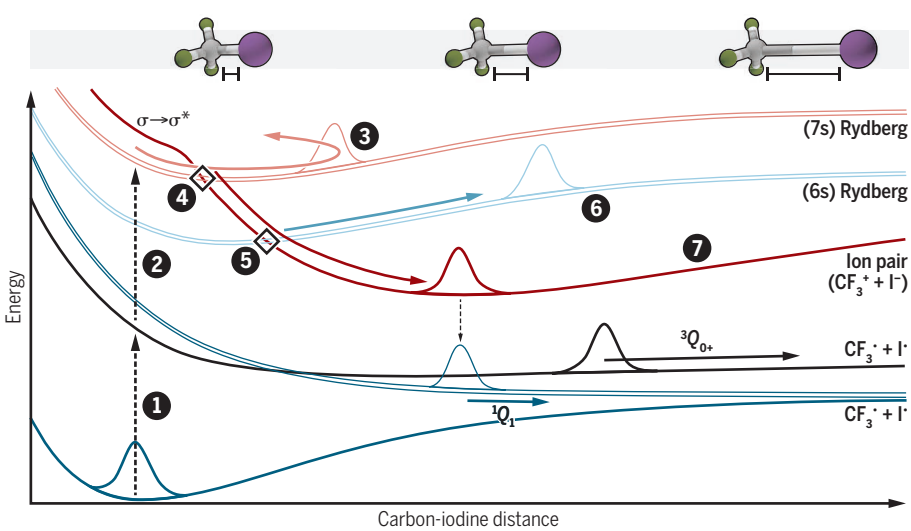

1 One-photon excitation
2 Two-photon excitation
3 Excited CF_3I oscillates along a higher-energy Rydberg state.
4 Some molecules cross at the conical intersection to an ion-pair state.
5 Some of the ion-pair population crosses from the ion-pair state to a lower-lying Rydberg state.
6 Population on the Rydberg state undergoes quantum interference.
7 The ion pair loses energy and drops to the radical-pair state.

GRAPHIC: A. KITTERMAN/*SCIENCE*

EVOLUTION

The search for ancient DNA heads east

Multiple migrations explain the peopling of Southeast Asia in the past 10,000 years

By **Peter Bellwood**

Anthropologists and prehistorians have debated the origins of the peoples of Southeast Asia for more than a century, often without consensus over the relative importance of successive migrations from external sources versus indigenous continuity through time. The analysis of ancient whole-genome DNA from archaeological skeletons brings a new view to this debate (*1*, *2*). On pages 88 and 92 of this issue, McColl *et al.* (*3*) and Lipson *et al.* (*4*), respectively, use genomic DNA sequencing data from 43 ancient Southeast Asian skeletons excavated by archaeologists to explain how the region was peopled during the past 10,000 years. Both teams show that human migration was highly significant, especially the migration of mid-Holocene Neolithic farming populations, ~5000 to 4000 years ago, from southern China into both mainland and island Southeast Asia.

Before ancient DNA sequencing was possible, explanations for the past 10,000 years of human history in Southeast Asia among archaeologists, linguists, and bioanthropologists tended to be polarized. One viewpoint minimized the importance of any Neolithic migration, especially for the islands of Southeast Asia, emphasizing regional continuity in genetics from the Pleistocene (2.6 million to 11,700 years ago). In this regard, a small minority of traditional hunter-gatherers in Malaysia, the Philippines, and the Andaman Islands (so-called "negritos") are generally agreed to have retained a close biological affinity with indigenous Australians and New Guinea Papuans, and thus to reflect in situ Pleistocene ancestry. The opposing view, which supports the importance of successive migrations, rather than universal continuity from the Pleistocene, posits that most modern Southeast Asians

School of Archaeology and Anthropology, Australian National University, Canberra ACT 2601, Australia. Email: peter.bellwood@anu.edu.au

are of mid-Holocene Neolithic agriculturalist origin, related to modern East Asians located to the north (*5*–*7*).

A large body of archaeological and skeletal evidence, including from careful statistical analysis of cranial and facial measurements, has recently provided support for the latter "two-layer" viewpoint (*8*). Currently, the majority opinion is that an original Pleistocene hunter-gatherer population, descended from the first *Homo sapiens* more than 50,000 years ago, once occupied Southeast Asia, Australia, and New Guinea. During the Southeast Asian Neolithic, starting ~5000 to 4500 years ago, there was an expansion of Asian farmers of southern Chinese origin. This Neolithic migration progressed southward into mainland Southeast Asia and Indonesia, and after 3000 years ago, eastward into the Micronesian and Polynesian regions of Oceania (*9*, *10*). The Neolithic migration generally ceased in eastern Indonesia before Australia and the interior of New Guinea were reached. The studies of McColl *et al.* and Lipson *et al.* support this two-layer viewpoint in full and also add further detail.

This supine skeleton with a flexed knee was buried ~2000 years ago into the base of a shell mound in the site of Nagsabaran, Cagayan Valley, Luzon Island, northern Philippines. McColl *et al.* have sampled DNA from a tooth dated to ~200 CE taken from a nearby skull buried in a pot at Nagsabaran.

For instance, ancient DNA genomes from the original hunter-gatherer populations of the Southeast Asian mainland, called Hòabìnhians by archaeologists and sampled by McColl *et al.*, are most similar to those of modern Onge negritos of the Andaman Islands and to the Jōmon [early- and mid-Holocene (~12,000 to 2500 years ago), pre-Japanese] inhabitants of Japan. These Hòabìnhians were genomically less closely related to modern Australians and Papuans, doubtless reflecting the distance between mainland Southeast Asia and Australasia, and the many intervening water barriers in eastern Indonesia, beyond the Ice Age Sundaland continent that extended eastwards to Borneo and Bali.

The movement of Neolithic populations from southern China commenced as two separate migrations. One, ancestral to modern speakers of Tai and perhaps also Austroasiatic languages (the latter including Khmer and Vietnamese), spread by land into mainland Southeast Asia. Along with it spread rice, millets, and domesticated pigs and dogs (*11*). The other, ancestral to speakers of Austronesian languages such as Malay and Hawaiian, spread by sea into Taiwan, later the Philippines, and onward into Indonesia and Oceania, again carrying a cultural component of food production. Lipson *et al.* indicate that the Hòabìnhian and Neolithic populations had already undergone some genomic mixing before Neolithic migrants expanded out of southern China. Furthermore, in the archaeological site of Man Bac in northern Vietnam (analyzed by Lipson *et al.*), skeletons of both populations are found buried together at around 1800 BCE (*12*). The Asian Neolithic population, however, appears to have been most prevalent amongst the skeletons at Man Bac.

Two other important observations can be made from these studies. Mainland Southeast Asian populations such as Tais and Vietnamese Kinh received, perhaps unsurprisingly, another layer of quite heavy gene flow from China starting around 2500 years ago. This was when the Warring States and subsequent Qin and Western Han (206 BCE to 220 CE) Chinese empires conquered southern China and northern Vietnam, imposing Sinitic (Han) settlement, languages, and literacy on many of the indigenous Bronze and Iron Age societies to the south.

Additionally, both studies suggest that "Austroasiatic"-speaking populations undertook a Neolithic colonization of western Indonesia before the arrival of the ancestors of the modern Austronesian-speaking inhabitants of that region. There is some faint archaeological and linguistic evidence for this colonization in Sumatra, Java, and Borneo (*13*, *14*), and hints in the DNA of some living western Indonesians (*15*). The timing and exact origins of this movement remain unclear, however, in the absence of larger samples of Neolithic DNA from both western Indonesia and from the southern mainland of Southeast Asia. No Austroasiatic languages are spoken in Indonesia today, and there are as yet no definite Neolithic archaeological connections between western Indonesia and Vietnam or the Malay Peninsula.

One temporary issue concerning these two studies is that the number of samples of ancient DNA is currently very small and restricted in geographical extent. Ancient DNA samples are rare in the humid tropics (although this situation is improving), and also currently difficult to access from China. Neither study reports ancient DNA from southern China, including Hainan Island, yet this will probably be crucial if we are to really understand the dramatic Neolithic dispersal into Oceania ~3500 years ago that ultimately reached the islands of Polynesia. There is also no ancient DNA from Taiwan and none yet of definite Neolithic date from the islands of Southeast Asia. We have a long way to go, but the analysis of ancient DNA offers an exciting future for our understanding of the human past. ■

REFERENCES

1. E. Callaway, *Nature* **555**, 575 (2018).
2. D. Reich, *Who We Are and How We Got Here* (Pantheon, 2018).
3. H. McColl *et al.*, *Science* **361**, 88 (2018).
4. M. Lipson *et al.*, *Science* **361**, 92 (2018).
5. P. Bellwood, *First Farmers* (Wiley-Blackwell, 2005).
6. P. Bellwood, *First Migrants* (Wiley-Blackwell, 2013).
7. P. Bellwood, *First Islanders* (Wiley-Blackwell, 2017).
8. H. Matsumura, M. F. Oxenham, *Am. J. Phys. Anthropol.* **155**, 45 (2014).
9. P. Bellwood, *Curr. Anthropol.* **52**, S363 (2011).
10. P. Skoglund *et al.*, *Nature* **538**, 510 (2016).
11. A. Barron *et al.*, *Sci. Rep.* **7**, 7410 (2017).
12. M. F. Oxenham *et al.*, Eds., *Man Bac: The Excavation of a Neolithic Site in Northern Vietnam*, Terra Australis 33 (Australian National Univ. Press, 2011).
13. T. Simanjuntak, in *New Perspectives in Southeast Asian and Pacific Prehistory*, Terra Australis 45, P. J. Piper *et al.*, Eds. (Australian National Univ. Press, 2017), pp. 201–211.
14. R. Blench, *Bull. Indo-Pac. Prehist. Assoc.* **30**, 133 (2010).
15. M. Lipson *et al.*, *Nat. Commun.* **5**, 4689 (2015).

10.1126/science.aat8662

PHOTO: HSIAO-CHUN HUNG

EPIGENETICS

Chromatin domains rich in inheritance

Only certain histone posttranslational modifications qualify as being epigenetic

By **Danny Reinberg**[1,2,3] *and* **Lynne D. Vales**[2]

Epigenetic phenomena are heritable changes to gene expression that occur without changes to the DNA sequence and that include posttranslational modifications (PTMs) to the histones that package DNA into chromatin. These PTMs are deposited on histones by enzymes in response to an "initiator," ultimately altering chromatin structure and, accordingly, gene expression. In multicellular organisms, cellular identity is established by master regulators (initiators) that can activate or repress transcription through their sequence-specific DNA binding activity. The accurate transmission of distinct gene expression profiles during cell division is essential for preserving the properties of cell lineages. Thus, a key feature of the epigenetic process is that after the initiator subsides, these informative chromatin PTMs must be inherited by subsequent cell generations. Numerous histone PTMs can occur, but can they all convey epigenetic information? We discuss the few histone PTMs that qualify as epigenetic and the distinct features of the enzymes that deposit them that account for their epigenetic status.

Histones undergo many PTMs, primarily on their amino-terminal "tails," which are about 40 amino acids in length, are nonstructured, and protrude away from the nucleosome units that comprise chromatin. When unmodified, the positively charged histone tails can engage in electrostatic interactions with DNA and neighboring nucleosomes, potentially forming compacted chromatin by default. How is the open structure of transcriptionally competent chromatin (euchromatin) established? Among the many histone PTMs that occur, acetylation of lysine 16 of histone H4 (H4K16ac), which is conserved from yeast to humans, functions to establish euchromatin (*1*). The subsequent combinatorial patterns of histone PTMs mostly operate to promote transcription. Sustaining transcription entails the constant presence of transcriptional activators (initiators) that bind to DNA regulatory sequences (see the figure). These activators recruit coactivators, including histone acetyltransferases that further acetylate the histones near promoter sequences. Additionally, distinct phosphorylation events of the carboxyl-terminal domain of RNA polymerase II (Ser^5-P and Ser^2-P) recruit specific methyltransferases that independently methylate H3K4 and H3K36 to further facilitate transcription (*2*).

We speculate that so-called "open" chromatin that is accessible to the transcription machinery is not per se inherited and, thus, not epigenetic. It is reestablished by H4K16ac after each round of DNA replication and/or mitosis, and gene expression requires an initiator. H4K16ac might be epigenetic, but currently there is no supporting evidence.

"Why should repressive histone [posttranslational modifications]...be epigenetically inherited?"

Instead, a few modifications that promote repressed, compacted chromatin domains exhibit epigenetic properties. Regions of repressed transcription can foster the deposition of specific histone PTMs that provide the platform for chromatin compaction. Upon subsidence of the initiator, this compacted chromatin must contain information that transmits its status to daughter cells after cell division, as its accurate inheritance preserves the integrity of repressed gene expression in a cell lineage.

Studies in baker's yeast, *Saccharomyces cerevisiae*, provide important evidence demonstrating that the local deacetylation of H4K16ac by the nicotinamide adenine dinucleotide (NAD)–dependent histone deacetylase, silent information regulator 2 (Sir2), is necessary to establish compacted (repressed) chromatin domains that can be maintained through multiple generations at mating-type loci, ribosomal DNA repeat sequences, and telomeres (*3*). Deacetylation of H4K16ac at these loci requires the initial recruitment of the Sir complex (Sir2-Sir3-Sir4). In the case of mating-type loci, the Sir complex is recruited through direct interaction of the Sir1 adaptor and an initiator, the origin recognition complex (Orc). Sir2 deacetylates H4K16ac, which is subsequently bound by Sir3. Sir3 interaction with Sir2 and Sir4 expands the deacetylated state. Importantly, the Sir1-Orc initiator is no longer required for persistence of the deacetylated state. Instead, the Sir2 histone deacetylase maintains the repressed chromatin domain through multiple cell divisions—a bona fide epigenetic phenomenon in yeast; it is unknown if this is also the case in higher eukaryotes.

Studies in higher eukaryotes show that the only heritable chromatin domains comprise trimethylation of H3K9 (H3K9me3) and of H3K27 (H3K27me3), which are associated with repressed chromatin. These PTMs provide binding sites for other factors that compact chromatin, forming large chromatin domains of constitutive (H3K9me3) or facultative (H3K27me3) heterochromatin in specific chromosome locations initiated by master regulators (*4*, *5*). Although still under study, these PTMs likely segregate to the appropriate daughter chromatin domains during DNA replication such that nucleosomes containing histones with parental PTMs are mixed with those containing newly synthesized, unmodified histones. The machinery that deposits H3K9me3 and H3K27me3 has a distinct "write-and-read" mechanism that allows these PTMs to qualify as epigenetic: The enzyme or complex that deposits the PTM can also bind to the PTM. This binding stimulates the enzyme to deposit the PTM on adjacent naïve nucleosomes—positive feedback that reinforces and establishes repressive chromatin domains in daughter cells. The methyltransferases SUV39H1 and Polycomb repressive complex 2 (PRC2) exhibit this self-contained write-and-read mechanism: The enzymatic writing module that trimethylates H3K9 and H3K27 (SET domain) is activated when the reading module (a chromodomain in SUV39H1 and an aromatic cage in PRC2) binds their respective enzymatic product. Thus, the presence of only the histone methyltransferase and the parental PTM suffice to restore the PTM to appropriate domains in daughter cells.

The methyltransferase cryptic loci regulator 4 (Clr4) in fission yeast, *Schizosaccharomyces pombe*, and its mammalian homolog, SUV39H1, establish and maintain H3K9me domains by binding to H3K9me, which in turn bolsters their enzymatic activity, giving rise to further H3K9me catalysis. In fission yeast, establishing H3K9me domains requires multiple factors (*3*). Yet, the role of Clr4 is piv-

[1]*Howard Hughes Medical Institute, New York University (NYU) School of Medicine, New York, NY, USA.* [2]*Department of Biochemistry and Molecular Pharmacology, NYU School of Medicine, New York, NY, USA.* [3]*Chaires Blaise Pascal, Genetics and Development Biology, Institut Curie, Paris, France. Email: danny.reinberg@nyumc.org*

Inheritance of repressive histone PTMs

Initiators must be present to establish and maintain histone PTMs that facilitate transcription on euchromatin. PRC2 and SUV39H1 trimethylate H3K27 and H3K9, respectively. These repressive histone PTMs are epigenetic owing to the distinct write-and-read mechanisms of PRC2 and SUV39H1.

Euchromatic active state: Open chromatin

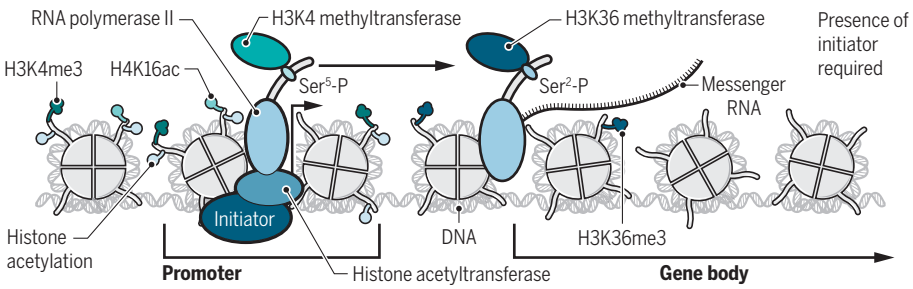

Heterochromatic repressive states: Compacted chromatin

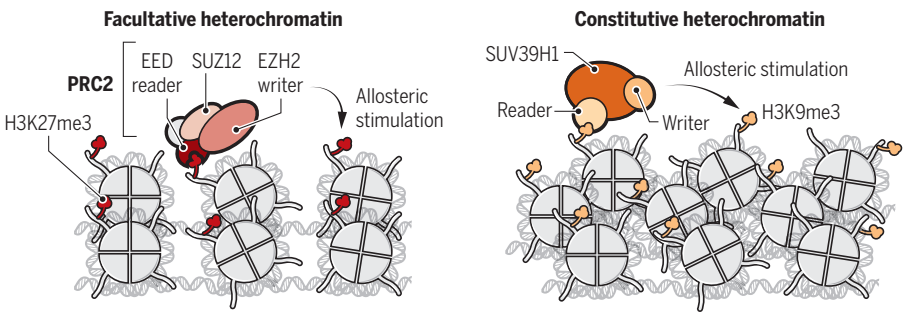

otal, as inheritance of a heterochromatic state depends on the maintenance of H3K9me at the site and requires both Clr4 H3K9me binding (chromodomain) and methyltransferase activity (*3*). The artificial recruitment of a Clr4 chromodomain mutant to an active chromatin site is sufficient to establish an H3K9me domain and transcriptional repression in the absence of endogenous Clr4. However, this Clr4 mutant cannot maintain H3K9me3 heterochromatin through subsequent cell generations (*3*). This points to the epigenetic relevance of the dual write-and-read function. In vitro, Clr4 binds equally well to unmodified and H3K9me3-containing mononucleosomes; however, its binding to a dinucleosome comprising H3K9me3 in one nucleosome activates its methyltransferase activity in a nonallosteric manner (*6*). Such binding is proposed to optimally position Clr4 for recognition of the neighboring naïve nucleosome, thereby increasing catalysis. Similarly, the self-contained write-and-read modules of SUV39H1 lead to propagation of H3K9me3 in vitro. In this case, the chromodomain of SUV39H1 binds to H3K9me3, resulting in allosteric activation of its SET (methyltransferase) domain (*7*).

In the case of H3K27me3, PRC2 comprises four core subunits, including supressor of zeste homolog 12 (SUZ12), embryonic ectoderm development (EED), and enhancer of zeste homolog 2 (EZH2). EED binds H3K27me3, this binding allosterically activates the SET domain of EZH2. This allosteric activation of PRC2 set the precedent for the write-and-read mechanism that, in this case, specifies the epigenetic character of H3K27me3 (*8*). After cells are depleted of EED and thus H3K27me2 or H3K27me3, EED expression can be restored either as wild type or mutant in the EED "read" function (*9*). Mammalian chromatin sites to which PRC2 is initially recruited (nucleation sites) and establishes de novo H3K27me3 are similar in both cases; however, only wild-type EED establishes H3K27me2 or H3K27me3 through chromatin domains, highlighting the importance of the read function. Another study generated nematode worm (*Caenorhabditis elegans*) embryos containing some chromosomes with H3K27me and some without (*10*). In the absence of PRC2, H3K27me disappeared through several rounds of cell division, but, in its presence, H3K27me was transmitted epigenetically throughout embryogenesis. Additionally, PRC2 in plants functions to maintain transcriptional repression not only during mitosis but also transgenerationally (*11*). Recent studies in the fruitfly, *Drosophila melanogaster*, suggest that sites of PRC2 recruitment to chromatin (Polycomb response elements) are required for long-term H3K27me3 inheritance, otherwise H3K27me3 is diluted during subsequent rounds of cell division (*12*, *13*). Yet, remarkably, the remaining H3K27me3 is inherited at appropriate daughter chromatin domains, underscoring its epigenetic character and the pivotal role of the PRC2 write-and-read mechanism in restoring H3K27me3. Whether mammalian PRC2 nucleation sites are also integral to H3K27me3 inheritance is yet to be determined.

Lastly, H4K20me is a repressive PTM bound by the malignant brain tumor (MBT) domain of histone methyl-lysine binding protein (L3MBTL1), leading to chromatin compaction (*14*). Interestingly, methylation of H4K20 is antagonistic with H4K16ac (*15*). Although potentially epigenetic, a corresponding write-and-read function for methylated H4K20 has yet to be demonstrated.

Although many other writers and readers of histone PTMs exist, for example, proteins with bromodomains that recognize acetylated histones, they are distinct from epigenetic agents in that the reader does not stimulate the activity of the writer. There are some chromatin-modifying enzymes that do bind to their products (*4*), but whether their binding results in stimulation of enzymatic activity has not been determined. Nonetheless, these enzymes operate on euchromatic regions, where an initiator is required for continued activity.

Why should repressive histone PTMs, but not activating PTMs, be epigenetically inherited? We propose that restraining improper activation of genes might be an evolutionary requirement of multicellularity. Positive feedback loops for gene activation could carry excessive risks as they might result in converting variable stimuli into permanent mistakes in cell fate decisions, with potentially deleterious consequences for the organism. When in doubt, genomes should keep their transcriptome under wraps. ■

REFERENCES AND NOTES

1. M. Shogren-Knaak *et al.*, *Science* **311**, 844 (2006).
2. R. J. Sims 3rd *et al.*, *Genes Dev.* **18**, 2437 (2004).
3. R. C. Allshire *et al.*, *Nat. Rev. Mol. Cell Biol.* **19**, 229 (2018).
4. D. Allis *et al.*, *Epigenetics* (Cold Spring Harbor Laboratory Press, Cold Spring Harbor, NY, ed. 2, 2015).
5. P. Trojer *et al.*, *Mol. Cell* **28**, 1 (2007).
6. B. Al-Sady *et al.*, *Mol. Cell* **51**, 80 (2013).
7. M. M. Müller *et al.*, *Nat. Chem. Biol.* **12**, 188 (2016).
8. R. Margueron *et al.*, *Nature* **461**, 762 (2009).
9. O. Oksuz *et al.*, *Mol. Cell* **70**, 1149 (2018).
10. L. J. Gaydos *et al.*, *Science* **345**, 1515 (2014).
11. H. Yang *et al.*, *Science* **357**, 1142 (2017).
12. R. T. Coleman *et al.*, *Science* **356**, eaai8236 (2017).
13. F. Laprell *et al.*, *Science* **356**, 85 (2017).
14. P. Trojer *et al.*, *Cell* **129**, 915 (2007).
15. K. Nishioka *et al.*, *Mol. Cell* **9**, 1201 (2002).

ACKNOWLEDGMENTS

We thank K.-J. Armache, S. Berger, R. Bonasio, D. Moazed, C. Desplan, S. Grewal, E. Heard, S. Henikoff, T. Jenuwein, R. Kingston, H. Klein, R. Margueron, R. Martienssen, E. Mazzoni, O. Oksuz, J. Skok, R. Schneider, M.-E. Torres Padilla, P. Voigt, and K. Zaret for comments on the manuscript.

10.1126/science.aat7871

GRAPHIC: C. BICKEL/*SCIENCE*

CHEMISTRY

The dynamic art of growing COF crystals

Growth modulation leads to large, high-quality covalent organic framework crystals

By **Jorge A. R. Navarro**

Diamonds consist of an ordered array of tetrahedral carbon atoms, held together by strong covalent bonds. Despite this simple structure, making diamond crystals is difficult, requiring extremely high pressures and temperatures that can only be achieved deep in Earth's crust or through sophisticated experiments. Building covalent organic frameworks (COFs) similarly involves the ordered spatial arrangement, in a two- or three-dimensional crystalline network, of organic units linked together by strong covalent bonds. Growing single crystals of robust COFs is challenging because it requires the dynamic formation and cleavage of strong covalent bonds. On page 48 of this issue, Ma *et al.* (*1*) report a simple method for growing large, high-quality single crystals of COF networks held together by strong imine covalent bonds.

COFs are a class of synthetic porous organic materials that provide well-structured, confined spaces for selective molecular recognition processes and enhance the reactivity of the hosted molecules. These properties are attractive for a wide variety of potential applications, including gas adsorption and separation, catalysis, sensing, and energy storage and generation (*2*).

The properties of the imine bond make it particularly suitable for building robust crystalline COF networks. First, the strength of this bond leads to highly chemically and thermally robust materials that can withstand the harsh conditions required for environmental and industrial applications (*3*). Second, the imine bond can form and dissociate dynamically, providing one of the few examples of dynamic covalent chemistry (*4*).

The difficulties encountered in trying to grow high-quality single crystals has hampered the use of single-crystal x-ray diffraction to obtain accurate structural data on COF materials; these data are necessary for a full understanding of their properties. Previous reports have shown the formation of robust two-dimensional (2D) and 3D COF networks based on imine bonds, but the crystalline order was limited to the nanoscale, which is unsuitable for single-crystal x-ray diffraction (*5*). Structural determinations of these porous materials therefore relied on x-ray powder and electron diffraction methods, which revealed the basic structural features but could not resolve the molecular conformation, the degree of framework interpenetration, or the nature of interactions with guest molecules.

Ma *et al.* now show that the use of a large excess of aniline during COF synthesis gives rise to the competitive formation of terminal benzene imine moieties at the COF crystal surface (see the figure). This approach provides an error-correction mechanism during crystal growth, ultimately leading to the formation of crystals with sufficiently high quality and size to obtain high-resolution single-crystal x-ray diffraction data in standard laboratory equipment. The authors illustrate the power of this approach by retrieving accurate structural features for single crystals of several imine-based 3D COFs, including COF-300 and COF-303. The results show that this approach is general for imine-based COFs and might eventually inspire related approaches to COF crystals based on additional types of dynamic covalent bonds (*6*).

Editing COF crystals with aniline

A competitive reaction with an excess of aniline provides an error-correction mechanism during COF crystal growth.

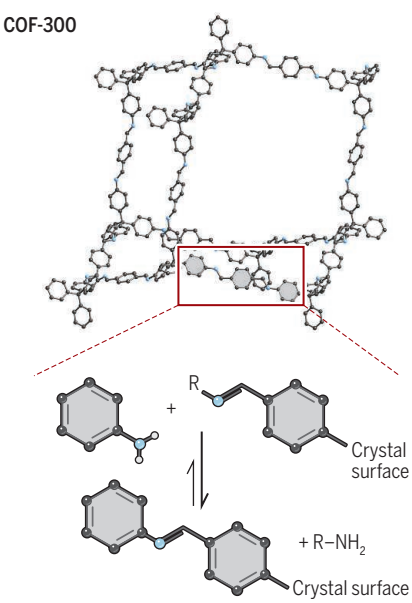

Growth modulation
The aniline excess promotes imine bond reversibility.

The accuracy of the retrieved structural features allows the authors to establish the degree of interpenetration and structural distortions in the diamond network of the COF-300 system without ambiguity. Moreover, they show that the single-crystal features are preserved in the hydrated form of COF-300. The authors could thus visualize the interactions of water molecules with the imine groups of the host framework via O–H···N hydrogen bonds, as well as resolve infinite water chains hosted in the pore channels. They could also accurately establish the subtle conformational differences between the imine and reversed imine isomeric networks COF-300 and COF-303.

Metal organic framework (MOF) chemistry, which is based on more labile coordination bonds, enabling high-quality single-crystal x-ray diffraction analysis that makes it possible to obtain single-crystal x-ray diffraction data. These data can reveal structural features of guest molecules (*7*), elucidate the stepwise formation and visualization of ultrasmall metal nanoparticles (*8*), and resolve catalytic steps (*9*). It is therefore envisaged that the possibility of obtaining good-quality single crystals will facilitate the synthesis, characterization, and applications of COFs and related materials of increased complexity, as already realized in MOFs. It remains to be seen whether this approach can be extended to highly anisotropic 2D (*10*, *11*) and/or entangled COF structures (*12*), in which the strengths of intra- and interlayer (polymer) interactions differ by several orders of magnitude. ■

REFERENCES AND NOTES

1. T. Ma *et al.*, *Science* **361**, 48 (2018).
2. F. Beuerle, B. Gole, *Angew. Chem. Int. Ed.* **57**, 4850 (2018).
3. J. L. Segura, M. J. Mancheno, F. Zamora, *Chem. Soc. Rev.* **45**, 5635 (2016).
4. M. E. Belowich, J. F. Stoddart, *Chem. Soc. Rev.* **41**, 2003 (2012).
5. C. S. Diercks, O. M. Yaghi, *Science* **355**, eaal1585 (2017).
6. D. Stewart *et al.*, *Nat. Commun.* **8**, 1102 (2017).
7. Y. Inokuma *et al.*, *Nature* **495**, 461 (2013).
8. F. R. Fortea-Pérez *et al.*, *Nat. Mater.* **16**, 760 (2017).
9. A. Burgun *et al.*, *Angew. Chem. Int. Ed.* **56**, 8412 (2017).
10. H. Xu, J. Gao, D. Jiang, *Nat. Chem.* **7**, 905 (2015).
11. A. M. Evans *et al.*, ChemRxiv 10.26434/chemrxiv.5702437.v2 (2017).
12. Y. Liu *et al.*, *Science* **351**, 365 (2016).

ACKNOWLEDGMENTS

The author gratefully acknowledges the financial support from Spanish MINECO (CTQ2017-84692-R) and EU FEDER funding.

10.1126/science.aau1701

Departamento de Química Inorgánica, Universidad de Granada, Av. Fuentenueva S/N, 18071 Spain. Email: jarn@ugr.es

GRAPHIC: A. KITTERMAN/*SCIENCE*

POLICY FORUM

TECHNOLOGY DEVELOPMENT

Autonomous vehicles: No driver...no regulation?

Driverless cars are on the road with no federal regulation, and the public is paying the price

By **Joan Claybrook**[1] *and* **Shaun Kildare**[2]

According to the latest statistics from the U.S. National Highway Traffic Safety Administration (NHTSA), 37,461 people were killed on the nation's roads in 2016 (*1*). Autonomous vehicle (AV) technology has the potential to reduce this number substantially. However, proper safeguards must be established immediately by federal regulators to govern the testing and deployment of AVs and ensure public safety. We must not undermine current safety standards for the sake of AV development. Moreover, reconsidering current requirements may be necessary to take advantage of this revolution. Nearly two-thirds (64%) of respondents in a recent CARAVAN public opinion poll expressed concern about sharing the road with driverless cars (*2*). If commonsense protections are not in place to govern AV development, and problems occur, the public will reject AVs, and the opportunity this new technology presents to improve public safety will be lost.

AV technology is still very much in development, as evidenced by the serious and fatal crashes that have occurred this year. In January of 2018, a Tesla Model S that was operating under its "Autopilot" system crashed into the rear of a stopped fire truck in California (*3*). On 18 March, an AV operated by Uber struck and killed a pedestrian crossing a road in Tempe, Arizona (*4*). Only 5 days later, a Tesla Model X was involved in a fatal crash in California, striking a safety barrier before bursting into flames (*5*). On 11 May, a Tesla crashed into the rear of another fire vehicle in Utah while operating under its Autopilot system (*6*). These crashes illustrate that sensors and algorithms of AVs are still having trouble identifying road hazards and potential obstacles reasonably expected to be in the driving path. The lack of regulation has allowed these unproven vehicles onto our roads. The crashes that have occurred were not unforeseeable and have shaken the public's trust in the technology. Commonsense requirements for the performance of AVs are necessary to protect the public and instill confidence in the technology.

Over 50 years ago, Congress passed the National Traffic and Motor Vehicle Safety Act of 1966 because of concerns about the death and injury toll on our highways. The law required the federal government to establish minimum vehicle safety performance standards to protect the public against "unreasonable risk of accidents occurring as a result of the design, construction or performance of motor vehicles" (*7*). Although motor vehicles have changed dramatically since that time and will continue to do so in the future, the underlying premise of this crucial law has not.

There are currently many regulatory gaps that need to be filled. Federal regulators should develop a list of operational scenarios and a range of conditions under which AVs must be evaluated to ensure that the public is not being placed in harm's way through the introduction of these vehicles. For example, problems associated with different weather and fouling conditions for different types of sensor need to be studied. There should be a minimum "vision test" for the AV system to make sure that it can properly identify its surroundings, including other cars, pedestrians, cyclists, road markings, and traffic signs, and respond appropriately. Moreover, manufacturers must be required to execute comprehensive testing and development before taking these vehicles onto public roads. To protect the public, strict protocols must also be established for testing of these vehicles on public roads. Recent work internationally has identified many of the same concerns with the development and deployment of AVs as noted throughout this work (*8*).

AVs that require monitoring by a human driver have been the first introduction of AV technology to the general public. However, humans are inherently bad at monitoring semi-autonomous systems and are readily distracted (*9*). Manufacturers must find a way to keep a driver engaged in the driving task, and regulators must require that engagement in a meaningful way. This is a conclusion reiterated in the findings of the National Transportation Safety Board (NTSB) investigation of a fatal Tesla crash in Florida in 2016 (*10*).

It is vital that there be standardized, mandatory data reporting. There needs to be a central repository by which all AV manufacturers and federal regulators are routinely made aware of situations identified during testing or deployment that have led to collisions or failures. Currently, there is no transparency regarding the algorithms that form the basis for AV function and thus no way to determine whether there are better approaches to solving problems that resulted in collisions or serious system malfunctions. The information required, however, is more than just that covered by an incident report but must include details on the dynamics of the collision, and more important, how the decision process of the AV may have led or contributed to the crash. Only through data collection and analysis can future regulatory needs be developed and justified. There are already examples of this type of data sharing for safety's sake, such as in commercial aviation (*11*).

Additionally, the possibility of a catastrophic cyberattack on transportation increases as the number of AVs on the road increases. Federal regulators must look across industries and adapt standards from other modes and fields (banking, military, aviation, etc.) to ensure that AVs have a means for detecting and responding to an attack appropriately and preventing a widespread threat to safety. The need for NHTSA to develop a strategy to address cybersecurity was raised more than 5 years ago in a report on the subject by the National Research Council of the National Academies (*12*); however, little progress toward meaningful regulation of this aspect of AV performance and safety has been achieved.

Despite the need for regulation, NHTSA, the federal agency responsible for keeping people safe on America's roadways through enforcement of vehicle performance standards, has issued mere voluntary guidelines that are unenforceable and place no mandates on the industry to develop and test AVs safely. In addition, the agency has failed to act to address the shortcomings of AV technology that have already been identified. For example, the NTSB determined that the driver of a Tesla Model S who had been killed in a 2016 crash in Florida had not been en-

[1]*President Emeritus, Public Citizen, Washington, DC, USA. From 1977 to 1981, she was administrator of the National Highway Traffic Safety Administration.* [2]*Director of Research, Advocates for Highway and Auto Safety, Washington, DC, USA. Email: joan@joanclaybrook.com; skildare@saferoads.org*

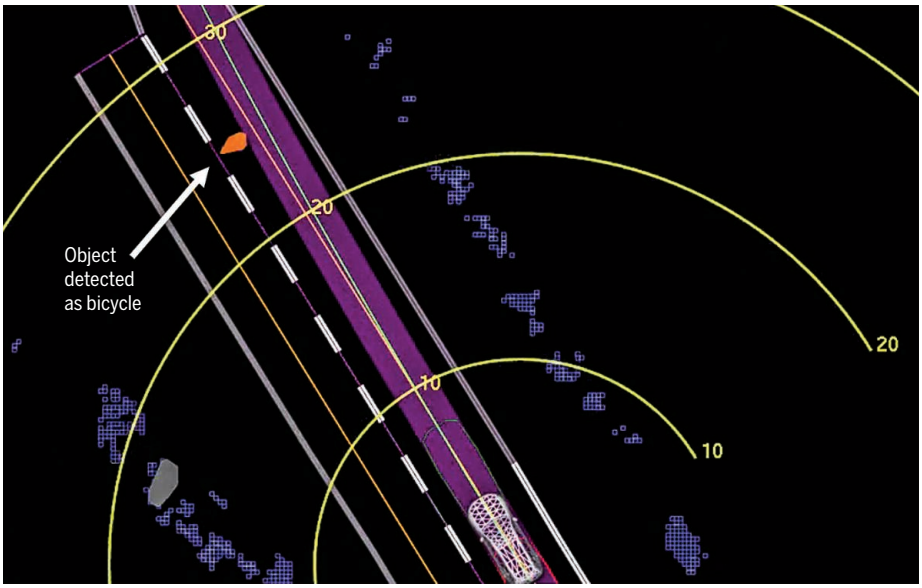

IMAGE: NTSB

Uber self-driving system data playback from the fatal, 18 March 2018, crash of an Uber Technologies, Inc., test vehicle in Tempe, Arizona. Yellow lines show meters ahead of the vehicle. According to the NTSB preliminary report (https://goo.gl/2C6ZCH), although the pedestrian pushing a bicycle was first detected 6 s before the crash, she was categorized by the self-driving system as an unknown object, as a vehicle, and then as a bicycle. At 1.3 s before impact, the self-driving system determined that emergency braking was needed. However, the automatic braking system was not enabled, and no alert was provided to the driver who was supposed to be monitoring the system.

gaged in the driving task, and that a probable cause was the operation design "contributing to the car driver's overreliance on the vehicle automation." Even worse, from an engineering standpoint, is that the design of the system allowed misuse. The NTSB found that these problems were not Tesla's alone but are industry-wide (*13*). Yet, NHTSA still has not initiated regulatory proceedings to address these serious safety issues. NHTSA needs to issue regulations governing the safe operation of these vehicles to ensure that development, testing, and eventual deployment into the public domain do not endanger lives.

Compounding the problem is legislation currently pending before Congress (*14*). Both a bill passed by the House of Representatives (SELF DRIVE Act, H.R. 3388) and a measure currently pending before the Senate (AV START Act, S. 1885) will allow automakers to receive broad exemptions from existing federal motor vehicle safety standards and ignore the need for NHTSA to issue minimum safety requirements. In 2015, Congress exempted test vehicles from having to comply with federal safety standards (*15*). The current legislation would allow for the potential sale of millions of AVs that can be exempt from standards that ensure occupant protection and crashworthiness. It would allow for wide-scale commercial introduction of AVs that fail to meet federal safety standards in order to increase industry profits. If this provision is not drastically altered, our nation's roads risk becoming corporate proving grounds for unverified technology, and the American public will end up being unwitting subjects in a potentially deadly experiment.

Another concern, for those cars that can be driven either autonomously or by a human driver, is that the Senate bill dangerously departs from well-settled federal law by allowing manufacturers to disconnect steering wheels, brakes, and other safety systems, when such a vehicle is operated in an autonomous mode, without any government review and approval. Furthermore, neither bill encompasses all AVs, including those that depend on a human driver to monitor their operation. These vehicles are already on the road, have been involved in multiple deadly crashes, and will comprise a sizable portion of the AV fleet for years to come. Neither bill being considered by Congress requires NHTSA to deal with the regulatory issues that we describe and develop critical standards that will be essential to assuring the proper development and operation of AVs. In addition to all of these concerns, Congress has not provided NHTSA with sufficient funds to deal with the expanded duties it will have in response to the advent of AVs. AVs are already being tested in states and cities across the country. Some state and local governments have started to put in place the first requirements to preserve public safety in the absence of any substantive action by the federal government. Unfortunately, both bills before Congress will preempt these regulations, despite NHTSA having yet to issue any federal standard for AVs. This unprecedented attack on the historic state responsibility to protect their residents will create a regulatory vacuum that will needlessly put the public at risk. Until NHTSA issues safety standards and regulations for AVs, state and local governments have every right, and in fact a duty, to protect their citizens. Traditionally, states are allowed to act where the federal government has not taken specific action; however, the issue of preemption may have to be resolved by the courts. NHTSA has failed to respond meaningfully to the development of AV technology. Although the technology has the ability to save lives once developed, at the same time it can risk lives (and has already claimed several) if it is not executed properly. A federal framework developed around ensuring safety, not just supporting corporate development, is necessary. Congress must end the deregulatory efforts and focus on balancing productive competition while maintaining the levels of safety required by established law and practice. A failure to put proper safeguards in place will result in the continued erosion of the public confidence in this potentially lifesaving and game-changing technology. ■

REFERENCES

1. National Center for Statistics and Analysis, *2016 Fatal Motor Vehicle Crashes: Overview*. Traffic Safety Facts Research Note. Report no. DOT HS 812 456 (National Highway Traffic Safety Administration, Washington, DC, October 2017).
2. ORC International, CARAVAN Public Opinion Poll: Driverless Cars (12 January 2018).
3. P. Valdes-Dapena, "Tesla in Autopilot mode crashes into fire truck," *CNN Tech*, 24 January 2018.
4. E. Rosenfield, "Tempe police release video of deadly Uber accident," *CNBC*, 21 March 2018.
5. D. Shephardson, "U.S. opens probe into fatal Tesla crash, fire in California," *Reuters*, 27 March 2018.
6. K. Allen, "Tesla Model S was in Autopilot mode during Utah crash, driver says," *ABC News*, 15 May 2018.
7. Public Law 89–563.
8. International Transport Forum, Safer Roads with Automated Vehicles? (ITF, 2018).
9. http://acrs.org.au/files/papers/arsc/2015/CunninghamM%20033%20Autonomous%20vehicles.pdf
10. National Transportation Safety Board, Collision between a Car Operating with Automated Vehicle Control Systems and a Tractor-Semitrailer Truck Near Williston, Florida, May 7, 2016, Accident Report NTSB/HAR-17/02, PB2017-102600 (12 September 2017).
11. www.faa.gov/news/fact_sheets/news_story.cfm?newsId=18195
12. *Transportation Research Board Special Report*, vol. 308, *The Safety Challenge and Promise of Automotive Electronics: Insights from Unintended Acceleration* (Transportation Research Board, Washington, DC, 2012); www.nap.edu/catalog.php?record_id=13342
13. Collision Between a Car Operating with Automated Vehicle Control Systems and a Tractor-Semitrailer Truck Near Williston, Florida, May 7, 2016; NTSB, Accident Report NYST/HAR-17/-2.
14. S. 1885, American Vision for Safer Transportation through Advancement of Revolutionary Technologies (AV START) Act, 115th Congress, 1st Session (2017); H.R. 3388, Safely Ensuring Lives Future Development and Research in Vehicle Evolution (SELF DRIVE) Act, 115th Congress, 1st Session (2017).
15. Fixing America's Surface Transportation Act, Sec. 24404, Public Law 114-94 (2015).

10.1126/science.aau2715

Corrected 6 July 2018. See full text

RESEARCH

Elucidating the structure of covalent organic frameworks

Evans et al., *p. 52*

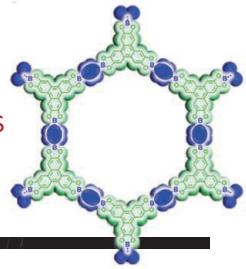

IN *SCIENCE* JOURNALS

Edited by **Stella Hurtley**

DOMESTICATION

How humans got their goats

Little is known regarding the location and mode of the early domestication of animals such as goats for husbandry. To investigate the history of the goat, Daly *et al*. sequenced mitochondrial and nuclear sequences from ancient specimens ranging from hundreds to thousands of years in age. Multiple wild populations contributed to the origin of modern goats during the Neolithic. Over time, one mitochondrial type spread and became dominant worldwide. However, at the whole-genome level, modern goat populations are a mix of goats from different sources and provide evidence for a multilocus process of domestication in the Near East. Furthermore, the patterns described support the idea of multiple dispersal routes out of the Fertile Crescent region by domesticated animals and their human counterparts. —LMZ

Science, this issue p. 85

Genomics traces ancient movements of domesticated goats.

ORGANIC CHEMISTRY

Cyclobutanes sourced right from ethylene

Ethylene is one of the highest-volume commodity chemicals manufactured from fossil fuels. It is mainly used to make plastic, although its ready availability incentivizes its expanded use in pharmaceutical synthesis. Pagar and RajanBabu now report that a cobalt catalyst can couple ethylene with enynes (another comparatively inexpensive feedstock bearing carbon-carbon double and triple bonds) to make complex chiral molecules. Initially, the ethylene reacts with the enyne's triple bond to form an isolable cyclobutene compound. At longer reaction times, the same catalyst can add a second equivalent of ethylene enantioselectively to form cyclobutanes with a quaternary chiral carbon center. —JSY

Science, this issue p. 68

QUANTUM INFORMATION

In search of the right diamond defect

Certain defects in diamond are among the most promising physical implementations of qubits, the building blocks of quantum computers. However, identifying a defect with balanced properties is tricky: Nitrogen vacancy centers have a long lifetime but comparatively poor optical properties, whereas negatively charged silicon vacancy centers have the opposite characteristics. Rose *et al*. used careful materials engineering to stabilize the neutral charge state of silicon vacancy centers and found that they combine long coherence times with excellent optical properties. —JS

Science, this issue p. 60

NEUROSCIENCE

Neurons that regulate feeding

The tuberal nucleus, an area of the hypothalamus, has not been studied in great detail. Luo *et al*. found that GABAergic somatostatin neurons in the tuberal nucleus are functionally involved in the regulation of feeding in mice (GABA, γ-aminobutyric acid) (see the Perspective by Diano). These neurons were activated by food deprivation or hunger hormone. Loss- and gain-of-function experiments indicated that these cells are necessary and sufficient to control systemic metabolic balance. This newly described regulatory center is extensively connected with other feeding control circuits via projections to other hypothalamic nuclei. —PRS

Science, this issue p. 76; see also p. 29

OCEANOGRAPHY

Pinpointing no-mining areas in the deep sea

Areas near mid-ocean ridges are being approved for mining, and protecting these diverse seafloor ecosystems is critical.

CREDITS: (FROM TOP) A. M. EVANS *ET AL.*; PHILIPUS/ALAMY STOCK PHOTO

Corrected 6 July 2018. See full text

The International Seabed Authority is responsible for regulating deep-sea mining in the high seas. This agency has developed environmental management plans to protect local diversity by identifying areas where mining should be prohibited. Dunn *et al*. developed an ecological framework to identify criteria for establishing such mining-free regions on mid-ocean ridges. The areas should be at least 200 kilometers long to hold regional biodiversity intact. Furthermore, the species within these areas should be distributed properly to maintain population connectivity. —PJB

Sci. Adv. 10.1126/sciadv.aar4313 (2018).

QUANTUM OPTICS

A single-photon gate

A long-standing goal in optics is to produce a solid-state all-optical transistor, in which the transmission of light can be controlled by a single photon that acts as a gate or switch. Sun *et al*. used a solid-state system comprising a quantum dot embedded in a photonic crystal cavity to show that transmission through the cavity can be controlled with a single photon. The single photon is used to manipulate the occupation of electronic energy levels within the quantum dot, which in turn changes its optical properties. With the gate open, about 28 photons can get through the cavity on average, thus demonstrating single-photon switching and the gain for an optical transistor. —ISO

Science, this issue p. 57

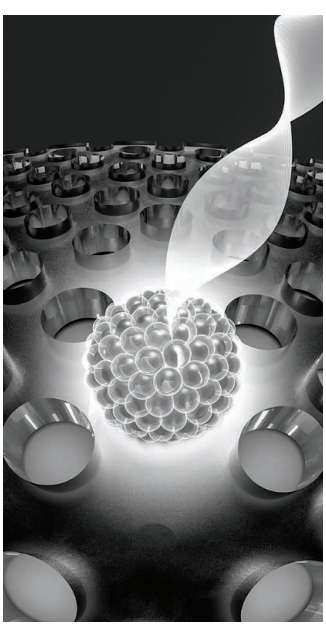

The makings of a photon transistor

CREDITS: (FROM LEFT) E. EDWARDS/JOINT QUANTUM INSTITUTE; GOLFX/ISTOCKPHOTO

PREMATURE AGING

Delaying premature aging

Cells from patients with Hutchinson-Gilford progeria syndrome (HGPS) have defects in nuclear architecture that lead to premature cellular senescence. Larrieu *et al*. investigated the mechanisms by which a small molecule called remodelin improves the phenotype of HGPS cells (see the Focus by Wilson). Remodelin restored a nuclear import pathway mediated by Transportin-1 that was defective in HGPS cells, thereby delaying premature senescence. These results could also be applied to delay cellular senescence in cells derived from aged healthy individuals. —AV

Sci. Signal. **11**, eaar5401; see also eaat9448 (2018).

ATMOSPHERIC CIRCULATION

A traffic jam of air

Persistent meandering of the jet stream can cause atmospheric blocking of prevailing eastward winds and result in weather extremes such as heat waves in the midlatitudes. Nakamura and Huang interpret the poorly understood origins of these systems as the meteorological equivalents of traffic congestion on a highway and show how they can be described by analogous mathematical theory. Climate change may affect the frequency of blocking as well as its geographic distribution, reflecting a simultaneous shift in the structure of the stationary atmospheric waves and the regional capacity of the jet stream. —HJS

Science, this issue p. 42

IN OTHER JOURNALS

Edited by **Caroline Ash** *and* **Jesse Smith**

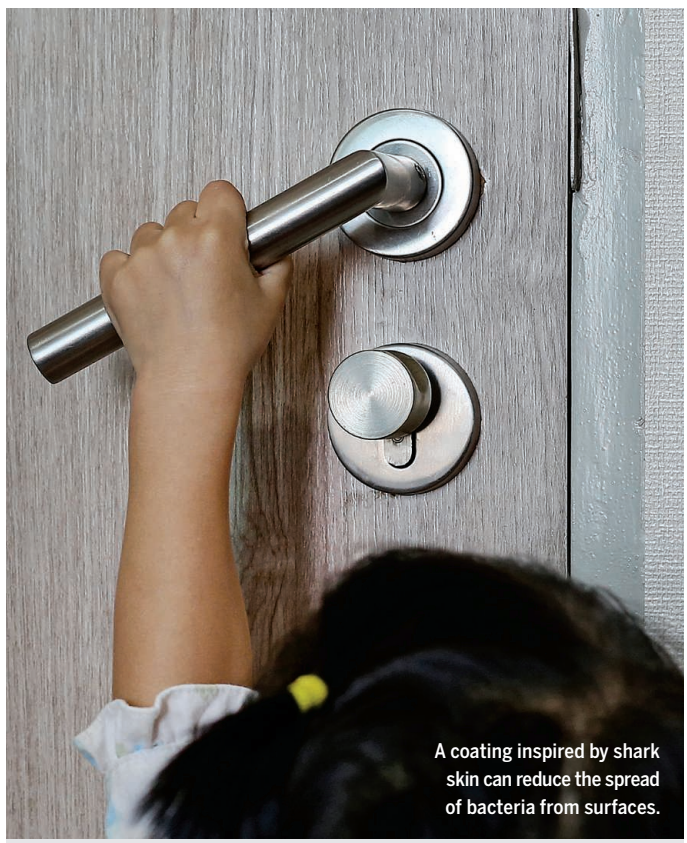

A coating inspired by shark skin can reduce the spread of bacteria from surfaces.

MICROBIOLOGY

Coatings join the fight against bacteria

Efforts to combat the spread of infections, especially in health care settings, mostly involve the use of antibacterial cleaning agents and antibiotic drugs. Another possible strategy is the use of coatings that are antibacterial (inactivating bacteria) or antifouling (preventing the build-up of bacteria) on surfaces such as doorknobs. Arisoy *et al.* report the development of such a coating with a structure inspired by shark skin. Bacterial attachment is reduced by 70% on the micropatterned, photocatalytic coating, compared with smooth films of the same composition. Most of the bacteria that do settle on the coating are inactivated when the coating is exposed to ultraviolet light. Because the coatings are imprinted onto a flexible substrate, it should be possible to use them in practical applications. —JFU

ACS Appl. Mater. Interfaces **10**, 20055 (2018).

DRUG DISCOVERY

Nanoscreening for drug combinations

Biological networks are complex, and effective therapies may require combinations of drugs to overcome redundancies, feedback mechanisms, or drug resistance. Such screening is challenging because of the multiplicity of combinations to test. Kulesa *et al*. describe a miniaturized process that automatically creates drug combinations

Police officers and demonstrators face off during the 2015 Baltimore protests.

PSYCHOLOGY

Online moral rhetoric and violent protests

Peaceful protests sometimes turn violent. To find out why, Mooijman *et al.* analyzed 18 million tweets sent during the 2015 Baltimore protests related to the death of Freddie Gray in police custody. They found that tweets expressing moral rhetoric predicted daily violence and police arrests in the hours after being sent. These data did not explore specific content or level of moral agreement in social networks. Follow-up vignette experiments and attitude surveys found that people endorse violent protest when they see an issue in moral terms and perceive that everyone agrees with them. These data have implications for understanding how online echo chambers may lead to violence and how to predict, and possibly prevent, the eruption of violence in social groups. —TSR

Nat. Hum. Behav. **2**, 389 (2018).

from nanoliter-scale droplets. Emulsions were made of a chemical compound, cell culture, and a fluorescent barcode. Pairs of droplets were loaded into wells of a microarray plate and mixed, and cell growth was monitored. This platform was successfully used to identify previously unsuspected drugs that synergize with antibiotics to kill *Escherichia coli*. —VV

Proc. Natl. Acad. Sci. U.S.A. 10.1073/pnas.1802233115 (2018).

NEUROINFLAMMATION

Joint pain impacts the brain

How does chronic peripheral inflammation affect the brain? In autoimmune disorders such as rheumatoid arthritis, joint inflammation is accompanied by fatigue and cognitive decline. Schrepf *et al*. have discovered that these symptoms are associated with changes in neural connectivity in specific brain regions. The authors used magnetic resonance imaging to examine 54 patients with rheumatoid arthritis over 6 months. Whole-brain searches and theoretical network analyses showed altered patterns of connectivity, with more positive connections involving the left inferior parietal lobule and the medial prefrontal cortex. These are the regions that function in attention and working memory. —LC

Nat. Commun. **9**, 2243 (2018).

CANCER

Aging and melanoma immunotherapy

Aging is a major risk factor for melanoma. Older patients are likely to develop more aggressive disease and usually respond poorly to treatment. Kugel *et al*. analyzed biopsies from melanoma patients and compared these samples with a murine model of disease. Unexpectedly, melanoma was less likely to progress in older patients and mice given pembrolizumab (an antibody therapy targeting the immune checkpoint regulator PD-1). The tumor microenvironments of older individuals were found to have fewer regulatory T cells (T_{regs}) that were positive for the marker FOXP3. Pembrolizumab was more effective in younger mice in which T_{regs} had been depleted by an antibody targeting CD25, indicating the possibility of a more effective therapeutic strategy for patients who respond poorly to anti-PD1 therapy. —MY

Clin. Cancer Res. 10.1158/1078-0432.CCR-18-1116 (2018).

AGING

Epigenetics, aging, and glycolysis

Aging brings reduced fitness and increased incidence of disease and death. Epigenetic changes are thought to be associated with various aging processes. By using CRISPR-Cas9 mutagenesis in the model fly, *Drosophila*, Ma *et al*. found that aging was associated with a loss of fidelity in histone modifications mediated by Polycomb proteins—specifically, a reduction in the repressive epigenetic mark called H3K27me2/3. If the Polycomb protein PRC2 was mutated, H3K27me2/3 was lost, glycolysis was elevated, and life span was restored. Transgenically increasing gene dosage for glycolytic enzymes also promoted life span, locomotion, and resistance to oxidative stress. —BAP

eLife 10.7554/eLife.35368 (2018).

ACADEMIC ENTREPRENEURS

Postprofessorial patents plummet

Curtailing academic inventors' rights to reap all benefits from their inventions and businesses—instead granting two-thirds of the rights to their university—can undermine university-based entrepreneurship and patenting. Hvide and Jones show that after Norway ended the so-called "professor's privilege" in 2003, the rate of university-based start-up company formation dropped by roughly 50%, and those start-ups exhibited less growth. The policy change, which moved Norway toward a U.S. Bayh-Dole model, also led to a roughly 50% drop in patenting, and the resulting patents received fewer citations. —BW

Amer. Econ. Rev. 10.1257/aer.20160284 (2018).

PHOTO: CHIP SOMODEVILLA/GETTY IMAGES

Corrected 6 July 2018. See full text

ALSO IN *SCIENCE* JOURNALS

Edited by **Stella Hurtley**

STRUCTURAL BIOLOGY

Target degradation of Type I CRISPR

The CRISPR adaptive immune systems defend bacteria against invaders. Type I CRISPR-Cas systems, the most prevalent type, use a Cascade complex to search the target DNA that is then degraded by Cas3 protein. Xiao *et al*. report cryo–electron microscopy structures of the Type I-E Cascade/Cas3 complex in the pre– and post–DNA-nicking states. These structures reveal how Cas3 captures Cascade only in its correct conformation to reduce off-targeting and how Cas3 switches from the initial DNA-nicking mode to the processive DNA degradation mode. —SYM

Science, this issue p. 41

FRAMEWORK MATERIALS

Covalent organic frameworks writ large

Covalent organic framework (COF) materials have been difficult to characterize structurally and to exploit because they tend to form powders or amorphous materials. Ma *et al.* studied a variety of three-dimensional COFs based on imine linkages (see the Perspective by Navarro). They found that the addition of aniline inhibited nucleation and allowed the growth of crystals large enough for single-crystal x-ray diffraction studies. Evans *et al.* describe a two-step process in which nanoscale seeds of boronate ester–linked two-dimensional COFs can be grown into micrometer-scale single crystals by using a solvent that suppresses the nucleation of additional nanoparticles. Transient absorption spectroscopy revealed superior charge transport in these crystallites compared with that observed in conventional powders. —PDS

Science, this issue p. 48, p. 52; see also p. 35

CHEMICAL PHYSICS

Motion picture of a conical intersection

In most chemical reactions, electrons move earlier and faster than nuclei. It is therefore common to model reactions by using potential energy surfaces that depict nuclear motion in a particular electronic state. However, in certain cases, two such surfaces connect in a conical intersection that mingles ultrafast electronic and nuclear rearrangements. Yang *et al*. used electron diffraction to obtain time-resolved images of CF_3I molecules traversing a conical intersection in the course of photolytic cleavage of the C–I bond (see the Perspective by Fielding). —JSY

Science, this issue p. 64; see also p. 30

OCEAN CHEMISTRY

Controlling zinc in the oceans

Zinc, a key micronutrient for marine phytoplankton, has a global distribution remarkably similar to that of silicic acid, even though Zn and Si have very different biogeochemical cycles. Weber *et al*. investigated why this is so by combining model calculations and observations. They found that biological uptake in the Southern Ocean and reversible scavenging of Zn onto sinking particles both affect the distribution of Zn in the ocean. Thus, Zn and Si distributions will be affected differently by future changes in ocean temperature, pH, and carbon fluxes. —HJS

Science, this issue p. 72

HUMAN GENOMICS

Ancient migrations in Southeast Asia

The past movements and peopling of Southeast Asia have been poorly represented in ancient DNA studies (see the Perspective by Bellwood). Lipson *et al*. generated sequences from people inhabiting Southeast Asia from about 1700 to 4100 years ago. Screening of more than a hundred individuals from five sites yielded ancient DNA from 18 individuals. Comparisons with present-day populations suggest two waves of mixing between resident populations. The first mix was between local hunter-gatherers and incoming farmers associated with the Neolithic spreading from South China. A second event resulted in an additional pulse of genetic material from China to Southeast Asia associated with a Bronze Age migration. McColl *et al*. sequenced 26 ancient genomes from Southeast Asia and Japan spanning from the late Neolithic to the Iron Age. They found that present-day populations are the result of mixing among four ancient populations, including multiple waves of genetic material from more northern East Asian populations. —LMZ

Science, this issue p. 92, p. 88; see also p. 31

DOMESTICATION

Lineage losses for man's best friend

Dogs have been present in North America for at least 9000 years. To better understand how present-day breeds and populations reflect their introduction to the New World, Ní Leathlobhair *et al*. sequenced the mitochondrial and nuclear genomes of ancient dogs (see the Perspective by Goodman and Karlsson). The earliest New World dogs were not domesticated from North American wolves but likely originated from a Siberian ancestor. Furthermore, these lineages date back to a common ancestor that coincides with the first human migrations across Beringia. This lineage appears to have been mostly replaced by dogs introduced by Europeans, with the primary extant lineage remaining as a canine transmissible venereal tumor. —LMZ

Science, this issue p. 81; see also p. 27

HIV

Learning from naïve B cells

Despite decades of intensive research, HIV vaccines are unable to generate the broadly neutralizing antibodies that are likely necessary for protection. Havenar-Daughton *et al.* inspected the potential of human naïve B cells to recognize the vaccine candidate eOD-GT8 and isolated B cells that use similar genes as those used to make the broadly neutralizing antibody VRC01. Interestingly, they also observed B cells with immunoglobulin genes similar to those used in other types of broadly neutralizing antibodies, some with a more conventional maturation path than VRC01. Thus, vaccination of humans with eOD-GT8 has the potential to induce CD4–binding site broadly neutralizing antibodies, which would be a major step forward in HIV vaccines. —LP

Sci. Transl. Med. **10**, eaat0381 (2018).

RESEARCH ARTICLE SUMMARY

STRUCTURAL BIOLOGY

Structure basis for RNA-guided DNA degradation by Cascade and Cas3

Yibei Xiao*, Min Luo*, Adam E. Dolan, Maofu Liao†‡, Ailong Ke†‡

INTRODUCTION: Type I CRISPR-Cas, the most prevalent CRISPR system, features a sequential target-searching and -degradation process. First, the multisubunit surveillance complex Cascade (CRISPR associated complex for antiviral defense) recognizes the matching double-stranded DNA target flanked by an optimal protospacer-adjacent motif (PAM), promotes the heteroduplex formation between CRISPR RNA (crRNA) and the target strand (TS) DNA, and displaces the nontarget strand (NTS) DNA, resulting in R-loop formation at the target site. The helicase-nuclease fusion enzyme Cas3 is then specifically recruited to Cascade/R-loop and nicks and processively degrades the DNA target. High-resolution structures of Type I-E Cascade/R-loop and Cas3/single-stranded DNA (ssDNA) complexes from *Thermobifida fusca* elucidate the PAM recognition and R-loop formation mechanism. However, the Cas3 recruitment and the DNA-nicking and -degradation mechanisms remain elusive.

RATIONALE: We reconstituted the *Tfu*Cascade/R-loop/Cas3 ternary complex and captured structures of the pre– and post–R-loop–nicking states using single-particle cryo–electron microscopy (cryo-EM). Together, these results provide the structural basis to understand crRNA-guided DNA degradation in Type I CRISPR-Cas systems.

RESULTS: We determined the *Tfu*Cascade/R-loop/Cas3 cryo-EM structure in the pre–NTS-nicking state at 3.7-Å resolution. Binding of Cas3 does not introduce further conformational changes to the R-loop–forming Cascade, suggesting that Cascade-Cas3 interaction for the most part features a conformation-capture rather than an induced-fit mechanism. The Cas3-Cascade interaction is exclusively mediated by the Cse1 subunit in Cascade. The recognitions are complementary in charge and surface contour to Cascade/R-loop but not to the apolipoprotein and seed-bubble states of Cascade. This is because before full R-loop formation, the C-terminal domain of Cse1 is in an alternative orientation. By making extensive contacts to both domains of Cse1, Cas3 is able to sense the altered surface landscape of Cse1 and reject the Cascade in such functional states. The conditional recruitment of Cas3 to Cascade serves as a mechanism to avoid mis-targeting a DNA with only partial complementarity [see the figure, (A)].

Moreover, we provided direct evidence that a substrate hand-over mechanism is essential for Type I-E CRISPR interference. The HD nuclease of Cas3 directly captures the NTS for strand-nicking, and this action bypasses the helicase moiety completely. Substrate capture relies on the presence of a flexible bulge in the NTS, and the nicking site preference is predetermined by the path of the recruitment pathway.

We further determined the post–NTS-nicking structure at 4.7-Å resolution, which allowed us to identify structural changes accompanying the strand-nicking reaction. The structure reveals that the entire NTS strand in the R-loop region disappears from its original path because of increased flexibility. Upon adenosine 5′-triphosphate (ATP) hydrolysis, the PAM-proximal half of NTS spontaneously relocates to the opening of the Cas3 helicase. It follows that upon ATP hydrolysis, the Cas3 helicase would feed the ssDNA through itself and further into its HD nuclease, entering into a processive DNA degradation mode [see the figure, (B)].

ON OUR WEBSITE

Read the full article at http://dx.doi.org/10.1126/science.aat0839

CONCLUSION: We completed the structure-function characterization of the molecular events that lead to Type I-E CRISPR interference. The onset of CRISPR interference is tightly controlled at the Cas3 recruitment step as a mechanism to reduce off-targeting. Upon NTS-nicking, however, Type I systems excel at target destruction because Cas3 degrades DNA processively rather than stopping at generating a double-strand break. Such characteristics may explain why Type I evolved to be the most prevalent CRISPR-Cas system found in nature. It would be interesting to see whether the Type I system may be repurposed into a genome-editing tool with distinct utilities from that of Cas9. ■

The list of author affiliations is available in the full article online.
*These authors contributed equally to this work.
†Corresponding author. Email: ailong.ke@cornell.edu (A.K.); maofu_liao@hms.harvard.edu (M.L.)
‡These authors contributed equally to this work.
Cite this article as Y. Xiao *et al.*, *Science* **361**, eaat0839 (2018). DOI: 10.1126/science.aat0839

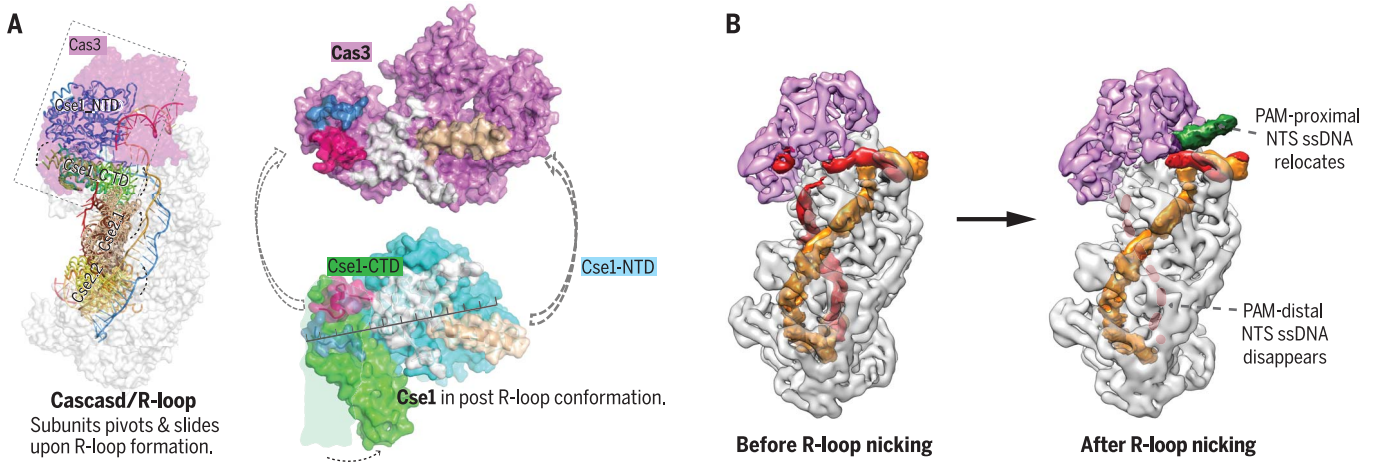

Type I-E CRISPR interference by Cascade and Cas3 zooming into focus. (**A**) Mechanism for R-loop–dependent Cas3 recruitment explained. This prevents mistargeting partial-matching DNA sequences. (**B**) Structural rearrangements after R-loop–nicking by Cas3. The NTS DNA spontaneously relocates to the opening of Cas3 helicase, ready to be threaded for processive degradation.

RESEARCH ARTICLE

STRUCTURAL BIOLOGY

Structure basis for RNA-guided DNA degradation by Cascade and Cas3

Yibei Xiao[1]*†, Min Luo[2]†, Adam E. Dolan[1], Maofu Liao[2]‡§, Ailong Ke[1]‡§

Type I CRISPR-Cas system features a sequential target-searching and degradation process on double-stranded DNA by the RNA-guided Cascade (CRISPR associated complex for antiviral defense) complex and the nuclease-helicase fusion enzyme Cas3, respectively. Here, we present a 3.7-angstrom-resolution cryo–electron microscopy (cryo-EM) structure of the Type I-E Cascade/R-loop/Cas3 complex, poised to initiate DNA degradation. Cas3 distinguishes Cascade conformations and only captures the R-loop–forming Cascade, to avoid cleaving partially complementary targets. Its nuclease domain recruits the nontarget strand (NTS) DNA at a bulged region for the nicking of single-stranded DNA. An additional 4.7-angstrom-resolution cryo-EM structure captures the postnicking state, in which the severed NTS retracts to the helicase entrance, to be threaded for adenosine 5′-triphosphate–dependent processive degradation. These snapshots form the basis for understanding RNA-guided DNA degradation in Type I-E CRISPR-Cas systems.

CRISPR (clustered regularly interspaced short palindromic repeats) and the nearby *cas* (CRISPR-associated) operon establish an RNA-based adaptive immunity system in prokaryotes (*1*–*6*). They are classified into two major classes: Class 1 systems use a multisubunit effector complex to search and destroy nucleic acid targets, whereas class 2 systems use a single effector complex (*7*, *8*). Type I CRISPR-Cas, the most prevalent CRISPR system, belongs to class 1 and can be further categorized into six subtypes (*7*). It features a sequential target searching and degradation process. First, a multisubunit surveillance complex called Cascade (CRISPR associated complex for antiviral defense) recognizes the matching double-stranded DNA (dsDNA) target flanked by an optimal protospacer-adjacent motif (PAM), promotes the heteroduplex formation between CRISPR RNA (crRNA) and the target strand (TS) DNA, and displaces the nontarget strand (NTS) DNA, resulting in R-loop formation at the target site (Fig. 1A) (*9*–*14*). The helicase-nuclease fusion enzyme Cas3 is specifically recruited to the Cascade/R-loop complex, nicks the NTS (Fig. 1A), and switches to a processive DNA degradation mode (*11*, *15*–*17*). Type I-E CRISPR-Cas systems from *Escherchia coli* and *Thermobifida fusca* have been extensively studied (*9*–*25*). In the *T. fusca* system (Fig. 1A), high-resolution structure snapshots elucidated the PAM recognition mechanism and revealed a concerted set of conformational changes as *Tfu*Cascade traverses from the intermediate (the seed-sequence bubble) to the full R-loop state; *Tfu*Cas3 selectively binds to the latter state (*25*). Previous efforts to define the Cascade-Cas3 interaction was not of sufficient resolution to resolve the molecular mechanisms concerning Cas3 recruitment and DNA degradation (*17*). A single-stranded DNA (ssDNA)–bound *Tfu*Cas3 crystal structure led to the speculation that the initial R-loop–nicking mechanism by Cas3 is likely different from the subsequent DNA-degradation mechanism (*24*). To resolve these mechanistic ambiguities, we reconstituted the *Tfu*Cascade/R-loop/Cas3 complex and obtained two cryo–electron microscopy (cryo-EM) structures representing the pre– and post–R-loop–nicking states, at 3.7 and 4.7 Å resolutions, respectively. The former snapshot explains how Cas3 specifically captures the full R-loop–forming Cascade as a mechanism to avoid mistargeting. The latter snapshot is particularly informative in revealing how Cas3 switches from the initial ssDNA-nicking mode to the later processive DNA degradation mode. Together, these results provide the structural basis for us to understand crRNA-guided DNA degradation in Type I CRISPR-Cas systems.

[1]Department of Molecular Biology and Genetics, Cornell University, 253 Biotechnology Building, Ithaca, NY 14853, USA. [2]Department of Cell Biology, Harvard Medical School, 250 Longwood Avenue, SGM 509, Boston, MA 02115, USA. *Present address: State Key Laboratory of Natural Medicines, Department of Pharmacology, China Pharmaceutical University, Nanjing 210009, P. R. China. †These authors contributed equally to this work. **‡Corresponding author. Email: ailong.ke@cornell.edu (A.K.); maofu_liao@hms.harvard.edu (M.L.)** §These authors contributed equally to this work.

Results

Reconstitution of Cascade/R-loop/Cas3 ternary complex from T. fusca

As previously shown (*25*), the *T. fusca* Type I-E system displays a steep temperature-dependent R-loop–formation behavior, allowing us to program *Tfu*Cascade into either dsDNA-binding, seed-bubble formation, or full R-loop state by changing the incubation temperatures. *Tfu*Cas3 only interacts with *Tfu*Cascade in the full R-loop state, but not the seed-bubble state, presumably by probing the conformational differences between them. In this study, we scaled up the reconstruction of the *Tfu*Cascade/R-loop/Cas3 ternary complex and purified it from individual components using a combination of affinity and size-exclusion chromatography methods (Fig. 1, B and C). In the ternary complex, *Tfu*Cas3 preferentially nicked after the 7th, 9th (strongly preferred), and 11th nucleotide (nt) of the NTS DNA in the R-loop, counting from the PAM-proximal side. When adenosine 5′-triphosphate (ATP) was introduced, *Tfu*Cas3 switched to a processive degradation mode, cleaving both strands of DNA to pieces (*25*). These behaviors are similar to the reported behaviors of Cas3 from *E. coli* and *Streptococcus thermophilus* Type I-E systems (*15*–*17*). Previously, the *Tfu*Cas3/ssDNA structure revealed the presence of two ferric ions at the HD nuclease center (*24*). We later found that their presence strongly inhibits the nuclease activity, whereas Co^{2+} supports ssDNA cleavage (*25*). Nonetheless, the combination of using iron-incorporated *Tfu*Cas3 and omitting ATP (or introducing nonhydrolyzable ATP analog adenylyl-imidodiphosphate) allowed us to program the *Tfu*Cascade/R-loop/Cas3 complex to a predominantly prenicking state; at least 74% of the NTS was intact according to ImageJ quantification, and processive degradation was not observed (Fig. 1D).

Overall architecture of the Cascade/R-loop/Cas3 complex in prenicking state

Single-particle cryo-EM analysis showed that the ternary complex embedded in ice was monodisperse and homogeneous, with distinct structural features clearly visible in two-dimensional (2D) averages (fig. S1, A and B). We determined a cryo-EM structure of the *Tfu*Cascade/R-loop/Cas3 interference complex at an overall resolution of 3.7 Å (fig. S1, C and D). The body of *Tfu*Cascade/R-loop is resolved at 3.5 Å or better. By contrast, finger domains of Cas7, Cas6e/crRNA, and outer shell of the dsDNAs are resolved at 4.7 Å or worse because of their conformational flexibilities (figs. S1D and S2). The inner shell of Cas3 is resolved at better than 4.1 Å, resolving most of the interface side chains in contact with Cascade; some outer-shell regions are at worse than 4.7 Å. Of the four domains, the HD nuclease and RecA1 domains of Cas3 are better resolved, and RecA2 has weaker density owing to hinge motion; C-terminal repeat domain (CTD) is not well resolved because of elevated thermomotion and is modeled with a rigid-body docked crystal structure (figs. S1D and S2).

Binding of Cas3 does not introduce further conformational changes to the R-loop–forming Cascade; the overall conformation of *Tfu*Cascade in the ternary complex agrees well with that in the binary complex [Protein Data Bank (PDB): 5U0A] (Fig. 2 and fig. S3) (*25*). These observations point to the possibility that the Cas3-Cascade interaction may use a conformation-capture rather than induced-fit binding mechanism, although this requires conformational dynamics analysis to confirm. The Cas3 conformation inside the ternary complex is in architectural agreement with that in the crystalline state (PDB: 4QQW) (*24*),

with the exception that the RecA2 and CTD domains undergo rigid body movements in the range of 2 and 10 Å, respectively (fig. S3). Cas3 binding is mediated exclusively by the Cse1 subunit of Cascade. The location and domain orientation of Cas3 are consistent with the biochemistry data (*15*–*17*, *25*, *26*). However, the nuclease center of Cas3 is ~20 Å away from the path of NTS. Therefore, a special mechanism must be in place to hand over the DNA substrate from Cascade to Cas3.

Cas3-Cascade interface: How does Cas3 capture the R-loop–forming Cascade?

The Cas3-Cascade interaction is exclusively mediated by the Cse1 subunit in Cascade. Previously, we showed that Cse1_CTD pivots 15° when Cascade transitions from the seed-bubble to the full R-loop state (Fig. 3A) (*25*). This hinge motion alters the orientation and distances between Cse1_NTD (N-terminal domain) and CTD. Therefore, any long-range contact from Cas3 that spans the two Cse1 domains would be sensitive to the conformation of Cse1. The conformational changes also altered the surface features at the Cse1_NTD-CTD interface. Any Cas3 contacts recognizing the newly exposed Cse1_NTD-CTD interface would also help distinguish the Cascade conformation.

Both principles are explored by Cas3 to sense the Cascade conformation (Fig. 3, B and C). The Cascade-Cas3 interface buries a large surface area of 2520 Å^2 and spans an entire side of Cas3. It can be roughly divided into four sectors (interfaces I to IV) (Fig. 3D). At interface I, Cas3 inserts a protruding loop from its HD nuclease domain (amino acids 157 to 171) into a groove between the Cse1_NTD and CTD (Fig. 3E), which is only exposed when the Cascade is in the full R-loop conformation (Fig. 3, B and C). Severe clashing would result if Cas3 were to bind Cascade in the seed-bubble conformation (Fig. 3C). Contacts at interface I feature shape complementarity; favorable hydrogen-bonding contacts mediated by Q160, R161, and N163 from Cas3 further strengthen the interaction. Charge-swapping mutagenesis, R162E, completely disrupted the Cascade-Cas3 contact (Fig. 3I), underlining the functional importance of these polar contacts.

Interfaces II and III flank interface I and serve as a molecular ruler to sense angular and distance changes between the two Cse1 domains. This serves as a proxy to readout whether Cascade has opened an R-loop on the target site. At the Cse1_CTD side, a surface loop from the Cas3 HD domain (amino acids 105 to 114) inserts into a groove perpendicular to the four-helical bundle in Cse1_CTD (interface II) (Fig. 3F). Although the specific contacts are weak, the two surfaces would misalign and clash if Cascade were not in the full R-loop state. On the Cse1_NTD side, the entire Cas3 linker region, composed of an α-helix (amino acids 779 to 798) and a flexible loop (amino acids 799 to 817), is buried at the interface (Fig. 3G). The long linker region is specific to the Cas3 branch of Super Family II helicases and has been implicated in our previous study to mediate interactions with Cascade; replacing this region with a Gly/Ser linker completely abolished Cas3 binding (*24*). Here, we define the area contacted by the flexible linker loop and the nearby Cas3 surface loops (amino acids 151 to 156, 503 to 508, and 826 to 828) as interface III (Fig. 3, D and G). In addition

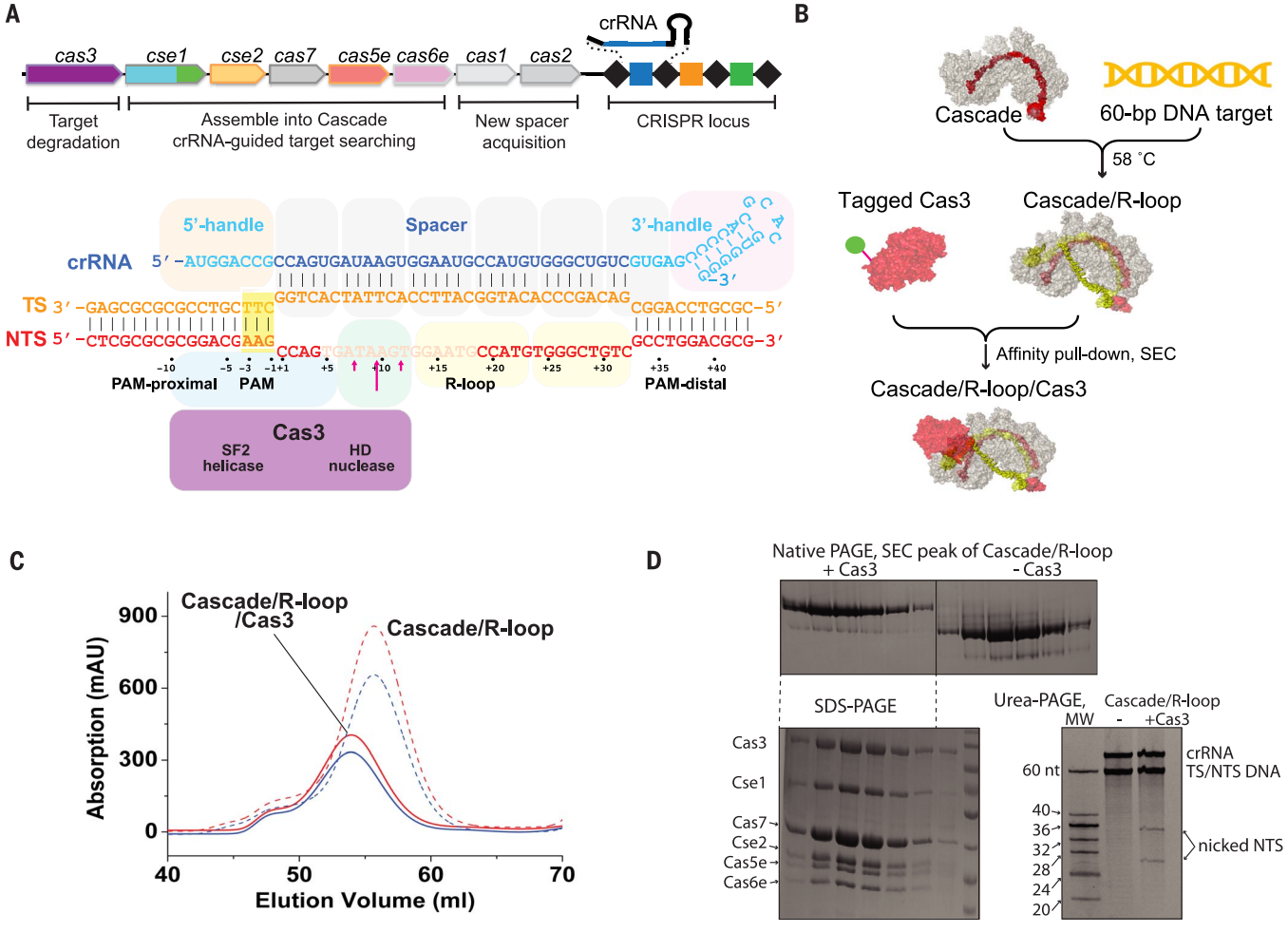

Fig. 1. *Tfu*Cascade/R-loop/Cas3 reconstitution. (**A**) Schematic diagram of the *T. fusca* Type I-E CRISPR-*cas* operon, *Tfu*Cascadeorganization, R-loop formation, *Tfu*Cas3 binding site, and NTS nicking site. Disordered NTS nucleotides are semitransparent, and *Tfu*Cas3 nicking sites are marked by red arrows. This coloring scheme is preserved in other figures. (**B**) Reconstitute and purification scheme of the *Tfu*Cascade/R-loop/Cas3 ternary complex. (**C** and **D**) Size exclusion chromatography, native–polyacrylamide gel electrophoresis (PAGE), SDS-PAGE, and urea-PAGE analyses of the ternary complex.

to mediating shape complementarity, contacts at this interface emphasize charge complementarity. In particular, an acidic patch in the linker loop (D802, D804, D805, E807, D808, N809, and N811) complements a basic patch in Cse1_NTD (N87 N89, K91, R92, and K93; interface III). Charge-swapping mutagenesis from either the Cas3 (E807K/D808K) or Cse1 (KRK91–93/DDD) side of the interface led to a complete loss-of-binding phenotype. Combining these two charge-swapping mutations rescued the binding defect (Fig. 3I), underlining the importance of charge complementarity at interface III.

The entire linker helix (amino acids 779 to 798) is buried at the Cas3-Cascade interface (interface IV), packing at a tilted angle against two parallel loops in Cse1_NTD (amino acids 258 to 269 and amino acids 301 to 309) (Fig. 3H). A set of hydrophobic residues at the N-terminal half of the linker helix interdigitates with hydrophobic residues on the Cse1 surface. However, alanine-scanning mutagenesis targeting the hydrophobic residues along the helix had little effect on Cascade-Cas3 interaction. The C-terminal half of the linker helix in Cas3 mediates a few salt-bridge interactions to Cse1. An R796E charge-swapping mutation in Cas3 significantly weakened its affinity for Cascade/R-loop (Fig. 3I). G793F mutation in Cas3 had a mild effect, presumably by perturbing the shape complementarity at the interface (Fig. 3I).

Taken together, our structural observations explain why Cas3 is only capable of binding to Cascades that have completed the target validation process. This serves as a mechanism to avoid the degradation of a target DNA with partial complementarity. Despite strong sequence and structural homology, we failed to assemble a hetero-complex from *T. fusca* Cas3 and *E. coli* Cascade/R-loop (fig. S4A). Docking of these two structures resulted in reasonable surface complementarity at the putative interface (fig. S4, B and C). However, nonideal charge complementarity can be found in several major interfaces, and steric clashes are present at interface III (fig. S4D). Sequence alignment further revealed that the interface residues in Cas3 are not conserved (fig. S5). These observations rationalized why *T. fusca* Cas3 and *E. coli* Cascade/R-loop failed to hetero-assemble. Given that multiple Type I systems frequently coexist in one bacterium—*T. fusca* itself maintains two Type I-E systems—this may be a mechanism to prevent cross-operon Cascade-Cas3 interaction, which may lead to mistargeting or misincorporation of new spacers during primed adaptation.

NTS handover and nicking mechanism

Available biochemical data suggest that Cas3 nicks the NTS after binding to Cascade, and then

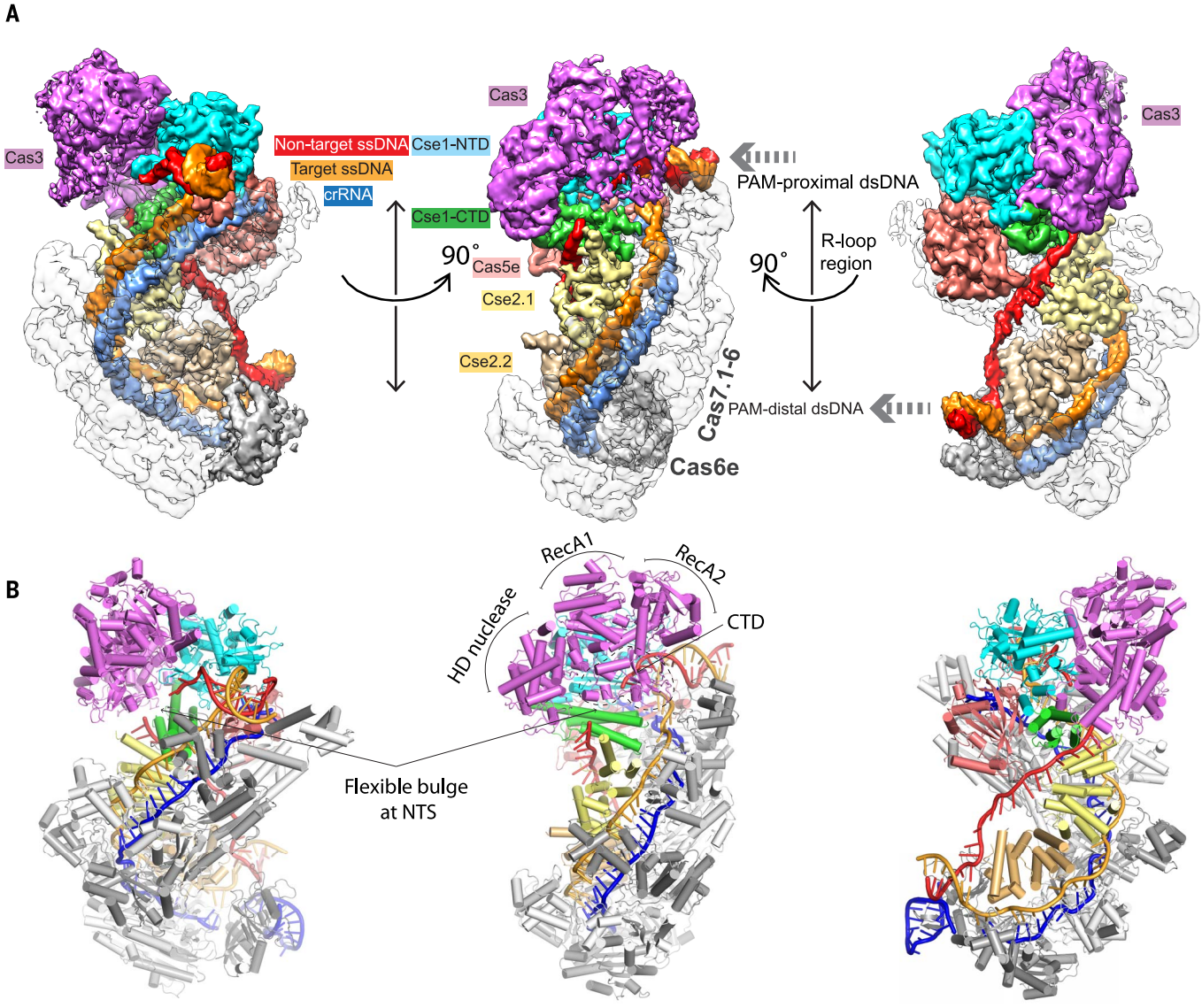

Fig. 2. Overall architecture of *Tfu*Cascade/R-loop/Cas3 in the prenicking state. (**A**) Cryo-EM map and (**B**) illustrated model of the prenicking ternary complex in three different orientations, revealing the Cas3 protein binding to the Cse1 subunit of Cascade. The cryo-EM maps are displayed without applying B-factor sharpening.

ATP hydrolysis mobilizes the helicase. These concerted actions lead to processive DNA degradation. In the *Tfu*Cascade/R-loop/Cas3 complex structure, the proximity of Cas3 to the PAM-side NTS is in architectural agreement with the observed DNA-nicking pattern. The Cas3 orientation relative to the NTS is consistent with the 3′-to-5′ directionality of its helicase (Fig. 4A). However, the ternary structure clearly reveals that the initial DNA-nicking mechanism is different from the processive degradation mechanism, which is depicted in the *Tfu*Cas3/ssDNA structure (*24*). The NTS in the ternary complex bypasses the helicase completely before NTS-nicking; nucleic acid densities are absent from the helicase core, as seen in the *Tfu*Cas3/ssDNA structure (Fig. 4B). Rather, the first four nucleotides 3′-to-PAM travel underneath the L3 loop of Cascade. The bases are not resolved in the EM map because of the lack of specific contacts, but the backbone can be traced with good confidence (Fig. 4C). The NTS density then disappears from the EM map at regions between the L3 loop and Cse1_CTD, before reappearing at the rim of Cse1_CTD and heading toward the backside of Cse2.1. A similar scenario was observed in the Cascade/R-loop binary structure, and we demonstrated that this was because the NTS assumed a flexible 8- to 10-nt bulge in this region (*25*). This was interpreted as a mechanism to hand over the NTS substrate to Cas3 for strand-nicking (*25*). Here, the ternary structure provides direct evidence that a hand-over mechanism is indeed essential for Type I-E CRISPR interference. In the cryo-EM structure, the HD nuclease center in Cas3 is ~20 Å away from the NTS on the surface of Cascade (Fig. 4A). Without a protruding ssDNA bulge, it would be impossible for Cas3 to cleave the NTS. Extra densities corresponding to the scissile phosphate and the backbone of the two preceding nucleotides are found in the HD nuclease center (Fig. 4C). These nucleotides are accommodated in a similar fashion by the di-metal HD active site, as observed in the *Tfu*Cas3/ssDNA structure (*24*). It takes a maximum of three additional nucleotides to model the entire 9-nt PAM-side NTS into the nuclease center of Cas3 (Fig. 4C), which rationalizes the strong preference of *Tfu*- and *Eco*Cas3 to nick after PAM+9 (*25*). Taken together, the structural observations converge with previous biochemistry to suggest that the Cas3 nuclease recruits the NTS ssDNA directly for strand-nicking. Substrate capture relies on the presence of a flexible bulge in the NTS, and the location of the nicking reaction is predetermined by the length of the recruitment pathway.

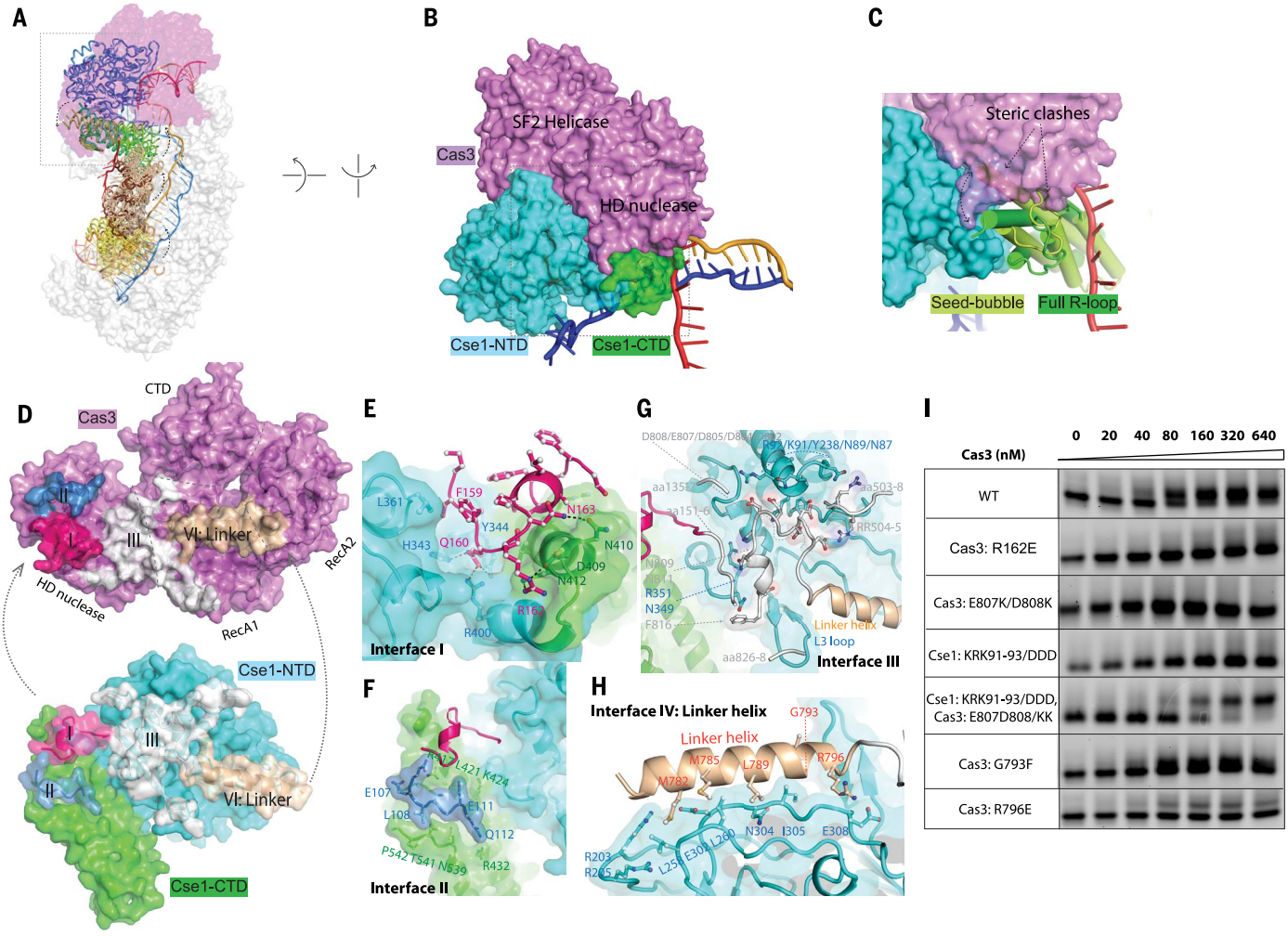

Fig. 3. Selective binding of Cas3 to the R-loop–forming Cascade. (**A**) Conformational differences between seed-bubble and full R-loop Cascade. Cas3 contacts the Cse1 subunit of Cascade exclusively. (**B**) A hind view of Cas3-Cse1 contact. Cas3 inserts a wedge into the groove between Cse1_NTD and CTD. (**C**) This groove is absent in the seed-bubble state, and Cas3-binding would lead to steric clash. (**D**) The four interfaces on Cas3 and Cse1, colored in pink, blue, white, and beige, respectively. (**E** to **H**) Detailed contacts at interface I through IV, respectively. Single-letter abbreviations for the amino acid residues are as follows: A, Ala; C, Cys; D, Asp; E, Glu; F, Phe; G, Gly; H, His; I, Ile; K, Lys; L, Leu; M, Met; N, Asn; P, Pro; Q, Gln; R, Arg; S, Ser; T, Thr; V, Val; W, Trp; and Y, Tyr. In the mutants, other amino acids were substituted at certain locations; for example, R162E indicates that arginine at position 162 was replaced by glutamic acid. (**I**) Native electrophoretic mobility shift assay to evaluate the interface residues. The lower and upper bands represent the Cascade/R-loop and Cascade/R-loop/Cas3 complexes, respectively.

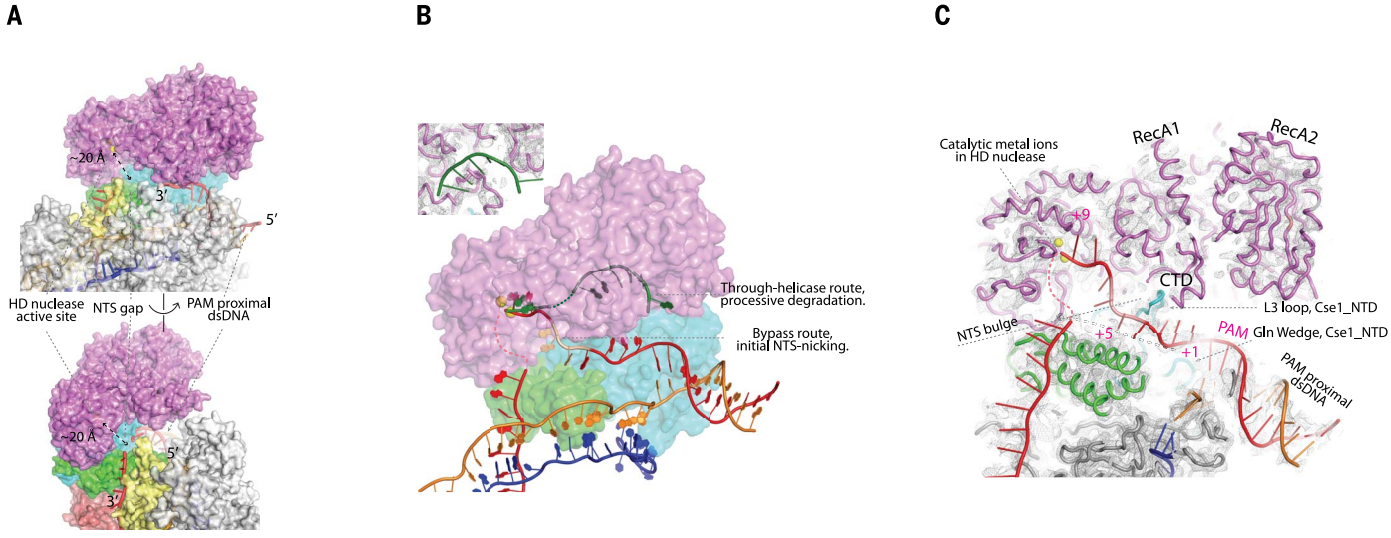

Fig. 4. NTS-nicking bypasses Cas3 helicase, and HD nuclease captures NTS at a flexible bulge. (**A**) The nuclease center of Cas3 is ~20 Å away from the NTS traveling on the Cascade surface. (**B**) The cryo-EM densities suggest that NTS (red) bypasses the Cas3 helicase and accesses its HD nuclease center directly. This route is different from the through-helicase route (green) observed in the *Tfu*Cas3/ssDNA structure. (Inset) Cryo-EM density showing that no nucleic acid densities are found inside the Cas3 helicase. (**C**) Path of NTS inside the *Tfu*Cascade/R-loop/Cas3 complex. A flexible bulge is present in NTS between the L3 loop and CTD of Cse1, where the EM density is absent. The bulge allows the Cas3 nuclease to capture and nick the NTS. Structure building and modeling explains why Cas3 preferentially nicks after PAM+9 in NTS. The backbone of nucleotides PAM+1–4 and PAM+8–9 can be traced from the cryo-EM map; PAM+5–7 are modeled. The minor nicking sites (PAM+7 and +11) can be rationalized on the basis of the observed NTS flexibility.

Postnicking snapshot: Nicked NTS retracts to Cas3 helicase, awaiting rethreading

Whereas most ternary complexes were trapped at the prenicking stage, a fraction of the complexes did undergo NTS nicking (Fig. 1D). These particles were partitioned computationally during 3D classification. They converge to give a cryo-EM structure at 4.7-Å resolution; variations in local resolution follows the same trend as in the prepicking structure (fig. S2). The following structural differences led us to conclude that this snapshot represents the postnicking ternary complex (Fig. 5A). First, the entire NTS DNA disappears from its original path in the R-loop region (Fig. 5B). The scenario seems analogous to when a rubber band is severed; the two halves snap back and become flexible. The PAM-distal dsDNA also disappears from the density, presumably because of increased flexibility, whereas the PAM-proximal dsDNA is held in its original location (Fig. 5B). As the PAM-side NTS disappears from its original path, a new blob of density appears by the side of the PAM-proximal dsDNA, pointing toward the opening of the Cas3 helicase moiety (Fig. 5, B and C). The density lacks recognizable structural feature, but its volume can accommodate ~6- to 7-nt ssDNA. The most logical explanation is that the density corresponds to the relocated NTS after strand-nicking. It follows then that upon ATP hydrolysis, the Cas3 helicase would thread the ssDNA through itself and further into the HD nuclease, as depicted in our previous published *Tfu*Cas3/ssDNA structure (*24*). This switches Cas3 into a processive DNA degradation mode. The Cascade-Cas3 contact at the helicase region is insulated by the linker region of Cas3. Therefore, the anticipated conformational changes in the Cas3 helicase in each ATP hydrolysis cycle would not disrupt the Cas3-Cascade complex. This further rationalizes the observation that Cas3 is capable of degrading dsDNA while on top of Cascade, before eventually breaking free (*26*, *27*).

Discussion

With this study, we complete the structure-function characterization of the key molecular events leading to the onset of CRISPR interference in Type I-E system. The theme before DNA target degradation appears to emphasize stringency, by establishing a sequence of causal events. To reduce off-targeting, two separate effector macromolecules are required, and their interaction is controlled by an R-loop–dependent conformation-capture mechanism. This ensures that the DNA substrate is not prematurely cleaved before the entire targeted sequence is validated. At the onset of CRISPR interference, upon NTS nicking, the mechanism then switches to favor efficiency. Rather than stopping at generating a double-strand break—as Cas9, Cas12a, and other single-effector CRISPR systems do—the helicase-nuclease Cas3 elicits more severe damage through processive DNA degradation. These characteristics may explain why Type I evolved to be the most prevalent CRISPR-Cas system found in nature. It would be interesting to see whether a Type I system could be reprogrammed to function as a genome-editing tool.

After Cas3 recruitment and NTS nicking, Cas3 enters into a processive DNA degradation mode. Single-molecule studies revealed that initially, Cas3 remains bound to Cascade and reels dsDNA toward itself, trapping a DNA loop and creating a ssDNA region within (*26*, *27*). As tension accumulates, Cas3 dissociates from Cascade in a stochastic fashion and travels alone for kilobase distances (*26*, *27*). Surprisingly, no obvious dsDNA break was observed in these studies. This does not agree with the interference efficiency observed in vivo. The inconsistency between bulk and single-molecule biochemistry leaves an empty spot in our molecular understanding of Type I CRISPR system.

Phages can evade CRISPR surveillance by acquiring mutations at PAM or the protospacer region. A mechanism called primed adaptation is in place in the Type I CRISPR-Cas system, where Cascade and Cas3 drive the preferential acquisition of new spacers by Cas1-Cas2 from evader phages that acquired mutations in the protospacer region. The molecular details remain murky; however, recent single-molecule imaging directly visualized Cas1-Cas2 enabling Cascade to specifically recruit Cas3 to protospacers adjacent to a mutated PAM (*26*, *27*). It is intriguing to speculate that the priming PAM sequences may trigger the Cascade to adopt a currently undefined conformation to recruit Cas3 and Cas1-Cas2, initiating the primed spacer acquisition process. Additional studies are required to address precisely how Cascade/Cas3/Cas1-Cas2 selects protospacers during primed adaptation.

Materials and methods

A detailed description of materials and methods is provided in the supplementary materials. Briefly, *Tfu*Cascade/R-loop and *Tfu*Cas3 were prepared as described (*24*, *25*). The ternary complex was

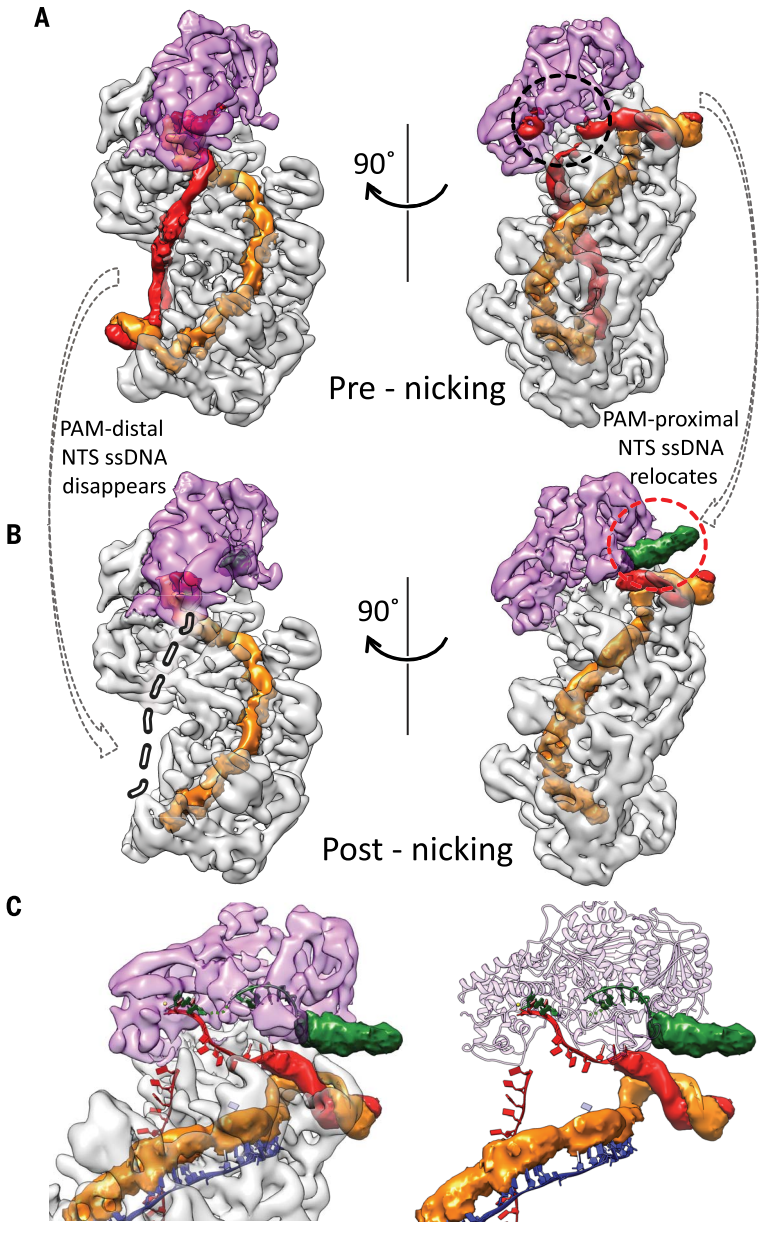

Fig. 5. NTS rearrangement observed in the postnicking state. (**A** and **B**) Density differences between the pre– and post–NTS-nicking states. Both maps are filtered to 6 Å without applying a B-factor. Extra densities in the postnicking 3D reconstruction are colored in green, in the red dotted circle. Disappeared densities are highlighted in the gray dashed lines and black dotted circle. (**C**) Zoom-in of the postnicking state, highlighting the fate of NTS after strand-nicking. Densities previously leading to the HD nuclease center are now missing, whereas extra densities accumulate at the opening of the Cas3 helicase.

assembled by incubating *Tfu*Cascade/R-loop and Twin-Strep-HRV-*Tfu*Cas3 at a 1:2 molar ratio at 4°C for 60 min, followed by Strep-tag pull-down to remove the unbound *Tfu*Cascade/R-loop, PreScission Protease cleavage to remove the Twin-Strep tag, and size-exclusion chromatography to remove the excess Cas3. Cryo-EM data acquisition, image acquisition, and structure reconstruction followed a similar procedure as described (*25*). Data processing and refinement statistics for the two cryo-EM structures are summarized in table S1.

REFERENCES AND NOTES

1. R. Barrangou *et al*., CRISPR provides acquired resistance against viruses in prokaryotes. *Science* **315**, 1709–1712 (2007). doi: 10.1126/science.1138140; pmid: 17379808
2. A. Bolotin, B. Quinquis, A. Sorokin, S. D. Ehrlich, Clustered regularly interspaced short palindrome repeats (CRISPRs) have spacers of extrachromosomal origin. *Microbiology* **151**, 2551–2561 (2005). doi: 10.1099/mic.0.28048-0; pmid: 16079334
3. F. J. Mojica, C. Díez-Villaseñor, J. García-Martínez, E. Soria, Intervening sequences of regularly spaced prokaryotic repeats derive from foreign genetic elements. *J. Mol. Evol.* **60**, 174–182 (2005). doi: 10.1007/s00239-004-0046-3; pmid: 15791728
4. C. Pourcel, G. Salvignol, G. Vergnaud, CRISPR elements in Yersinia pestis acquire new repeats by preferential uptake of bacteriophage DNA, and provide additional tools for evolutionary studies. *Microbiology* **151**, 653–663 (2005). doi: 10.1099/mic.0.27437-0; pmid: 15758212
5. L. A. Marraffini, E. J. Sontheimer, CRISPR interference limits horizontal gene transfer in staphylococci by targeting DNA. *Science* **322**, 1843–1845 (2008). doi: 10.1126/science.1165771; pmid: 19095942
6. K. S. Makarova, N. V. Grishin, S. A. Shabalina, Y. I. Wolf, E. V. Koonin, A putative RNA-interference-based immune system in prokaryotes: Computational analysis of the predicted enzymatic machinery, functional analogies with eukaryotic RNAi, and hypothetical mechanisms of action. *Biol. Direct* **1**, 7 (2006). doi: 10.1186/1745-6150-1-7; pmid: 16545108
7. K. S. Makarova, E. V. Koonin, Annotation and classification of CRISPR-Cas systems. *Methods Mol. Biol.* **1311**, 47–75 (2015). doi: 10.1007/978-1-4939-2687-9_4; pmid: 25981466
8. S. Shmakov *et al*., Discovery and functional characterization of diverse class 2 CRISPR-Cas systems. *Mol. Cell* **60**, 385–397 (2015). doi: 10.1016/j.molcel.2015.10.008; pmid: 26593719
9. S. J. Brouns *et al*., Small CRISPR RNAs guide antiviral defense in prokaryotes. *Science* **321**, 960–964 (2008). doi: 10.1126/science.1159689; pmid: 18703739
10. B. Wiedenheft *et al*., Structures of the RNA-guided surveillance complex from a bacterial immune system. *Nature* **477**, 486–489 (2011). doi: 10.1038/nature10402; pmid: 21938068
11. E. R. Westra *et al*., CRISPR immunity relies on the consecutive binding and degradation of negatively supercoiled invader DNA by Cascade and Cas3. *Mol. Cell* **46**, 595–605 (2012). doi: 10.1016/j.molcel.2012.03.018; pmid: 22521689
12. M. Rutkauskas *et al*., Directional R-loop formation by the CRISPR-Cas surveillance complex cascade provides efficient off-target site rejection. *Cell Reports* **S2211–1247**, 00135–00137 (2015). pmid: 25753419
13. T. R. Blosser *et al*., Two distinct DNA binding modes guide dual roles of a CRISPR-Cas protein complex. *Mol. Cell* **58**, 60–70 (2015). doi: 10.1016/j.molcel.2015.01.028; pmid: 25752578
14. M. M. Jore *et al*., Structural basis for CRISPR RNA-guided DNA recognition by Cascade. *Nat. Struct. Mol. Biol.* **18**, 529–536 (2011). doi: 10.1038/nsmb.2019; pmid: 21460843
15. T. Sinkunas *et al*., In vitro reconstitution of Cascade-mediated CRISPR immunity in Streptococcus thermophilus. *EMBO J.* **32**, 385–394 (2013). doi: 10.1038/emboj.2012.352; pmid: 23334296
16. S. Mulepati, S. Bailey, In vitro reconstitution of an Escherichia coli RNA-guided immune system reveals unidirectional, ATP-dependent degradation of DNA target. *J. Biol. Chem.* **288**, 22184–22192 (2013). doi: 10.1074/jbc.M113.472233; pmid: 23760266
17. M. L. Hochstrasser *et al*., CasA mediates Cas3-catalyzed target degradation during CRISPR RNA-guided interference. *Proc. Natl. Acad. Sci. U.S.A.* **111**, 6618–6623 (2014). doi: 10.1073/pnas.1405079111; pmid: 24748111
18. R. E. Haurwitz, M. Jinek, B. Wiedenheft, K. Zhou, J. A. Doudna, Sequence- and structure-specific RNA processing by a CRISPR endonuclease. *Science* **329**, 1355–1358 (2010). doi: 10.1126/science.1192272; pmid: 20829488
19. D. G. Sashital, B. Wiedenheft, J. A. Doudna, Mechanism of foreign DNA selection in a bacterial adaptive immune system. *Mol. Cell* **46**, 606–615 (2012). doi: 10.1016/j.molcel.2012.03.020; pmid: 22521690
20. R. N. Jackson *et al*., Structural biology. Crystal structure of the CRISPR RNA-guided surveillance complex from Escherichia coli. *Science* **345**, 1473–1479 (2014). doi: 10.1126/science.1256328; pmid: 25103409
21. H. Zhao *et al*., Crystal structure of the RNA-guided immune surveillance Cascade complex in *Escherichia coli*. *Nature* **515**, 147–150 (2014). doi: 10.1038/nature13733; pmid: 25118175
22. S. Mulepati, A. Héroux, S. Bailey, Structural biology. Crystal structure of a CRISPR RNA-guided surveillance complex bound to a ssDNA target. *Science* **345**, 1479–1484 (2014). doi: 10.1126/science.1256996; pmid: 25123481
23. R. P. Hayes *et al*., Structural basis for promiscuous PAM recognition in type I-E Cascade from E. coli. *Nature* **530**, 499–503 (2016). doi: 10.1038/nature16995; pmid: 26863189
24. Y. Huo *et al*., Structures of CRISPR Cas3 offer mechanistic insights into Cascade-activated DNA unwinding and degradation. *Nat. Struct. Mol. Biol.* **21**, 771–777 (2014). doi: 10.1038/nsmb.2875; pmid: 25132177

25. Y. Xiao *et al*., Structure basis for directional R-loop formation and substrate handover mechanisms in Type I CRISPR-Cas system. *Cell* **170**, 48–60.e11 (2017). doi: 10.1016/j.cell.2017.06.012; pmid: 28666122
26. S. Redding *et al*., Surveillance and processing of foreign DNA by the *Escherichia coli* CRISPR-Cas system. *Cell* **163**, 854–865 (2015). doi: 10.1016/j.cell.2015.10.003; pmid: 26522594
27. M. W. Brown *et al*., Assembly and translocation of a CRISPR-Cas primed acquisition complex. *bioRxiv* 10.1101/208058 (2017).

ACKNOWLEDGMENTS

We thank R. Battaglia, A. Dolan, and S. Ng for critical reading of the manuscript and I. Finkelstein for discussions. **Funding:** Research in the Ke laboratory is supported by the National Institutes of Health (GM118174 and GM102543). **Author contributions:** Y.X., M.Lu., M.Li., and A.K. designed the research. Y.X. and M.Lu. are the main contributors to biochemical reconstitutions, structure determination, and structure-function analyses. A.E.D. contributed to mutagenesis studies. M.Li. and A.K. led to structural and biochemical analyses. A.K. and the rest of the authors wrote the manuscript. **Competing interests:** The authors have no competing interest. **Data and materials availability:** The 3D cryo-EM density maps of the *Tfu*Cascade/R-loop/Cas3 complex have been deposited in the Electron Microscopy Data Bank under the accession nos. EMD-7347 (prenicking state) and EMD-7346 (postnicking state). The atomic coordinate for the prenicking state has been deposited in PDB under the accession no. 6C66.

SUPPLEMENTARY MATERIALS

www.sciencemag.org/content/361/6397/eaat0839/suppl/DC1
Materials and Methods
Figs. S1 to S5
Tables S1
References (*28*–*33*)

23 January 2018; accepted 22 May 2018
Published online 7 June 2018
10.1126/science.aat0839

RESEARCH ARTICLE

ATMOSPHERIC CIRCULATION

Atmospheric blocking as a traffic jam in the jet stream

Noboru Nakamura* and Clare S. Y. Huang

Atmospheric blocking due to anomalous, persistent meandering of the jet stream often causes weather extremes in the mid-latitudes. Despite the ubiquity of blocking, the onset mechanism is not well understood. Here we demonstrate a close analogy between blocking and traffic congestion on a highway by using meteorological data and show that blocking and traffic congestion can be described by a common mathematical theory. The theory predicts that the jet stream has a capacity for the flux of wave activity (a measure of meandering), just as the highway has traffic capacity, and when the capacity is exceeded, blocking manifests as congestion. Stationary waves modulate the jet stream's capacity for transient waves and localize block formation. Climate change likely affects blocking frequency by modifying the jet stream's proximity to capacity.

Winds in Earth's mid-latitudes blow predominantly eastward, and their speeds increase with altitude to form a jet stream in the middle to upper troposphere. Winds steer cyclones and anticyclones, and these weather systems in turn cause the jet stream to meander over thousands of kilometers. This undular pattern also migrates eastward, forming the transient Rossby waves (*1*, *2*). However, occasionally the jet stream develops persistent meandering in a certain region, disrupting the passage of the transient waves—a condition known as blocking (*3*–*5*). A block can last for a few days to more than a week and often brings about anomalous, sometimes extreme, weather in the mid-latitudes. For example, the unprecedented heat wave that claimed tens of thousands of lives in Europe in the summer of 2003 was due at least partially to a strong anticyclonic blocking (*6*). In late October 2012, a highly meandering jet stream due to North Atlantic blocking steered Superstorm Sandy into a surprising westward path to make landfall on the New Jersey coast of the eastern United States (*7*).

Figure 1, A and B, illustrates observed blocking over the eastern Pacific and Euro-Atlantic sectors of the Northern Hemisphere [data are from (*8*)]. The crowded contours of the 500-hPa geopotential height (Z500, roughly a midtropospheric stream function) and high wind speeds define the jet stream, and its pronounced poleward excursion in the respective regions marks blocking. In the boreal winter, blocking often occurs when a preexisting quasistationary ridge amplifies and obstructs transient waves. For example, in the longitude-time diagram of Z500 (Fig. 1C), the diagonal streaks of transient waves are suppressed around 20 to 40°W in late January and mid-February. Though this suggests a role of stationary waves in block formation (*9*), the onset of blocking is still poorly understood, and it remains a challenging problem in numerical weather prediction (*10*, *11*). Previously proposed mechanisms

Department of the Geophysical Sciences, University of Chicago, Chicago, IL 60637, USA.
***Corresponding author. Email: nnn@uchicago.edu**

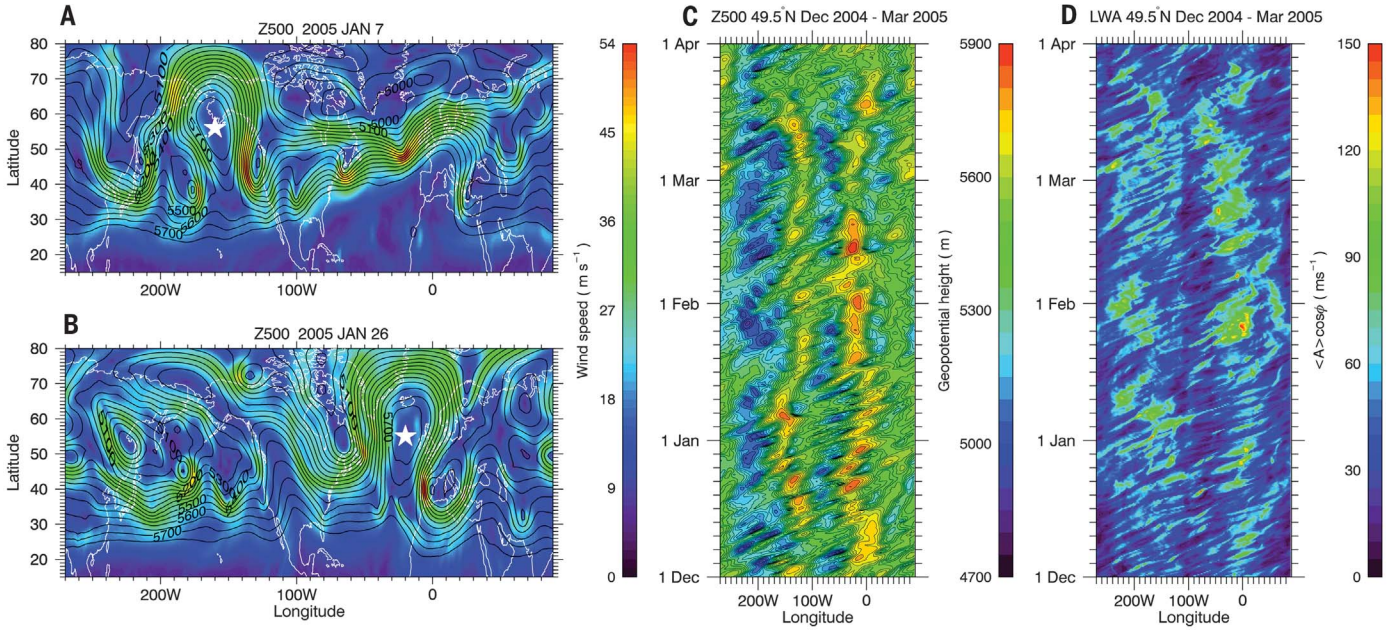

Fig. 1. A blocked jet stream disrupts wave propagation. (**A**) Z500 (500-hPa geopotential height) (contours every 50 m) and horizontal wind speed (color) in the Northern Hemisphere extratropics for 7 January 2005 (18 UTC). The star identifies the center of a block. (**B**) As in (A) but for 26 January 2005 (06 UTC). (**C**) Z500 at 49.5°N as a function of longitude and time (1 December 2004 to 31 March 2005). The contour interval is 50 m. (**D**) As in (C) but for column LWA. In all panels, the zero longitude corresponds to the International Reference Meridian. Data were obtained by using the ERA-Interim reanalysis product (*8*).

of block formation and maintenance include forcing by transient eddies and intrinsic instability of low-frequency dynamics (*12*–*19*), yet no definitive theory exists for the onset criterion. Because of incomplete mechanistic understanding, even the definition of blocking remains somewhat subjective, and various blocking indices do not agree on the effects of climate change on them (*20*, *21*).

In this article, we propose a mechanism of block formation on the basis of observation and simple mathematical theory. The main tool of investigation is a recently developed metric for the jet stream's meandering, finite-amplitude local wave activity (LWA, herein denoted by the symbol A) (*22*, *23*). Based on the displacement of quasigeostrophic potential vorticity (*24*), LWA is a dynamic field that quantifies Rossby wave packets and their interaction with eastward wind on regional scales [see materials and methods (MM) in supplementary materials for theoretical background and the definitions of mathematical symbols]. Given that blocking signal is largely tropospheric and vertically coherent (*5*, *22*), we make extensive use of density-weighted, vertically averaged ("column") LWA, $\langle A \rangle$ (the angle bracket denotes the column average). The column budget of LWA reveals marked similarity between atmospheric blocking and traffic congestion on a highway. The analogy enables us to understand block formation with the well-known traffic theory, which not only predicts a threshold of onset but also aids in the formation of testable hypotheses for the influence of climate change on blocking.

Jet stream behaviors analyzed with column LWA

To unravel the dynamics of block formation, we rely on the following properties of column LWA: (i) It qualitatively distinguishes blocking from wave propagation; (ii) it quantifies compensating tendencies between the jet stream's meander and the speed of eastward wind; and (iii) it obeys a simple budget evaluable with data. Figure 1D shows column LWA in the same format as Fig. 1C. Diagonal streaks and clusters of large LWA events are readily recognized. The former delineate eastward propagation of transient Rossby waves, whereas the latter identify blocking. The distinction is more pronounced than that in Fig. 1C, and it is easy to isolate major blocking events such as those in Fig. 1, A and B.

Figure 2A shows in color the temporal covariance between column LWA $\langle A \rangle$ and column eastward wind $\langle u \rangle$ for the boreal winter [December-January-February (DJF)], averaged for 1979 to 2016. Here and throughout the article, both quantities are multiplied by the cosine of latitude (ϕ) to make an explicit connection to angular momentum. Covariance is almost everywhere negative (red indicates zero): That is, when the jet stream meanders more, the eastward wind slows down (and is sometimes reversed to westward). The most strongly negative covariance is found in the downstream of the climatological jets (contours), where blocks form frequently (*25*, *26*). At the locations of maximum covariance, A (9°W, 45°N) and B (147°W, 42°N), a mutually compensating tendency of $\langle A \rangle$ and $\langle u \rangle$ is evident in the scatter diagrams (Fig. 2, B and C), which suggests an approximate relation

$$\langle u \rangle \approx u_0 - \alpha \langle A \rangle \qquad (1)$$

where u_0 and α are empirically determined positive constants. This relation is associated with the conservation of the longitudinal average of $\langle A \rangle + \langle u \rangle$ through Kelvin's circulation theorem, although locally the conservation is not perfect, so there is significant scatter and α deviates from 1 (*22*, *27*, *28*). The minimum value of column LWA is finite at both locations (Fig. 2, B and C), which we interpret as the stationary wave component of LWA (*23*).

Figure 3 compares the DJF climatology of column LWA (color) and Z500 (contours) with the composites of the large LWA events marked by the red diamonds in Fig. 2, B and C. These diamonds identify 4-day periods in which $\langle A \rangle$ and $\langle u \rangle$ are simultaneously in the top and bottom 5 percentiles, respectively, of all 858 sampled

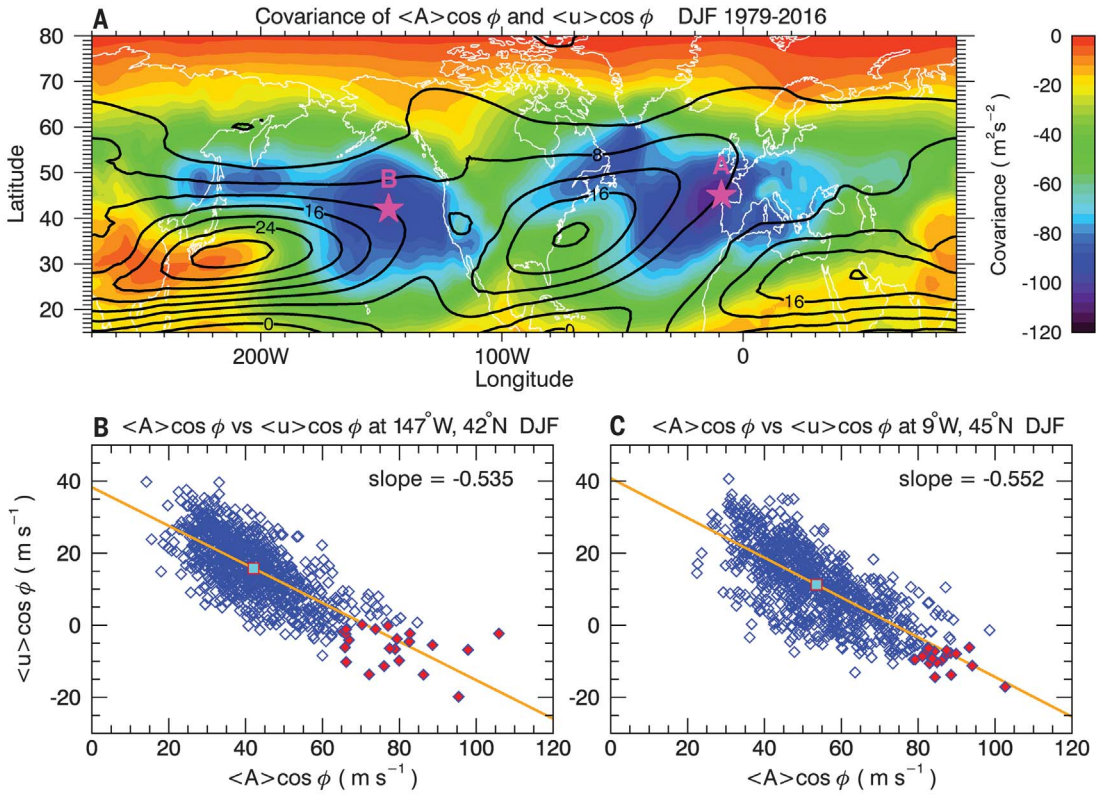

Fig. 2. LWA and eastward wind covary negatively. (**A**) Color indicates the covariance between $\langle A \rangle \cos\phi$ and $\langle u \rangle \cos\phi$ in the boreal winter, and contours indicate DJF climatology of $\langle u \rangle \cos\phi$ expressed in meters per second. The locations of peak covariance are labeled A (9°W, 45°N) and B (147°W, 42°N). Data were obtained by using the ERA-Interim reanalysis product for 1979 to 2016 (*8*). (**B**) Scatter diagram of 4-day average $\langle A \rangle \cos\phi$ versus 4-day average $\langle u \rangle \cos\phi$ for the same period at location B. The cyan box represents the DJF climatological mean. The red diamonds represent periods in which $\langle A \rangle \cos\phi$ and $\langle u \rangle \cos\phi$ are simultaneously in the top and bottom 5 percentiles, respectively, of all 858 sampled values (listed in tables S1 and S2). The orange line is a least-squares fit whose slope is indicated. (**C**) Same as (B) but for location A.

periods (24 for location A and 22 for location B, listed in tables S1 and S2). The climatology in Fig. 3A shows large LWA events on the poleward and downstream sides of the jet maxima (packed contours of Z500), as well as stationary ridges over the west coasts of North America and Europe, in agreement with Fig. 1C. The composite of the Atlantic events (Fig. 3B) shows a protruding ridge over the eastern North Atlantic, with a peak LWA in the close vicinity of the height anomaly. The Pacific events display a similar structure, except the ridge tilts in the opposite way and the LWA maximum is weaker (Fig. 3C). Both composites exhibit characteristics of a block: enhanced regional meandering of the jet stream that persists at least for a few days. Figures S1 and S2 repeat the analysis using eddy kinetic energy and eddy potential enstrophy instead of LWA. These more traditional Eulerian metrics are less successful at identifying blocks—to a varying degree they capture the properties of the displaced jets rather than those of the blocks themselves.

The column budget of LWA reads (*22*, *23*)

$$\frac{\partial}{\partial t}\langle A\rangle\cos\phi = \underbrace{-\frac{1}{a\cos\phi}\frac{\partial\langle F_\lambda\rangle}{\partial\lambda}}_{(I)} \underbrace{+\frac{1}{a\cos\phi}\frac{\partial}{\partial\phi'}\langle u_e v_e\cos^2(\phi+\phi')\rangle}_{(II)} + \underbrace{\frac{f\cos\phi}{H}\left(\frac{v_e\theta_e}{\partial\bar{\theta}/\partial z}\right)_{z=0}}_{(III)} + \underbrace{\langle\dot{A}\rangle\cos\phi}_{(IV)} \quad (2)$$

where the right-hand side (RHS) terms are (I) convergence of the zonal LWA flux (the form of $\langle F_\lambda\rangle$ will be discussed shortly), (II) divergence of the meridional eddy momentum flux, (III) meridional eddy heat flux at the lower boundary, and (IV) nonadiabatic sources and sinks of LWA (see MM for the definitions of variables). Equation 2 is similar to the linearized (small-amplitude) wave activity budget (*29*) yet applies to waves of arbitrary amplitude. Term IV does not subsume any cubic or higher-order term commonly neglected in the small-amplitude limit. The relative importance of the terms in Eq. 2 depends on the time scale (*23*). On synoptic time scales, term I dominates the RHS; when evaluated with data for locations A and B in Fig. 2A, this term explains about 70 percent of the total variance of the left-hand side, whereas the other terms play much smaller roles (table S3). (Term IV is evaluated as the residual of the budget, so it inevitably contains some analysis error.) The finding suggests that, to the lowest order, the jet stream may be viewed as a waveguide in longitude. This renders the column budget of LWA a one-dimensional (1D) transport problem—perhaps an oversimplification for the mature stage of blocking but adequate for periods leading up to the block formation. We therefore take a closer look at the zonal LWA flux $\langle F_\lambda\rangle$ in Eq. 2 and its relation to column LWA.

Zonal flux of LWA and analogy to traffic flow

The explicit form of $\langle F_\lambda\rangle$ is (*22*, *23*)

$$\langle F_\lambda\rangle = \underbrace{\langle u_{REF}A\cos\phi\rangle}_{F_1} \underbrace{-a\langle\int_0^{\Delta\phi}u_e q_e\cos(\phi+\phi')d\phi'\rangle}_{F_2} + \underbrace{\frac{\cos\phi}{2}\langle v_e^2 - u_e^2 - \frac{R}{H}\frac{e^{-\kappa z/H}}{\partial\bar{\theta}/\partial z}\theta_e^2\rangle}_{F_3} \quad (3)$$

Two of the RHS terms (F_1 and F_3) are associated with group propagation of the Rossby waves in the reference state (including advection by u_{REF}, the zonal wind speed in a wave-free reference state) (MM). The sum $F_1 + F_3$ varies approximately linearly with column LWA, where the proportionality constant is the mean zonal group velocity of the waves (see the orange diamonds in Fig. 4, A and C). This linear relation corresponds to the diagonal streaks in Fig. 1D with modest magnitudes of LWA. The remaining term (F_2) represents nonlinear modification of the flux by large-amplitude waves. With this term included, the total flux $\langle F_\lambda\rangle$ (blue diamonds) exhibits considerable scatter against column LWA [because of the irregular covariance of u_e and q_e (the deviation in potential vorticity) in F_2]. However, the majority of the blue diamonds reside below the orange cluster, and their separation becomes more pronounced at greater LWAs. The curve fits and quartile plots in Fig. 4, B and D, further summarize this. Despite the considerable range of bars in the quartile plots, it is fair to say that $\langle F_\lambda\rangle$ maximizes at an intermediate value of column LWA (50 to 60 ms^{-1}), beyond which it decreases with increasing LWA. The deviation of $\langle F_\lambda\rangle$ from $F_1 + F_3$ means that F_2 is predominantly negative and more so at higher LWAs. This is because at large wave amplitudes, the zonal wind is decelerated relative to the reference state, so $u_e \propto -\langle A\rangle$ (Eq. 1). From Eq. 3 and eq. S2a, we then expect $F_2 \propto -\langle A\rangle^2$, which prevails over $F_1 + F_3 \propto \langle A\rangle$ at large values of $\langle A\rangle$ and suppresses $\langle F_\lambda\rangle$. For this reason, we use a parabolic curve fit for $\langle F_\lambda\rangle$ in Fig. 4, B and D. The fitted blue curves trace the median values reasonably well at high LWAs and come close to the orange lines at lower values (20 to 40 ms^{-1}).

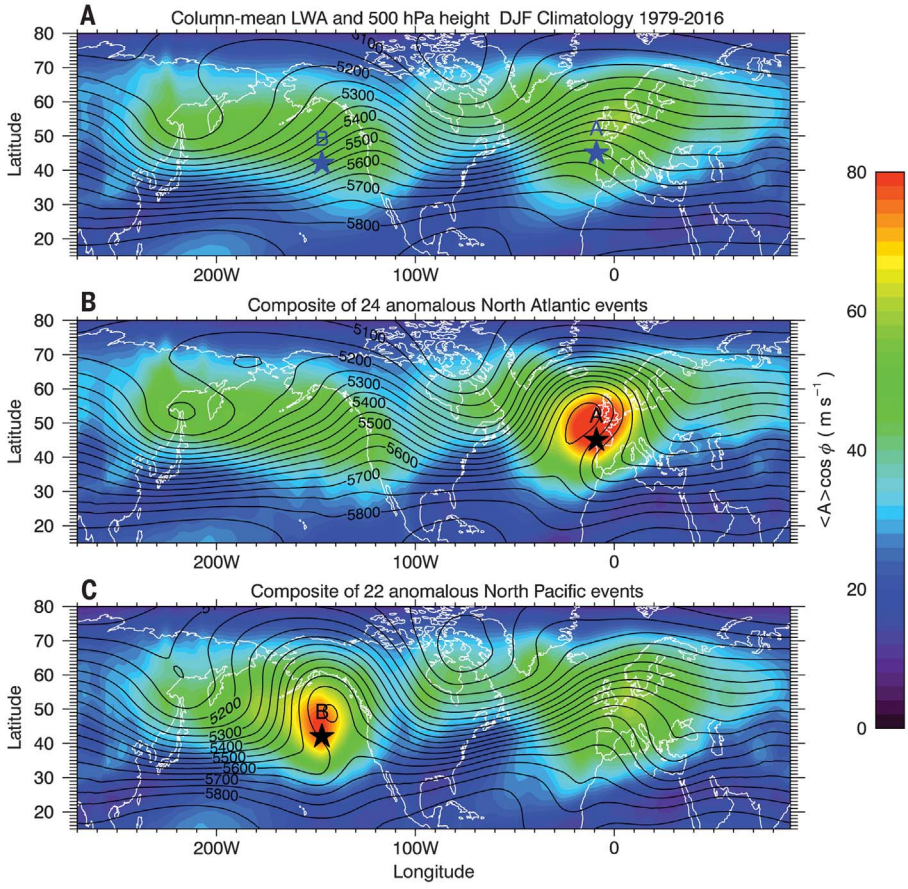

Fig. 3. LWA in climatology and blocked states. (**A**) DJF climatology of $\langle A\rangle\cos\phi$ (color) and Z500 (contours, in meters) in the Northern Hemisphere extratropics. (**B**) Same as (A) but a composite of 24 anomalous Atlantic events. (**C**) Same as (A) but a composite of 22 anomalous Pacific events. The analysis locations (A and B) are the same as those in Fig. 2.

There is a close parallelism between Fig. 4 and the so-called fundamental diagram of traffic flow in transportation engineering (*30*, *31*). The latter describes traffic flow (or flux, the number of cars passing through a point of highway per unit of time) as a function of traffic density (the number of cars per unit of length of highway). For a major highway and a network of highways, traffic flow maximizes at an intermediate value of traffic density, which defines highway capacity (*30*, *32*). When the traffic is light, most cars travel at or near the speed limit, so the traffic flow is proportional to traffic density, just like the orange lines in Fig. 4, B and D, if we substitute traffic density for column LWA. However, as the traffic becomes heavier, the increasing density slows down the traffic because of changes in the drivers' braking practices and other driving behaviors, which will eventually suppress the flow despite the increasing density. This is analogous to the blue curves in Fig. 4: Waves slow the winds and limit the growth of the LWA flux (i.e., the effect of F_2 on $\langle F_\lambda \rangle$). When this happens, a traffic bottleneck (shock) forms quickly because a decreasing flow in the direction of traffic causes convergence and hence rapid accumulation of density (*33*, *34*). Traffic congestion therefore occurs at the high-density–low-flow end of the fundamental diagram after the highway capacity is reached. Similarly, the red diamonds in Fig. 4, A and C, corresponding to the block-producing red diamonds in Fig. 2, B and C, occupy high LWA and low zonal LWA flux. The analogy suggests that atmospheric blocking occurs much the same way as traffic congestion: The jet stream possesses a capacity for the zonal LWA flux, which when exceeded triggers block formation.

To test this hypothesis with a simple model, we first documented the observed life cycle of blocking for a reference. Figure 5 shows a composite of the 24 Atlantic events listed in table S1, in longitude-time diagrams of column LWA, column zonal wind, and $\langle F_\lambda \rangle$ along 45°N. The composite shows gradual buildup and decay of the column LWA anomaly and the simultaneous deceleration (reversal) and acceleration of the zonal wind. The life span of the event is approximately a week, and the signal is longitudinally isolated (Fig. 5, A and B). The zonal LWA flux turns slightly negative within the block, but in the immediate upstream (40° to 10°W) there is a prolonged period of enhanced flux, with particularly large values appearing from 13 to 7 days before the event (Fig. 5C). This supports the notion that an elevated wave activity flux in the upstream (due, for example, to anomalous storm track activity) triggers a block formation downstream (*35*, *36*).

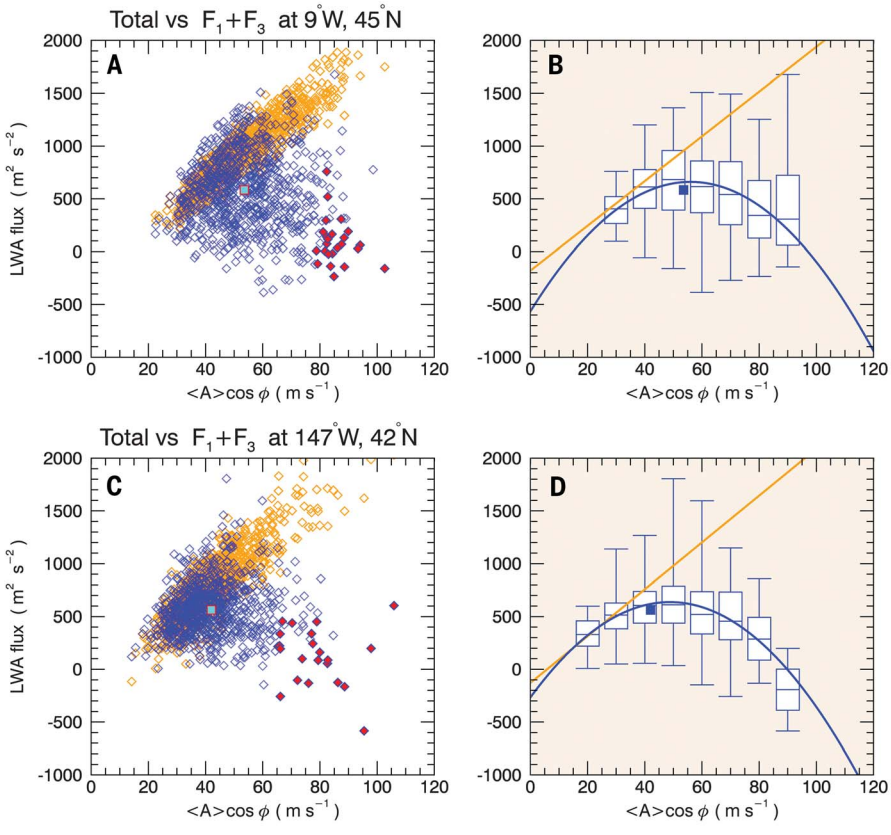

Fig. 4. LWA and its zonal flux at the jet exit. Relationships between $\langle A \rangle \cos\varphi$ (abscissa) and the flux terms on the RHS of Eq. 3 (ordinate). (**A** and **B**) 9°W, 45°N (location A). (**C** and **D**) 147°W, 42°N (location B). [(A) and (C)] Four-day averages of $F_1 + F_3$ (orange) and $\langle F_\lambda \rangle$ (blue) against the 4-day average of column LWA, sampled during DJF of 1979 to 2016. The red diamonds correspond to those in Fig. 2, B and C. [(B) and (D)] Diagrams simplifying (A) and (C) with a least-squares fit (orange), a chi-square fit with a parabolic curve (blue), and quartile plots. The quartile plots show maximum, minimum, and median values, together with the upper and lower quartiles of $\langle F_\lambda \rangle$, for 10-ms^{-1} intervals of $\langle A \rangle \cos\phi$. Boxes and bars were not drawn if the interval contains fewer than five data points. The cyan squares in (A) and (C) and blue squares in (B) and (D) indicate the DJF climatological mean values.

A simple model of blocking life cycle

To conceptualize what we have observed so far, we propose the nonlinear partial differential equation

$$\frac{\partial}{\partial t}\hat{A}(x,t) = -\frac{\partial}{\partial x}\left[\left(C(x) - \alpha\hat{A}\right)\hat{A}\right] + \hat{S} - \frac{\hat{A}}{\tau} + D\frac{\partial^2 \hat{A}}{\partial x^2} \quad (4)$$

where x is longitude and t is time. Equation 4 governs the evolution of the transient-wave component of column LWA, $\hat{A}$. It is derived from Eqs. 2 and 3 with Eq. 1 and other simplifying assumptions, and by partitioning LWA into stationary- and transient-wave components: $A(x,t) = A_0(x) + \hat{A}(x,t)$ (see MM for derivation). $[C(x) - \alpha\hat{A}]\hat{A} \equiv F$ is the nonlinear flux of $\hat{A}$, where $C(x) \equiv u_{\mathrm{REF}} + c_g - 2\alpha A_0(x)$ denotes the background group velocity modulated by the stationary wave A_0 ($u_{\mathrm{REF}} + c_g$ is a constant zonal group velocity in the reference state). The dependence of C on A_0 introduces interaction between stationary and transient waves. The parameter α is an empirical constant introduced in Eq. 1, which is assumed to be independent of space and time. The last three terms in Eq. 4 replace terms II to IV in Eq. 2 with a simple source and sink of $\hat{A}$ plus numerical diffusion that keeps $\hat{A}$ smooth. By analogy, Eq. 4 also describes the traffic flow problem (*33*, *34*). In that context, $C(x)$ plays the role of speed limit. Table S4 summarizes parallel interpretations of Eq. 4 for traffic and blocking problems.

We integrate Eq. 4 from $\hat{A} = 0$ with a constant forcing $\hat{S} > 0$ (representing a homogeneous transient-wave source associated with storm activities and nonadiabatic processes), a prescribed stationary wave $A_0(x)$ with zonal wave number 2, and periodic boundary conditions in x (see MM for the details of the experiment). Eventually the total LWA, $A = A_0 + \hat{A}$, settles into a steady state with two peaks, notably higher than A_0 because of the forcing. This corresponds to Fig. 3A. Subsequent evolution of A is depicted in Fig. 6A and movie S1. To mimic anomalous weather activity in the upstream (*35*), we increase the forcing $\hat{S}$ temporarily with a peak value around 44°W and day −4. (A highway

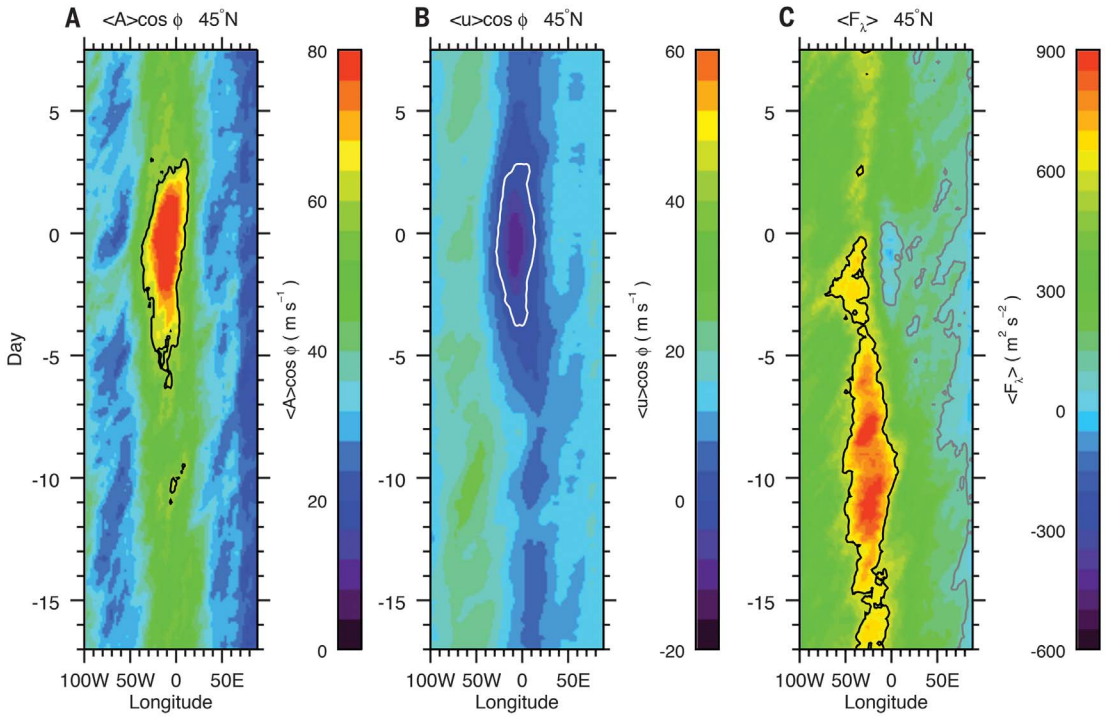

Fig. 5. Composite life cycle of Atlantic blocks. (**A**) Composite longitude-time diagram of $\langle A \rangle \cos\phi$ along 45°N for the 24 Atlantic events listed in table S1 in supplementary materials. The black contour indicates 60 ms^{-1}. Day 0 corresponds to the peak of blocking. (**B**) Same as (A) but for $\langle u \rangle \cos\phi$. The white contour indicates 0. (**C**) Same as (A) but for $\langle F_\lambda \rangle$. The gray and black contours indicate 0 and 600 $m^2\ s^{-2}$, respectively.

analogy would be a sudden merging of traffic that increases traffic density.) In a few days, A begins to grow downstream, most markedly at a point slightly upstream of the preexisting ridge. The growth culminates in a shock formation around 15°W (movie S1), a well-known behavior in the traffic flow problem and an indication of wave breaking in our context. See our previous work (*37*) as to how shock formation in one dimension relates to wave breaking and block formation in two dimensions. After a maximum value is reached, A slowly recedes to the steady state through damping, while the shock migrates downstream.

Figure 6 also shows $u \equiv 40 - \alpha A$ (eastward wind) (Fig. 6B) and $F = [C(x) - \alpha\hat{A}]\hat{A}$ (zonal LWA flux) (Fig. 6C) for this experiment. Broad agreements with Fig. 5 attest to the ability of Eq. 4 to capture the rudimentary characteristics of blocking. There are also notable differences: For example, in Fig. 6, u and F do not turn negative. (Traffic may come to a halt, but it never reverses on its own.) This is one of the limitations of the 1D model. Another discrepancy is that the growth phase of the wave event is shorter in Fig. 6, with the peak flux concentrated within 5 to 2 days prior to blocking (Fig. 6C), whereas in the observation the peak flux occurs farther in advance (Fig. 5C). This is probably because of the specific form of forcing used in the experiment. The decay of the block in the simulation is dictated by a constant damping rate, but in reality processes such as the meridional redistribution of momentum by waves (term II in Eq. 2) may alter this rate once the block matures. Generally, we regard Eq. 4 as a minimal model of block formation; to capture the fuller details of life cycle, one needs a 2D (or 3D) model.

Despite its crudeness, Eq. 4 provides a useful threshold for wave breaking and subsequent block formation. Without the last three terms, Eq. 4 develops a shock after F saturates; that is, after it reaches the capacity $C^2/4\alpha$ (or equivalently, $\hat{A}$ exceeds $C/2\alpha$) where $C' < 0$ (i.e., the background group velocity decreases downstream) (*38*). Figure S3 describes the evolution of Γ, the saturation level of LWA flux defined as

$$\Gamma(x,t) \equiv \frac{4\alpha F(x,t)}{C^2(x)}$$

$$= \frac{4\alpha}{[u_{\mathrm{REF}} + c_g - 2\alpha A_0(x)]^2} \frac{F(x,t)}{} \leq 1 \qquad (5)$$

during the experiment. Γ is already as high as 0.9 initially (day −17) at 9°E, where C is at minimum because of large stationary wave A_0. Γ first reaches 1 around 0° on day −3.5, where $C' < 0$, after which the shock forms in the upstream. Therefore, even with additional terms in Eq. 4, the flux saturation (Γ = 1) is an important threshold for the onset of blocking. The precise timing and location of saturation in the real atmosphere may be hard to predict because of large uncertainty in $\langle F_\lambda \rangle$ (Fig. 4), but regions with higher values of Γ (closer to saturation) are more conducive to block formation. The exit regions of the storm tracks are prime examples for this, where diffluence of the jet stream associated with stationary waves keeps the flux capacity small (analogous to a reduced speed limit on a highway) and a large LWA flux is frequently seeded by cyclogenesis in the upstream. The observed climatological mean states indicated by the blue boxes in Fig. 4, B and D, are close to the vertices of the blue curves, analogous to Γ ~ 1 in the model.

Discussion

The present study provides a theoretical framework to quantify processes that cause block formation. Previously, Charney and DeVore (*39*) characterized blocking as a metastable state of the atmosphere arising from the resonance between topographic forcing and the Rossby waves, but they were unable to identify the mechanism of transition into this state. In contrast to their theory, Eq. 4 has only one stable equilibrium. Such equilibrium could reach capacity and form a perpetual block (shock) if the forcing $\hat{S}$ were excessive. However, in the experiment described above (and in the real atmosphere), steady state is subcritical (nonblocking) (Fig. 3A). When a localized, transient forcing (e.g., explosive cyclogenesis) is applied, it causes the downstream flow to reach capacity for a limited time, giving rise to a blocking episode.

Climate change potentially affects blocking frequency by altering the jet stream's proximity to capacity (Γ). Though much of the ongoing debate concerns the role of reduced meridional temperature gradients associated with polar amplification (*21*), Eq. 5 suggests that many factors affect Γ: a shift in the stationary waves, reference-state jet speed, transient-wave LWA flux, or any combination of these. As the response of Γ to climate change is likely nonuniform, it can affect blocking frequency heterogeneously. For

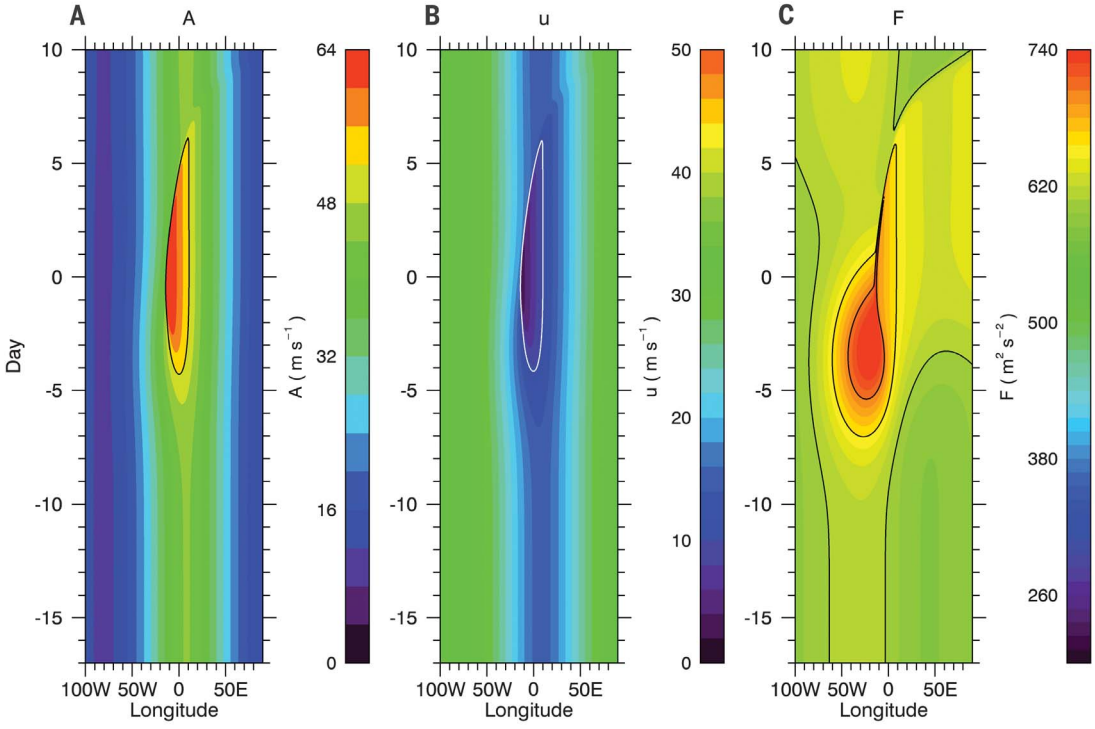

Fig. 6. Blocking life cycle simulated by Eq. 4. (**A**) Longitude-time diagram of $A = A_0 + \hat{A}$ for a 1D experiment. The black contour indicates 52 ms^{-1}. Day 0 corresponds to the peak of the wave event. (**B**) Same as (A) but for u. The white contour indicates 11 ms^{-1}. (**C**) Same as (A) but for F. The contours indicate 608, 656, and 704 m^2 s^{-2}. In all panels, only a part of the computational domain is shown. See movie S1 for more details.

example, the vast majority of the 24 Atlantic events in table S1 occurred after 1997, whereas the opposite is true for the 22 Pacific events in table S2. Linear trends in the DJF seasonal mean of column LWA north of 40°N show that over the years LWA has decreased in the Pacific, with generally opposite trends in the zonal wind (fig. S4). At 147°E, 42°N (location B), we find a statistically significant shift in the distributions of LWA and zonal wind to corroborate this trend (fig. S5). The increased eastward wind may have rendered the jet stream less saturated and contributed to the decreased blocking frequency in table S2.

REFERENCES AND NOTES

1. C. G. Rossby, *J. Mar. Res.* **2**, 38–55 (1939).
2. G. W. Platzman, *Q. J. R. Meteorol. Soc.* **94**, 225–248 (1968).
3. D. F. Rex, *Tellus* **2**, 275–301 (1950).
4. T. Woollings, A. Hannachi, B. Hoskins, *Q. J. R. Meteorol. Soc.* **136**, 856–868 (2010).
5. R. Berggren, B. Bolin, C. G. Rossby, *Tellus* **1**, 14–37 (1949).
6. R. García-Herrera, J. Diaz, R. M. Trigo, J. Luterbacher, E. M. Fischer, *Crit. Rev. Environ. Sci. Technol.* **40**, 267–306 (2010).
7. A. H. Sobel, *Storm Surge* (HarperCollins, 2014).
8. D. P. Dee *et al.*, *Q. J. R. Meteorol. Soc.* **137**, 553–597 (2011).
9. S. J. Colucci, *J. Atmos. Sci.* **58**, 933–942 (2001).
10. J. L. Pelly, B. J. Hoskins, *Q. J. R. Meteorol. Soc.* **129**, 1683–1702 (2003).
11. X. Jia, S. Yang, W. Song, B. He, *J. Meteorol. Res.* **28**, 76–90 (2014).
12. G. J. Shutts, *Q. J. R. Meteorol. Soc.* **109**, 737–761 (1983).
13. K. E. Trenberth, *J. Atmos. Sci.* **43**, 2061–2069 (1986).
14. S. L. Mullen, *J. Atmos. Sci.* **44**, 3–22 (1987).
15. K. Haines, J. Marshall, *Q. J. R. Meteorol. Soc.* **113**, 681–704 (1987).
16. H. Nakamura, M. Nakamura, J. L. Anderson, *Mon. Weather Rev.* **125**, 2074–2093 (1997).
17. K. L. Swanson, *Q. J. R. Meteorol. Soc.* **127**, 1341–1355 (2001).
18. B. A. Cash, S. Lee, *J. Atmos. Sci.* **57**, 3202–3218 (2000).
19. D. Luo, *J. Atmos. Sci.* **62**, 5–21 (2005).
20. E. A. Barnes, J. Slingo, T. Woollings, *Clim. Dyn.* **38**, 2467–2481 (2012).
21. E. A. Barnes, E. Dunn-Sigouin, G. Masato, T. Woollings, *Geophys. Res. Lett.* **41**, 638–644 (2014).
22. C. S. Y. Huang, N. Nakamura, *J. Atmos. Sci.* **73**, 211–229 (2016).
23. C. S. Y. Huang, N. Nakamura, *Geophys. Res. Lett.* **44**, 5673–5682 (2017).
24. J. G. Charney, "On the scale of atmospheric motions," *Geofys. Publ.* (vol. 17, no. 2) (1948).
25. J. L. Pelly, B. J. Hoskins, *J. Atmos. Sci.* **60**, 743–755 (2003).
26. D. Barriopedro, R. Garcia-Herrera, A. R. Lupo, E. Hernandez, *J. Clim.* **19**, 1042–1063 (2006).
27. N. Nakamura, D. Zhu, *J. Atmos. Sci.* **67**, 2701–2716 (2010).
28. L. Wang, N. Nakamura, *Geophys. Res. Lett.* **42**, 8192–8200 (2015).
29. R. A. Plumb, *J. Atmos. Sci.* **43**, 1657–1678 (1986).
30. B. D. Greenshields, *Highway Res. Board Proc.* **14**, 448–477 (1935).
31. M. Treiber, A. Kesting, *Traffic Flow Dynamics: Data, Models and Simulation* (Springer, 2013).
32. N. Geroliminis, C. F. Daganzo, *Transp. Res. Part B* **42**, 759–770 (2008).
33. M. Lighthill, G. B. Whitham, *Proc. R. Soc. London Ser. A* **229**, 317–345 (1955).
34. P. I. Richards, *Oper. Res.* **4**, 42–51 (1956).
35. S. J. Colucci, *J. Atmos. Sci.* **42**, 2701–2717 (1985).
36. H. Nakamura, J. M. Wallace, *Mon. Weather Rev.* **121**, 1892–1903 (1993).
37. N. Nakamura, C. S. Y. Huang, *J. Atmos. Sci.* **74**, 2341–2362 (2017).
38. R. LeVeque, *Finite Volume Methods for Hyperbolic Problems* (Cambridge Univ. Press, 2002).
39. J. G. Charney, J. G. DeVore, *J. Atmos. Sci.* **36**, 1205–1216 (1979).

ACKNOWLEDGMENTS

Funding: This work has been supported by NSF grant AGS1563307. **Author contributions**: N.N. laid out the conceptual framework for the finite-amplitude wave activity diagnostic and identified the connection between atmospheric blocking and the traffic flow problem. He formulated and conducted the 1D experiment and also produced all but two figures. C.S.Y.H. worked out the LWA budget as part of her Ph.D. dissertation study and performed most of the data analysis described in this article. She also produced figs. S4 and S5. **Competing interests**: The authors do not have any competing interests. **Data and materials availability**: To evaluate the terms in Eqs. 1 to 3 and to create Figs. 1 to 5; figs. S1, S2, S4, and S5; and tables S1 to S3, we used the European Centre for Medium-Range Weather Forecasts (ECMWF) ERA-Interim reanalysis product (*8*). Six-hourly global pressure–level analysis for u, v (meridional wind speed), temperature, and geopotential was obtained from http://apps.ecmwf.int/datasets/data/interim-full-daily/levtype=pl/ with 1.5° by 1.5° horizontal grid resolution. We have also used the daily North Atlantic oscillation index downloaded from NOAA's Climate Prediction Center at http://www.cpc.ncep.noaa.gov/products/precip/CWlink/pna/nao_index.html to compute data in the last column of table S1. The python package that contains the modules to compute LWA and u_{REF} from ERA-Interim reanalysis data can be found at https://github.com/csyhuang/hn2016_falwa. The scripts to produce the analyses in this paper are contained in the folder https://github.com/csyhuang/hn2016_falwa/tree/master/examples/nh2018_science.

SUPPLEMENTARY MATERIALS

www.sciencemag.org/content/361/6397/42/suppl
Materials and Methods
Figs. S1 to S5
Tables S1 to S4
References (*40*–*43*)
Movie S1

21 January 2018; accepted 11 May 2018
Published online 24 May 2018
10.1126/science.aat0721

REPORT

FRAMEWORK MATERIALS

Single-crystal x-ray diffraction structures of covalent organic frameworks

Tianqiong Ma[1,2]*, Eugene A. Kapustin[3]*, Shawn X. Yin[4], Lin Liang[1], Zhengyang Zhou[2], Jing Niu[1], Li-Hua Li[1], Yingying Wang[1], Jie Su[2], Jian Li[2], Xiaoge Wang[2], Wei David Wang[1], Wei Wang[1,5]†, Junliang Sun[2]†, Omar M. Yaghi[3,6]†

The crystallization problem is an outstanding challenge in the chemistry of porous covalent organic frameworks (COFs). Their structural characterization has been limited to modeling and solutions based on powder x-ray or electron diffraction data. Single crystals of COFs amenable to x-ray diffraction characterization have not been reported. Here, we developed a general procedure to grow large single crystals of three-dimensional imine-based COFs (COF-300, hydrated form of COF-300, COF-303, LZU-79, and LZU-111). The high quality of the crystals allowed collection of single-crystal x-ray diffraction data of up to 0.83-angstrom resolution, leading to unambiguous solution and precise anisotropic refinement. Characteristics such as degree of interpenetration, arrangement of water guests, the reversed imine connectivity, linker disorder, and uncommon topology were deciphered with atomic precision—aspects impossible to determine without single crystals.

Covalent organic frameworks (COFs) are constructed from organic building units using strong covalent bonds between light atoms (e.g., H, B, C, N, O, Si) (*1*–*3*). Progress in developing their chemistry depends on understanding their structure, but their synthesis often yields polycrystalline or amorphous products rather than single crystals. Although structures modeled from powder x-ray diffraction (XRD) have advanced the field, definitive structural solutions by single-crystal XRD (SXRD) are needed for several reasons: (i) Modeling of COF structures from powder diffraction data is difficult, especially when they are not based on the anticipated default nets (*3*, *4*); (ii) atomic positions and geometric parameters (bond lengths and angles) are usually unattainable; (iii) complexity arising from interpenetrated frameworks and disorder remains uncovered; and (iv) guest arrangement within their pores is unknown.

[1]State Key Laboratory of Applied Organic Chemistry, College of Chemistry and Chemical Engineering, Lanzhou University, Lanzhou, Gansu 730000, China. [2]College of Chemistry and Molecular Engineering, Beijing National Laboratory for Molecular Sciences, Peking University, Beijing 100871, China. [3]Department of Chemistry, University of California-Berkeley; Materials Sciences Division, Lawrence Berkeley National Laboratory; Kavli Energy NanoSciences Institute at Berkeley; Berkeley Global Science Institute, Berkeley, CA 94720, USA. [4]Drug Product Science & Technology, Bristol-Myers Squibb Co., One Squibb Drive, New Brunswick, NJ 08903, USA. [5]Collaborative Innovation Center of Chemical Science and Engineering, Tianjin 300071, China. [6]King Abdulaziz City for Science and Technology, Riyadh 11442, Saudi Arabia.
*These authors contributed equally to this work.
†Corresponding author. Email: wang_wei@lzu.edu.cn (W.W.); junliang.sun@pku.edu.cn (J.-L.S.); yaghi@berkeley.edu (O.M.Y.)

Previous work related to single crystals of COFs has been limited to either electron diffraction on small crystals (*5*–*8*), which are not amenable to SXRD, or to two studies of intrinsically nonporous organic networks held together by weak covalent bonds (*9*, *10*). Here, we report a general approach involving the use of aniline as a modulator to grow high-quality large single crystals of three-dimensional (3D) porous COFs held together by strong imine bonds (~600 kJ/mol) (*11*). Aniline has a reactivity similar to that of COF constituents, but it is monofunctional and acts as an inhibitor to nucleation, and thus alters the crystallization process. The exceptional quality of the crystallographic data collected on these crystals enabled the anisotropic refinement of a series of COFs with resolutions of up to 0.83 Å, similar to that commonly obtained for small discrete molecules (*12*).

These data allowed us to answer outstanding questions pertaining to reported COFs and also solve and refine with atomic precision the crystal structures of completely new ones. Specifically, the degree of interpenetration in imine-based COF-300 was deciphered, and the arrangement of water guests in the hydrated form of COF-300 was determined. The reversed imine connectivity for COF-303 was distinguished from the nonreversed analog, and the crystal structure of an isoreticularly expanded COF (LZU-79) was obtained. In addition, we solved and refined the single-crystal structure of a newly synthesized chiral LZU-111 with the rare *lon-b-c3* topology (*13*), which, owing to its complexity, would have been difficult to model and refine from powder XRD.

The critical step in the crystallization of COFs is the establishment of conditions for the formation of well-ordered, defect-free crystals. Such reaction conditions should be designed to allow the covalent linkage (imine in our structures) between the building blocks to be reversible, yet slow enough for efficient self-correction of defects. In a typical imine COF synthesis, the formation of amorphous solid is initially observed, and over time this material transforms into a crystalline phase through an error-correction mechanism (*8*). Thus, immediate precipitation causes the COF solid to be invariably amorphous or polycrystalline rather than single crystalline.

We sought to increase the reversibility of imine bond formation and dissociation by means of the imine-exchange strategy (*14*, *15*). This was achieved by adding a large excess of aniline to the reaction mixture, where aniline functions as a modulator (Fig. 1A). First, the reactivity of aniline is comparable to that of the building blocks used in the synthesis of most imine-based 3D COFs. Other substituted anilines (e.g., *p*-methoxyaniline, *p*-methylaniline, *o*-, *m*-toluidine, *p*-iodoaniline), produced more poorly crystalline phases or even did not produce any crystalline materials, presumably because of the mismatch of their reactivity with the amine building blocks (section S2 of the supplementary materials) (*16*, *17*). Aniline is a monofunctional molecule, so it acts as a nucleation inhibitor and competitive modulator with the multifunctional amine-based building units (*18*, *19*). Second, imine bonds are more susceptible to nucleophilic attack by amines rather than by water (*20*).

Thus, the addition of aniline increases the overall concentration of amine in the reaction, enhancing the reversibility of imine bond formation and the process of error corrections, and ultimately, crystallization (Fig. 1A). As a result of adding aniline modulator to the reaction mixture, single crystals of various imine-based 3D COFs were obtained: COF-300, COF-303, LZU-79, and LZU-111 (Fig. 1B). Notably, the crystal size of single-crystalline COFs was controlled by adjusting the amount of aniline, as exemplified for COF-300 (crystal sizes of 10 to 60 μm).

Our initial goal was to crystallize the well-known COF-300 (*21*) as a single-crystalline phase. Its tetratopic amine building block, tetrakis(4-aminophenyl)methane (TAM), was reticulated with terephthaldehyde (BDA) into a porous 3D framework (Fig. 2A). In preliminary experiments, yellow amorphous solids precipitated immediately at ambient temperature when 6 M aqueous acetic acid was added into a solution of TAM and BDA in 1,4-dioxane. After the mixture was heated at 120°C for 72 hours, polycrystals of COF-300 (~500 nm) were produced (Fig. 1B) (*17*). The reaction parameters such as time, temperature, pH, solvent, and concentration were systematically varied and optimized. However, similar to other COFs, the crystal size could not be further increased, and the crystallinity remained poor.

By using the aforementioned imine-exchange approach, in the presence of a large excess of aniline (15 equiv.), single crystals of COF-300 up to 100 μm in size were produced within 30 to 40 days

in the shape of well-defined, uniform blocks. This sharp increase in size from 0.5 to 100 μm enabled the successful SXRD data collection. By using laboratory source of x-ray, the structure of COF-300 was solved and refined with a resolution of 0.85 Å. This COF crystallized in the space group $I4_1/a$ with unit-cell parameters of $a = b = 26.2260(18)$ Å, $c = 7.5743(10)$ Å, and a unit-cell volume of 5209.6(10) Å^3. Given the default diamond topology for COF-300 and the body-centered tetragonal space group $I4_1/a$, the degree of interpenetration (N) for its structure was initially determined from the unit-cell parameters ($N = 2a/c = 7$) (*21*). The crystal structure was solved and refined anisotropically, and indeed, was sevenfold interpenetrated (*dia-c7*, class Ia of interpenetration) (*22*, *23*).

In the case of previously reported COF-300, which was made under different conditions and characterized as polycrystalline powder, the degree of interpenetration was determined to be fivefold (*dia-c5*, class Ia of interpenetration) (*21*). There was ambiguity as to the degree of interpenetration in this *dia-c5* phase, because it did not closely obey the N formula ($N = 2a/c = 4.5$). Without a single-crystal structure, the ambiguity was further deepened by the possibility of framework distortion not accounted for by the formula. In the present single-crystal structure of COF-300, these ambiguities were resolved. The sevenfold interpenetrated structure was distorted from ideal adamantane cages (natural tile for *dia* topology); the angles between the tetratopic nodes were 89.4(3)° and 120.4(3)° instead of 109.5°. In addition, the SXRD data that we collected using synchrotron source allowed for the assignment of the positional disorder of the BDA linker, a feature usually omitted during structural modeling based on powder XRD data.

We then monitored the hydration of COF-300 using SXRD measurements. Exposure of COF-300 crystals to water led to the formation of a new phase that was initially detected by measurement of the unit-cell parameters. This new phase of hydrated COF-300 adopts the same space group but with $a = b = 19.6394(9)$ Å, $c = 8.9062(4)$ Å, and a much smaller unit-cell volume of 3435.2(4) Å^3 (Fig. 2B). Despite the drastic 34% reduction in the unit-cell volume and subsequent mechanical stress on the crystal, the crystallinity of this new phase increased, enabling data collection with a resolution of 0.83 Å: a standard requirement for molecular SXRD crystallography (*12*). The hydrated COF-300 structure was solved and refined anisotropically, and the degree of interpenetration remained at 7, in stark contrast with what one would predict based on the unit-cell parameters of the hydrated form ($N = 2a/c = 4.4$). The structure was accommodated by further deviations of the angles between the tetrahedral nodes [64.4(3)° and 135.7(3)°]. Thus, the assignment of the degree of interpenetration based on the unit-cell parameters alone (as would be the case in powder diffraction) would lead to an incorrect conclusion.

The distortion in hydrated COF-300 may be caused by the presence of the strongly bound water guests at the imine functional group via the O–H···N hydrogen bond of d(O–H···N) = 3.086(7) Å, where the lone pair on nitrogen acts as an acceptor of the hydrogen bond. These water guests made infinite chains within the channels of COF-300 (Fig. 2C). The cooperative effect of hydrogen bonding within the pore led to shrinkage of the framework, which resulted in a denser structure, manifested by the increased resolution of the collected data. It was not possible to determine the nature of the host-guest interactions when the polycrystalline sample was the only available one. The hydration of COF-300 single crystals was reversible, and the macroscopic effect of hydration could be seen even in their morphology change in Fig. 1B (COF-300 versus hydrated COF-300).

To further explore imine-based 3D COF structural chemistry, we synthesized analogs of COF-300 (COF-303 and LZU-79) as large single crystals and studied them. In contrast to COF-300, COF-303 was a result of reversed imine condensation between a tetratopic aldehyde, tetrakis(4-formylphenyl)methane (TFM), and a ditopic amine, phenylenediamine (PDA) (Fig. 3A). As expected, this COF is almost identical to COF-300 in terms of its symmetry, framework geometry, topology, and degree of interpenetration, but not in its imine connectivity. Indeed, COF-300 and COF-303 were indistinguishable by powder XRD or electron diffraction. SXRD was the only technique that could detect the "switch" of this imine bond, as confirmed by the comparison of the C–C=N–C and C–C–C=N torsion angles (for both COFs) in the aniline and benzylidene moieties, respectively (Fig. 3B and table S5) (*17*, *24*).

Isoreticular expansion of COF-300 led to the formation of LZU-79, which is reticulated by

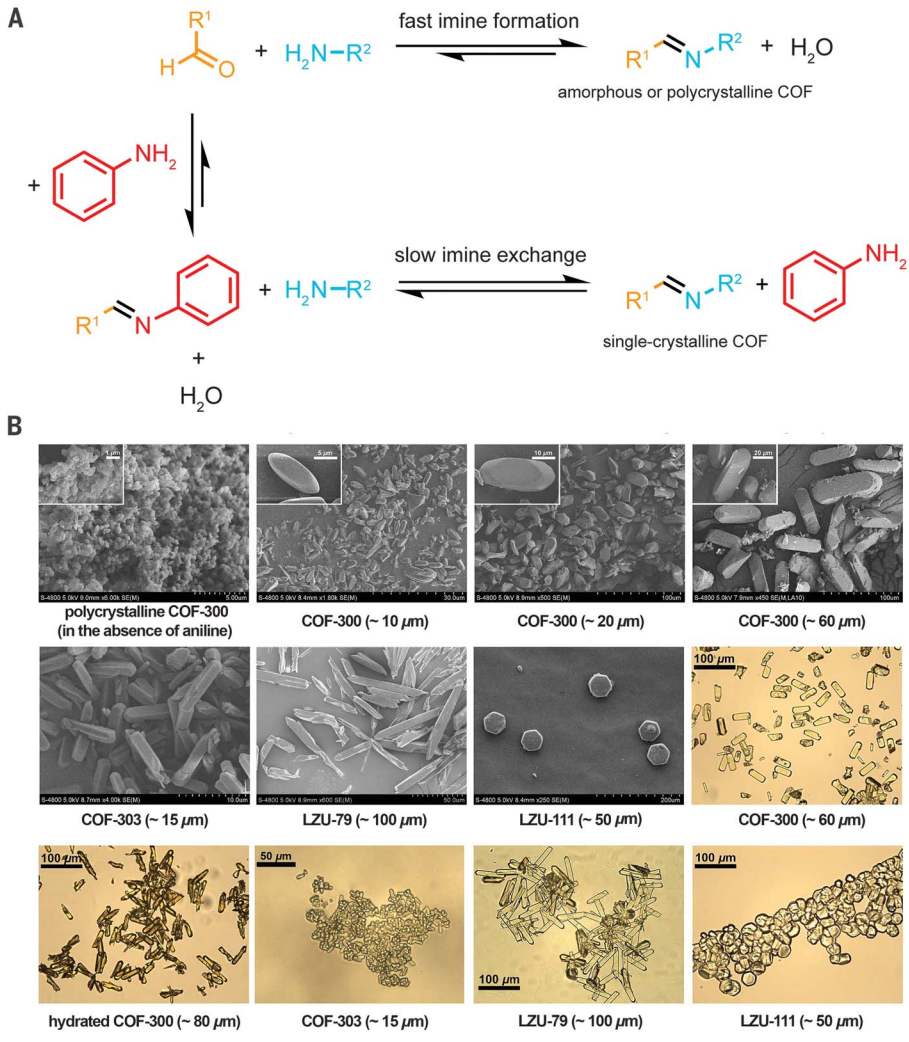

Fig. 1. Crystal growth of large imine-based COFs modulated by aniline. (**A**) In the absence of aniline, the imine-formation equilibrium is shifted toward the product, amorphous or polycrystalline COFs, whose formation is governed by fast nucleation and limited crystal growth. In the presence of aniline, the initial imine bond formation is comparably fast; however, slow imine exchange enables the growth of single-crystalline COFs. (**B**) Scanning electron microscopy (SEM) and optical microscopy images of single-crystalline COFs, obtained in the presence of aniline, the structures of which were solved and refined in this report. The SEM image of polycrystalline COF-300 without addition of aniline is shown for comparison.

tetratopic TAM and 4,7-bis(4-formylbenzyl)-1*H*-benzimidazole (BFBZ). LZU-79 crystallized in the space group $P4_2/n$ with unit-cell parameters of $a = b = 27.838(2)$ Å, $c = 7.5132(12)$ Å and a unit-cell volume of 5822.4(3) Å^3. The solved and refined SXRD structure showed that LZU-79 possessed a *dia-c10* network (class Ia of interpenetration), one of the highest degrees of interpenetration reported in COFs (Fig. 3C) (*25*).

To confirm the generalizability of our approach for growing large single crystals of COFs, we accessed a single-crystalline phase of a new chiral COF LZU-111. This COF is composed of two types of tetrahedral building blocks [methane-based tetraamine (TAM)] and [silane-based tetraaldehyde (TFS)], linked by imine bonds into a 3D chiral porous framework (Fig. 4A). Similar to COF-300 crystallization, preliminary experiments yielded only polycrystalline material. Addition of a large excess of aniline (80 equiv.) afforded single crystals of LZU-111 up to ~60 μm in the shape of well-defined hexagonal prisms within 80 days. Initially, we measured hexagonal unit-cell parameters using the data collected with a laboratory source of x-ray radiation and $a = b = 20.17(3)$ Å, $c = 34.0(3)$ Å and a unit-cell volume of 11980.4(2) Å^3.

To obtain higher resolution, we then collected the SXRD datasets with a synchrotron light source. Data resolution for single-crystal LZU-111 reached 1.2 Å, which is lower than that of typical molecular crystals (0.8 Å) but higher than that of proteins (2.5 Å). On the basis of the reflection conditions ($00l$, $l = 6n$) and Laue class ($6/m$), the space group was determined as $P6_1$ or $P6_5$. Only the positions of the relatively heavy Si atoms were located with Si–Si distances of 21.2 and 8.2 Å. The first corresponds to the shortest Si–Si distance within the four-connected network, while the second is the Si–Si distance between adjacent interpenetrating networks. Therefore, the LZU-111 topology was determined as a threefold interpenetrated lonsdaleite network *lon-b-c3* related by a threefold axis, a rare example of class IIa of interpenetration. The network is binary owing to different carbon and silicon tetrahedral nodes. This topology is rarely found in reticular chemistry of frameworks such as metal-organic frameworks (*26*) and has not been reported in COFs, precluding the correct choice of starting structural model for the accurate refinement simply on the basis of powder XRD data. Ultimately, the crystal structure of LZU-111 was fully assigned and isotropically refined in the space group $P6_5$. The chirality of LZU-111 originates from the threefold interpenetration; the intersections of the networks generates a 6_5 screw axis.

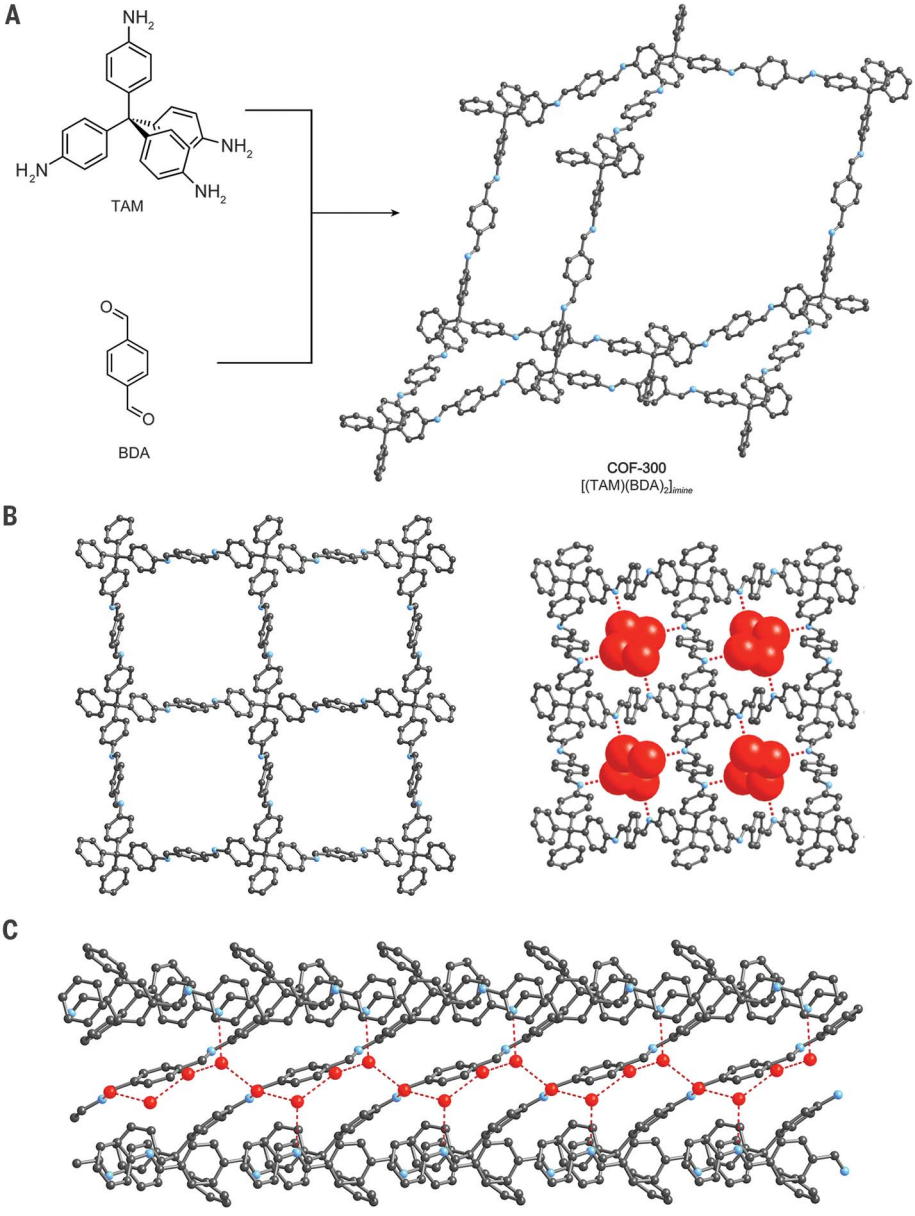

Fig. 2. Single-crystal XRD structures of COF-300 and its form containing water guests. (**A**) Imine condensation between TAM and BDA produced single-crystalline COF-300. It crystallizes in the space group $I4_1/a$ with *dia* topology and sevenfold interpenetrated framework. (**B**) Upon exposure to water, the crystal structure of COF-300 contracts substantially to form hydrated COF-300. This distortion is due to the formation of highly favorable hydrogen bonds between the imine functional groups and the water guests. (**C**) The cooperative effect of the hydrogen bonds leads to infinite chains of water guests within the channels of the framework, resulting in a much denser structure. Color scheme: C, gray; N, blue; O, red. Red dotted lines represent hydrogen bonding.

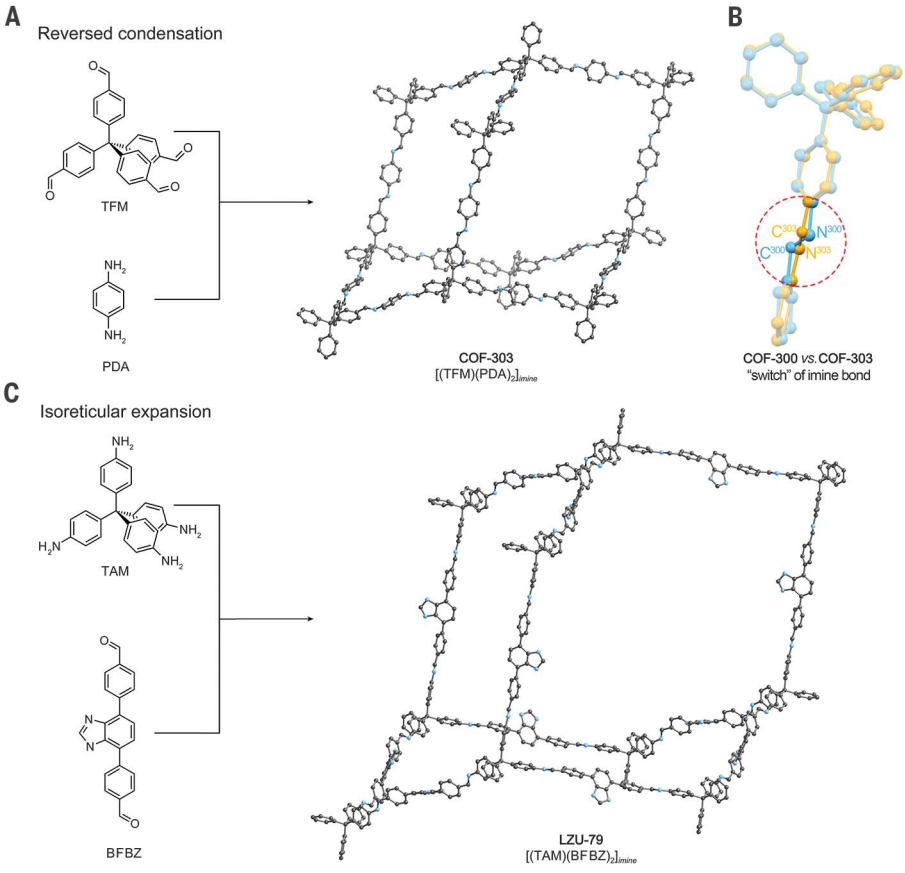

Fig. 3. Single-crystal XRD structures of COF-303 and LZU-79. (**A**) Reversed imine condensation between TFM and PDA produced COF-303. It crystallizes in the same space group as COF-300, preserving the framework geometry, the *dia* topology, and the sevenfold interpenetration. (**B**) Ball-and-stick models of COF-300 (blue) and COF-303 (yellow) are overlaid to show the only structural difference, "switched" imine connectivity, which can be distinguished from the torsion angles in the aniline and benzylidene moieties. (**C**) Isoreticular expansion of COF-300 results in LZU-79 produced by imine condensation of TAM and BFBZ. LZU-79 crystallizes in the space group $P4_2/n$. It preserves the *dia* topology but has a higher degree of interpenetration (*dia-c10*). Color scheme: C, gray; N, blue. Hydrogen atoms are omitted for clarity.

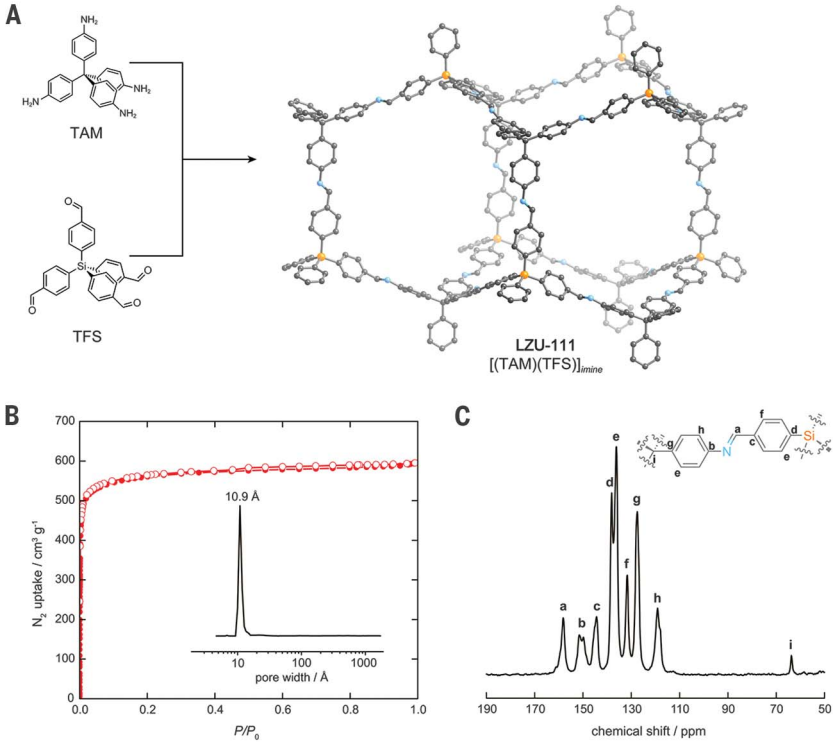

Fig. 4. Single-crystal XRD structure of chiral LZU-111 and its characterization. (**A**) Imine condensation between TAM and TFS produced LZU-111. It crystallizes in the chiral space group $P6_5$ and possesses *lon-b-c3* topology. (**B**) Activated single-crystalline LZU-111 was also characterized by nitrogen sorption at 77 K, which clearly shows a steep type I isotherm and narrow pore-size-distribution, supporting the defect-free nature of its single crystals. Solid and open circles represent the adsorption and desorption branches, respectively. (**C**) Solid-state ^{13}C CP/MAS NMR spectroscopy verified the anticipated covalent bonding at the atomic level. The ^{13}C CP/MAS NMR signals have been fully assigned: very narrow NMR signals indicate the high crystallinity and low number of defects in the structure. Color scheme: C, gray; N, blue; Si, orange.

To support the single-crystal structural refinement of LZU-111, we characterized porosity, crystallinity, and degree of defects of this new COF (Fig. 4, B and C). The nitrogen sorption isotherm at 77 K showed the classic type I isotherm with a steep uptake P/P_0 below = 0.001, characteristic for microporous materials (*27*). The experimental Brunauer-Emmett-Teller (BET) surface area of 2120 $m^2 g^{-1}$ and total pore volume of 0.918 $cm^3 g^{-1}$ are almost identical with those estimated theoretically from the SXRD model (2209 $m^2 g^{-1}$ and 0.828 $cm^3 g^{-1}$, respectively). Nonlocal density functional theory derived a narrow pore-size-distribution centered at 10.9 Å, the value of which is fully consistent with that determined from the crystal structure (~11 Å) (fig. S31) (*17*). Solid-state ^{13}C and ^{29}Si cross-polarization magic angle spinning (CP/MAS) nuclear magnetic resonance (NMR) spectroscopy verified the anticipated covalent bonding at the atomic level. The ^{13}C CP/MAS NMR signals have been fully assigned as shown on Fig. 4C. A single isotropic peak at δ = −14 parts per million (ppm) in the ^{29}Si CP/MAS NMR spectrum indicates that all the Si atoms are symmetrically equivalent, which is consistent with the SXRD analysis (fig. S20) (*17*).

REFERENCES AND NOTES

1. A. P. Côté *et al*., *Science* **310**, 1166–1170 (2005).
2. H. M. El-Kaderi *et al*., *Science* **316**, 268–272 (2007).
3. C. S. Diercks, O. M. Yaghi, *Science* **355**, eaal1585 (2017).
4. P. J. Waller, F. Gándara, O. M. Yaghi, *Acc. Chem. Res.* **48**, 3053–3063 (2015).
5. Y. Liu *et al*., *Science* **351**, 365–369 (2016).
6. Y.-B. Zhang *et al*., *J. Am. Chem. Soc.* **135**, 16336–16339 (2013).
7. A. M. Evans *et al*., Seeded growth of single-crystal two-dimensional covalent organic frameworks. *ChemRxiv* [Preprint]. 12 December 2017.
8. Y. Zhao *et al*., *J. Am. Chem. Soc.* **139**, 13166–13172 (2017).
9. P. Kissel *et al*., *Nat. Chem.* **4**, 287–291 (2012).
10. D. Beaudoin, T. Maris, J. D. Wuest, *Nat. Chem.* **5**, 830–834 (2013).
11. C. Sandorfy, in *The Chemistry of Functional Groups*, S. Patai, Ed. (Wiley, New York, 1969), vol. 3, chap. 1, pp. 5–6.
12. http://journals.iucr.org/c/services/cif/reqdata.html
13. M. O'Keeffe, M. A. Peskov, S. J. Ramsden, O. M. Yaghi, *Acc. Chem. Res.* **41**, 1782–1789 (2008).
14. M. E. Belowich, J. F. Stoddart, *Chem. Soc. Rev.* **41**, 2003–2024 (2012).
15. E. Vitaku, W. R. Dichtel, *J. Am. Chem. Soc.* **139**, 12911–12914 (2017).
16. P. T. Corbett *et al*., *Chem. Rev.* **106**, 3652–3711 (2006).
17. Materials and methods are available as supplementary materials.
18. N. Stock, S. Biswas, *Chem. Rev.* **112**, 933–969 (2012).
19. M. Calik *et al*., *J. Am. Chem. Soc.* **138**, 1234–1239 (2016).
20. E. H. Cordes, W. P. Jencks, *J. Am. Chem. Soc.* **84**, 826–831 (1962).
21. F. J. Uribe-Romo *et al*., *J. Am. Chem. Soc.* **131**, 4570–4571 (2009).
22. V. A. Blatov, L. Carlucci, G. Ciani, D. M. Proserpio, *CrystEngComm* **6**, 377–395 (2004).
23. I. A. Baburin, V. A. Blatov, L. Carlucci, G. Ciani, D. M. Proserpio, *J. Solid State Chem.* **178**, 2452–2474 (2005).
24. H. B. Bürgi, J. D. Dunitz, *J. Chem. Soc. D* **9**, 472–473 (1969).
25. X. Guan *et al*., *J. Am. Chem. Soc.* **140**, 4494–4498 (2018).
26. K. M. Patil, M. E. Dickinson, T. Tremlett, S. C. Moratti, L. R. Hanton, *Cryst. Growth Des.* **16**, 1038–1046 (2016).
27. M. Thommes *et al*., *Pure Appl. Chem.* **87**, (2015).

ACKNOWLEDGMENTS

T.M., W.W., and J.-L.S. thank Q. Zheng for advice on this project and M. Li at Shanghai Synchrotron Radiation Facility (SSRF) for assisting with the SXRD data collection at the beginning of the project. E.A.K. and O.M.Y. thank H.-B. Bürgi for discussions of structure refinement. O.M.Y. acknowledges the collaboration, input, and support of Prince Turki bin Saud bin Mohammed Al-Saud (President of KACST). The staff of beamline BL14B1 at SSRF, beamlines BL17B/BL17U of National Facility for Protein Science Shanghai (NFPS) at SSRF, and beamline I19 of Diamond Light Source are acknowledged for providing assistance during data collection. **Funding:** The authors gratefully acknowledge the financial support from the National Natural Science Foundation of China (nos. 21632004, 21425206, 21471009, and 21527803). Work performed at the Advanced Light Source is supported by the Director, Office of Science, Office of Basic Energy Sciences, of the U.S. Department of Energy under contract no. DE-AC02–05CH11231. **Author contributions:** T.M., W.W., J.-L.S., and O.M.Y. conceived the idea and led the project. T.M., S.Y., L.L., and Y.W. conducted the synthesis and crystal growth. J.-L.S., E.A.K., T.M., Z.Z., S.Y., J.S., J.L. carried out the crystallographic studies. T.M., J.N., and W.D.W. carried out the NMR measurements. T.M., L.L., Z.Z., and X.W. took the crystals images and photos. T.M., L.-H.L., and Y.W. carried out the Fourier transform–infrared measurements. E.A.K., T.M., W.W., J.-L.S., and O.M.Y. interpreted the results and wrote the manuscript. **Competing interests:** None declared. **Data and materials availability:** Crystallographic data reported in this paper are tabulated in the supplementary materials and archived at the Cambridge Crystallographic Data Centre under reference numbers CCDC 1846135 to 1846140. All other data needed to evaluate the conclusions in the paper are present in the paper or the supplementary materials.

SUPPLEMENTARY MATERIALS

www.sciencemag.org/content/361/6397/48/suppl/DC1
Materials and Methods
Supplementary Text
Tables S1 to S7
Figs. S1 to S35
References (*28*–*39*)

2 April 2018; accepted 22 May 2018
10.1126/science.aat7679

FRAMEWORK MATERIALS

Seeded growth of single-crystal two-dimensional covalent organic frameworks

Austin M. Evans[1], Lucas R. Parent[1,2,3], Nathan C. Flanders[1], Ryan P. Bisbey[1,4], Edon Vitaku[1], Matthew S. Kirschner[1], Richard D. Schaller[1,5], Lin X. Chen[1,6], Nathan C. Gianneschi[1,2,3], William R. Dichtel[1]*

Polymerization of monomers into periodic two-dimensional networks provides structurally precise, layered macromolecular sheets that exhibit desirable mechanical, optoelectronic, and molecular transport properties. Two-dimensional covalent organic frameworks (2D COFs) offer broad monomer scope but are generally isolated as powders comprising aggregated nanometer-scale crystallites. We found that 2D COF formation could be controlled using a two-step procedure in which monomers are added slowly to preformed nanoparticle seeds. The resulting 2D COFs are isolated as single-crystalline, micrometer-sized particles. Transient absorption spectroscopy of the dispersed COF nanoparticles revealed improvement in signal quality by two to three orders of magnitude relative to polycrystalline powder samples, and suggests exciton diffusion over longer length scales than those obtained through previous approaches. These findings should enable a broad exploration of synthetic 2D polymer structures and properties.

Polymerizing monomers into periodic two-dimensional (2D) networks yields macromolecular sheets linked by robust covalent bonds (*1*–*4*). Such polymers differ from established linear, branched, or cross-linked polymer architectures and promise distinct combinations of properties that emerge from their designed structures and uniform, nanometer-scale pores (*4*, *5*). This promise has been hindered by the limited materials quality provided by current 2D polymerization methods (*4*, *6*). Previous work has resulted in 2D polymers with large crystalline domains, obtained by crystallizing tritopic monomers into layered crystals capable of topochemical photopolymerizations, some of which have been characterized as single-crystal to single-crystal transformations (*7*, *8*). But the strict geometric requirements of topochemical polymerizations and the difficulty of designing molecules that crystallize appropriately have limited the generality of this approach to just nine monomers across three design motifs.

In contrast, the simultaneous polymerization and crystallization of monomers into 2D polymers known as covalent organic frameworks (COFs) is more general, with more than 200 reported examples (*9*–*20*). However, 2D COFs typically form as insoluble, polycrystalline powders or films with small crystalline domains (typically smaller than 50 nm), which we attribute to poorly controlled nucleation and growth processes (*21*–*23*). Wuest and co-workers reported three 3D COFs isolated as large single crystals (*24*), but these are linked by weak azodioxy bonds, are unstable to elevated temperatures and solvent removal, and have not been generalized to 2D COF single crystals. Here, we report 2D COFs as discrete particles comprising single-crystalline domains with sizes ranging from 500 nm to 1.5 μm. They were prepared through a two-step approach that separates the nucleation and growth processes. These 2D COF samples have superior properties and can be studied more rigorously than polycrystalline samples, as demonstrated by a transient absorption study that provides improved signal quality by three orders of magnitude and offers evidence for exciton delocalization at length scales larger than the crystalline domains of the powders. These findings represent a major advance in 2D COF materials quality that will greatly broaden the monomer scope available for accessing well-defined 2D polymers.

2D COF formation is poorly understood because effective reaction conditions are identified by empirically screening for the formation of the desired materials as polycrystalline powders. The appropriate rates of polymerization and exchange processes needed for defect correction are unknown, and we postulate that any attempt to identify reactions that produce polycrystalline powders is inherently predisposed to identify conditions with uncontrolled nucleation. Our recent mechanistic studies of boronate ester–linked 2D COF formation revealed a nucleation-elongation process that was interrupted by the aggregation and precipitation of microcrystalline COF powders (*22*). We later found that nitrile-containing cosolvents prevented aggregation and precipitation, resulting in stable colloidal suspensions of 30-nm crystalline 2D COF nanoparticles that could be solution-processed into films (*25*). Here, we enlarged the COF colloids into faceted single crystals with lateral dimensions greater than 1.5 μm through a second growth step in which additional monomers were introduced slowly to suppress further nucleation. This approach is shown to be general for three boronate ester–linked COFs, including a pyrene-containing structure previously shown to be photoconductive (*26*). These seeded 2D COF polymerizations provide 2D COFs as nonaggregated single crystals and demonstrate a means to obtain high-quality 2D polymers using modular and versatile directional bonding approaches.

The solvothermal condensation of 1,4-phenylenebis(boronic acid) (PBBA) and 2,3,6,7,10,11-hexahydroxytriphenylene (HHTP) in a mixture of 1,4-dioxane and mesitylene (4:1 v/v) affords a boronate ester–linked 2D COF (COF-5), which precipitates within minutes (*22*). However, when 80 volume percent (vol %) of CH_3CN is included as a cosolvent, a stable colloidal suspension of COF-5 nanoparticles is obtained instead (*25*). Having identified 2D COF polymerization conditions that prevent aggregation and precipitation, we hypothesized that newly introduced monomers would add to the existing nanoparticles rather than nucleating new particles under appropriate conditions. Indeed, adding monomers gradually to the reaction mixture limited the steady-state monomer concentration, and the colloids grew without forming new particles. In contrast, when the monomers were introduced quickly, their concentration increased above a critical nucleation concentration, and the reaction was dominated by the formation of new particles (Fig. 1).

We prepared an initial COF-5 colloidal suspension by heating HHTP and PBBA to 90°C in CH_3CN:1,4-dioxane:mesitylene (80:16:4 vol %) for 18 hours. The formation of crystalline COF-5 colloids with an average diameter of 30 nm was confirmed by dynamic light scattering (DLS) and synchrotron small-angle and wide-angle x-ray scattering (SAXS/WAXS) experiments. At first, we screened conditions that provide seeded growth by adding monomers at various concentrations and rates and monitoring colloid size by DLS. These exploratory experiments were successful and provided COF-5 nanoparticles that had grown from 30 nm to 400 nm (see supplementary materials) (fig. S2). The 400-nm particles were used in more careful growth studies (depicted in Fig. 2, A to C) because they are sufficiently large to enable easy differentiation of newly formed colloids from the preexisting seeds using DLS and other tools.

We observed both seeded growth and new particle formation regimes by adding monomers at different rates to dispersions of the 400-nm colloids. A COF-5 colloidal suspension was heated to 85°C and separate solutions of PBBA (6 mM) and HHTP (4 mM) were simultaneously added

[1]Department of Chemistry, Northwestern University, Evanston, IL 60208, USA. [2]Department of Materials Science and Engineering, Northwestern University, Evanston, IL 60208, USA. [3]Department of Biomedical Engineering, Northwestern University, Evanston, IL 60208, USA. [4]Department of Chemistry and Chemical Biology, Baker Laboratory, Cornell University, Ithaca, NY 14853, USA. [5]Center for Nanoscale Materials, Argonne National Laboratory, Argonne, IL 60439, USA. [6]Chemical Sciences and Engineering Division, Argonne National Laboratory, Argonne, IL 60439, USA.
***Corresponding author. Email: wdichtel@northwestern.edu**

using a syringe pump. The size distributions of the COF-5 nanoparticles were monitored by DLS and are plotted as a function of molar equivalents of the monomers added relative to those present in the initial colloids (equiv HHTP added/equiv HHTP in the COF-5 seed solution; Fig. 2). When monomers were added slowly (0.10 equiv hour^{-1}), the average particle size steadily increased (Fig. 2A); the size distribution remained monomodal as particle size increased (Fig. 2C). The added monomers were incorporated into the existing colloids, which grew from 400 to 1000 nm after addition of 4.0 equiv HHTP, and no evidence for new nanoparticle formation was observed by DLS (Fig. 2C), x-ray diffraction, or microscopy (see below). In contrast, when the rate of monomer addition was increased by a factor of 10 (1.0 equiv hour^{-1}), the average particle size began to decrease after addition of 0.5 equiv of monomers (Fig. 2A). The particle size distribution was bimodal with a new population at 50 nm after addition of 0.8 equiv HHTP, and this population of smaller particles developed into the dominant signal in the DLS measurements as more monomers were added (Fig. 2C). Control experiments in which the reaction solvent lacking HHTP and PBBA was added to the colloids resulted in no change of the size distribution of the colloids (fig. S3), indicating that the increased particle size observed during slow monomer addition is not attributable to Ostwald ripening or other particle fusion processes.

These experiments indicate that the faster addition rate causes the monomer concentration to exceed that needed to nucleate new nanoparticles. As indicated by the point at which the DLS curves for the fast and slow addition experiments diverge, HHTP and PBBA concentrations of ~1 mM represent an upper bound needed for nucleation of new COF-5 particles under these conditions. However, this estimate of the critical nucleation concentration is likely to be influenced by several reaction parameters. These experiments demonstrate that COF-5 colloidal suspensions remain stable and available for continued 2D polymerization when the monomer concentrations are sufficiently low.

Simultaneous WAXS, which characterizes the crystallinity of the colloids, and SAXS, which tracks the average particle size, also differentiate the seeded growth and new particle formation regimes. In the seeded growth regime, the average crystallite size and particle size increase as monomers are added slowly. In contrast, the average crystallite size and particle size decrease when monomers are added quickly. The WAXS data indicate that the initial COF seeds diffracted at q = 0.24 and 0.42 Å^{-1}, corresponding to the 100 and 010 Bragg directions of a hexagonal lattice with in-plane lattice parameters $a = b$ = 29.9 Å (fig. S6). These parameters match well with calculated (30.0 Å) and measured (29.7 Å) values previously reported for COF-5 powders (*27*). When monomers were added slowly, the 100 peak intensified and sharpened, and the 200 and 210 Bragg peaks became visible at q = 0.48 and 0.64 Å^{-1} after addition of 0.8 equiv HHTP. These observations indicate that the size of the COF-5 crystalline domains and the crystallinity within the domain both increased as the monomers were added to the solution. However, when monomers were added at 1.0 equiv hour^{-1}, the WAXS peaks broadened and decreased in intensity; this observation is consistent with the nucleation of new particles with smaller crystalline domains. The SAXS results were fully consistent with the DLS studies described above, validating that the WAXS experiments were done under conditions relevant to each growth regime. The SAXS traces (fig. S13) trended toward higher intensities at low scattering angles at the slow monomer addition rate (0.10 equiv hour^{-1}), which indicates an increased average particle size. SAXS of solutions with rapid monomer addition (1.0 equiv hour^{-1}) trended to lower intensities at low scattering angles, consistent with decreased average particle size. Together, these experiments demonstrate that the average crystalline domain size of the COF-5 colloids increases along with the particle size as monomers are added sufficiently slowly to suppress nucleation.

We demonstrated the generality of the seeded growth approach for two other boronate ester–linked 2D COFs, COF-10 and TP-COF (Fig. 1), which are synthesized by the condensation of HHTP with 4,4′-biphenylbis(boronic acid) and 2,7-pyrenebis(boronic acid), respectively. Both systems exhibited growth behavior similar to that of COF-5. For each network, an initial colloidal suspension was generated by heating HHTP and the corresponding boronic acid in a mixture of CH_3CN:1,4-dioxane:mesitylene (80:16:4 vol %) for 18 hours at 90°C. Once the colloids were formed, separate solutions of HHTP and the diboronic acid were added at 0.10 equiv hour^{-1} to the 2D COF nanoparticle suspensions. DLS of the reaction solutions showed monomodal particle size distributions that shifted to larger average sizes as monomers were added. The DLS particle size of the COF-10 colloids shifted from 80 nm to 190 nm after 1.5 equiv HHTP and 2.25 equiv 4,4′-biphenylbis(boronic acid) were added (Fig. 2D). The TP-COF particle size (Fig. 2F) increased from 400 nm to 750 nm after 1.50 equiv HHTP and 2.25 equiv 2,7-pyrenebis(boronic) acid were added at 0.10 equiv HHTP hour^{-1}. These

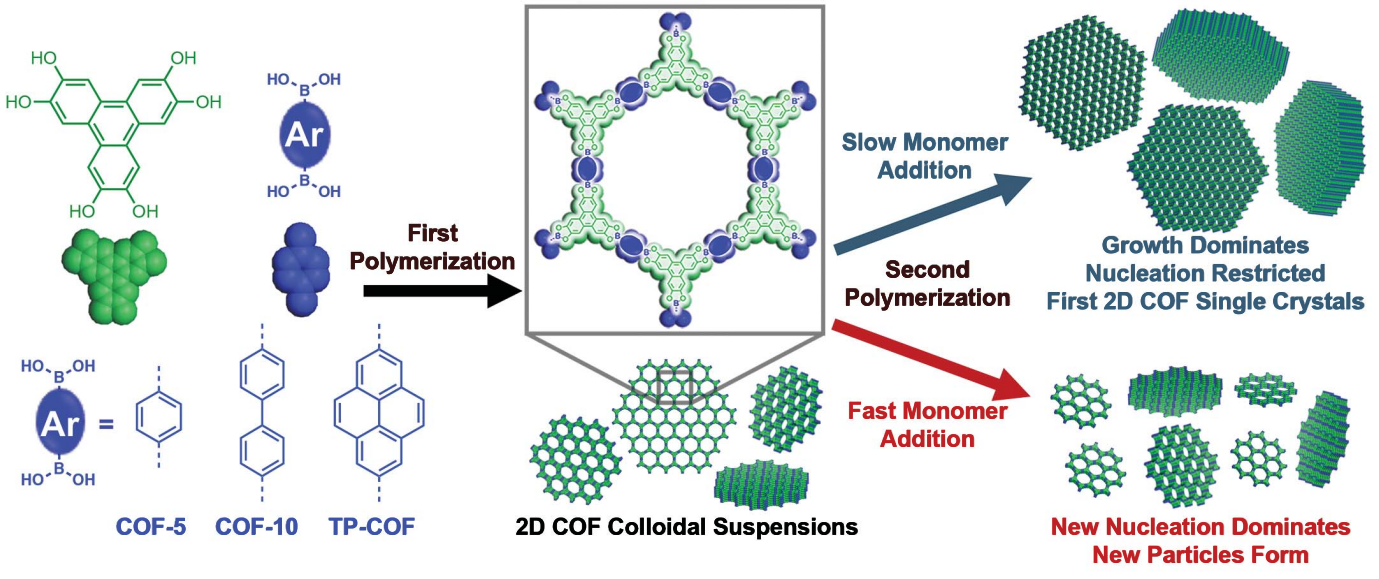

Fig. 1. Schematic of controlled 2D polymerization. A two-step seeded growth approach provides 2D COF single crystals. When HHTP and a linear bis (boronic acid) monomer are condensed in a solvent mixture containing CH_3CN, crystalline 2D COF nanoparticles are formed as stable colloidal suspensions. These nanoparticles are enlarged in a second polymerization step in which the monomers are slowly added to the solution. If the monomers are added more quickly, their concentration increases above a critical nucleation threshold, which leads to uncontrolled nucleation and smaller average particle size.

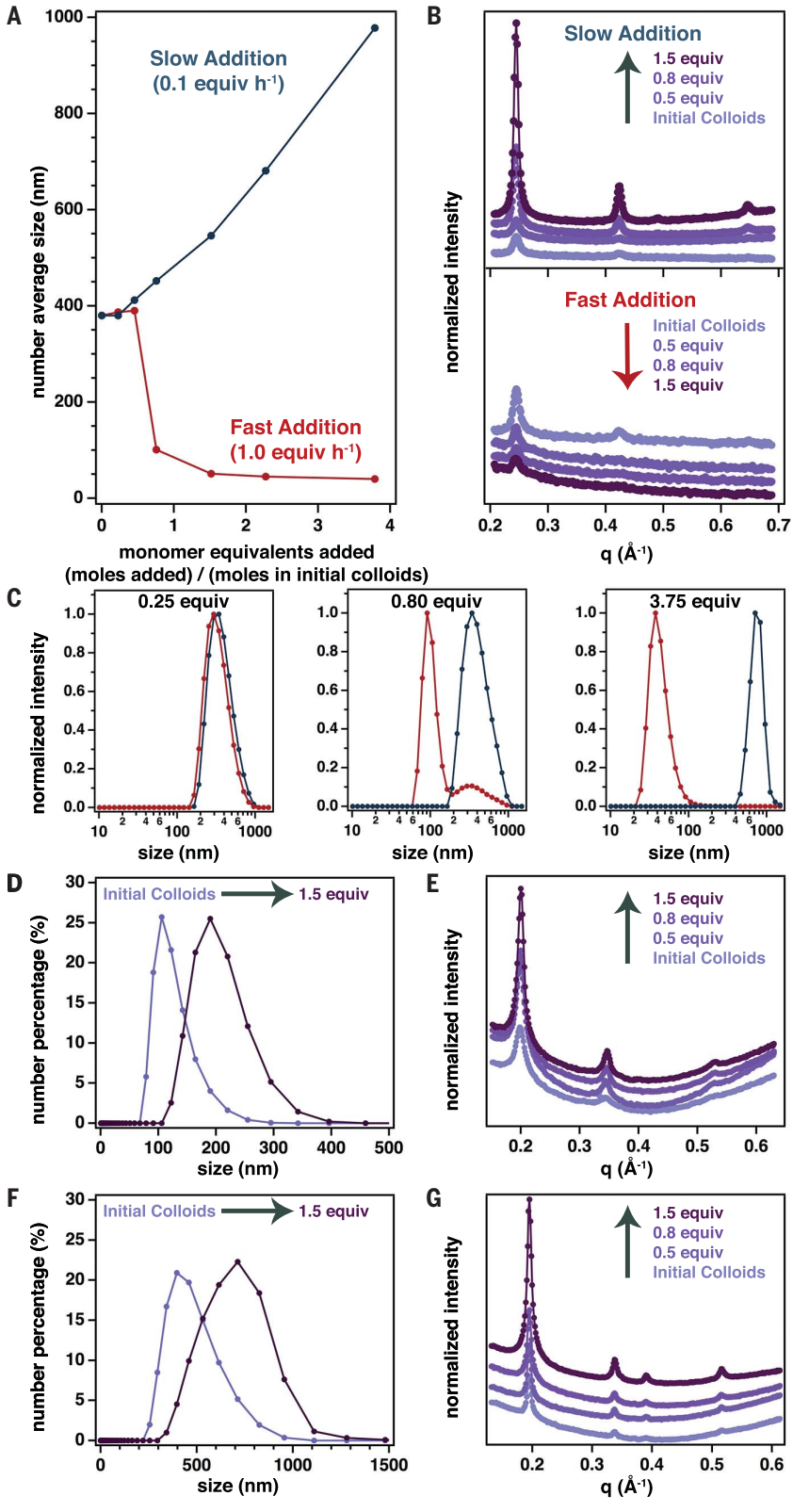

Fig. 2. The monomer addition rate defines seeded growth and nucleation regimes. (**A**) The DLS number-average size of COF-5 particles as a function of added monomer equivalents. (**B**) Wide-angle x-ray scattering of COF-5 particles as a function of the amount of added monomers at the two monomer addition rates. (**C**) DLS number-average size distributions obtained at three points shown in (A). (**D**) DLS number-average size distributions for the initial and final particle sizes of COF-10 during slow monomer addition. (**E**) WAXS traces of COF-10 particles as a function of the amount of added monomers. (**F**) DLS number-average size distributions for the initial and final particle sizes of TP-COF during slow monomer addition. (**G**) WAXS traces of TP-COF particles as a function of the amount of added monomers.

experiments suggest that nucleation is suppressed under these conditions and that the existing COF domains are enlarged through addition of the added monomers. Furthermore, nucleation predominated when the monomer solutions were added quickly (1.0 equiv hour^{-1}), resulting in smaller COF particle sizes of approximately 50 nm (figs. S4 and S5).

We also used in-solution x-ray diffraction techniques to interrogate the crystallinity of these colloidal suspensions. For TP-COF, WAXS peaks were observed at q = 0.19, 0.34, 0.39, and 0.52 Å^{-1} (Fig. 2G), corresponding to the Bragg directions 100, 110, 200, and 210 that were reported in its powder pattern (fig. S8) (*26*). Likewise, COF-10 colloid diffraction peaks were observed at q = 0.20, 0.34, and 0.52 Å^{-1} (Fig. 2E), which correspond to the 100, 110, and 210 Bragg diffractions (fig. S8) (*28*). These observations are consistent with those of the seeded growth of COF-5, in which the intensity of the diffraction peaks increased and the width (as judged by their full width at half of the maximum intensity) decreased. Here again, the 200 and 210 diffraction peaks became visible after addition of 0.8 equiv HHTP to each initial sample. These observations indicate that as monomers are introduced to COF nanoparticles sufficiently slowly, they add to and enlarge existing crystalline domains.

The enlarged COF nanoparticles were heated at 85°C for 14 days and then analyzed by low-dose, high-resolution transmission electron microscopy (HRTEM) to visualize their morphology, size, aspect ratio, and crystallinity (Fig. 3). TEM imaging of discrete particles was possible for COF-5 and COF-10, with TP-COF appearing aggregated when prepared on TEM substrates; this precluded close analysis of its lattice structure by microscopy (fig. S9). TEM imaging at low magnification revealed that the COF-5 particles (Fig. 3A) have uniform six-fold symmetry and hexagonal faceting in projection. Most individual particles were 300 to 500 nm in diameter, with some reaching >1 μm. The COF-5 particles were observed at random orientations by TEM (no preferential orientation when drop-cast on TEM substrates), and all orientations appeared dimensionally isotropic. Lattice-resolution images of individual COF-5 particles show that they are single-crystalline (Fig. 3, B to D), as consistent and continuous lattice fringes extend throughout the particles. For the particle selected in Fig. 3, B to D, which is tilted just off a zone axis, the fringe spacing is ~10 Å (fitting d_{210} for COF-5), as measured by fast Fourier transform (FFT; Fig. 3B, inset) and the left-to-right intensity profile (Fig. 3D) of the

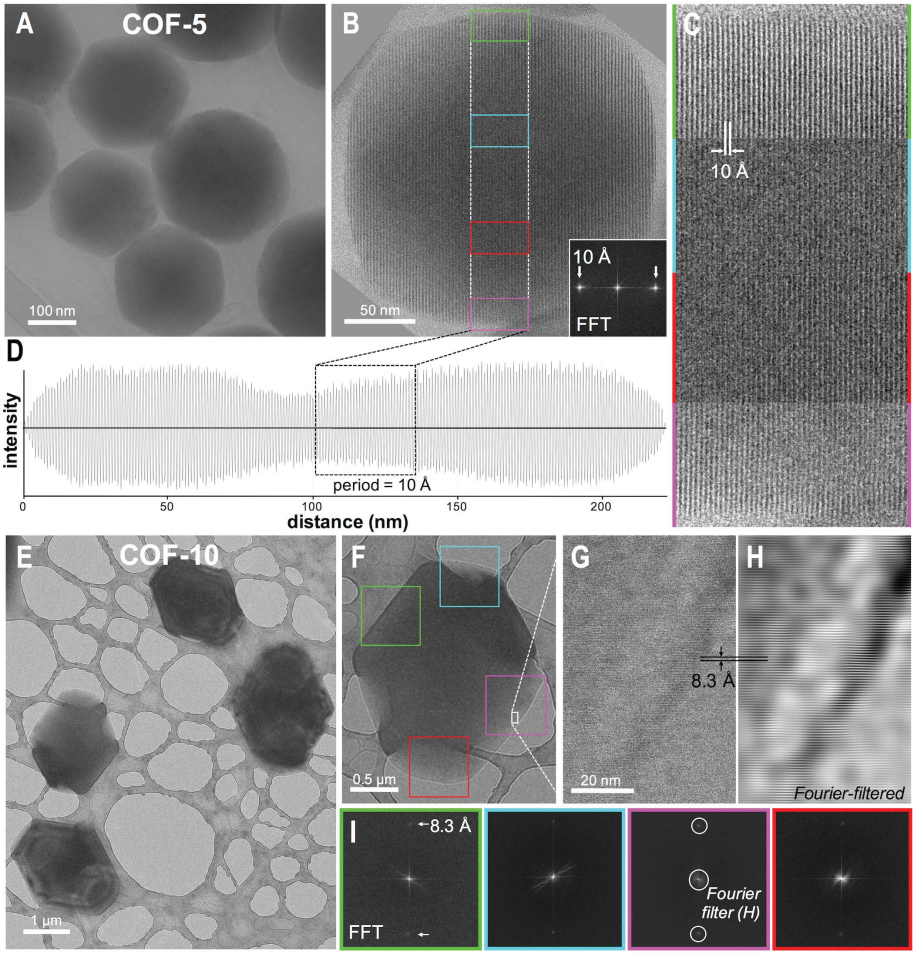

Fig. 3. Low-dose HRTEM characterization of COF single-crystalline particles. Cumulative dose per image: ~25 e^{-} $Å^{-2}$ s^{-1}. (**A** and **E**) Low-magnification images of COF-5 and COF-10 particles, respectively. (**B**) Lattice-resolution HRTEM image of a COF-5 particle with consistent lattice fringes extending across the entire particle. Inset: FFT of the image, cropped at the predominant fringe spacing (~10 Å, d_{210}). (**C**) Four regions of interest at higher magnification corresponding to the green, teal, red, and magenta boxed regions of the particle in (B), which are aligned vertically and parallel with the 10 Å fringes. (**D**) Intensity profile plot (left to right across the particle) of the image in (B) after applying a bandpass filter. The periodicity of the intensity profile is constant and continuous with a period of ~10 Å. (**F**) Overview image of one COF-10 particle, from which higher-magnification images were acquired at four regions of interest (green, teal, magenta, and red). (**G**) Lattice-resolution HRTEM image at the lower right edge of the particle in (F) where 8.3 Å lattice fringes are resolved, corresponding to d_{400}. (**H**) The HRTEM image in (G) after applying a Fourier filter to select the central spot and the two 8.3 Å spots in the FFT. (**I**) The FFTs of the four high-magnification images from the four color-coded regions of interest in (F).

particle. The magnified lattice images of vertically aligned regions in this particle show the continuous single-crystalline structure that extends vertically (parallel with the fringes) from edge to edge, as shown in several regions of a particle juxtaposed in Fig. 3C. The intensity profile (Fig. 3D) similarly shows that the single-crystalline structure is continuous horizontally (perpendicular to the fringes) from edge to edge.

The COF-10 particles (Fig. 3, E to I) were also highly uniform in size and morphology. They were hexagonally faceted in projection yet lacked the six-fold symmetry of the COF-5 particles; their sizes were predominantly 4 to 5 μm across their major length and ~3 μm across their minor length (Fig. 3E). When prepared on TEM substrates, the particles preferentially oriented with their intersheet stacking dimension normal to the substrate, which was likely caused by their *z*-dimension (particle thickness) being smaller than their lateral dimension (fig. S10). Because of the large size of these particles (thickness ~0.5 to 1 μm), analysis was limited to their edges; many particles were too large for high-resolution TEM characterization. Therefore, we acquired high-magnification images at various regions of interest around the perimeter of a single particle that was sufficiently thin (Fig. 3, F to H). Lattice fringes (Fig. 3, G and H) could not be visually resolved in the images for all regions, but the FFTs all contained more subtle periodic information, which revealed that all regions were consistently crystalline throughout the particle (Fig. 3, H and I). The FFTs of all four regions contained ~8.3 Å fringe spots (fitting d_{400} for COF-10) at the same radial location (Fig. 3I), indicating consistency of the crystal structure and crystal orientation at each of the four regions of interest (fig. S11). These observations strongly suggest that the particle is a single continuous crystalline domain. We note that low-magnification images of the COF-10 particles contain very prominent diffraction contrast with no detectable grain boundaries, which is consistent with the particles being single crystals (Fig. 3E). Collectively, the TEM characterization of the individual, single-crystalline COF-5 and COF-10 particles further indicates that the well-controlled, seeded growth procedure represents a major advance in COF materials quality and the modular synthesis of 2D polymers.

The well-dispersed, single-crystalline COF colloids enable characterization of emergent electronic properties of these 2D layered assemblies that were not previously possible in polycrystalline aggregates. The optical signatures and exciton dynamics of the COF-5 colloids were characterized using optical transient absorption (TA) spectroscopy measurements. Delocalized excitons and charge carriers in 2D COFs have been of interest since the earliest reports of these materials, but their small crystalline domain sizes and aggregated powder forms have severely limited their characterization to qualitative photoconductivity measurements (*11*, *29*). Previous TA experiments on 2D COFs were performed either on polycrystalline samples dispersed in solvent or on polycrystalline thin films (*30*–*32*). Although the first reported TA measurements showed reasonable data quality, they were inconsistent with more recent results from the same group on the same systems, which were noisy and dominated by scattering (*30*, *32*). Similar noise sources were also observed in our TA measurements on COF-5 powder samples obtained by solvothermal growth (fig. S12). In comparison, the TA data from our dispersed COF-5 colloids show signal-to-noise enhancement by approximately three orders of magnitude relative to the powder sample measured under the same experimental conditions (Fig. 4B). The well-defined structures of these colloids now make it possible to correlate their optical TA spectra to exciton dynamics and decay pathways inherent in the nature of the COF itself.

TA spectroscopy was performed on COF-5 colloids of varying particle size and as a function of pump fluence. These spectra were dominated by a broad excited-state absorption that decayed on a time scale of hundreds of picoseconds while remaining spectrally consistent, as well as a

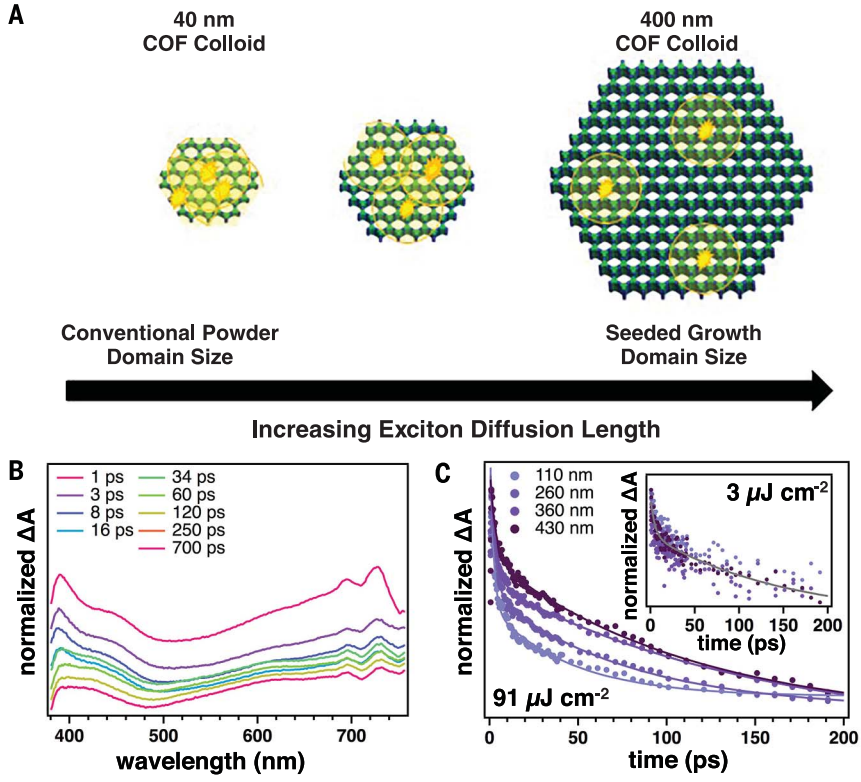

Fig. 4. Exciton diffusion studies of COF-5. (**A**) Depiction of exciton distribution in COF-5 single crystals of different sizes. Exciton interactions at boundaries are highlighted. (**B**) Transient absorption spectra (excitation wavelength 360 nm) as a function of indicated probe delay time for 110-nm COF-5 colloids. (**C**) Exciton decay kinetics (dots) and fits (lines) of COF-5 colloids of different sizes at high photon fluence (91 μJ/pulse) observed at 410 nm. Inset: Exciton decay kinetics (dots) and fit (line) at low photon fluence (3 μJ/pulse) observed at 410 nm.

stimulated emission feature that was longer than the time scale of the experiment and was subtracted to ensure consistent baselines for the time scale of observation. The identity of this feature is likely related to the singlet excitons of the triphenylene cores. However, dynamics clearly differed according to the particle size for high photon fluence (Fig. 4C), with the emergence of faster decays that were not observed at the low photon fluences (Fig. 4C, inset). We attribute this high fluence, fast exciton decay kinetics, and particle size dependence at the high excitation photon fluences to exciton-exciton annihilation, which occurs when multiple excitons within a diffusion length of each other are excited within the same particle sufficiently close to each other so as to diffuse and interact (*33*–*35*). At a given number density, excitons in smaller COF crystallites more readily undergo exciton-exciton annihilation because they are confined to a smaller effective volume (Fig. 4A). These combined observations demonstrate that the optical quality of our COF colloid nanoparticles enables high-quality spectroscopic measurements that were previously inaccessible. The fluence-sensitive exciton decay dynamics convey size-dependent photophysical properties and will lead to an improved understanding and leveraging of emergent electronic processes in these materials.

REFERENCES AND NOTES

1. J. Sakamoto, J. van Heijst, O. Lukin, A. D. Schlüter, *Angew. Chem. Int. Ed.* **48**, 1030–1069 (2009).
2. C. S. Diercks, O. M. Yaghi, *Science* **355**, eaal1585 (2017).
3. J. W. Colson, W. R. Dichtel, *Nat. Chem.* **5**, 453–465 (2013).
4. R. P. Bisbey, W. R. Dichtel, *ACS Cent. Sci.* **3**, 533–543 (2017).
5. M. Servalli, A. D. Schlüter, *Annu. Rev. Mater. Res.* **47**, 361–389 (2017).
6. R. Bhola *et al.*, *J. Am. Chem. Soc.* **135**, 14134–14141 (2013).
7. P. Kissel, D. J. Murray, W. J. Wulftange, V. J. Catalano, B. T. King, *Nat. Chem.* **6**, 774–778 (2014).
8. M. J. Kory *et al.*, *Nat. Chem.* **6**, 779–784 (2014).
9. S. Wan, J. Guo, J. Kim, H. Ihee, D. Jiang, *Angew. Chem. Int. Ed.* **48**, 5439–5442 (2009).
10. X. Ding *et al.*, *Angew. Chem. Int. Ed.* **50**, 1289–1293 (2011).
11. X. Feng *et al.*, *Angew. Chem. Int. Ed.* **51**, 2618–2622 (2012).
12. H. Ding *et al.*, *Chem. Eur. J.* **20**, 14614–14618 (2014).
13. S.-Y. Ding *et al.*, *J. Am. Chem. Soc.* **133**, 19816–19822 (2011).
14. Y. Zeng *et al.*, *J. Am. Chem. Soc.* **137**, 1020–1023 (2015).
15. S. Kandambeth *et al.*, *Angew. Chem. Int. Ed.* **52**, 13052–13056 (2013).
16. S. Chandra *et al.*, *J. Am. Chem. Soc.* **136**, 6570–6573 (2014).
17. M. Dogru *et al.*, *Angew. Chem. Int. Ed.* **52**, 2920–2924 (2013).
18. T. Sick *et al.*, *J. Am. Chem. Soc.* **140**, 2085–2092 (2018).
19. D. Bessinger, L. Ascherl, F. Auras, T. Bein, *J. Am. Chem. Soc.* **139**, 12035–12042 (2017).
20. C. R. DeBlase, K. E. Silberstein, T.-T. Truong, H. D. Abruña, W. R. Dichtel, *J. Am. Chem. Soc.* **135**, 16821–16824 (2013).
21. D. D. Medina *et al.*, *J. Am. Chem. Soc.* **137**, 1016–1019 (2015).
22. B. J. Smith, W. R. Dichtel, *J. Am. Chem. Soc.* **136**, 8783–8789 (2014).
23. B. J. Smith, N. Hwang, A. D. Chavez, J. L. Novotney, W. R. Dichtel, *Chem. Commun.* **51**, 7532–7535 (2015).
24. D Beaudoin, T. Maris, J. D. Wuest, *Nat. Chem.* **5**, 830–834 (2013).
25. B. J. Smith *et al.*, *ACS Cent. Sci.* **3**, 58–65 (2017).
26. S. Wan, J. Guo, J. Kim, H. Ihee, D. Jiang, *Angew. Chem. Int. Ed.* **47**, 8826–8830 (2008).
27. J. W. Colson *et al.*, *Science* **332**, 228–231 (2011).
28. C. J. Doonan, D. J. Tranchemontagne, T. G. Glover, J. R. Hunt, O. M. Yaghi, *Nat. Chem.* **2**, 235–238 (2010).
29. E. L. Spitler, W. R. Dichtel, *Nat. Chem.* **2**, 672–677 (2010).
30. S. Jin *et al.*, *Angew. Chem. Int. Ed.* **52**, 2017–2021 (2013).
31. D. D. Medina *et al.*, *ACS Nano* **8**, 4042–4052 (2014).
32. S. Jin *et al.*, *J. Am. Chem. Soc.* **137**, 7817–7827 (2015).
33. Y. Tamai, Y. Matsuura, H. Ohkita, H. Benten, S. Ito, *J. Phys. Chem. Lett.* **5**, 399–403 (2014).
34. A. Suna, *Phys. Rev. B* **1**, 1716–1739 (1970).
35. D. Sun *et al.*, *Nano Lett.* **14**, 5625–5629 (2014).

ACKNOWLEDGMENTS

We thank J. Bower and the cryo-electron microscopy facility at UC San Diego for assistance in low-dose HRTEM imaging. **Funding:** Supported by the Army Research Office for a Multidisciplinary University Research Initiatives (MURI) award under grant W911NF-15-1-0447. A.M.E. is supported by the NSF Graduate Research Fellowship under grant DGE-1324585, the Ryan Fellowship, and the Northwestern University International Institute for Nanotechnology. This study made use of the IMSERC and EPIC at Northwestern University, both of which have received support from the Soft and Hybrid Nanotechnology Experimental (SHyNE) Resource (NSF NNCI-1542205 and NSF ECCS1542205, respectively), the State of Illinois, and the International Institute for Nanotechnology (IIN). L.R.P. is supported by the National Institute of Biomedical Imaging and Bioengineering under award F32EB021859. N.C.G. was supported through a MURI through the Army Research Office under award W911NF-5-1-0568. Portions of this work were performed at the DuPont-Northwestern-Dow Collaborative Access Team (DND-CAT) located at Sector 5 of the Advanced Photon Source (APS). DND-CAT is supported by Northwestern University, E.I. DuPont de Nemours & Co., and the Dow Chemical Company. This research used resources of the Advanced Photon Source and Center for Nanoscale Materials, both U.S. Department of Energy (DOE) Office of Science User Facilities operated for the DOE Office of Science by Argonne National Laboratory under contract DE-AC02-06CH11357. N.C.F. and L.X.C. are partially supported by Basic Energy Science, CBG Division, DOE through Argonne National Laboratory under contract DE-AC02-06CH11357. Resources at the Advanced Photon Source were funded by NSF under award 0960140. **Author contributions:** A.M.E., N.C.F., R.P.B., E.V., and W.R.D. performed and interpreted the COF growth and structural characterization experiments; L.R.P. and N.C.G. performed and interpreted the TEM experiments; N.C.F., M.S.K., R.D.S., and L.X.C. performed and interpreted the time-resolved spectroscopy experiments; and all authors wrote and revised the manuscript. **Competing interests:** None declared. **Data and materials availability:** All data needed to evaluate the conclusions in the paper are present in the paper or the supplementary materials.

SUPPLEMENTARY MATERIALS

www.sciencemag.org/content/361/6397/52/suppl/DC1
Materials and Methods
Supplementary Text
Figs. S1 to S13
Tables S1 to S4

18 December 2017; resubmitted 9 March 2018
Accepted 3 May 2018
Published online 21 June 2018
10.1126/science.aar7883

QUANTUM OPTICS

A single-photon switch and transistor enabled by a solid-state quantum memory

Shuo Sun[1], Hyochul Kim[1], Zhouchen Luo[1], Glenn S. Solomon[2], Edo Waks[1]*

Single-photon switches and transistors generate strong photon-photon interactions that are essential for quantum circuits and networks. However, the deterministic control of an optical signal with a single photon requires strong interactions with a quantum memory, which has been challenging to achieve in a solid-state platform. We demonstrate a single-photon switch and transistor enabled by a solid-state quantum memory. Our device consists of a semiconductor spin qubit strongly coupled to a nanophotonic cavity. The spin qubit enables a single 63-picosecond gate photon to switch a signal field containing up to an average of 27.7 photons before the internal state of the device resets. Our results show that semiconductor nanophotonic devices can produce strong and controlled photon-photon interactions that could enable high-bandwidth photonic quantum information processing.

Photons are ideal carriers of quantum information, but the lack of deterministic photon-photon interactions has limited their applications in quantum computation and quantum networking. Recent advances in strong light-matter interactions using neutral trapped atoms (*1*–*5*) have enabled optical nonlinearities operating at the fundamental single-photon regime. However, neutral atoms require large and complex laser traps and operate at low bandwidths on the order of megahertz, which makes it challenging to integrate into compact devices. Circuit quantum electrodynamics systems also support strong nonlinearities (*6*, *7*), but they operate only in the microwave regime and are difficult to scale to optical frequencies. The realization of a compact solid-state single-photon nonlinearity at optical frequencies remains a key missing ingredient for scalable chip-integrated quantum photonic circuits.

Nanophotonic structures coupled to quantum emitters offer an attractive approach to realize single-photon nonlinearities in a compact solid-state device. However, most previous works used quantum emitters that act as two-level atomic systems (*8*), which are fundamentally limited by a time-bandwidth trade-off that makes deterministic single-photon switching impossible in either waveguides (*9*, *10*) or cavities (*11*, *12*). A quantum memory can overcome this limit, enabling a single photon to deterministically switch a second photon (*13*). It can also realize a single-photon transistor where one photon switches a signal containing multiple photons (*14*), a crucial building block for scalable quantum circuits (*15*). Recently, there has been great progress in controlling photons with solid-state qubits (*16*, *17*), as well as controlling a solid-state qubit with a photon (*18*). However, neither a single-photon switch nor a single-photon transistor has been realized using a solid-state quantum memory.

We report a single-photon switch and transistor enabled by a solid-state spin qubit coupled to a nanocavity. Our spin qubit comprises a single electron in a charged quantum dot. The quantum dot energy level structure (Fig. 1A) includes two ground states with opposite electron spin that form a stable quantum memory, labeled as $|\uparrow\rangle$ and $|\downarrow\rangle$, and two excited states that contain a pair of electrons and a single hole with opposite spins, labeled as $|\uparrow\downarrow, \Uparrow\rangle$ and $|\uparrow\downarrow, \Downarrow\rangle$. We apply a magnetic field in the Voigt configuration to break the spin degeneracy. In this condition, all four transitions are optically allowed, but the polarization of transitions σ_1 and σ_4 is orthogonal with transitions σ_2 and σ_3. Figure 1B shows a scanning electron microscope image of the fabricated cavity, which is based on a three-hole defect in a two-dimensional photonic crystal (*19*). The cavity mode is linearly polarized and makes a 30° angle with the polarization of transition σ_1 (*19*). We attain spin-dependent coupling by applying a magnetic field of 5.5 T. At this magnetic field, transition σ_1 is resonant with the cavity while all other transitions are detuned. Using cross-polarized reflectivity measurements, we determine the coupling strength g, cavity energy decay rate κ, and transition σ_1 dipole decoherence rate γ to be $g/2\pi$ = 10.7 ± 0.2 GHz, $\kappa/2\pi$ = 35.5 ± 0.6 GHz, and $\gamma/2\pi$ = 3.5 ± 0.3 GHz, respectively (*19*).

In the working principle of the single-photon switch and transistor (Fig. 1C), a gate pulse first sets the internal quantum memory of the switch. If the gate pulse contains zero photons, the spin stays in the spin-down state. But if the gate pulse contains one photon, it sets the spin to spin-up. Subsequently, the spin-state controls the cavity reflection coefficient, thereby changing the polarization of reflected signal photons. Figure 1D shows the pulse sequence to implement these two steps. We first prepare the quantum dot in a superposition of its spin ground states given by $(|\uparrow\rangle + |\downarrow\rangle)/\sqrt{2}$ using an initialization pulse to optically pump the spin to spin-down, followed by a circularly polarized optical rotation pulse that creates a $\pi/2$ spin rotation through cavity leaky modes (*20*, *21*). The system then freely evolves for a time τ, followed by a second identical rotation pulse. We inject the gate pulse between these two spin rotation pulses. If we set the free evolution time to be an integer number plus one-half of spin precession period, then in the absence of a gate photon the spin will evolve to the state $(|\uparrow\rangle - |\downarrow\rangle)/\sqrt{2}$ and the second rotation pulse will rotate it back to the spin-down state. But if a single gate photon reflects from the cavity, it applies a relative π phase shift between the spin-up and spin-down state, which reflects the spin along the x axis of the Bloch sphere. In this case the second rotation pulse rotates the spin to the spin-up state. A circularly polarized signal field then reflects off the cavity and undergoes a spin-dependent polarization rotation (*19*).

We prepare the pulse sequence in Fig. 1D using a pair of synchronized mode-locked lasers and an amplitude-modulated external cavity laser diode (*19*). We first characterize the switching behavior of the device using a signal field that has an average of 13.3 photons per pulse after the objective lens, corresponding to N_s = 0.42 ± 0.05 photons per pulse contained within the transverse spatial mode of the cavity. We determine the coupling efficiency (3.16 ± 0.35%) using the back-action of the input photons on the spin (*19*). We also measure the average power of each $\pi/2$-rotation pulse to be 20 μW after the objective lens. We prepare the incident signal field in the right-circular polarization and measure the intensity of the left-circular polarization component of the reflected signal field using a fixed polarizer after the cavity. Figure 2A shows the measured transmittance of the signal field passing through the polarizer as a function of τ in the absence of the gate pulse. We define the transmittance contrast as $\delta = T_{up} - T_{down}$, where T_{up} and T_{down} are the transmittance of the signal field when the rotation pulses prepare the spin to spin-up and spin-down, respectively, corresponding to the maximum and minimum transmittance in the oscillation. From the numerical fit (solid line) (*19*), we calculate the transmittance contrast to be δ = 0.24 ± 0.01. This value differs from the ideal contrast of unity due to both imperfect spin preparation fidelity of F = 0.78 ± 0.01 after the two rotation pulses and a finite cooperativity of $C = 2g^2/\kappa\gamma$ = 1.96 ± 0.19.

We next inject a 63-ps gate pulse containing an average of 13.3 photons after the objective lens, corresponding to 0.21 photons per pulse coupled to the cavity. We prepare the gate field in the same circular polarization as the signal, and post-select those events where the gate photon couples to the cavity using a two-photon coincidence measurement between the reflected gate and signal photons (*19*). Figure 2B shows the transmittance of the signal field conditioned on the presence of an

[1]Department of Electrical and Computer Engineering, Institute for Research in Electronics and Applied Physics, and Joint Quantum Institute, University of Maryland, College Park, MD 20742, USA. [2]Joint Quantum Institute, National Institute of Standards and Technology, and University of Maryland, Gaithersburg, MD 20899, USA.
*Corresponding author. Email: edowaks@umd.edu

incident gate photon that couples to the cavity. The oscillations of the transmittance shift by π due to spin-flips induced by a single gate photon.

The vertical solid line (labeled as *a* in Fig. 2) indicates the condition where the spin undergoes an integer number of rotations plus one half rotation around the Bloch sphere during its free evolution time. At this condition, a gate photon causes the polarization of the signal field to rotate and preferentially transmit through the polarizer, as described in Fig. 1C. The vertical dashed line *b* shows a second operating condition that also leads to optimal switching operation. This condition corresponds to the reverse switching behavior where the gate photon prevents the signal field polarization from rotating, thereby decreasing the transmittance. At both conditions, the gate pulse induces a change in the signal transmittance by 0.21 ± 0.02. For an ideal gate pulse containing a single photon, the transmittance change should be equal to the transmittance contrast of 0.24 calculated in Fig. 2A. In our case, the change in transmittance is slightly degraded because we use an attenuated laser to produce the gate pulse, which has a small probability of containing multiple photons. We define the switching contrast ξ as the change in the transmittance induced by a single gate photon. By correcting for multiphoton events in the gate field (*19*), we attain ξ = 0.24 ± 0.02, which matches the transmittance contrast δ.

The quantum memory in our device has a lifetime that is appreciably longer than the bandwidth of the switch. Thus, once a gate photon sets the memory state, the device can switch many signal photons before the spin-state decays. This property enables a single-photon transistor where a single gate photon can control a signal composed of many photons, an important distinction from switches lacking a quantum memory (*9*–*12*). Figure 2C shows the transmittance of the signal field as a function of delay time τ, where the average number of signal photons N_s per pulse is set to be 4.4 ± 0.5, 10.9 ± 1.2, and 23.0 ± 2.5, respectively. Here, we fixed the signal pulse to be 1.34 ns long, which is much longer than device bandwidth ($1/2g$ = 7 ps) but much shorter than the spin T_1 time (microseconds to milliseconds) (*22*). These conditions guarantee that the switching contrast depends only on the signal photon number as long as we are in the weak excitation regime (N_s << 115). The transmittance shows clear switching behavior for all cases. We calculate the switching contrast at the three signal photon numbers to be ξ = 0.22 ± 0.03, ξ = 0.17 ± 0.02, and ξ = 0.12 ± 0.02, respectively.

The switching contrast degrades with increasing signal photon number because each signal photon can apply a weak back-action on the spin through inelastic Raman scattering, inducing an undesired spin-flip that resets the internal quantum memory. This weak back-action limits the number of signal photons that can reflect from the cavity before a spin-flip event resets the spin-state. It therefore limits many applications. For example, in nondestructive single-photon detection, the maximum number of signal photons sets the overall detection efficiency. The blue circles in Fig. 3A show the measured transmittance contrast in the absence of the gate pulse as a function of the average signal photon number. This contrast quantifies the degree of self-switching induced by the signal without a gate field. The solid line shows a numerical fit of the data to an exponential function of the form $\exp(-N_s/N_{avg})$, where N_{avg} is the average number of signal photons it takes to flip the spin. From the fit, we determine N_{avg} = 27.7 ± 8.3.

An important feature of transistors is that they exhibit a gain above unity. We define the gain as the change in the average number of transmitted signal photons induced by a single gate photon

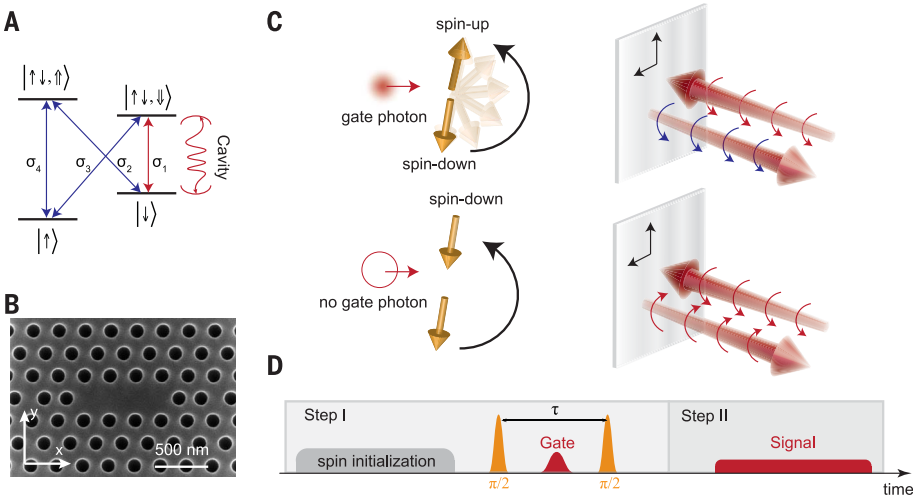

Fig. 1. Schematics of a single-photon switch and transistor. (**A**) Energy-level structure of a charged quantum dot in the Voigt configuration. The quantum dot has four optical transitions labeled as σ_1 to σ_4. Only transition σ_1 resonantly couples to the optical cavity. (**B**) Scanning electron microscope image of a fabricated photonic crystal cavity. (**C**) Schematic of the working principle of the single-photon switch and transistor. In the first step, a gate photon controls the state of the spin. In the second step, the spin determines the polarization of the signal field. (**D**) Pulse timing diagram to implement the single-photon switch and transistor.

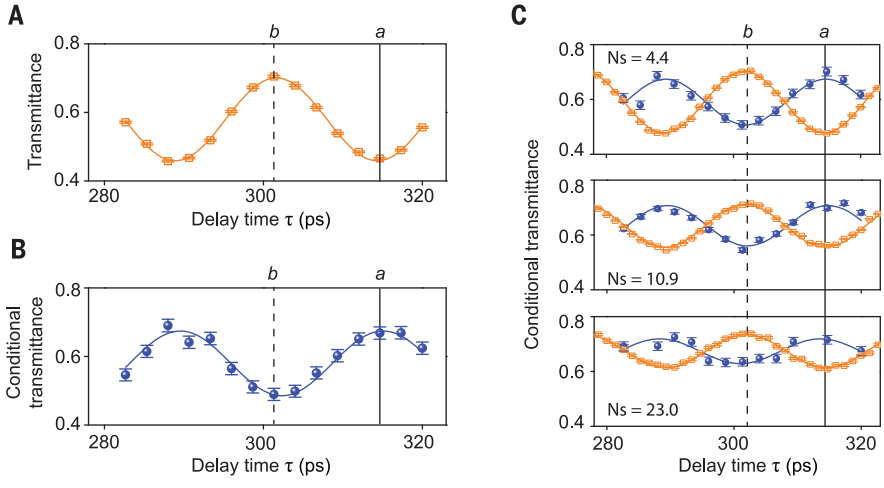

Fig. 2. Demonstration of a single-photon switch and transistor. (**A**) Transmittance of the signal field in the absence of the gate field as a function of delay time τ between two spin rotation pulses. (**B**) Transmittance of the signal field conditioned on detecting a gate photon as a function of delay time τ between the two spin rotation pulses. (**C**) Conditional transmittance of the signal field as a function of delay time τ between the two spin rotation pulses with (blue) and without (orange) a gate photon when we set the average signal photon number per pulse to be 4.4 ± 0.5, 10.9 ± 1.2, and 23.0 ± 2.5, respectively. In all panels, the orange squares and blue circles show measured transmittance without the gate field and conditioned on detecting a gate photon, respectively. The solid lines show numerically calculated values. The vertical solid line (*a*) and dashed line (*b*) denote the two optimal operating conditions of the single-photon switch and transistor.

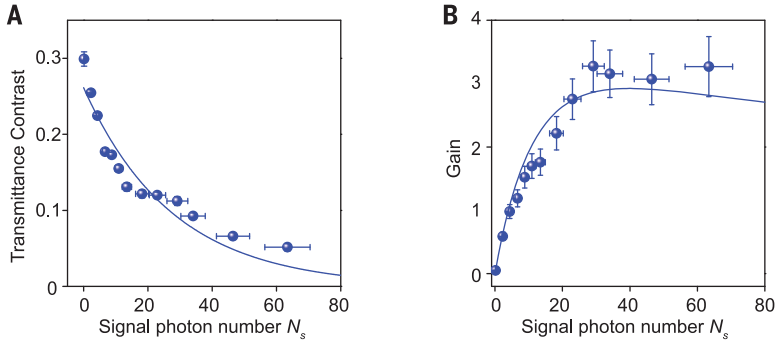

Fig. 3. Gain of the single-photon transistor. (**A**) Transmittance contrast as a function of average signal photon number. (**B**) Transistor gain as a function of average signal photon number. In both panels, blue circles show the measured values, and blue solid lines show the numerical fits.

(*1*–*3*). We determine the gain using the difference in the number of transmitted signal photons averaged over many pulse cycles when the spin is coherently prepared in spin-up and spin-down states, respectively, given by $G = N_s\delta$. The gain increases initially with the signal photon number (Fig. 3B) but saturates at strong signal fields and tapers down due to an increased probability of spin-flip from inelastic scattering and deviations from the weak excitation regime. We achieve the maximum gain of $G = 3.3 \pm 0.4$ with a photon number of $N_s = 29.2 \pm 3.2$.

The switching contrast and gain of our current device is limited by the spin preparation fidelity and finite cooperativity. The spin preparation fidelity could be improved by incorporating actively charged device structures (*21*). Electric gating could also reduce spectral wandering to enable much larger cooperativities (*23*). Higher-Q cavities and better alignment of the cavity polarization could create a larger selective Purcell enhancement for transition σ_1 that would reduce Raman scattering and therefore increase the device gain. Currently, we excite and collect from the out-of-plane direction, which results in low coupling and collection efficiency that limits the usable gain. A scalable device suitable for quantum information processing will require much higher efficiencies, because photon loss constitutes a dominant error mechanism for photonic qubits. Recent progress has been made in improving coupling efficiency of nanophotonic devices, including using adiabatic tapered structures to directly couple to fiber (*24*), adopting designs that have better spatial mode-matching with a fiber (*25*), or by coupling directly to on-chip waveguides (*26*). On-chip tuning (*27*) or hybrid integration (*28*, *29*) could further enable integration of multiple qubits and cascaded devices. Ultimately, such a device could enable a variety of important applications using compact chip-integrated platforms, including low-energy electro-optics (*30*), photonic quantum circuits (*15*), nondestructive photon detection (*31*), and scalable quantum repeaters for quantum networks (*32*).

REFERENCES AND NOTES

1. W. Chen *et al.*, *Science* **341**, 768–770 (2013).
2. H. Gorniaczyk, C. Tresp, J. Schmidt, H. Fedder, S. Hofferberth, *Phys. Rev. Lett.* **113**, 053601 (2014).
3. D. Tiarks, S. Baur, K. Schneider, S. Dürr, G. Rempe, *Phys. Rev. Lett.* **113**, 053602 (2014).
4. I. Shomroni *et al.*, *Science* **345**, 903–906 (2014).
5. B. Hacker, S. Welte, G. Rempe, S. Ritter, *Nature* **536**, 193–196 (2016).
6. J. M. Fink *et al.*, *Nature* **454**, 315–318 (2008).
7. L. Neumeier, M. Leib, M. J. Hartmann, *Phys. Rev. Lett.* **111**, 063601 (2013).
8. P. Lodahl, S. Mahmoodian, S. Stobbe, *Rev. Mod. Phys.* **87**, 347–400 (2015).
9. J. H. Shapiro, *Phys. Rev. A* **73**, 062305 (2006).
10. S. Rosenblum, S. Parkins, B. Dayan, *Phys. Rev. A* **84**, 033854 (2011).
11. D. J. Brod, J. Combes, *Phys. Rev. Lett.* **117**, 080502 (2016).
12. A. Nysteen, D. P. McCutcheon, M. Heuck, J. Mørk, D. R. Englund, *Phys. Rev. A* **95**, 062304 (2017).
13. L.-M. Duan, H. J. Kimble, *Phys. Rev. Lett.* **92**, 127902 (2004).
14. D. E. Chang, A. S. Sørensen, E. A. Demler, M. D. Lukin, *Nat. Phys.* **3**, 807–812 (2007).
15. J. L. O'Brien, A. Furusawa, J. Vučković, *Nat. Photonics* **3**, 687–695 (2009).
16. C. Arnold *et al.*, *Nat. Commun.* **6**, 6236 (2015).
17. A. Sipahigil *et al.*, *Science* **354**, 847–850 (2016).
18. S. Sun, H. Kim, G. S. Solomon, E. Waks, *Nat. Nanotechnol.* **11**, 539–544 (2016).
19. Materials and methods are available as supplementary materials.
20. D. Press, T. D. Ladd, B. Zhang, Y. Yamamoto, *Nature* **456**, 218–221 (2008).
21. S. G. Carter *et al.*, *Nat. Photonics* **7**, 329–334 (2013).
22. C.-Y. Lu *et al.*, *Phys. Rev. B* **81**, 035332 (2010).
23. L. De Santis *et al.*, *Nat. Nanotechnol.* **12**, 663–667 (2017).
24. R. S. Daveau *et al.*, *Optica* **4**, 178–184 (2017).
25. V. Giesz *et al.*, *Nat. Commun.* **7**, 11986 (2016).
26. R. Bose, D. Sridharan, G. S. Solomon, E. Waks, *Opt. Express* **19**, 5398–5409 (2011).
27. J.-H. Kim, C. J. Richardson, R. P. Leavitt, E. Waks, *Nano Lett.* **16**, 7061–7066 (2016).
28. J.-H. Kim *et al.*, *Nano Lett.* **17**, 7394–7400 (2017).
29. M. Davanco *et al.*, *Nat. Commun.* **8**, 889 (2017).
30. A. E. Willner, S. Khaleghi, M. R. Chitgarha, O. F. Yilmaz, *J. Lightwave Technol.* **32**, 660–680 (2014).
31. N. Imoto, H. A. Haus, Y. Yamamoto, *Phys. Rev. A* **32**, 2287–2292 (1985).
32. W. Munro, A. Stephens, S. Devitt, K. Harrison, K. Nemoto, *Nat. Photonics* **6**, 777–781 (2012).

ACKNOWLEDGMENTS

The authors acknowledge G. Baumgartner and M. Morris at the Laboratory for Telecommunication Sciences for providing superconducting nanowire single-photon detectors. **Funding:** This work was supported by the Physics Frontier Center at the Joint Quantum Institute, the National Science Foundation (grants PHY1415485 and ECCS1508897), and the ARL Center for Distributed Quantum Information. **Author contributions:** S.S. and E.W. conceived and designed the experiment, prepared the manuscript, and carried out the theoretical analysis. S.S. carried out the measurement and analyzed the data. H.K. contributed to sample fabrication. Z.L. contributed to optical measurement. G.S.S. provided samples grown by molecular beam epitaxy. **Competing interests:** The authors declare no competing financial interests. **Data and materials availability:** All data are available in the manuscript or the supplementary materials.

SUPPLEMENTARY MATERIALS

www.sciencemag.org/content/361/6397/57/suppl/DC1
Materials and Methods
Supplementary Text
Figs. S1 to S7
References (*33*–*44*)

19 February 2018; accepted 4 May 2018
10.1126/science.aat3581

QUANTUM INFORMATION

Observation of an environmentally insensitive solid-state spin defect in diamond

Brendon C. Rose[1]*, Ding Huang[1]*, Zi-Huai Zhang[1], Paul Stevenson[1], Alexei M. Tyryshkin[1], Sorawis Sangtawesin[1], Srikanth Srinivasan[1], Lorne Loudin[2], Matthew L. Markham[3], Andrew M. Edmonds[3], Daniel J. Twitchen[3], Stephen A. Lyon[1], Nathalie P. de Leon[1]†

Engineering coherent systems is a central goal of quantum science. Color centers in diamond are a promising approach, with the potential to combine the coherence of atoms with the scalability of a solid-state platform. We report a color center that shows insensitivity to environmental decoherence caused by phonons and electric field noise: the neutral charge state of silicon vacancy (SiV^0). Through careful materials engineering, we achieved >80% conversion of implanted silicon to SiV^0. SiV^0 exhibits spin-lattice relaxation times approaching 1 minute and coherence times approaching 1 second. Its optical properties are very favorable, with ~90% of its emission into the zero-phonon line and near–transform-limited optical linewidths. These combined properties make SiV^0 a promising defect for quantum network applications.

Point defects in diamond known as color centers are a promising physical platform for quantum science and quantum information processing. As atomlike systems, they can exhibit excellent spin coherence and can be manipulated with light. As solid-state defects, they can be placed together at high densities and incorporated into scalable devices. Diamond is an unusually excellent host: it has a large bandgap, can be synthesized with impurity concentrations below the parts-per-billion scale, and can be isotopically purified to eliminate magnetic noise from nuclear spins (*1*). The well-studied negatively charged nitrogen vacancy (NV^-) center exhibits long electron spin coherence times even at room temperature and has been used to demonstrate basic building blocks of quantum networks, including spin-photon entanglement (*2*), entanglement with nearby nuclear spins to form quantum registers (*3*, *4*), remote entanglement of two NV^- centers (*5*, *6*), quantum teleportation (*7*), and entanglement distillation (*8*). Despite these experimental achievements, the NV^- center suffers from a low spin-photon entanglement generation rate that is limited by its optical properties. In particular, only a small fraction of NV^- emission is at the zero-phonon line (ZPL), which can be parameterized by its Debye-Waller factor of 0.03 (*9*). Furthermore, NV^- exhibits a large static inhomogeneous linewidth (*10*) and substantial spectral diffusion (*11*), particularly when placed near surfaces (*12*), which results from a large difference in the permanent electric dipole moment between the ground and excited states. These optical properties severely limit the utility of NV^- centers for future scalable quantum networks.

Recently, the negatively charged silicon vacancy (SiV^-) center has been demonstrated to have more favorable optical properties. The SiV^- center exhibits a large Debye-Waller factor of 0.7 (*13*), narrow inhomogeneous linewidth, and single-center linewidths with minimal spectral diffusion (*14*, *15*). These narrow linewidths arise from its D_{3d} molecular configuration, as inversion symmetry guarantees a vanishing permanent electric dipole moment, making the optical transition frequency insensitive to electric field noise. These properties have enabled demonstrations of two-photon interference from distinct emitters (*15*) and strong atom-photon interactions in a nanophotonic cavity (*16*). However, orbital relaxation through electron-phonon coupling limits the SiV^- electron spin coherence time (T_2) to 38 ns at liquid helium temperature, 4.5 K (*14*). This results from its imbalanced electronic spin configuration, with total spin $S = ½$ in doubly degenerate orbitals, making SiV^- prone to phonon-mediated, dynamic Jahn-Teller–like orbital relaxation (*17*).

These promising demonstrations motivated us to search for other color centers in diamond that combine the attractive optical properties of SiV^- with the long spin coherence time of NV^-. A natural approach is to tune the Fermi level of diamond to stabilize a different charge state of the silicon vacancy center for the purpose of accessing a different spin configuration (*18*, *19*) while preserving inversion symmetry. There is some evidence that different charge states of SiV have been observed in uncontrolled samples (*20*–*22*). Previous work has helped to establish a connection between photoluminescence (PL) at 946 nm and the KUL1 defect observed in electron spin resonance (ESR) measurements ($S = 1$, zero field splitting $D = 942$ MHz) (*20*–*22*) by correlating the PL intensity with ESR transitions across several samples. Charge transfer experiments from SiV^- suggest that the KUL1 center is the neutral charge state of the same center, SiV^0 (*21*).

Here we report the stabilization and characterization of SiV^0 by deliberate engineering of the diamond host. We accomplish this by careful control over the concentration of co-occurring defects in the diamond to pin the Fermi level such that the neutral charge state has the lowest formation energy (*23*). Fermi level engineering in diamond is challenging, as it relies on charge compensation between deep defects (*24*) and thus requires meticulous characterization and control of all defects, including heteroatoms, molecular point defects, lattice damage, and extended defects. Furthermore, the presence of other defects in the lattice can complicate characterization of fundamental properties of color centers, and we show that through careful materials engineering, we are able to uncover highly coherent optical and spin properties of SiV^0.

To disentangle the contributions of different defects, we first studied a modulation-doped diamond (the layered sample) that allowed a wide range of relative co-defect concentrations to be accessed in a single sample (Fig. 1B, left). This diamond was grown by microwave plasma–enhanced chemical vapor deposition on a (100) high-pressure, high-temperature substrate, and both the boron and silicon concentrations were ramped throughout the growth (*25*). The boron precursor was shut off to create a 200-μm low-boron {[B] < 35 parts per billion (ppb)} region in the middle of the sample. In this layered sample, we observed emission at 946 nm in bulk PL (Fig. 1A) as well as the KUL1 center in bulk X-band (9.7 GHz) ESR (Fig. 1C). Specifically, we observed four sets of peaks with the external magnetic field aligned along a <111> axis, consistent with the two inequivalent orientations with splittings that correspond to $S = 1$, $D = 942$ MHz. Furthermore, the hyperfine structure of a single peak is consistent with prior measurements (*20*) (Fig. 1C, inset), and the single pair of ^{13}C hyperfine peaks is indicative of the inversion symmetry of the center. From the Hahn echo intensities compared to the known Si concentration in the sample, we estimated that only a small fraction of the Si exists as SiV^0 (*25*).

The apparent optical and spin properties of SiV^0 in the layered sample were complicated by heterogeneity and the presence of co-defects. The PL spectrum shows broad emission to the red of 946 nm, as well as three peaks at 952, 975, and 985 nm, which may be associated with other defects (Fig. 1A). Time-resolved pulsed ESR measurements of this sample exhibit multiexponential decays for both T_1 (spin relaxation time) and T_2 (fig. S8), most likely because of dipolar interactions between SiV^0 centers and interactions with uncontrolled co-defects.

[1]Department of Electrical Engineering, Princeton University, Princeton, NJ 08544, USA. [2]Gemological Institute of America, New York, NY 10036, USA. [3]Element Six, Harwell OX11 0QR, UK.
*These authors contributed equally to this work.
†Corresponding author. Email: npdeleon@princeton.edu

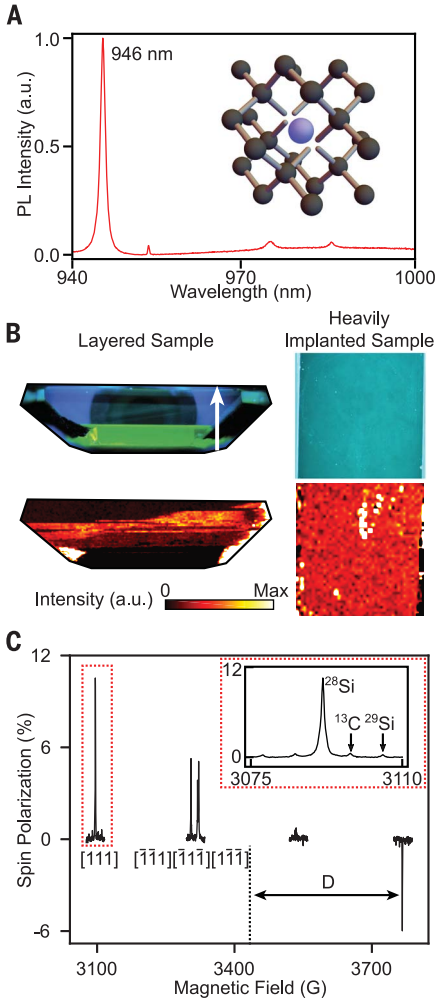

Fig. 1. Stabilizing SiV^0 centers in diamond. (**A**) Bulk PL spectrum of SiV^0 at 77 K showing a ZPL at 946 nm. (Inset) Ball-and-stick model of the SiV center in diamond. The interstitial Si atom (blue sphere) and split vacancy are aligned along the [111] direction in the diamond lattice. a.u., arbitrary units. (**B**) PL with above-bandgap excitation (top) and PL map of emission at 946 nm using 780-nm excitation (bottom) for the two samples under investigation. The above-bandgap PL images are color-calibrated DiamondView images that show all luminescence with wavelengths above 225 nm (*25*). The color bar for the 946-nm emission shows intensity scaled to enhance contrast. Layered diamond (left) is grown by plasma-enhanced chemical vapor deposition with B and Si concentrations varied during the growth. The growth direction is indicated with a white arrow. PL at 946 nm is localized to a few growth bands. The heavily implanted sample (right) with uniform boron doping and implanted Si has nearly uniform PL at 946 nm. Saturated intensity (white) corresponds to background and interference arising from the graphitic edges of the sample or broadband PL from the metallic cold finger. (**C**) Pulsed ESR spectrum at 9.7 GHz with magnetic field **B** parallel to [111], identifying KUL1 (S = 1, D = 942 MHz or 336 G) in the heavily implanted sample under green laser excitation for optically enhanced spin polarization. The resonant field for S = ½ and a free electron g-factor is indicated as a dashed vertical line near the center of the plot. Four sets of peaks correspond to the two inequivalent orientations: one aligned with the field and three equivalent orientations at 109.5° from the field. The outer peaks at low and high magnetic field correspond to the orientation aligned with the magnetic field, [111]. The two sets of inner peaks closer to the vertical dashed line (marking the resonant field for a free electron g-factor) correspond to the other three orientations, and a slight misalignment of the field from [111] splits the peaks into three resolvable lines. The optical spin polarization has the opposite sign with respect to thermal polarization, so the two sets of higher field lines are diminished by the combination of mechanisms. Optical spin polarization is also less efficient in the presence of strong off-axis magnetic fields, so the inner peaks have lower intensity than the outer peaks. (Inset) Hyperfine structure of an individual transition shows ^{13}C and ^{29}Si peaks. The same pulsed ESR spectrum is observed in both the layered and heavily implanted samples. The red boxes denote the region of the plot that is contained in the inset.

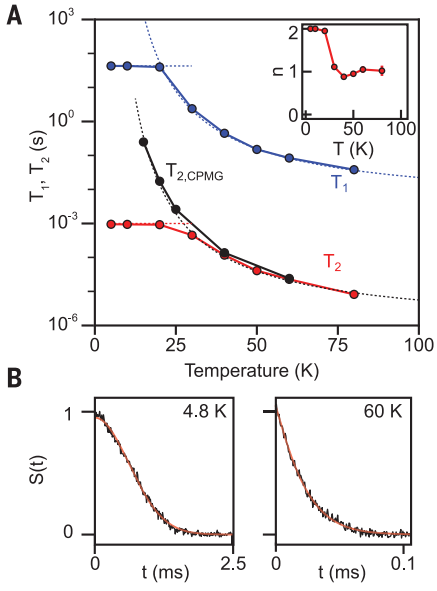

Fig. 2. Spin relaxation time (T_1) and coherence time (T_2) measurements. (**A**) Temperature dependence of T_1 (blue symbols), T_2 (red symbols), and $T_{2,CPMG}$ (black symbols) for SiV^0 measured on the m_s = 0 ↔ +1 transition of the orientation aligned with the magnetic field. Below 20 K, both T_1 and T_2 are independent of temperature, with T_1 = 43 ± 2 s and T_2 = 0.954 ± 0.025 ms. Above 20 K, both T_1 and T_2 show a temperature dependence consistent with an Orbach process with an activation energy of 16.8 meV (dashed blue and black lines are fits). Dynamical decoupling with CPMG (black symbols) extends the coherence time to $T_{2,CPMG}$ = 255 ± 20 ms at 15 K. (Inset) Temperature dependence of the exponential stretching factor, n, in the T_2 decay showing a step in the stretching factor at 20 K. (**B**) Selected Hahn echo decay curves illustrating n = 2 in the low-temperature regime (4.8 K) and n = 1 in the high-temperature regime (60 K).

We definitively verified the connection between the ESR and PL transitions by scanning a laser across the optical transition while measuring the polarization of the m_s = 0 ↔ +1 spin transition (m_s, magnetic component of the spin quantum number) at cryogenic temperatures (4.8 K) (fig. S10). We observed strong changes in bulk spin polarization as we scanned the laser across 946 nm, showing that the optical and ESR transitions arise from the same defect. Armed with this assignment, spatially resolved PL mapping reveals that 946-nm emission is localized in specific growth bands in the layered sample (Fig. 1B, bottom left), suggesting that SiV^0 may form more efficiently in certain growth environments. Correlating these regions with spatially resolved secondary ion mass spectrometry indicates that SiV^0 forms in regions with [B] = 1 to 3 parts per million (ppm), [Si] = 400 ppb, and [N] below the detection limit of the technique, estimated to be ~1 ppb from prior characterization of growth conditions (fig. S4). Using this information, we prepared a homogeneous, heavily implanted sample with a uniform distribution of SiV^0 by implanting ^{28}Si into high-purity diamond with [B] = 1 ppm and [N] < 5 ppb. A range of implantation energies (table S2) was used to generate a sample with a signal large enough for bulk ESR and density low enough to avoid dipolar interactions between pairs of SiV^0 (<50 ppb). Before ion implantation, we etched 5 to 10 μm of diamond to remove subsurface damage from polishing (*12*). After ion implantation, thermal annealing at 800° and 1200°C forms SiV^0 and repairs implantation-induced lattice damage (*12*). Both steps are critical for suppressing environmental noise and Fermi level pinning from lattice damage. In contrast to the layered sample, PL mapping of this heavily implanted sample shows a homogeneous distribution of 946-nm emission (Fig. 1B, bottom right), and ESR spin counting indicates a conversion efficiency from implanted ^{28}Si to SiV^0 of >80% (fig. S7).

The heavily implanted sample exhibits markedly different behavior in time-resolved ESR compared with the layered sample. Both the electron spin coherence and relaxation times show single exponential behavior, indicating that the SiV^0 environment is homogeneous (Fig. 2B). Below 20 K, the electron spin coherence time measured using a Hahn echo sequence is T_2 = 0.954 ± 0.025 ms, and the spin relaxation time is measured to be T_1 = 43 ± 2 s (Fig. 2A) (*26*). Both are

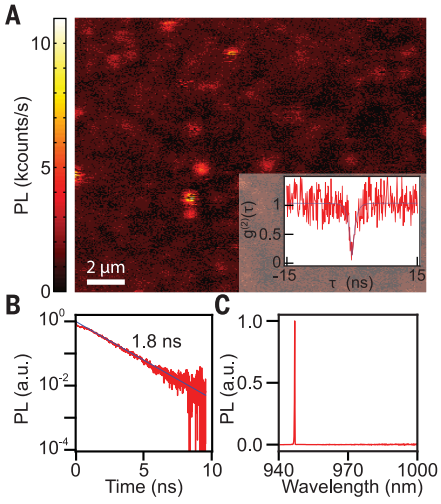

Fig. 3. Optical properties of SiV^0. (**A**) Scanning confocal PL image of SiV^0 centers in the lightly implanted sample. (Inset) Second-order correlation function $g^{(2)}(\tau)$ (τ, time delay between photon arrivals) of the PL from a single spot with $g^{(2)}(0) < 0.5$, indicating that the PL originates primarily from a single emitter. (**B**) Time-dependent PL measured using a pulsed laser at 780 nm. The single exponential fit indicates an excited-state lifetime of 1.8 ns at 4 K. (**C**) PL spectrum of a single SiV^0 center. The emission is collected into a spectrometer-limited peak on a charge-coupled device spectrometer (0.1-nm resolution), and there is no observable phonon sideband out to 1000 nm.

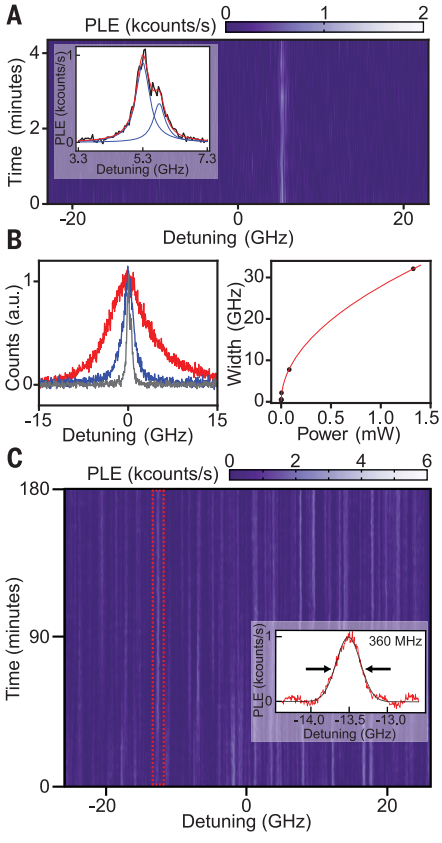

Fig. 4. PLE spectroscopy. (**A**) PLE scan on a single center in the lightly implanted sample, showing a single line that is spectrally stable over ~4 min of interrogation. (Inset) PLE integrated over all the scans (black), with the baseline subtracted (*25*). The fit (red) represents the sum of two overlapping Lorentzians (blue) with individual widths [full width at half maximum (FWHM)] of 450 and 499 MHz for the left and right peaks, respectively. (**B**) (Left) PLE scans of the line from (A) at different excitation powers: 150 nW (gray), 3.2 μW (blue), and 81 μW (red), resulting in linewidths of 450 MHz, 2.2 GHz, and 7.8 GHz, respectively. (Right) The linewidth as a function of excitation power P, showing the power broadening in detail. The red line corresponds to $\Gamma(P) = G\sqrt{1 + P/P_0}$ where Γ is the FWHM of the optical transition, G = 0.255 GHz, and P_0 = 78 nW. (**C**) Ensemble PLE in the heavily implanted sample. The scan reveals many lines that are stable across 80 iterations spanning a 3-hour period. (Inset) Gaussian fit to a single isolated peak, integrated over all of the scans, with the baseline subtracted, showing a FWHM of 360 MHz.

independent of temperature. This spin coherence time is more than four orders of magnitude longer than the T_2 = 35 ns reported for SiV$^-$ at 4.5 K (*14*), which is limited by an orbital T_1 = 38 ns (*14*). The temperature independence of the spin relaxation in SiV^0 is similar to previous observations of NV$^-$ ensembles (*27*). The mechanism limiting T_1 at low temperatures remains unknown, but the direct (single-phonon) relaxation process can be excluded because it would have a T^{-1} dependence.

The decoherence mechanism at low temperature can be inferred by the stretching factor, n, extracted from the Hahn echo decay signal $S(t)$ (Fig. 2B) by fitting the data to a stretched exponential, $S(t) = A \cdot \exp[-(t/T_2)^n]$ (t, time). The stretching factor n = 2 (Fig. 2A, inset) indicates that the coherence time is dominated by slowly-varying noise, which likely arises from the 1.1% natural abundance of ^{13}C nuclei in this sample (*28*), similar to what is observed for NV$^-$ centers (*29*, *30*). Dynamical decoupling with the Carr-Purcell-Meiboom-Gill (CPMG) sequence (*31*) refocuses decoherence from ^{13}C spectral diffusion, extending the coherence time to $T_{2,\mathrm{CPMG}}$ = 255 ± 20 ms at 15 K (Fig. 2A, black symbols), limited in our experiments by pulse error accumulation.

At temperatures above 20 K, both T_1 and T_2 rapidly decrease with increasing temperature. The temperature dependence of the spin relaxation is consistent with an Orbach spin relaxation process, $T_1 \propto \exp(-E_a/k_B T)$, with an activation energy E_a = 16.8 meV (k_B, Boltzmann constant; T, temperature). Both T_2 and $T_{2,\mathrm{CPMG}}$ exhibit a similar temperature dependence to the spin relaxation but scaled by a constant factor of 4100, indicating that the decay in T_2 with temperature is related to the same Orbach process.

We then turned our attention to optical characterization of SiV^0 at low temperature. To optically examine single SiV^0 centers, we implanted silicon ions at a dose of 10^9 cm^{-2} into a lightly boron-doped diamond, followed by high-temperature annealing to form SiV^0 (the lightly implanted sample). A confocal scan at 5 K with off-resonant excitation (905 nm, 28 mW) and detection at wavelengths longer than 930 nm shows isolated and diffraction-limited PL spots with a peak intensity >10 kilocounts per second (kcounts/s) (Fig. 3A). Second-order photon correlation statistics from an isolated spot show a dip at zero-time delay, $g^{(2)}(0) = 0.126 \pm 0.037$ (Fig. 3A, inset), confirming that these spots arise from single-photon emitters. A power dependence of the PL intensity reveals that the saturated count rate is 37.5 kcounts/s (fig. S12A). Taking the saturated photon count rate and accounting for the low quantum efficiency of the detector (22%), transmission through a beamsplitter (55%), and transmission through the high–numerical aperture and fiber-coupling objectives (74 and 85%, respectively) in this wavelength range, we estimate that this corresponds to a photon emission rate of ~500,000 photons/s (*25*). Additionally, we note that bright emitters have a broader inhomogeneous distribution (>20 nm) than the bulk PL linewidth of <1 nm measured in the heavily implanted sample (fig. S16). This distribution in wavelength is most likely a result of surface-related strain and is consistent with recent measurements of SiV$^-$ where inhomogeneous distributions of ~20 nm have been observed in nanodiamonds (*32*, *33*).

In contrast to bulk PL in the layered sample, the emission spectra of single centers in the implanted samples exhibit narrow, spectrometer-limited peaks (0.1-nm resolution) with no discernible phonon sideband (Fig. 3C). We estimate a lower bound on the Debye-Waller factor by comparing the intensity at the ZPL with the integrated intensity from 947 to 1000 nm, which includes background and noise. Using this comparison, we estimate that 90 ± 10% of the emission is in the ZPL (*25*). This is counter to previous estimates of the Debye-Waller factor of SiV^0, which were complicated by the presence of uncontrolled co-defects in this wavelength range (*21*).

We thoroughly investigated the optical transitions of SiV^0 by using photoluminescence excitation (PLE) spectroscopy (Fig. 4), in which a narrow-linewidth laser (<200 kHz) is scanned across the SiV^0 ZPL while emission is measured at wavelengths above 960 nm. Despite the absence of a clear phonon sideband above the noise in the PL spectrum (Fig. 3C), we observed a small but measurable increase in photon counts (1 to 5 kcounts/s) at wavelengths above 960 nm with resonant excitation at 946 nm. PLE scans of a single center in the lightly implanted sample reveal two overlapping lines with linewidths 450 and 499 MHz that are observed to be spectrally stable over minutes of investigation (Fig. 4A).

These linewidths are five times as large as the transform-limited linewidth of 88 MHz determined by the bulk PL excited-state lifetime of 1.8 ns (Fig. 3B). At higher laser excitation powers, the PLE linewidths increase (Fig. 4B), and the saturation power extracted from the fit is 78 nW. This is somewhat larger than the predicted value of 10 nW, with the discrepancy likely attributable to mismatch between the laser and dipole polarizations and a finite decay probability into other ground states (*25*).

A PLE scan of the heavily implanted sample reveals many narrow lines with linewidths ranging from 250 to 500 MHz (Fig. 4C). Repeated scans over a 3-hour period show that these lines are completely stable in frequency, showing no measurable sign of spectral diffusion. This indicates that stable, near–transform-limited optical lines are a robust property of SiV^0, in stark contrast to implanted NV^- centers, which exhibit optical linewidths 10 to 100 times their natural linewidth (*12*).

Building on this demonstration of a color center in diamond with long spin coherence time and spectrally stable optical transitions, the high-purity, homogeneous samples discussed here will allow for detailed characterization of the fine structure and selection rules of the optical transitions, accurate determination of quantum efficiency, and further characterization of the ground-state spin. Ongoing investigations include studies of the origin of the Orbach process above 20 K (*34*) and schemes for dynamic stabilization of the charge state during optical excitation. We achieved up to 44% bulk spin polarization by using resonant optical excitation (fig. S10), suggesting the existence of spin-conserving and spin-pumping optical transitions, which are key ingredients for quantum networks. In addition, SiV^0 contains an intrinsic longer-lived quantum memory in the form of the ^{29}Si nuclear spin within the defect. Preliminarily, we measured nuclear spin coherence times of $T_{2n} = 0.45 \pm 0.03$ s in a ^{29}Si-enriched sample (fig. S9), and future work will explore the limits of this coherence in samples with lower spin density.

Furthermore, SiV^0 is a particularly attractive candidate for implementing a single-atom quantum memory in a quantum network through integration with quantum nanophotonic devices. The high conversion efficiency for implanted centers is advantageous for nanoscale patterning and registration (*35*). The emission wavelength at 946 nm is compatible with heterogeneously integrated GaAs photonics (*36*), and efficient, low-noise frequency conversion to telecommunications wavelengths (1550 nm) at the single-photon level using three-wave mixing has already been demonstrated at 980 nm (*37*).

Our methods for Fermi level engineering using careful control over co-occurring defects can be broadly applied to alter the charge state of other known color centers, such as the germanium (*38*) and tin (*39*) vacancy centers, as well as for discovery of entirely new color centers in diamond.

REFERENCES AND NOTES

1. G. Balasubramanian *et al.*, *Nat. Mater.* **8**, 383–387 (2009).
2. E. Togan *et al.*, *Nature* **466**, 730–734 (2010).
3. P. C. Maurer *et al.*, *Science* **336**, 1283–1286 (2012).
4. F. Dolde *et al.*, *Nat. Phys.* **9**, 139–143 (2013).
5. H. Bernien *et al.*, *Nature* **497**, 86–90 (2013).
6. B. Hensen *et al.*, *Nature* **526**, 682–686 (2015).
7. W. Pfaff *et al.*, *Science* **345**, 532–535 (2014).
8. N. Kalb *et al.*, *Science* **356**, 928–932 (2017).
9. P. E. Barclay, K.-M. C. Fu, C. Santori, A. Faraon, R. G. Beausoleil, *Phys. Rev. X* **1**, 011007 (2011).
10. P. Olivero *et al.*, *New J. Phys.* **15**, 043027 (2013).
11. J. Wolters, N. Sadzak, A. W. Schell, T. Schröder, O. Benson, *Phys. Rev. Lett.* **110**, 027401 (2013).
12. Y. Chu *et al.*, *Nano Lett.* **14**, 1982–1986 (2014).
13. A. Dietrich *et al.*, *New J. Phys.* **16**, 113019 (2014).
14. L. J. Rogers *et al.*, *Phys. Rev. Lett.* **113**, 263602 (2014).
15. A. Sipahigil *et al.*, *Phys. Rev. Lett.* **113**, 113602 (2014).
16. A. Sipahigil *et al.*, *Science* **354**, 847–850 (2016).
17. K. D. Jahnke *et al.*, *New J. Phys.* **17**, 043011 (2015).
18. A. Gali, M. Fyta, E. Kaxiras, *Phys. Rev. B* **77**, 155206 (2008).
19. J. R. Maze *et al.*, *New J. Phys.* **13**, 025025 (2011).
20. A. M. Edmonds, M. E. Newton, P. M. Martineau, D. J. Twitchen, S. D. Williams, *Phys. Rev. B* **77**, 245205 (2008).
21. U. F. S. D'Haenens-Johansson *et al.*, *Phys. Rev. B* **84**, 245208 (2011).
22. J. P. Goss, R. Jones, S. J. Breuer, P. R. Briddon, S. Öberg, *Phys. Rev. Lett.* **77**, 3041–3044 (1996).
23. A. Gali, J. R. Maze, *Phys. Rev. B* **88**, 235205 (2013).
24. A. T. Collins, *J. Phys. Condens. Matter* **14**, 3743–3750 (2002).
25. See supplementary materials.
26. During the preparation of this manuscript, a related study on SiV^0 spin relaxation and optical spin polarization was published (*40*).
27. A. Jarmola, V. M. Acosta, K. Jensen, S. Chemerisov, D. Budker, *Phys. Rev. Lett.* **108**, 197601 (2012).
28. W. B. Mims, K. Nassau, J. D. McGee, *Phys. Rev.* **123**, 2059–2069 (1961).
29. P. L. Stanwix *et al.*, *Phys. Rev. B* **82**, 201201(R) (2010).
30. B. C. Rose, C. D. Weis, A. M. Tyryshkin, T. Schenkel, S. A. Lyon, *Diamond Related Materials* **72**, 32–40 (2017).
31. S. Meiboom, D. Gill, *Rev. Sci. Instrum.* **29**, 688–691 (1958).
32. E. Neu *et al.*, *New J. Phys.* **13**, 025012 (2011).
33. E. Neu, M. Fischer, S. Gsell, M. Schreck, C. Becher, *Phys. Rev. B* **84**, 205211 (2011).
34. B. C. Rose *et al.*, arXiv:1710.03196 [quant-ph] (9 October 2017).
35. D. M. Toyli, C. D. Weis, G. D. Fuchs, T. Schenkel, D. D. Awschalom, *Nano Lett.* **10**, 3168–3172 (2010).
36. D. Englund *et al.*, *Phys. Rev. Lett.* **95**, 013904 (2005).
37. Q. Li, M. Davanco, K. Srinivasan, *Nat. Photonics* **10**, 406–414 (2016).
38. T. Iwasaki *et al.*, *Sci. Rep.* **5**, 12882 (2015).
39. T. Iwasaki *et al.*, *Phys. Rev. Lett.* **119**, 253601 (2017).
40. B. L. Green *et al.*, *Phys. Rev. Lett.* **119**, 096402 (2017).
41. B. C. Rose *et al.*, Replication Data for: Observation of an environmentally insensitive solid state spin defect in diamond, version 1, Harvard Dataverse (2018) https://doi.org/10.7910/DVN/FUQDFQ.

ACKNOWLEDGMENTS

We thank A. Stacey, W. Wang, U. D'Haenens-Johansson, and A. Zaitsev for advice and help with materials characterization; N. Yao and J. Schreiber at the Princeton Imaging and Analysis Center for help with diamond surface characterization; and A. Gali, M. Warner, and J. Thompson for fruitful discussions. **Funding:** This work was supported by the NSF under the EFRI ACQUIRE program (grant 1640959) and through the Princeton Center for Complex Materials, a Materials Research Science and Engineering Center (grant DMR-1420541). This material is also based on work supported by the Air Force Office of Scientific Research under award number FA9550-17-0158. D.H. acknowledges support from a National Science Scholarship from the Agency for Science, Technology, and Research (A*STAR) of Singapore. **Author contributions:** Confocal microscopy measurements, sample preparation, and materials characterization were performed by B.C.R., D.H., Z.-H.Z., P.S., S.Sa., and S.Sr. under the supervision of N.P.d.L. The electron spin resonance measurements were performed by B.C.R. and A.M.T. under the supervision of S.A.L. and N.P.d.L. The SiV^0 PL mapping, some bulk PL measurements, and DiamondView measurements were performed by L.L. and N.P.d.L. at the Gemological Institute of America. M.L.M., A.M.E., and D.J.T. synthesized the boron-doped and layered diamonds and performed detailed materials characterization at Element Six. **Competing interests**: N.P.d.L., B.C.R., D.H., Z.-H.Z., A.M.T., S.Sa., S.Sr. L.L., M.L.M., A.M.E., D.J.T., and S.A.L. filed for a provisional patent (62/559,918) that relates to synthetic engineered diamond materials with spin impurities and methods for materials engineering. **Data and materials availability:** All data from the main paper and supplementary materials are publicly available through Harvard Dataverse (*41*).

SUPPLEMENTARY MATERIALS

www.sciencemag.org/content/361/6397/60/suppl/DC1
Materials and Methods
Supplementary Text
Figs. S1 to S17
Tables S1 and S2
References (*42*–*46*)

6 June 2017; resubmitted 13 November 2017
Accepted 4 May 2018
10.1126/science.aao0290

CHEMICAL PHYSICS

Imaging CF_3I conical intersection and photodissociation dynamics with ultrafast electron diffraction

Jie Yang[1,2]*, Xiaolei Zhu[2,3], Thomas J. A. Wolf[2], Zheng Li[2,4,5], J. Pedro F. Nunes[6], Ryan Coffee[2,7,8], James P. Cryan[2], Markus Gühr[2,9], Kareem Hegazy[2,8], Tony F. Heinz[2,10], Keith Jobe[1], Renkai Li[1], Xiaozhe Shen[1], Theodore Veccione[1], Stephen Weathersby[1], Kyle J. Wilkin[11], Charles Yoneda[1], Qiang Zheng[1], Todd J. Martinez[2,3]*, Martin Centurion[11]*, Xijie Wang[1]*

Conical intersections play a critical role in excited-state dynamics of polyatomic molecules because they govern the reaction pathways of many nonadiabatic processes. However, ultrafast probes have lacked sufficient spatial resolution to image wave-packet trajectories through these intersections directly. Here, we present the simultaneous experimental characterization of one-photon and two-photon excitation channels in isolated CF_3I molecules using ultrafast gas-phase electron diffraction. In the two-photon channel, we have mapped out the real-space trajectories of a coherent nuclear wave packet, which bifurcates onto two potential energy surfaces when passing through a conical intersection. In the one-photon channel, we have resolved excitation of both the umbrella and the breathing vibrational modes in the CF_3 fragment in multiple nuclear dimensions. These findings benchmark and validate ab initio nonadiabatic dynamics calculations.

Light-induced molecular dynamics usually cannot be described within the framework of the Born-Oppenheimer approximation. The picture of nuclear motion on a single adiabatic potential energy surface (PES), determined by treating the fast-moving electrons separately from the slower nuclei, breaks down wherever two or more adiabatic PESs come close in energy (*1*, *2*). At the crossing point of PESs, the degeneracy is lifted along at least two internal degrees of freedom, and the resultant conical intersection guides efficient radiationless transitions between electronic states at specific nuclear configurations (*3*). Examples of important nonadiabatic reactions include photosynthesis (*4*), retinal isomerization in vision (*5*), ultraviolet-induced DNA damage (*6*), and formation of vitamin D (*7*).

Several experimental methods have been developed for studying nonadiabatic dynamics through conical intersections (*8*–*13*). Among these, time-averaged photofragment imaging can identify distinct spectral features of nonadiabatic coupling (*8*, *9*) but does not allow the observation of dynamics in real time. Time-resolved laser spectroscopy is the most widely used real-time method for following electronic dynamics, but nuclear dynamics can only be inferred on the basis of an indirect comparison with simulated transient spectroscopic features (*11*–*14*). In addition, comparison with theoretical predictions requires explicit modeling of the probing process, which can be more complex than the nonadiabatic dynamics in question. Recent developments in both x-ray (*15*, *16*) and electron-based (*17*, *18*) time-resolved diffraction techniques open an opportunity for direct imaging of conformational changes during chemical reactions—molecular movies with atomic resolution in space and time. Despite the great importance of nonadiabatic dynamics through conical intersections, spatiotemporal resolution has not been sufficient to image a coherent nuclear wave packet traversing a conical intersection with time-resolved diffraction techniques.

The nonadiabatic transitions of molecules between different PESs are inherently quantum mechanical. A wide variety of computational methods can be used to simulate dynamics through conical intersections. For small systems, nonadiabatic dynamics can be treated with exact full quantum dynamics (*19*) and the highly accurate multiconfigurational time-dependent Hartree approximation (*20*). For larger systems, semiclassically motivated approaches such as Tully's surface hopping (*21*), Meyer-Miller formalism (*22*), or ab initio multiple spawning (AIMS) (*23*) are routinely used. Although simulations can provide rich details of the dynamics through conical intersections, nontrivial approximations at many different stages of the calculations are required, even for relatively small systems. Therefore, confirmation with experimental measurements is crucial.

Here, we report the direct imaging of both conical intersection dynamics and photodissociation dynamics of gas-phase CF_3I molecules with atomic resolution by use of ultrafast gas-phase electron diffraction (UGED). A 264.5-nm pump laser pulse initiates two photoexcitation channels: a one-photon transition to the dissociative A band and a two-photon transition to the $[5p\pi^3, {}^2\Pi_{1/2}](7s)$ (*24*) Rydberg state (referred to as 7s below) (*25*), as illustrated in Fig. 1. The adiabatic dissociation dynamics through A-band excitation of CF_3I and its analog, CH_3I, have been studied extensively (*26*–*29*). We created a multidimensional movie of the structural changes in the CF_3 fragment immediately after iodide dissociation, with a precision of ±0.01 Å in bond length and ±1° in bond angle. Various groups have studied the two-photon transition into the 7s channel by using pump-probe photoelectron and photoion spectroscopy (*25*, *30*–*32*). These studies identified the decay time scale and anisotropy of fragment ions, but the reaction pathway remained elusive. Specifically, it was only a speculation that a nearby ion-pair state might be involved in the reaction dynamics (*31*). We have mapped out the nuclear wave-packet trajectory in real space, which directly shows wave-packet bifurcation though a conical intersection. Through cross-verification with AIMS simulations, we have clarified that the σσ* state correlates asymptotically to a CF_3^+–I^- ion-pair state (referred to as IP) at large C–I separation, and that this state plays a key role in this channel. The reaction pathway is predominantly determined by the nonadiabatic coupling between IP and multiple states: the 7s and $[5p\pi^3, {}^2\Pi_{1/2}](6s)$ Rydberg states (referred to as 6s below) and valence states.

The UGED experimental setup is shown in Fig. 2A, which is described in detail in (*33*, *34*) and the supplementary materials. For diffraction pattern analysis, we used a two-dimensional (2D) Fourier transform followed by Abel inversion to convert data from momentum space to real space. This procedure returns a pair-distribution-function (PDF) that reports all the interatomic distances, as explained in Fig. 2, B to E.

The one-photon channel preferentially excites molecules with the C–I axis aligned along the laser polarization. This results in a $\cos^2\theta$ angular distribution of excited-state molecules, where θ is the angle between the C–I bond and the laser polarization (Fig. 2, B and C). In this case, C–I and F–I pairs mostly appear in the parallel direction ($PDF_{||}$), and the C–F and F–F pairs preferentially appear in the perpendicular direction ($PDF_{\perp}$). The two-photon channel corresponds to a perpendicular excitation ($\sin^4\theta$ distribution) (Fig. 2, D and E). In this case, C–I and F–I pairs preferentially appear in $PDF_{\perp}$, whereas C–F and F–F slightly favor $PDF_{||}$. This analysis simultaneously

[1]SLAC National Accelerator Laboratory, Menlo Park, CA, USA. [2]Stanford PULSE Institute, SLAC National Accelerator Laboratory, Menlo Park, CA, USA. [3]Department of Chemistry, Stanford University, Stanford, CA, USA. [4]Center for Free-Electron Laser Science, Deutsches Elektronen-Synchrotron (DESY), Hamburg, Germany. [5]Max Planck Institute for the Structure and Dynamics of Matter, Hamburg, Germany. [6]Department of Chemistry, University of York, Heslington, York, UK. [7]Linac Coherent Light Source, SLAC National Accelerator Laboratory, Menlo Park, CA, USA. [8]Department of Physics, Stanford University, Stanford, CA, USA. [9]Institut für Physik und Astronomie, Universität Potsdam, Potsdam, Germany. [10]Department of Applied Physics, Stanford University, Stanford, CA, USA. [11]Department of Physics and Astronomy, University of Nebraska–Lincoln, Lincoln, NE, USA. ***Corresponding author. Email: jieyang@slac.stanford.edu (J.Y.); todd.martinez@stanford.edu (T.J.M.); martin.centurion@unl.edu (M.C.); wangxj@slac.stanford.edu (X.W.)**

yields information about atom pair distances and their corresponding angular distribution, which is critical for assigning the reaction channels and acquiring multidimensional structural reconstructions of the target molecule during the reaction.

We first concentrated on the experimental evidence for nonadiabatic dynamics in the two-photon channel. The experimental $\Delta PDF_\perp$ as a function of pump-probe time delay is shown in Fig. 3A, with blue indicating loss and red indicating gain of atom pair distances as compared with unexcited molecules. This signal contains structural information from both two-photon (C–I and F–I pairs) and one-photon (C–F and F–F pairs) channels. They can be roughly separated by time scales: The one-photon channel dominates the signal at time delay (Δt) < 200 fs, and the two-photon channel dominates the signal at Δt > 200 fs, at which point the only contribution from the one-photon channel, once dissociation is complete, is a smoothly decaying signal due to rotational dephasing (supplementary materials). The evolution of $\Delta PDF_\perp$ is plotted in Fig. 3B at three specific pair distances: the initial C–I distance (2.14 Å), a position between the initial C–I and F–I distances (2.52 Å), and the initial F–I distance (2.90 Å). After a time delay of Δt = 100 fs, the signals corresponding to 2.14 and 2.52 Å oscillate out of phase. This result clearly indicates that the C–I bond is vibrationally excited, and the ~200-fs period matches well with the documented C–I stretching mode on the 7s surface (*35*). The 2.9-Å signal shows oscillatory decay up to Δt = 400 fs, with a surprisingly strong recurrence at Δt = 500 fs. This recurrence time scale cannot be explained by any previously reported vibrational mode on the 7s surface.

The real-space reaction trajectory is encoded in $\Delta PDF_\perp$ and can be extracted by using a ridge-detection algorithm. First, we extracted the two-photon $PDF_\perp$ by removing a common decaying signal from $\Delta PDF_\perp$. Second, we used a ridge-detection algorithm to locate 1D local maxima, or ridges. Last, we generated the reaction trajectory by connecting nearby ridges (supplementary materials). The excited-state $PDF_\perp$ is shown in Fig. 3E together with identified ridges (Fig. 3E, black dots) and trajectory (Fig. 3E, blue arrows). In this trajectory map, at least two wave-packet bifurcation events can be identified: One occurs at ~2.7 Å/300 fs, and the other at ~2.4 Å/420 fs. In addition, a two-branch crossover event can be seen at ~3.3 Å/400 fs. These features serve as strong evidence for the involvement of multiple electronic states and nonadiabatic coupling through conical intersections.

We support our experimental results by using AIMS simulations. The nuclear wave-packet density is shown in Fig. 3G projected along the C–I distance and color-coded according to diabatic state character. The color mixing reflects the composition of the population on these diabatic states. For example, orange indicates that 7s and IP states are dominantly populated, and magenta indicates a dominant population in 6s and IP. Upon excitation, the wave packet takes ~100 fs to reach the 7s-IP conical intersection seam, where electronic transitions cause the wave packet to bifurcate into two branches. The branch remaining on the 7s surface has a strong C–I stretching character; the center of the wave packet oscillates with a period of about 200 fs, with relatively little dispersion. For the branch transferred to IP, a large fraction of the wave-packet amplitude is further transferred to the 6s surface through the IP-6s conical intersection seam and returns to the Franck-Condon region at ~500 fs. The vibrational wave packet on 7s reaches the 7s-IP conical intersection seam again at ~280 and 480 fs, giving rise to the second and the third population transfer events to

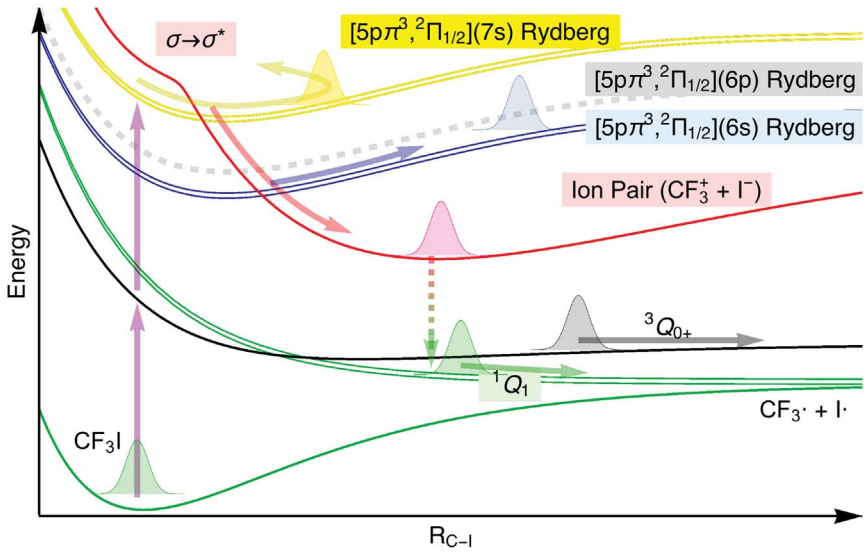

Fig. 1. Two-channel excitation in CF_3I. PES along the C–I bond length coordinate, with major states labeled and reaction pathways marked by arrows. Color coding indicates different electronic states: yellow, 7s; red, ion pair (IP); blue, 6s; green, valence open-shell states. C_{3v} symmetry is retained in this plot. The two relevant states in the A band are $^3Q_{0+}$ and $^1Q_1$ (using Mulliken notation). The 6s, 7s, and $^1Q_1$ states are of E symmetry, as indicated by two closely spaced parallel surfaces.

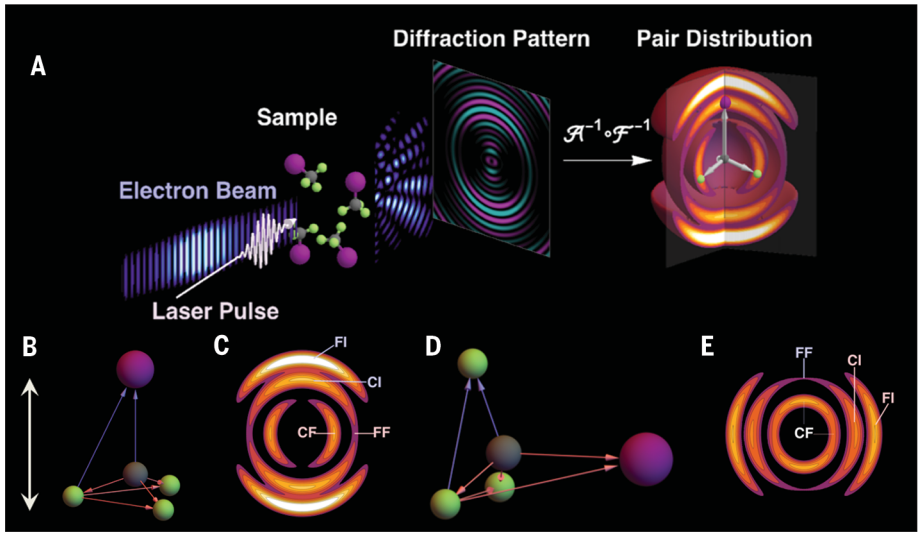

Fig. 2. Real-space analysis of diffraction patterns. (**A**) Schematic drawing of the experiment. (**B**) A model for a CF_3I molecule oriented along the laser polarization axis. (**C**) Simulated PDF for molecular ensemble with a $\cos^2\theta$ angular distribution. (**D**) A model for a CF_3I molecule oriented perpendicular to the laser polarization. (**E**) Simulated PDF for molecular ensemble with a $\sin^4\theta$ angular distribution. In (B) to (E), the laser polarization is indicated by the double-headed arrow. Gray, light green, and purple represent carbon, fluorine, and iodine, respectively.

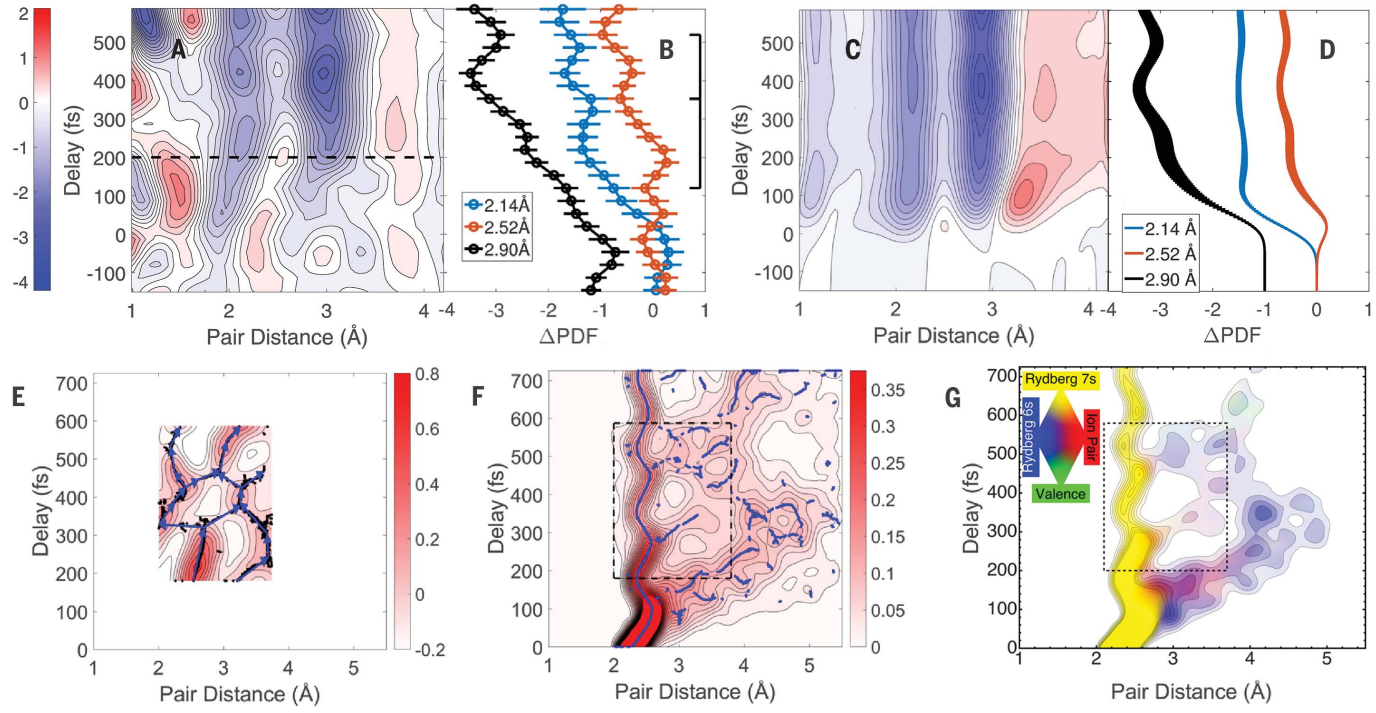

Fig. 3. Nuclear wave-packet conical intersection dynamics in the two-photon channel. (**A**) Experimental $\Delta PDF_{\perp}$, smoothed by an 80-fs Gaussian kernel. The dashed line at 200 fs shows a rough separation between contributions from the one-photon and the two-photon channels. (**B**) Experimental time evolution of $\Delta PDF_{\perp}$ at 2.14, 2.52, and 2.90 Å, error bars corresponding to 1 SD of a bootstrapped dataset (supplementary materials). A comb illustrates the first two periods of the C–I stretching vibration. (**C**) Simulated $\Delta PDF_{\perp}$ of the two-photon channel. (**D**) Simulated time evolution of $\Delta PDF_{\perp}$ at 2.14, 2.52, and 2.90 Å. Curve width represents 1 SD of a bootstrapped simulation dataset. (**E**) Two-photon $PDF_{\perp}$ generated by removing a common decaying signal from $\Delta PDF_{\perp}$. Black dots indicate identified ridges, and blue arrows indicate trajectories generated by connecting nearby ridges. The axes are the same as (F) for easy comparison. (**F**) Simulated nuclear wave packet along the C–I coordinate. Blue dots indicate identified ridges. (**G**) Simulated nuclear wave packet along the C–I coordinate as in (F), with color-coding to reflect diabatic state character, as shown in the legend. The dashed box in (F) and (G) matches the region captured in (E). The simulation results are generated by averaging over more than 2000 spawned trajectories from 50 initial conditions. In (B) and (D), the 2.90 Å curve is shifted by −1 for visibility.

the 6s surface through IP. The third outgoing wave packet on IP transiently overlaps with the returning wave packet on 6s, causing a strong recurrence of population at 500 fs at ~3Å.

The simulated $\Delta PDF_{\perp}$ of the two-photon channel is shown in Fig. 3C, and its evolution at 2.14, 2.52, and 2.90 Å is shown in Fig. 3D. Comparison between Fig. 3, A and C, and Fig. 3, B and D, shows that the ~200-fs vibration and the strong recurrence at 2.90 Å/500 fs match very well. The vibration is more pronounced in the experimental data, possibly because of various approximations adopted in the simulation. The result of the ridge-detection algorithm on the simulated nuclear wave packet is shown in Fig. 3F. The dashed box in Fig. 3F shows a very similar trajectory as that in Fig. 3E: Two wave-packet bifurcation events can be found at 2.6 Å/270 fs and 2.5 Å/460 fs, and a two-branch crossover event is seen at ~3.6 Å/420 fs. All three events are within a 0.3-Å/40-fs spatiotemporal displacement in comparison with experimental data. Comparison between Fig. 3E and Fig. 3F shows that the real-space reaction trajectory, including nonadiabatic events through conical intersections, is directly captured in the experimental data.

We next concentrated on photodissociation after single-photon excitation to the $^3Q_0$ state and explored the ensuing structural changes in multiple nuclear coordinates. After the breaking of the C–I bond, the most obvious diffraction signature is the loss of C–I and F–I atom pairs. This is reflected by the two strong bleaching bands in $\Delta PDF_{||}$ around 2.14 and 2.9 Å in Fig. 4A. The time dependence of these two bleaching signals is plotted in Fig. 4B. The C–I bleaching signal starts ~30 fs earlier than the F–I signal on account of comparatively fast recoil of the lighter carbon relative to the heavier iodine. Both the iodine and the three fluorine atoms move on a slower time scale, leading to an observable delay between the loss of C–I pair and F–I pair. The AIMS simulation shows a 16-fs separation of the two bleaching signals, which is in reasonable agreement with the experiment. The simulated $\Delta PDF_{||}$ of the one-photon channel is given in Fig. 4C. Three main features in Fig. 4A are reproduced in Fig. 4C: The two bleaching bands correspond to the loss of C–I and F–I atom pairs, and a positive feature ~1.3 Å after 300 fs is caused by the rotational dephasing of CF_3 radicals.

More details about the very early motion after photodissociation can be extracted from the C–F and F–F pairs encoded in $\Delta PDF_{\perp}$ for $\Delta t < 200$ fs. We performed a χ^2 fit in $\Delta PDF_{\perp}$ in order to extract the change of molecular structure (supplementary materials) and the fitted C–F bond length change (ΔR_{C-F}) and F–C–F bond angle change ($\Delta\angle FCF$) are given in Fig. 4D. The dynamics assembled from the data are shown in movie S1. Upon dissociation, the $\angle FCF$ immediately opens up by ~4°, followed by R_{C-F} elongating by ~0.03 Å with a ~50-fs delay.

We performed AIMS simulations on the $^3Q_0$ state. Upon dissociation, both the umbrella and the breathing vibrational modes are strongly activated with a difference in phase. The angle $\angle FCF$ immediately opens up and vibrates, whereas R_{C-F} shrinks slightly before the strong lengthening. This difference in initial motion is again caused by the recoil of the carbon atom, and when blurred by the instrumental response, results in a measurable delay between the opening of $\angle FCF$ and stretching of R_{C-F}. The red and blue lines in Fig. 4D indicate the simulated changes in R_{C-F} and $\angle FCF$ convolved with an 80-fs Gaussian cross-correlation function so as to incorporate instrumental response. The simulation predicts umbrella opening, R_{C-F} lengthening, and the delay between these, which is in agreement with the experimental observation. A small amount (10%) of intersystem crossing from the $^3Q_0$ to the $^1Q_1$ state has been reported in previous experiments (*27*), but this effect is not observable in our

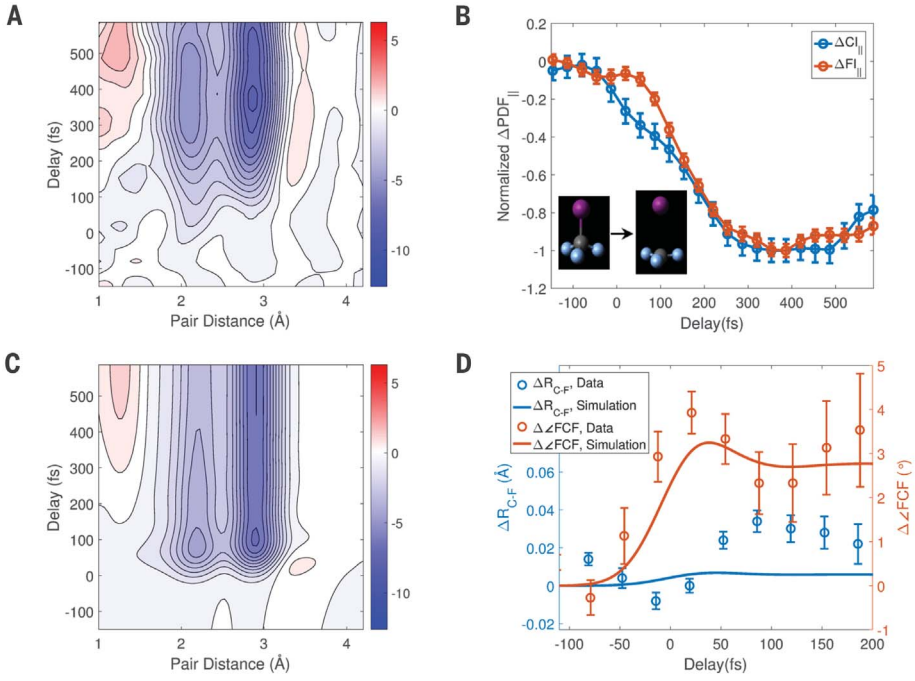

Fig. 4. Multidimensional structural evolution during photodissociation in the one-photon excitation channel. (**A**) Experimental $\Delta PDF_{||}$, smoothed by an 80-fs Gaussian kernel. (**B**) C–I and F–I bleaching signal in $\Delta PDF_{||}$. Different onset time reflects the transient recoil of the carbon atom, as shown in the inset. Error bars correspond to 1 SD of a bootstrapped dataset. (**C**) Simulated $\Delta PDF_{||}$ of the one-photon channel. (**D**) Structural evolution of CF_3 group from experiment (circles with error bars representing the standard error of the fit), plotted together with temporal-blurred structural evolution from AIMS simulation (solid curves). R_{C-F} and ∠FCF are color-coded blue and red, respectively. In (D), the vertical axis ranges for length and angle are adjusted to match each other with a 1.33-Å (ground state C–F distance) radius.

experiments owing to the spatiotemporal resolution limit.

We have shown that UGED can track a nuclear wave packet with atomic spatiotemporal resolution during nonadiabatic processes involving conical intersections, measuring multidimensional nuclear geometry changes, and simultaneously observing dynamics from different excitation channels in polyatomic molecules. In addition, UGED provides a direct probing method for nuclear degrees of freedom, complementing the standard ultrafast laser spectroscopic techniques that directly probe electronic degrees of freedom. Both the experiment and the data analysis of UGED are generally applicable to a wide range of systems in the gas phase. This approach opens the door for studying many important problems in fundamental photochemistry.

REFERENCES AND NOTES

1. G. Herzberg, *Molecular Spectra and Molecular Structure III (Polyatomic Molecules)* (1966).
2. J. Michl, V. Bonacic-Koutecky, *Electronic Aspects of Organic Photochemistry* (Wiley, 1990).
3. W. Domcke, D. R. Yarkony, H. Köppel, *Conical Intersections—Electronic Structure, Dynamics and Spectroscopy* (World Scientific Pub, 2004).
4. Y.-C. Cheng, G. R. Fleming, *Annu. Rev. Phys. Chem.* **60**, 241–262 (2009).
5. D. Polli *et al.*, *Nature* **467**, 440–443 (2010).
6. C. E. Crespo-Hernández, B. Cohen, P. M. Hare, B. Kohler, *Chem. Rev.* **104**, 1977–2019 (2004).
7. M. F. Holick, *Fed. Proc.* **46**, 1876–1882 (1987).
8. J. S. Lim, S. K. Kim, *Nat. Chem.* **2**, 627–632 (2010).
9. J. A. DeVine *et al.*, *Science* **358**, 336–339 (2017).
10. H. J. Wörner *et al.*, *Science* **334**, 208–212 (2011).
11. A. Stolow, A. E. Bragg, D. M. Neumark, *Chem. Rev.* **104**, 1719–1757 (2004).
12. J. Brazard, L. A. Bizimana, T. Gellen, W. P. Carbery, D. B. Turner, *J. Phys. Chem. Lett.* **7**, 14–19 (2016).
13. T. J. A. Wolf *et al.*, *Nat. Commun.* **8**, 29 (2017).
14. A. H. Zewail, *Angew. Chem. Int. Ed.* **39**, 2586–2631 (2000).
15. M. P. Minitti *et al.*, *Phys. Rev. Lett.* **114**, 255501 (2015).
16. J. Küpper *et al.*, *Phys. Rev. Lett.* **112**, 083002 (2014).
17. J. Yang *et al.*, *Phys. Rev. Lett.* **117**, 153002 (2016).
18. A. A. Ischenko, P. M. Weber, R. J. D. Miller, *Chem. Rev.* **117**, 11066–11124 (2017).
19. R. Chen, H. Guo, *J. Chem. Phys.* **105**, 3569–3578 (1996).
20. H.-D. Meyer, U. Manthe, L. S. Cederbaum, *Chem. Phys. Lett.* **165**, 73–78 (1990).
21. J. C. Tully, *J. Chem. Phys.* **93**, 1061–1071 (1990).
22. H.-D. Meyer, W. H. Miller, *J. Chem. Phys.* **70**, 3214–3223 (1979).
23. M. Ben-Nun, J. Quenneville, T. J. Martínez, *J. Phys. Chem. A* **104**, 5161–5175 (2000).
24. The square bracket encloses the electronic configuration, symmetry, and spin-orbit state of the cation core, and the parenthesis indicates the configuration of the Rydberg electron.
25. S. Yin *et al.*, *Chem. Phys. Lett.* **372**, 904–910 (2003).
26. L. J. Butler, *Annu. Rev. Phys. Chem.* **49**, 125–171 (1998).
27. F. Aguirre, S. T. Pratt, *J. Chem. Phys.* **122**, 234303 (2005).
28. M. Zahedi, J. Harrison, J. W. Nibler, *J. Chem. Phys.* **100**, 4043–4055 (1994).
29. A. Furlan, T. Gejo, J. R. Huber, *J. Phys. Chem.* **100**, 7956–7961 (1996).
30. H. P. Liu, Z. G. Sun, S. D. Hogan, N. Q. Lou, *Eur. Phys. J. D* **40**, 357–362 (2006).
31. W. G. Roeterdink, M. H. M. Janssen, *Phys. Chem. Chem. Phys.* **4**, 601–612 (2002).
32. W. G. Roeterdink, M. H. M. Janssen, *Chem. Phys. Lett.* **345**, 72–80 (2001).
33. J. Yang *et al.*, *Nat. Commun.* **7**, 11232 (2016).
34. S. P. Weathersby *et al.*, *Rev. Sci. Instrum.* **86**, 073702 (2015).
35. S. Eden, P. Limão-Vieira, S. V. Hoffmann, N. J. Mason, *Chem. Phys.* **323**, 313–333 (2006).
36. J. Yang *et al.*, Imaging CF3I conical intersection and photodissociation dynamics by ultrafast electron diffraction. Figshare (2018); doi:10.6084/m9.figshare.6169427.

ACKNOWLEDGMENTS

We thank G. M. Stewart from SLAC National Accelerator Laboratory for the assistance with making movie S1. **Funding:** The experimental part of this research was performed at SLAC MeV-UED, which is supported in part by the U.S. Department of Energy (DOE) Office of Basic Energy Sciences (BES) SUF Division Accelerator and Detector R&D program, the LCLS Facility, and SLAC under contracts DE-AC02-05-CH11231 and DE-AC02-76SF00515. J.Y., T.F.H., J.P.C., R.C., T.J.A.W., X.Z., and T.J.M. acknowledge support by the AMOS program within the Chemical Sciences, Geosciences, and Biosciences Division, BES of the DOEunder contract DE-AC02-76SF00515. J.P.F.N. acknowledges support by the Wild Overseas Scholars Fund of Department of Chemistry, University of York. T.J.M. acknowledges support from Office of Naval Research grant N00014-12-1-0828 and the Global Climate and Energy Project. This work used the XStream computational resources supported by the National Science Foundation Major Research Instrumentation program (ACI-1429830). Z.L. acknowledges support by the Volkswagen Foundation. M.G. is funded via a Lichtenberg Professorship of the Volkswagen Foundation. K.J.W. and M.C. were supported by the DOE Office of Science, BES under award DE-SC0014170. **Author contributions:** J.Y., T.J.A.W., J.P.F.N., J.P.C., K.H., R.L., X.S., T.V., S.W., Q.Z., and X.W. carried out the experiments; R.C., J.P.C., J.Y., T.J.A.W, and S.W. developed the laser system; M.G., J.Y., K.J., C.Y., X.S., R.L., and K.J.W. constructed and commissioned the setup for gas phase experiments; J.Y. performed the data analysis with input from M.C., T.J.A.W, J.P.C, X.Z., T.F.H., and M.G; M.C., J.Y., M.G., X.Z., and Z.L. conceived the experiment; X.Z. and T.J.M. performed the AIMS simulations; Z.L. and T.J.M performed the 3D full quantum wave-packet simulation; and J.Y., X.Z., T.J.M, M.G., M.C., and X.W. prepared the manuscript with discussion and improvements from all authors. **Competing interests:** The authors declare no competing interests. **Data and materials availability:** Both the experimental data and the simulated trajectories, after basic noise removal and statistical averaging, are available on figshare.com (*36*). The raw experimental data are archived at SLAC's centrally managed GPFS storage, and the raw simulated data are stored at T.J.M.'s group at Stanford University. All the raw data will be made available upon request.

SUPPLEMENTARY MATERIALS

www.sciencemag.org/content/361/6397/64/suppl/DC1
Materials and Methods
Supplementary Text
Figs. S1 to S17
Table S1
References (*37*–*63*)
Movie S1

14 January 2018; accepted 15 May 2018
10.1126/science.aat0049

ORGANIC CHEMISTRY

Tandem catalysis for asymmetric coupling of ethylene and enynes to functionalized cyclobutanes

Vinayak Vishnu Pagar and T. V. RajanBabu*

Transformation of simple precursors into structurally complex cyclobutanes, present in many biologically important natural products and pharmaceuticals, is of considerable interest in medicinal chemistry. Starting from 1,3-enynes and ethylene, both exceptionally inexpensive starting materials, we report a cobalt-catalyzed route to vinylcyclobutenes, as well as the further enantioselective addition of ethylene to these products to form complex cyclobutanes with all-carbon quaternary centers. These reactions can proceed in discrete stages or in a tandem fashion to achieve three highly selective carbon-carbon bond formations in one pot using a single chiral cobalt catalyst.

Development of highly efficient and enantioselective routes to chemical intermediates for the preparation of medicinally relevant compounds has been among the most active areas of research in modern organic synthesis (*1*, *2*). Especially attractive in this area are catalytic reactions that combine readily available precursors and feedstock materials, which in turn can affect the way we synthesize and manufacture fine chemicals (*3*–*10*). In this context, enantioselective methods for the synthesis of cyclobutanes have attracted substantial attention (*11*, *12*) because of their widespread occurrence in medicinally relevant natural products and pharmaceuticals (Fig. 1A) (*13*–*19*). The chiral all-carbon quaternary centers present in many of these molecules often prove challenging to install efficiently (*20*). Cyclobutane derivatives have also found broad use as intermediates for the synthesis of more advanced target structures such as stereo-defined 1,3-dienes, cyclopentanes, and ligands for catalytic applications (*21*, *22*). Most routes to cyclobutane derivatives rely on two strategies for the installation of the stereogenic centers: either enantioselective ring closure (Fig. 1, B and C), most often via [2+2] cycloadditions with few notable exceptions (*23*–*25*), or enantioselective functionalization of prochiral cyclobutane or cyclobutene intermediates (Fig. 1D). Cycloadditions of alkenes and alkynes proceed photochemically (*26*, *27*) or via Lewis acid or transition metal catalysis (*28*). Except for a single example (*29*) of an Fe(0)-catalyzed reaction between butadiene and ethylene (to yield achiral vinylcyclobutane), no use of ethylene [annual production 130 million metric tons (*30*)] for a practical synthesis of cyclobutanes has been reported. Although few enantioselective functionalizations of preformed cyclobutane derivatives using organocatalytic methods are known (*12*), the more versatile transition metal–catalyzed reactions are rare and the reported routes use precursor cyclobutane carboxylic acid derivatives that must be synthesized in several steps (*31*–*33*). Here, we report cobalt catalysis of a [2+2] cycloaddition between readily available 1,3-enynes and ethylene followed by an enantioselective hydrovinylation of the resulting vinylcyclobutene (Fig. 1E) to give highly functionalized cyclobutanes carrying a chiral, all-carbon quaternary center in the ring.

Our studies started with attempts to effect a [2+2] cycloaddition reaction between ethylene and an enyne for the synthesis of vinylcyclobutenes. The reported procedures using Zn/ZnI_2 for related processes (*34*) were limited to racemic product formation from activated and strained alkenes. For example, we found that cobalt-catalyzed cycloadditions with ethylene and a prototypical enyne **1a** with Zn/ZnI_2 led to unacceptably low yields of the product **3a** along with other contaminants including a dimeric product, **2a** (Fig. 2A, Eq. 1). A systematic optimization of the cobalt-catalyzed reaction (see table S1) led us to Lewis acids containing aluminum as the optimal activators to promote the desired reaction(s). For example, the [2+2] cycloadditions between a 1,3-enyne (**1a**) and ethylene (balloon) could be carried out under dry and oxygen-free conditions with excellent yield and selectivity at low temperatures, using a variety of chelating bis-phosphine cobalt complexes and trimethylaluminum (TMA) as the activator (Fig. 2A, Eq. 2, and table S1). At room temperature and/or slightly longer reaction times, this reaction gave not only the cyclobutene (**3a**) but also a hydrovinylated product (**4a**) with an all-carbon quaternary center. At lower temperatures and shorter reaction times, the [2+2] adduct **3a** could be isolated in excellent yield. The ligand effects in these cobalt-catalyzed reactions were striking, with complexes of 1,1-bis-diphenylphosphinomethane (dppm) and 1,2-bis-diphenylphosphinoethane (dppe) giving only modest yields of the products even after prolonged reaction times (table S1). Cobalt complexes of ligands with larger bite angles [1,3-bis-diphenylphosphinopropane (dppp), 1,4-bis-diphenylphosphinobutane (dppb), 1,5-bis-diphenylphosphinopentane (dpppent), 1,1′-bis-diphenylphosphinoferrocene (dppf), and 2,2′-bis-diphenylphosphenobinaphthyl (BINAP)] were more efficient (table S1), and (dppf)$CoCl_2$ proved exceptionally active: With 5 molar percent of the catalyst, the tandem sequence was complete in less than 2 hours to give nearly quantitative yield of **4a**. Even at –20°C, this complex was competent to carry out the initial [2+2] cycloaddition. From control experiments, it is clear that at least 0.5 equiv of TMA is needed for the reaction. The reaction was easily scaled up and an isolated yield of 81% (**4a**) was obtained on a 5-mmol scale. Further, optimizations revealed that in addition to TMA, methyl aluminoxane or Et_2AlCl (Et, ethyl) could be used as activators, and CH_2Cl_2, was the best solvent for carrying out the reaction. With the cobalt-dppf complex, traditional activators [Zn/ZnI_2, diisobutylaluminum hydride, $EtAlCl_2$, $LiEt_3BH$, or Ph_3B (Ph, phenyl)] and solvents (toluene, tetrahydrofuran, or *t*-butyl methyl ether) were unsatisfactory. No reaction ensued in the absence of either the cobalt catalyst or the activating agent.

The [2+2] cycloadditions between enynes and ethylene catalyzed by (dppf)$CoCl_2$/TMA have wide scope, as illustrated by the examples in Fig. 2B. At low temperatures and shorter periods, the reaction could be carried out selectively to obtain the cyclobutene product **3** (Fig. 2B, **3a**–**3r**). Prolonged exposure to the catalyst at room temperature led to exclusive formation of the cyclobutane **4** as a mixture of (*E*)- and (*Z*)-isomers (Fig. 2C, **4a**–**4h**). In addition to straight-chain alkene and cycloalkane substituents (**3a**–**3f**), chloroalkyl (**3g**), aromatic (**3h**–**3j**), and cyclopropyl substituents on the enyne were tolerated in these reactions. 1,3-Enynes with a terminal alkyne readily underwent the [2+2] cycloaddition but not the subsequent hydrovinylation (**3l**). Products **3m** and **3n** with additional substituents on the alkene also reacted similarly. Although unencumbered aromatic substituents on the alkynes were tolerated in the tandem reactions (e.g., **3h**→**4h**), 1-naphthyl derivative **3o** underwent only the initial [2+2]-cycloaddition, presumably because of steric effects hindering the subsequent reaction. Simple dialkyl and diaryl alkynes also underwent the cycloaddition reaction (**3p**–**3r**) with no complication from other side reactions including further hydrovinylation.

Next, we sought to develop an asymmetric version of the tandem process for synthesis of chiral cyclobutanes **4** (Fig. 3A). Early investigations with prototypical enynes **1a** and **1b** revealed that the ligands (Fig. 3D) we had successfully used in several other cobalt-catalyzed reactions (*35*), while giving high yields and excellent *E*:*Z* ratios of the products, gave unacceptable enantioselectivities (table S3, entries 1 to 14). These included the bis-diphenylphosphino ligands (*S*,*S*)-BDPP (**L1**), (*S*,*S*)-DIOP (**L2**), and JOSIPHOS (**L3a** and **L3b**), BINAP, and the bis-phospholane ligand **L4** (Fig. 3D). For a more complete list of ligands, see fig. S1. After an extensive search (*36*), we identified $CoCl_2$

Department of Chemistry and Biochemistry, The Ohio State University, Columbus, OH 43210, USA.
*Corresponding author. Email: rajanbabu.1@osu.edu

complexes of phosphinooxazoline ligands (e.g., **L8** and **L9**) (*37*) as the most suitable catalysts for this tandem sequence (tables S3 and S4). Among the activators, Et_2AlCl was found to be the most general (table S4), often giving significantly better enantioselectivities than TMA, which was used in initial screening studies. Several other activators including Zn/ZnX_2 (X = Br, I) with complexes of various cobalt halides showed poor catalytic activity (*36*). To establish the absolute configuration of the product, we synthesized an authentic sample of (*R*)-**4b** from the known ketone (*R*)-**5** (Fig. 3B) (*25*, *36*). Comparison of chiroptical properties and chromatographic behavior on chiral stationary-phase gas chromatography established the product from the enyne **1b** as (*S*)-**4b**. The configurations of the other products (Fig. 3E) were assigned by analogy.

The extreme sensitivity of this exacting tandem sequence toward the choice of ligand is apparent from the documented results (table S3) (*36*). It is notably exemplified by the bisphospholane **L4** and the phosphinooxazoline ligand **L10** (Fig. 3D). Whereas (**L4**)$CoCl_2$ was viable only for the second step (asymmetric hydrovinylation; table S4, entry 5), (**L10**)$CoCl_2$ catalyzed only the first step, the [2+2] cycloaddition (table S4, entry 14). Among the ligands examined, ligands **L8a** (entry 7) and **L8c** (entry 9) gave the best selectivities. The solid-state structure of the most versatile precatalyst complex is shown in Fig. 3C. Substituents on the *P*-aryl groups of the phosphinooxazoline ligands had only marginal effects on the selectivity except when there was an *ortho* substituent, which gave inferior results. Aliphatic substituents other than benzyl on the oxazoline moiety gave unsatisfactory results.

The optimized conditions using the readily available complex [**L8a**]$CoCl_2$ and Et_2AlCl as an activator were applied to several enynes to examine the scope and limitations of the reaction; the results are shown in Fig. 3E. Generally the reactions proceeded in very good yield and excellent enantioselectivity to give the products **4**, bearing an all-carbon quaternary center, as the (*E*)-isomer, except in the case **4a** and **4c** where less than 5% of the (*Z*)-isomers were also seen. Primary, secondary, and tertiary alkyl substituents on the alkyne were tolerated. The reaction was compatible with a chloroalkyl substituent (**4g**).

The ligand, counterion, and solvent effects documented here and in the literature for cobalt-catalyzed olefin dimerization reactions point to a Co(I)/Co(III) catalytic cycle, not much different from what we proposed recently for the dimerization of 1,3-dienes and methyl acrylate (*38*). As in the case of that heterodimerization, the tandem sequence disclosed here does not proceed with isolated Co(I) complexes. Specifically, we have attempted to carry out the reaction of **1a** with ethylene (Fig. 3A) under catalysis by isolated cobalt(I) sources [**L8a**]CoCl and [**L8a**]CoEt (*38*) in the absence of any activators and found no reaction except for decomposition of the starting materials on prolonged time. However, addition of a Lewis acid, $B(C_6F_5)_3$, resulted in modest yields (up to 50%) of the cyclobutene product **3a**. This result suggests a key role of a cationic Co(I) species in these reactions. We propose the scheme shown in Fig. 4 as a possible mechanism for the overall transformation.

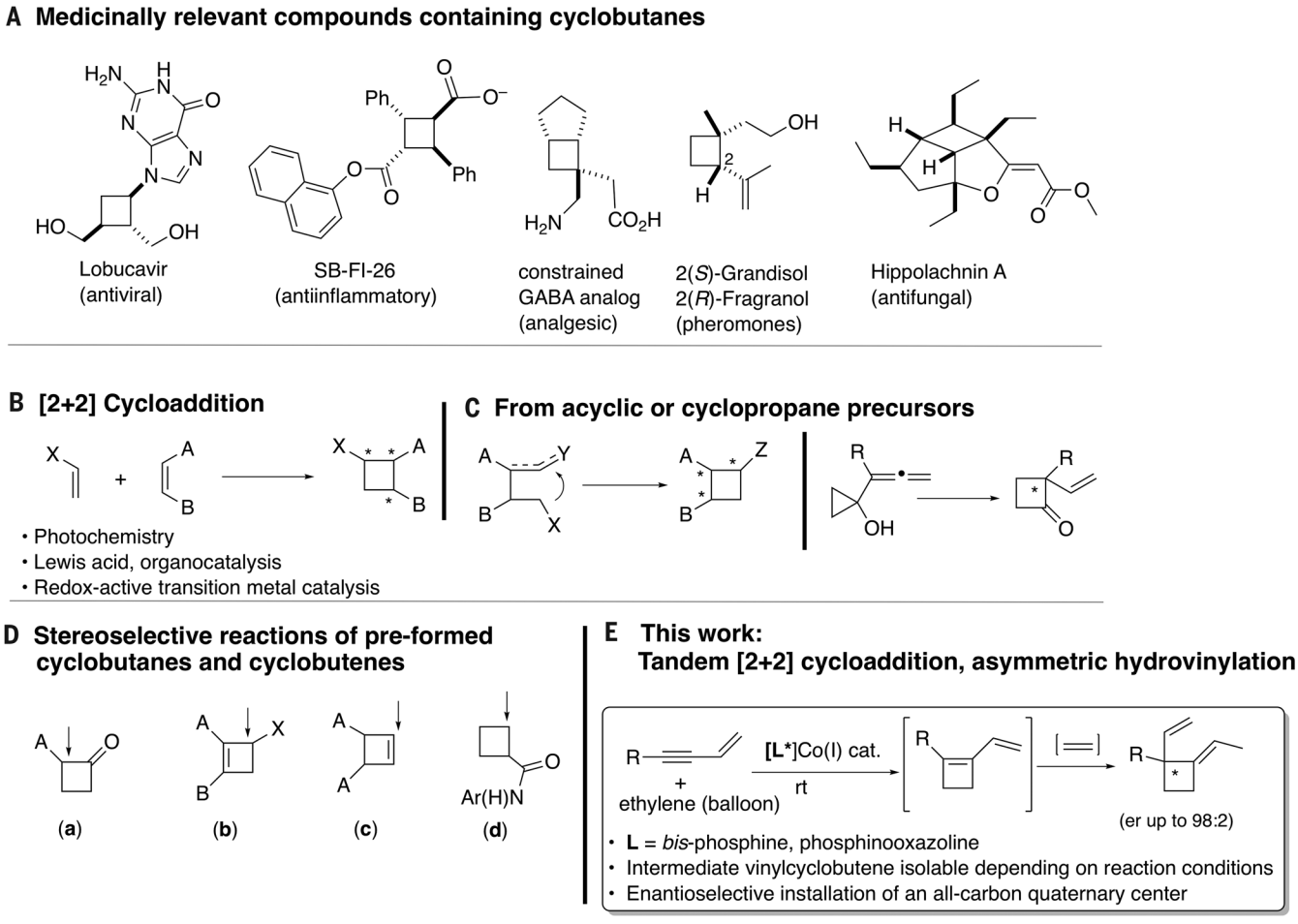

Fig. 1. Background for asymmetric cyclobutane synthesis. (**A**) Cyclobutanes in drugs and natural products. Many of these compounds have chiral all-carbon quaternary centers, which pose a major synthetic challenge. (**B** and **C**) Current methods for the synthesis of chiral cyclobutanes from acyclic precursors. (**D**) Synthesis from preformed cyclobutanes. Arrows show location of functionalization: (a) α-functionalization; (b) nucleophilic substitution; (c) desymmetrization; (d) C-H activation/functionalization. (**E**) A single cobalt catalyst for a [2+2] cycloaddition of ethylene and an enyne to vinylcyclobutene followed by a subsequent asymmetric hydrovinylation. rt, room temperature; er, enantiomeric ratio.

At the initial stage of the reaction, an oxidative dimerization of ethylene and the enyne in the coordination sphere of an activated Co(I) species gives a metallacyclopentene **6**, which undergoes reductive elimination to give the cyclobutene **3**. The subsequent hydrovinylation of a diene **3** is possibly initiated by yet another oxidative dimerization between the diene and ethylene to give the metallacycloheptene **8**. β-Hydrogen elimination and reductive elimination from the Co(III) intermediate **9** would lead to the expected product **4**. The sterically encumbered (*Z*)-allyl cobalt(III)-hydride could undergo (*Z*)/(*E*)-isomerization through an η^3-(allyl) organometallic as shown, which would result in the (*E*)-**4**-isomer

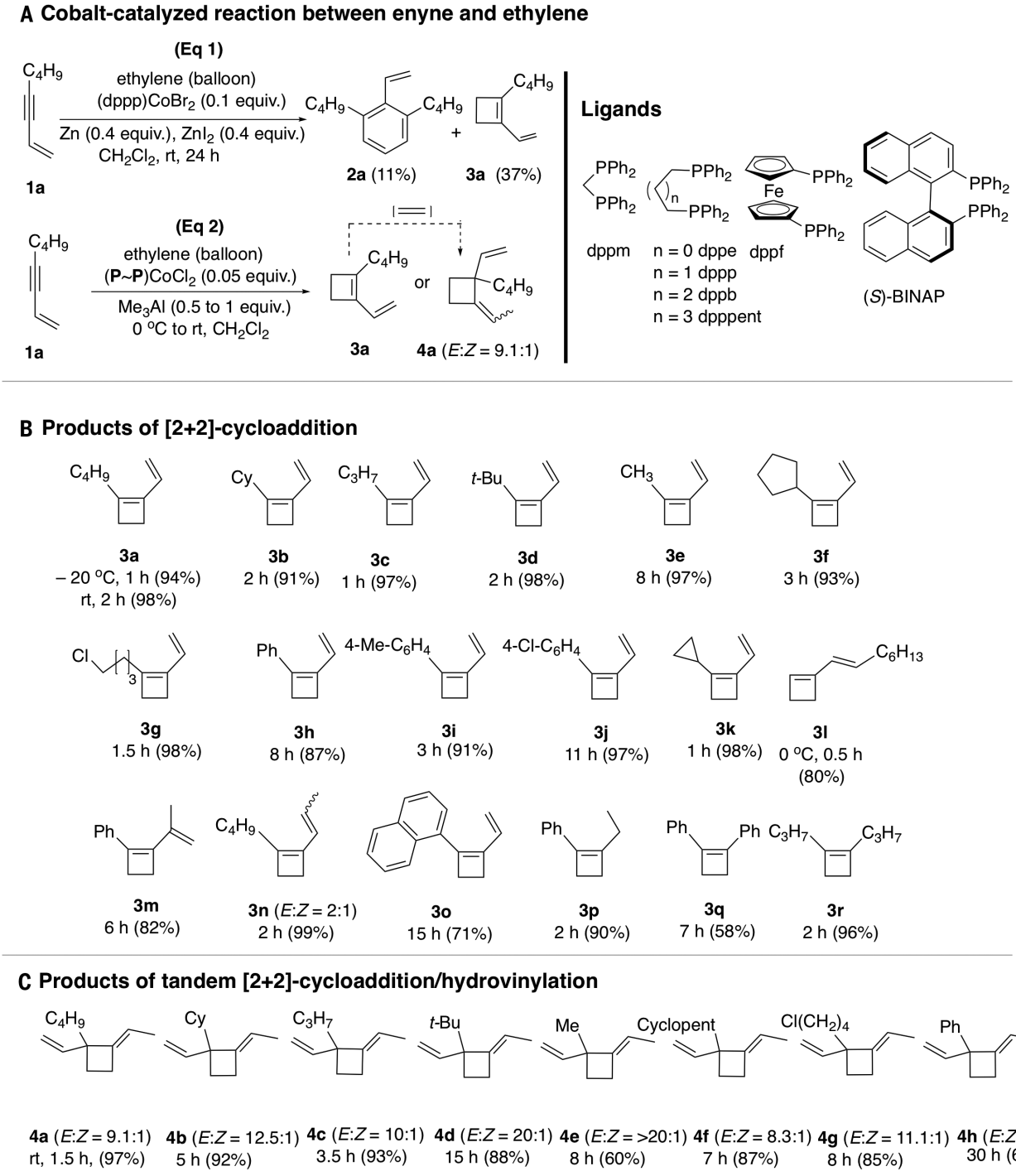

Fig. 2. Cobalt-catalyzed reaction between 1,3-enyne 1a and ethylene. (**A**) Use of aluminum-based activators markedly improves the yield, scope, and selectivity of this reaction. Typical ligands used in Eq. 2 are shown on the right. (**B**) Scope of cobalt-catalyzed [2+2] cycloaddition and subsequent hydrovinylation; dppf ligand and TMA (Eq. 2) are optimal for both the [2+2] cycloaddition and the subsequent hydrovinylation. Isolated yields are shown in parentheses. See table S2 for exact reaction conditions for the synthesis of **3** or **4**. Products (**3a**–**3r**) of the initial [2+2] cycloaddition between the enyne and ethylene could be isolated in high yield at low temperature and short reaction times. (**C**) Functionalized cyclobutanes (**4a**–**4h**) with an all-carbon quaternary center were products of the tandem sequence obtained at room temperature and longer reaction times.

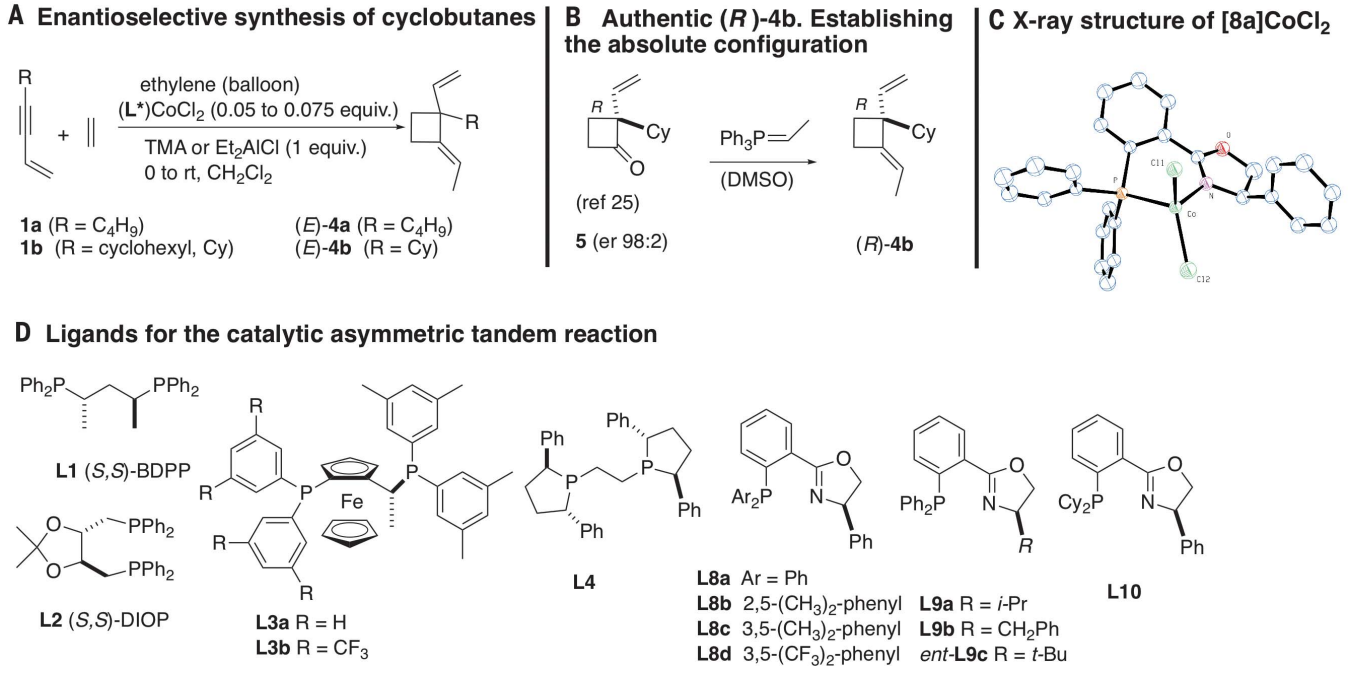

Fig. 3. Development of enantioselective version of the tandem cyclization/hydrovinylation. (**A**. Best protocol uses Et_2AlCl as activator and phosphinooxazoline ligands. See table S4. (**B**) Configuration of product established by comparison to authentic product (*R*)-**4b**. DMSO, dimethyl sulfoxide. (**C**) Characterization of the structure of the most versatile precatalyst by x-ray crystallography in solid state. (**D**) Viable ligands for the tandem sequence. For a more complete set of ligands **L1** to **L10**, see table S3. *i*-Pr, isopropyl; *t*-Bu, *tert*-butyl. (**E**) Cyclobutane products with chiral all-carbon quaternary centers. All isolated yields shown.

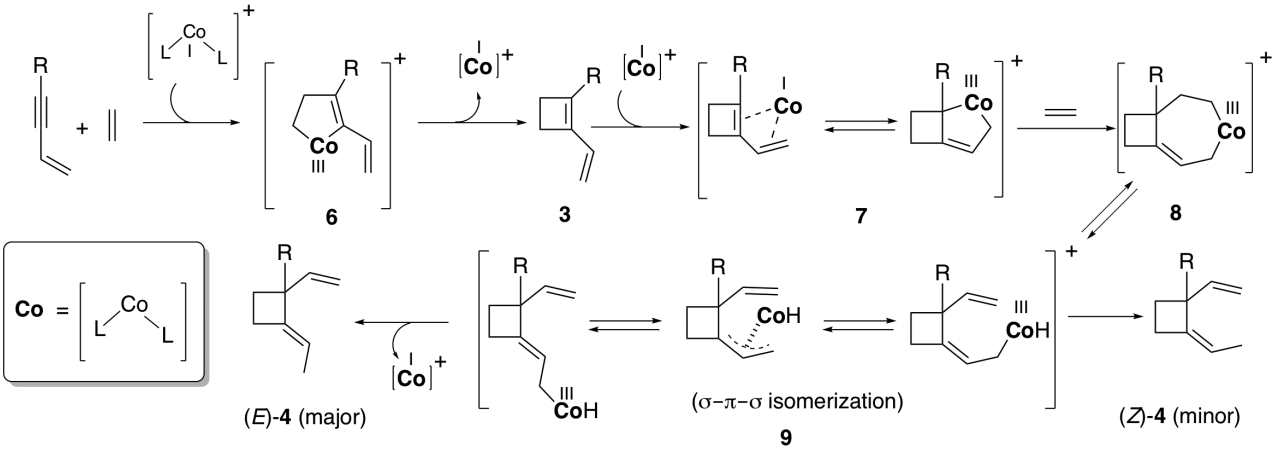

Fig. 4. Possible mechanism of tandem [2+2] cycloaddition/hydrovinylation. This mechanism invokes an oxidative dimerization via a cobaltametallacyclopentene (**6**) for the [2+2] cycloaddition and a metallacycloheptene (**8**) for the subsequent heterodimerization of the diene and ethylene.

as the major product. As expected, the isomer ratio depends on the ligands used and the nature of the substituent R.

REFERENCES AND NOTES

1. E. M. Carreira, H. Yamamoto, Eds., *Comprehensive Chirality* (Elsevier, 2012).
2. I. Ojima, Ed., *Catalytic Asymmetric Synthesis* (Wiley, ed. 3, 2010).
3. L. Bayeh, P. Q. Le, U. K. Tambar, *Nature* **547**, 196–200 (2017).
4. S. L. Shi, Z. L. Wong, S. L. Buchwald, *Nature* **532**, 353–356 (2016).
5. W. Zhang *et al.*, *Science* **353**, 1014–1018 (2016).
6. J. R. Zbieg, E. Yamaguchi, E. L. McInturff, M. J. Krische, *Science* **336**, 324–327 (2012).
7. J. Klosin, C. R. Landis, *Acc. Chem. Res.* **40**, 1251–1259 (2007).
8. G. G. Wu, F. X. Chen, K. Yong, in *Comprehensive Chirality*, E. M. Carreira, H. Yamamoto, Eds. (Elsevier, 2012), pp. 147–208.
9. T. V. RajanBabu, *Org. React.* **75**, 1–73 (2011).
10. M. Tokunaga, J. F. Larrow, F. Kakiuchi, E. N. Jacobsen, *Science* **277**, 936–938 (1997).
11. Y. Xu, M. L. Conner, M. K. Brown, *Angew. Chem. Int. Ed.* **54**, 11918–11928 (2015).
12. F. Secci, A. Frongia, P. P. Piras, *Molecules* **18**, 15541–15572 (2013).
13. V. M. Dembitsky, *Phytomedicine* **21**, 1559–1581 (2014).
14. W. T. Berger *et al.*, *PLOS ONE* **7**, e50968 (2012).
15. T. T. Wager *et al.*, *J. Med. Chem.* **54**, 7602–7620 (2011).
16. D. C. Blakemore *et al.*, *Bioorg. Med. Chem. Lett.* **20**, 461–464 (2010).
17. D. Hughes, P. Wheeler, D. Ene, *Org. Process Res. Dev.* **21**, 1938–1962 (2017).
18. J. Slade *et al.*, *Org. Process Res. Dev.* **11**, 825–835 (2007).
19. J. Singh *et al.*, *Org. Process Res. Dev.* **2**, 393–399 (1998).
20. K. W. Quasdorf, L. E. Overman, *Nature* **516**, 181–191 (2014).
21. T. Seiser, T. Saget, D. N. Tran, N. Cramer, *Angew. Chem. Int. Ed.* **50**, 7740–7752 (2011).
22. J. C. Namyslo, D. E. Kaufmann, *Chem. Rev.* **103**, 1485–1537 (2003).
23. D. K. Kim, J. Riedel, R. S. Kim, V. M. Dong, *J. Am. Chem. Soc.* **139**, 10208–10211 (2017).
24. Y. M. Wang, N. C. Bruno, A. L. Placeres, S. Zhu, S. L. Buchwald, *J. Am. Chem. Soc.* **137**, 10524–10527 (2015).
25. F. Kleinbeck, F. D. Toste, *J. Am. Chem. Soc.* **131**, 9178–9179 (2009).
26. S. Poplata, A. Tröster, Y.-Q. Zou, T. Bach, *Chem. Rev.* **116**, 9748–9815 (2016).
27. J. Du, K. L. Skubi, D. M. Schultz, T. P. Yoon, *Science* **344**, 392–396 (2014).
28. M. R. Fructos, A. Prieto, *Tetrahedron* **72**, 355–369 (2016).
29. S. K. Russell, E. Lobkovsky, P. J. Chirik, *J. Am. Chem. Soc.* **133**, 8858–8861 (2011).
30. I. Amghizar, L. A. Vandewalle, K. M. Van Geem, G. B. Marin, *Engineering* **3**, 171–178 (2017).
31. K. J. Xiao *et al.*, *J. Am. Chem. Soc.* **136**, 8138–8142 (2014).
32. C. M. Reeves, C. Eidamshaus, J. Kim, B. M. Stoltz, *Angew. Chem. Int. Ed.* **52**, 6718–6721 (2013).
33. A. Misale, S. Niyomchon, N. Maulide, *Acc. Chem. Res.* **49**, 2444–2458 (2016).
34. J. Treutwein, G. Hilt, *Angew. Chem. Int. Ed.* **47**, 6811–6813 (2008).
35. Y. N. Timsina, R. K. Sharma, T. V. RajanBabu, *Chem. Sci.* **6**, 3994–4008 (2015).
36. See supplementary materials.
37. G. Helmchen, A. Pfaltz, *Acc. Chem. Res.* **33**, 336–345 (2000).
38. S. M. Jing, V. Balasanthiran, V. Pagar, J. C. Gallucci, T. V. RajanBabu, *J. Am. Chem. Soc.* **139**, 18034–18043 (2017).

ACKNOWLEDGMENTS

We thank J. C. Gallucci for the determination of this solid-state structure. **Funding:** Supported by NIH grant R01 GM108762 and NSF grant CHE-1362095. **Author contributions:** V.V.P. carried out the experiments and helped to plan, execute, and document the experimental part. T.V.R. conceived the project and, together with V.V.P., wrote the manuscript. **Competing interests:** The authors declare no competing financial interests. **Data and materials availability:** X-ray crystallographic data for compound [**L8a**]$CoCl_2$ are available free of charge from the Cambridge Crystallographic Data Centre under CCDC 1562422. Full experimental details for the preparation of all new compounds, and their spectroscopic and chromatographic data, can be found in the supplementary materials.

SUPPLEMENTARY MATERIALS

www.sciencemag.org/content/361/6397/68/suppl/DC1
Materials and Methods
Fig. S1
Tables S1 to S5
Chromatographic and Spectroscopic Data
References (*39*–*44*)

18 March 2018; accepted 15 May 2018
10.1126/science.aat6205

OCEAN CHEMISTRY

Biological uptake and reversible scavenging of zinc in the global ocean

Thomas Weber[1]*†, Seth John[2]†, Alessandro Tagliabue[3], Tim DeVries[4]

Zinc (Zn) is a key micronutrient for marine phytoplankton, with a global distribution that is similar to silicic acid. The processes that govern this relationship, despite the very different biological cycling of Zn and silica, remain poorly understood. Here, we use diagnostic and mechanistic models to show that only a combination of Southern Ocean biological uptake and reversible scavenging of Zn onto sinking particles can explain the observations. The distinction between organic and adsorbed Zn can also reconcile the vertical distribution and mass balance of Zn isotopes, which previously appeared at odds. This holistic understanding explains the Zn deficiencies observed throughout the low-latitude ocean and implies a greater sensitivity of the marine Zn cycle to climate-driven changes in organic matter cycling than previously recognized.

Zn is the second most abundant micronutrient in phytoplankton biomass (*1*), with fundamental roles in DNA replication and transcription and as a cofactor in carbonic anhydrase and alkaline phosphatase enzymes (*2*). Since the earliest trace metal clean observations (*3*), and further exemplified by the global GEOTRACES program (*4*), a close correlation between the oceanic distributions of Zn and silicic acid [$Si(OH)_4$ (Si) hereafter] has been observed (Fig. 1A). Like Si, Zn is systematically enriched in deep water masses and deficient in intermediate water masses relative to other algal nutrients, such as phosphate (PO_4^{3-}). This results in widespread Zn scarcity throughout the low-latitude ocean, potentially affecting biological activity and plankton community structure, particularly in low PO_4^{3-} regions (*5*, *6*).

The spatial covariation of Zn and Si is surprising given their distinct biogeochemical cycles. Si is assimilated by diatoms and used to build external opal frustules, whereas Zn is assimilated by all phytoplankton taxa, with cellular quotas that scale with Zn availability up to ~10 mmol Zn per mol P (*7*). Only 1 to 3% of cellular Zn is directly incorporated into the frustules of cultured diatoms (*8*), whereas the vast majority is colocated with phosphorus (P) in internal organelles (*1*). Zn is released from decomposing organic particles at the same rate as P (*9*), and both are released shallower in the water column than Si (*10*, *11*). These observations suggest a fundamental decoupling between Zn and Si during the vertical cycling of organic matter that appears at odds with their correlated ocean concentrations (Fig. 1A). Identifying the "missing" processes that facilitate this linkage is essential to understand the climate sensitivity of the marine Zn cycle.

Recently, it has been hypothesized that the global Zn/Si covariation emerges from physical coupling in the Southern Ocean (*12*). As upwelling deep water flows northward in the region, surface Zn and Si are exhausted earlier than PO_4^{3-} (*13*). This results in a band of Zn- and Si-deficient water in the Polar Frontal Zone that is subducted northward within Antarctic Intermediate Water (AAIW), while Zn and Si remain enriched in Antarctic Bottom Water (AABW) that flows north from Antarctica at greater depth (*14*). Because these water masses ventilate much of the ocean interior, the stoichiometry of their formation regions is thought to propagate globally and overwhelm differences in organic Zn and Si cycling.

If the "Southern Ocean hypothesis" is complete, Zn concentrations must be modified very little as water masses spread northward beyond the Southern Ocean. Any significant accumulation of remineralized Zn would drive a shallower concentration maximum, making the Zn distribution diverge from Si and converge toward PO_4^{3-}.

We tested this hypothesis from an observational perspective by taking a representative observed profile of [Zn] from the North Pacific Ocean (Fig. 1B) and dividing it analytically into two components. The first component represents the quantity of Zn transported from the Southern Ocean to the North Pacific site (Fig. 1C) and was computed using a data-constrained ocean circulation model to propagate the Zn distribution of the Southern Ocean (statistically mapped south of 40°S) throughout the Pacific Ocean interior (*15*). The difference between the circulated component and the observed [Zn] then

[1]Department of Earth and Environmental Sciences, University of Rochester, Rochester, NY 14618, USA. [2]Department of Earth Sciences, University of Southern California, Los Angeles, CA 90089, USA. [3]School of Environmental Sciences, University of Liverpool, Liverpool, UK. [4]Department of Geography and Earth Research Institute, University of California, Santa Barbara, CA, USA.
*Corresponding author. Email: t.weber@rochester.edu
†These authors contributed equally to this work.

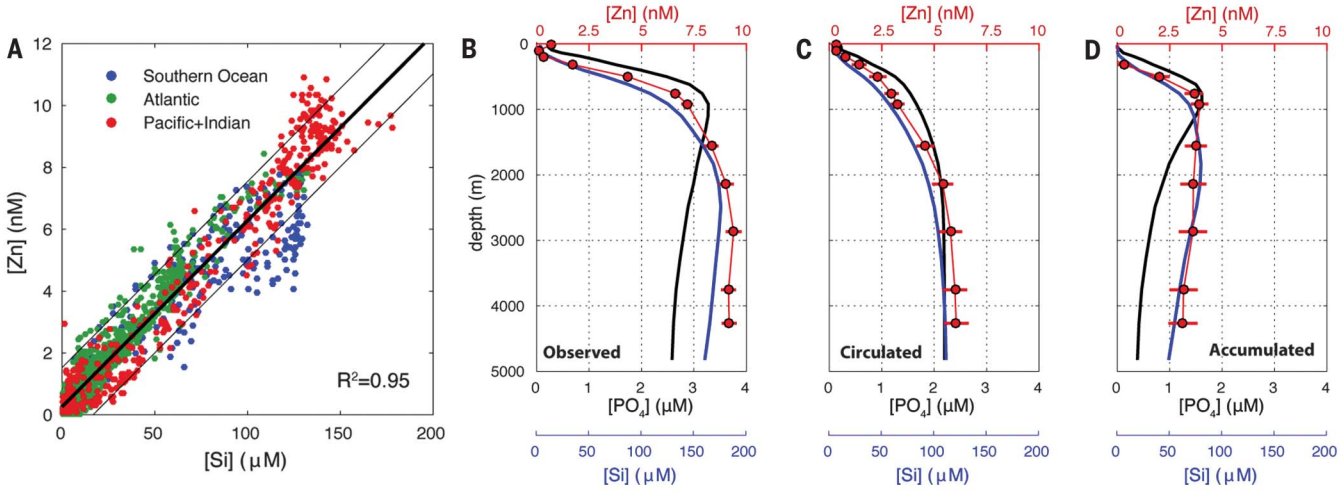

Fig. 1. Oceanic Zn distribution and components. (**A**) Scatter plot of observed Zn versus Si, with best-fit regression line (thick black line) and 95% prediction intervals (thin black lines). Zn data are from the GEOTRACES IDP 2014 and (*9*, *21*, *31*). (**B**) Observed profiles of Zn, Si, and PO_4^{3-} in the North Pacific Ocean (30°N, 140°W) (*9*). These profiles are divided into a component transported from the Southern Ocean (**C**) and a component accumulated by water masses since leaving the Southern Ocean (**D**). Uncertainty in each component was quantified using a Monte Carlo method (*15*).

quantifies the additional Zn that has accumulated during northward transport from the Southern Ocean—e.g., from remineralization or other internal cycling processes (Fig. 1D).

Our analysis reveals that only ~6 nM (~65%) of the observed Zn in the deep North Pacific is accounted for by circulation from the Southern Ocean (Fig. 1C). Therefore, ~3 nM (~35%) is unaccounted for and must have accumulated since these waters passed 40°S (Fig. 1D). Conducting a similar exercise for Si and PO_4^{3-} profiles (*15*) reveals that the accumulated Zn component does not share the same depth profile as accumulated PO_4^{3-}, which reaches a shallow peak centered around ~800 m, but rather exhibits a broad deep peak between 1000 and 3000 m, similar to accumulated Si (Fig. 1D). The same pattern is found repeating this analysis in the Tropical Pacific (fig. S1).

To further assess the role of the Southern Ocean, we developed a mechanistic model of global PO_4^{3-}, Zn, and Si cycling embedded within our data-constrained circulation model (*15*). Surface [PO_4^{3-}] and [Si] are restored toward observations to quantify the export of particulate organic P and biogenic Si, which remineralize over depth scales that were optimized to best match observed global PO_4^{3-} and Si distributions (fig. S2 and table S1). Zn complexation by organic ligands is represented by an equilibrium model (*16*), and biological uptake of uncomplexed Zn is coupled to PO_4^{3-} in a ratio that increases with [Zn] (*7*). Particulate organic Zn is assumed to remineralize over the same depth scale as organic P. Four parameters governing Zn complexation and uptake were optimized to best fit a range of observational constraints (*4*), including a Southern Ocean surface [Zn] transect and profiles from the Atlantic, Pacific, Indian, and Southern Oceans (fig. S3 and table S2). The optimization procedure is an important facet of our approach, allowing us to interpret remaining model-data discrepancies as genuine model deficiencies, rather than poor parameter choices.

Our optimized model produces a near-linear relationship between Zn and Si (Fig. 2A) when Southern Ocean surface [Zn] is accurately reproduced (Fig. 2B). However, the correlation (R^2 = 0.86) is weaker than observed (R^2 = 0.95) and systematic biases are evident, contrary to results of a previous modeling study (*12*). Modeled [Zn] is overestimated at low Si concentrations in intermediate water masses (Fig. 2, A and C) and underestimated in deep waters of the Pacific and Indian Oceans (Fig. 2C and fig. S3). Furthermore, our model requires Zn:P export ratios approaching 20 mmol:1 mol in order to sufficiently deplete [Zn] in the Southern Ocean (Fig. 2B and fig. S4), which exceeds the observed biological range (*1*).

Taken together, our diagnostic results and mechanistic modeling demonstrate that Southern Ocean uptake and circulation are important but insufficient factors to explain the global Zn distribution. Soft organic tissue cycling causes Zn to accumulate too shallowly in the water column, indicating that an additional process is required to explain the deep accumulation pattern

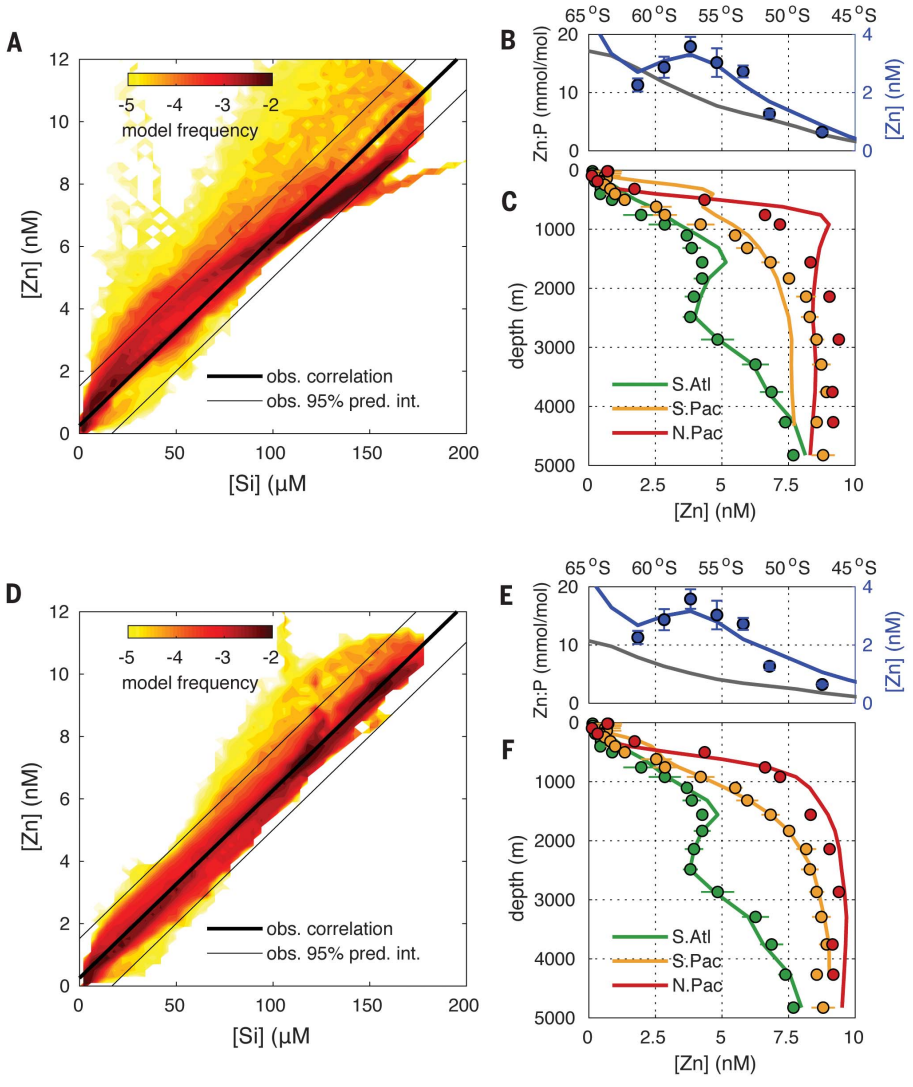

Fig. 2. Mechanistic models of Zn cycling. (**A** to **C**) Model representing the Southern Ocean Zn-Si hypothesis, with optimized surface Zn uptake. (**D** to **F**) Model that resolves reversible scavenging of Zn onto sinking particles. Models are evaluated against the observed Zn versus Si correlation [(A) and (D)], Southern Ocean surface distribution [(B) and (E)], and Atlantic and Pacific profiles [(C) and (F)]. In (A) and (D), the color map shows the log fraction of the ocean volume with [Si] and [Zn] that fall within 1 μM by 0.1 nM bins. In (B), (C), (E), and (F), dots are observed [Zn] ± 1 S.D. (*4*, *9*, *13*, *31*) and lines are corresponding model results, averaged within small spatial regions (*15*).

(Fig. 1D). Model sensitivity tests indicate that neither hydrothermal Zn inputs (*17*) nor spatially varying remineralization scales of organic matter (*18*) can resolve the discrepancy (fig. S5). A candidate hypothesis, supported by laboratory culture studies, is that Zn is reversibly "scavenged" (adsorbed) onto sinking organic particles, enhancing its flux to the deep ocean relative to nonscavenged elements like P (*9*).

We investigated whether a second model configuration that explicitly includes reversible scavenging (*15*) can reconcile the Si-like distribution of Zn with its P-like remineralization behavior. The model computes the equilibrium partitioning of uncomplexed Zn between the dissolved phase and a phase adsorbed to sinking particulate organic matter based on a globally uniform partition coefficient (*19*) and does not consider potential adsorption to mineral phases. Following parameter optimization, this model successfully reproduces the observed tight correlation between Zn and Si (R^2 = 0.98) without leaving systematic biases (Fig. 2D). Although Zn concentrations in the surface Southern Ocean remain relatively unchanged from the original model (Fig. 2E), scavenging redistributes Zn from intermediate to deep water masses as they age, bringing its simulated depth structure in line with observations (Fig. 2F and fig. S3). This occurs even though only a small fraction of total Zn is adsorbed onto particles: ~0.5% in the upper ocean and <0.01% in the deep ocean (fig. S6). Overall, resolving reversible scavenging reduces the root mean square error between simulated

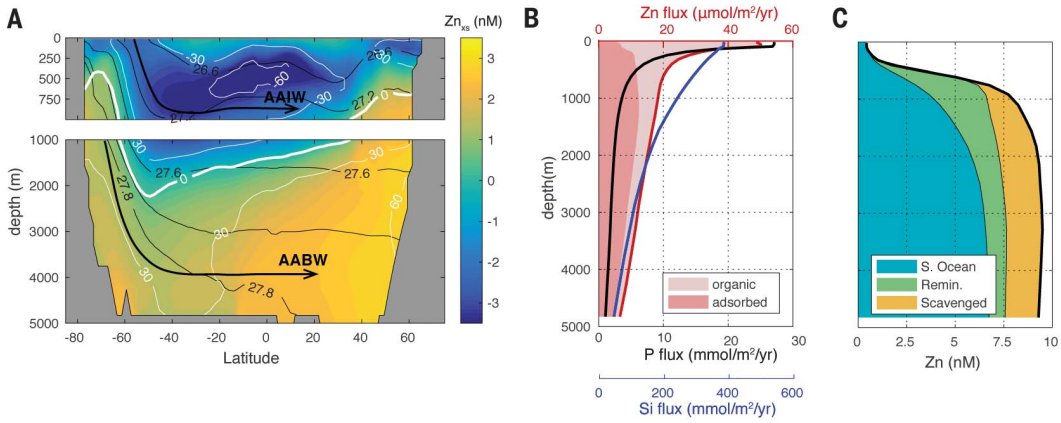

Fig. 3. Holistic understanding of the model Zn cycle. (**A**) The stoichiometric tracers Zn_{xs} (color map) and Si_{xs} (white contours) measure the excess or deficit of Zn and Si relative to PO_4^{3-} and illustrate the relationship between the three nutrient cycles in our model. Both tracers show distinctive signatures circulated by AAIW and AABW from the Southern Ocean and similar modifications along isopycnals outside of the Southern Ocean. (**B**) Vertical flux profiles of P, Si, and Zn. Organic Zn attenuates over depth like P, but adsorbed and organic components sum to a flux profile that is more similar to Si. (**C**) Simulated North Pacific Zn (site analyzed in Fig. 1) is divided into a component circulated from the Southern Ocean and components accumulated from remineralization and scavenging.

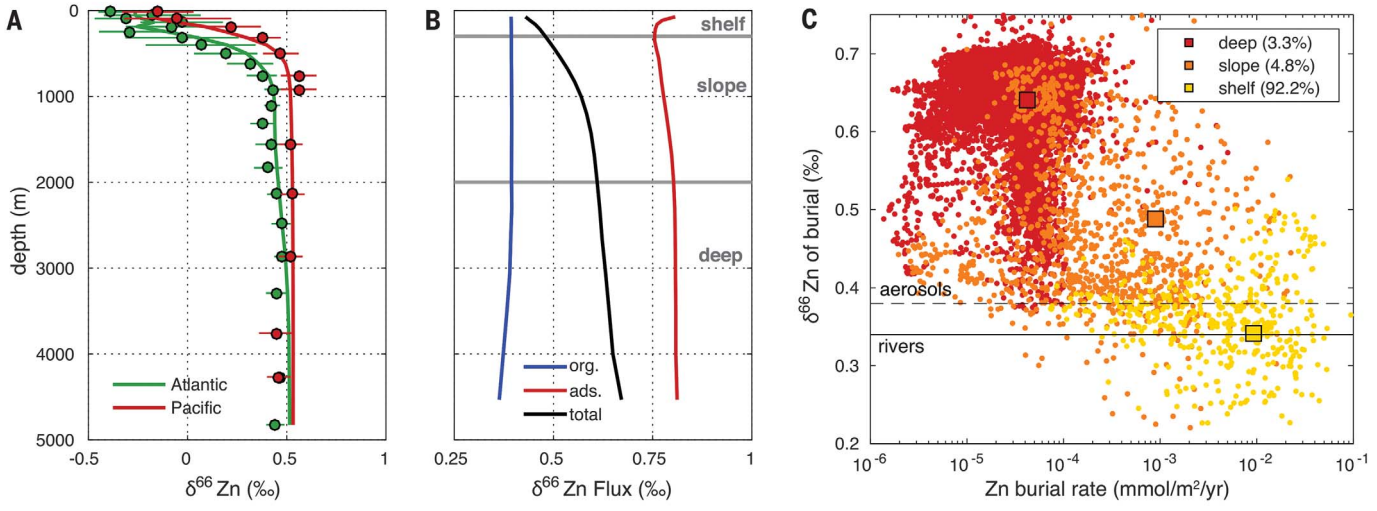

Fig. 4. Zn isotope distribution and mass balance. (**A**) Model fit to observed δ^{66}Zn profiles in the Atlantic and Pacific Oceans. (**B**) Simulated isotopic composition of organic, adsorbed, and total particulate fluxes. The decrease in δ^{66}Zn toward the surface in (A) results from the flux of heavy adsorbed Zn to the deep ocean. (**C**) Relationship between Zn burial rate in sediments, computed offline from high-resolution topography and estimates of carbon burial (*15*), and δ^{66}Zn of the flux to seafloor. Square symbols integrate across shelf (0 to 200 m), slope (200 to 2000 m), and deep ocean (>2000 m) regions. Most burial occurs in shallow shelf regions, where light organic Zn dominates the sinking flux (B), allowing the total δ^{66}Zn sink to match the source from aerosol and river inputs.

and observed Zn by a factor of ~2 relative to the original model (0.59 nM versus 1.03 nM) (table S3). Additionally, inclusion of scavenging permits realistic surface depletion without the excessive Zn:P export ratios seen in our earlier model (Fig. 2E and fig. S4). Model sensitivity tests demonstrate that reversible scavenging must be active throughout the water column, and not confined to low-oxygen waters, to best match the observations (fig. S5). This suggests that the scavenging mechanism is not related to trace metal sulfide precipitation in particle microenvironments (*20*), which might be more important at smaller scales and for other metals, such as cadmium.

By linking Southern Ocean water masses with reversible scavenging, our model provides a holistic understanding of the oceanic Zn cycle and its relationships to Si and PO_4^{3-}. The roles of physical and biogechemical processes can be isolated using stoichiometric tracers that measure the excess or deficit of Zn and Si relative to PO_4^{3-}. Here, we define $Zn_{xs} = [Zn]\text{-}R_{Zn:P}[PO_4^{3-}]$ and $Si_{xs} = [Si]\text{-}R_{Si:P}[PO_4^{3-}]$, where $R_{Zn:P}$ and $R_{Si:P}$ represent mean-ocean elemental ratios. Nutrient utilization in the Southern Ocean surface produces water masses with distinct stoichiometries that are conserved by circulation: AAIW carries strongly negative Zn_{xs} (–1.5 nM) and Si_{xs} (–40 μM) into low latitudes, whereas deeper AABW carries weakly positive values (Fig. 3A).

Modification of these tracers along circulation pathways reflects biogeochemical processes that decouple Zn and Si from PO_4^{3-}. Si_{xs} decreases in AAIW as it ages equatorward and increases in AABW (Fig. 3A), reflecting remineralization of P in intermediate waters and excess Si remineralization in the deep ocean (Fig. 3B) (*11*). Zn_{xs} undergoes almost identical modifications (Fig. 3A) but via a different set of mechanisms. In the upper ~400 m, where organic Zn remineralizes rapidly like P, net adsorption transfers dissolved Zn onto particles (Fig. 3B), constituting a sink of Zn_{xs}. Deeper, the equilibrium between adsorbed and dissolved Zn shifts due to lower particle concentrations, driving net desorption and accumulation of Zn, relative to PO_4^{3-} in AABW (Fig. 3A). Outside the Southern Ocean, the combined flux profiles of organic and adsorbed Zn are more similar to Si than P, with ~30% of Zn transferred from the base of the euphotic zone to 2000 m, compared with ~40% and ~5% for Si

and P, respectively (Fig. 3B). By the time AABW reaches the North Pacific Ocean, the accumulation of desorbed Zn adds ~2 nM to the concentration leaving the Southern Ocean in AABW, compared with ~1 nM accumulated from remineralization (Fig. 3C), demonstrating that reversible scavenging is a critical process explaining the deep accumulation of Zn (Fig. 1D).

In our optimized model, removing the reversible scavenging process and preventing elevated uptake of Zn in the Southern Ocean degrade the fit to observations to a similar degree (*15*). This suggests that both processes are equally responsible for decoupling the Zn distribution from other soft-tissue nutrients and its global similarity to Si. Nevertheless, in young water masses that have not undergone extensive scavenging, shallow remineralization of Zn can locally decouple its concentration from Si (fig. S3), as observed in the subarctic North Pacific Ocean (*21*), although the mechanism for this decoupling was not previously clear.

The existence of distinct organic and adsorbed sinking Zn phases might also resolve an apparent conflict between the vertical distribution of Zn isotopes and the isotopic mass balance of the ocean as a whole. In the low-latitude ocean, the ratio of ^{66}Zn to ^{64}Zn (expressed as δ^{66}Zn) decreases toward the surface, implying preferential removal of heavy isotopes from the upper ocean and their transfer to depth (Fig. 4A) (*22*). However, light isotopes must be preferentially buried from the ocean as a whole to balance fluvial, atmospheric, and hydrothermal sources that are isotopically light [0.3 to 0.35 per mil (‰)] relative to mean-ocean Zn (~0.5‰) (*23*).

We expanded our global model to distinguish the cycles of ^{66}Zn and ^{64}Zn—which are fractionated during biological uptake, complexation, and scavenging (*15*)—and the magnitude of each fractionation effect was optimized within reasonable ranges to match observed δ^{66}Zn profiles (Fig. 4A and fig. S7). In the optimal model, ^{66}Zn is preferentially adsorbed onto sinking particles due to its weaker binding by ligands, consistent with culture studies (*9*) and new observations from the subtropical Pacific (*15*). This fractionation is strongest in the upper 1000 m where ligand binding is most complete (figs. S6 and S8). The flux of heavy adsorbed Zn from the upper ocean then leaves a light δ^{66}Zn signature that is transferred into sinking organic matter when phytoplankton consume residual Zn in the surface (Fig. 4B and fig. S8). The δ^{66}Zn of the sinking Zn flux is therefore light (<0.5‰) in the upper ~500 m, where organic Zn dominates, and heavy (>0.5‰) in deeper layers where the adsorbed flux is dominant (Fig. 4B). Because particulate matter is disproportionately buried on shallow continental shelves (*24*), our model predicts a negative relationship between δ^{66}Zn flux to the seafloor and burial rate (Fig. 4C and fig. S9) (*15*), consistent with observations of light Zn burial on Pacific shelves (*25*). Integrated globally, this yields a δ^{66}Zn sink of 0.36 ± 0.04‰, which is in balance with source estimates (*23*).

Our findings have important implications for Zn biogeochemical cycling in past and future oceans. The geological record exhibits millennial cycles (*26*, *27*) and billion-year trends (*28*) in δ^{66}Zn, currently attributed to Zn speciation and changes in biological productivity. Our findings suggest that changes in the relative burial of adsorbed and organic Zn are an important mechanism controlling mean-ocean δ^{66}Zn on geological time scales. In the modern ocean, deep remineralization of Si and reversible scavenging of Zn produce similar accumulation patterns of the two nutrients, but these processes likely have different sensitivities to ocean change. Whereas Si cycling will respond to changing ocean temperature and pH (*29*), Zn will be sensitive to projected variations in organic carbon fluxes (*30*) that underpin Zn scavenging, potentially decoupling the Zn and Si supply to low-latitude phytoplankton communities.

REFERENCES AND NOTES

1. B. S. Twining, S. B. Baines, *Ann. Rev. Mar. Sci.* **5**, 191–215 (2013).
2. F. M. M. Morel *et al.*, *Nature* **369**, 740–742 (1994).
3. K. W. Bruland, G. A. Knauer, J. H. Martin, *Nature* **271**, 741–743 (1978).
4. E. Mawji *et al.*, *Mar. Chem.* **177**, 1–8 (2015).
5. C. Mahaffey, S. Reynolds, C. E. Davis, M. C. Lohan, *Front. Mar. Sci.* **1**, 73 (2014).
6. Y. Shaked, Y. Xu, K. Leblanc, F. M. M. Morel, *Limnol. Oceanogr.* **51**, 299–309 (2006).
7. W. G. Sunda, S. A. Huntsman, *Limnol. Oceanogr.* **37**, 25–40 (1992).
8. M. J. Ellwood, K. Hunter, *Limnol. Oceanogr.* **45**, 1517–1524 (2000).
9. S. G. John, T. M. Conway, *Earth Planet. Sci. Lett.* **394**, 159–167 (2014).
10. B. Twining *et al.*, *Limnol. Oceanogr.* **59**, 689–704 (2014).
11. M. Holzer, F. W. Primeau, T. DeVries, R. Matear, *J. Geophys. Res. Oceans* **119**, 313–331 (2014).
12. D. Vance *et al.*, *Nat. Geosci.* **10**, 202–206 (2017).
13. Y. Zhao, D. Vance, W. Abouchami, H. J. W. de Baar, *Geochim. Cosmochim. Acta* **125**, 653–672 (2014).
14. J. L. Sarmiento, N. Gruber, M. A. Brzezinski, J. P. Dunne, *Nature* **427**, 56–60 (2004).
15. Materials and methods are available as supplementary materials.
16. T. Kim, H. Obata, Y. Kondo, H. Ogawa, T. Gamo, *Mar. Chem.* **173**, 330–341 (2015).
17. S. Roshan, J. Wu, W. Jenkins, *Mar. Chem.* **183**, 25–32 (2016).
18. T. Weber, J. A. Cram, S. W. Leung, T. DeVries, C. Deutsch, *Proc. Natl. Acad. Sci. U.S.A.* **113**, 8606–8611 (2016).
19. M. P. Bacon, R. F. Anderson, *J. Geophys. Res.* **87**, 2045–2056 (1982).
20. D. J. Janssen *et al.*, *Proc. Natl. Acad. Sci. U.S.A.* **111**, 6888–6893 (2014).
21. D. J. Janssen, J. T. Cullen, *Mar. Chem.* **177**, 124–133 (2015).
22. T. M. Conway, S. G. John, *Global Biogeochem. Cycles* **28**, 1111–1128 (2014).
23. S. H. Little, D. Vance, C. Walker-Brown, W. M. Landing, *Geochim. Cosmochim. Acta* **125**, 673–693 (2014).
24. J. P. Dunne, J. L. Sarmiento, A. Gnanadesikan, *Global Biogeochem. Cycles* **21**, GB4006 (2007).
25. S. H. Little, D. Vance, J. McManus, S. Severmann, *Geology* **44**, 207–210 (2016).
26. S. Pichat, C. Douchet, F. Albarede, *Earth Planet. Sci. Lett.* **210**, 167–178 (2003).
27. M. Kunzmann *et al.*, *Geology* **41**, 27–30 (2013).
28. M. L. Pons *et al.*, *Geobiology* **11**, 201–214 (2013).
29. M. A. Brzezinski, D. M. Nelson, *Deep Sea Res. Part I Oceanogr. Res. Pap.* **42**, 1215–1237 (1995).
30. L. Bopp *et al.*, *Biogeosciences* **10**, 6225–6245 (2013).
31. S. G. John, J. Helgoe, E. Townsend, *Mar. Chem.* **2017**, 10.1016/j.marchem.2017.06.003 (2017).

ACKNOWLEDGMENTS

We thank R. Bundy and D. Repeta for providing organic Zn samples from the North Pacific for isotope analysis. **Funding:** This work was supported by NSF (OCE-1658042 to T.W., OCE-1649439 and OCE-1658436 to S.J., and OCE-1658392 to T.D.), NERC (NE/N001079/1 to A.T.), and the Simons Foundation (329108 to S.J.). **Author contributions:** T.W. and S.J. designed the study and developed the biogeochemical model. T.D. developed the ocean circulation model. T.W., S.J., and A.T. interpreted the model output. All authors contributed to writing the paper. **Competing interests:** None declared. **Data and materials availability:** Data used in this paper are presented in the supplementary materials or available from the GEOTRACES archive (www.geotraces.org/). The ocean circulation model is available from www.geog.ucsb.edu/~devries/Home/Models.html.

SUPPLEMENTARY MATERIALS

www.sciencemag.org/content/361/6397/72/suppl/DC1
Materials and Methods
Supplementary Text
Figs. S1 to S9
Tables S1 to S3
References (*32*–*52*)

1 September 2017; accepted 11 May 2018
10.1126/science.aap8532

NEUROSCIENCE

Regulation of feeding by somatostatin neurons in the tuberal nucleus

Sarah Xinwei Luo[1]*, Ju Huang[2]*, Qin Li[1,3]*, Hasan Mohammad[1], Chun-Yao Lee[1], Kumar Krishna[4], Alison Maun-Yeng Kok[1], Yu Lin Tan[1], Joy Yi Lim[1], Hongyu Li[1], Ling Yun Yeow[1], Jingjing Sun[2], Miao He[5], Joanes Grandjean[1], Sreedharan Sajikumar[4], Weiping Han[1], Yu Fu[1,4]†

The tuberal nucleus (TN) is a surprisingly understudied brain region. We found that somatostatin (SST) neurons in the TN, which is known to exhibit pathological or cytological changes in human neurodegenerative diseases, play a crucial role in regulating feeding in mice. GABAergic tuberal SST (^{TN}SST) neurons were activated by hunger and by the hunger hormone, ghrelin. Activation of ^{TN}SST neurons promoted feeding, whereas inhibition reduced it via projections to the paraventricular nucleus and bed nucleus of the stria terminalis. Ablation of ^{TN}SST neurons reduced body weight gain and food intake. These findings reveal a previously unknown mechanism of feeding regulation that operates through orexigenic ^{TN}SST neurons, providing a new perspective for understanding appetite changes.

The nucleus tuberalis lateralis (NTL; lateral tuberal nucleus) in the hypothalamus is revealed by the "lateral eminences on the ventral surface of the tuber cinereum" in humans and primates (*1*), but the homologous structure in other animals is less well defined, and knowledge about the NTL is scarce (*2*). Pathological or cytological changes in the NTL have been observed in several neurodegenerative and neurological diseases (*2*–*8*). Deep hypothalamic lesions that probably went into the NTL in human patients have led to hypophagia, and NTL pathology has been correlated with cachexia (*4*, *9*–*11*), suggesting that the NTL plays a role in the regulation of feeding, but this notion has never been tested. The human NTL neighbors the tuberomammillary nucleus (TMN) and is marked by dense staining with somatostatin (SST) antibody (*12*). We therefore searched for SST-positive neurons in the mouse tuberal nucleus (TN) and studied their potential role in feeding regulation.

We bred SST-Cre mice with Ai14 reporter mice (*13*), and SST neurons thus were labeled with the red fluorescent protein tdTomato. In the mouse hypothalamus, SST neurons appeared in a scattered distribution in the medial-dorsal hypothalamus and in enriched clusters in the ventral hypothalamus. Specifically, SST neurons were prevalent in the arcuate area (we refer to these as ^{Arc}SST neurons) and the TN (^{TN}SST neurons). The arcuate cluster extended slightly anteriorly, and the TN cluster extended slightly posteriorly (Fig. 1A). The arcuate nucleus plays a critical role in feeding regulation and contains well-studied orexigenic agouti-related peptide (AgRP) neurons, tyrosine hydroxylase (TH)–positive neurons, and anorexic proopiomelanocortin (POMC) neurons (*14*–*16*). Immunohistochemistry showed that the ^{Arc}SST neurons were distinct from POMC- and TH-positive neurons but exhibited minor overlap (9.04 ± 2.16% of ^{Arc}SST neurons; $n = 3$ mice) with AgRP neurons (Fig. 1B) (*17*). The ^{TN}SST neurons were distinct and spatially segregated from lateral hypothalamic orexin- and melanin-concentrating hormone (MCH)–positive neurons (Fig. 1C), both of which have been implicated in feeding and metabolic regulation (*18*, *19*). The ^{TN}SST did not show obvious overlap with histaminergic neurons [revealed by staining for histidine decarboxylase (HDC)], the key neuronal subtype in the nearby TMN region (*20*) (Fig. 1C and fig. S1). Therefore, as in humans, the TN in mouse is marked by a dense cluster of SST-positive neurons, which constitute a hypothalamic neuronal subtype that is distinct from the neurons currently known to support feeding and metabolic regulation. Either overnight fasting or intraperitoneal (i.p.) injection of the hunger hormone, ghrelin—the levels of which are increased by the hunger state (*21*)—induced robust expression of the immediate early gene *c-Fos* in ^{TN}SST neurons (Fig. 1, D to G, and fig. S2), but not in ^{Arc}SST neurons (fig. S3). Further analysis showed no obvious difference in the percentage of c-Fos–positive ^{TN}SST neurons at different positions, indicating a homogeneous activation of ^{TN}SST neurons (fig. S2). In acute slices of SST-Cre::Ai14 mice, bath application of ghrelin excited 7 out of 17 ^{TN}SST neurons, as determined by whole-cell recording (Fig. 1, H and I). Under the presence of synaptic blockers, 6 out of 18 ^{TN}SST neurons were excited by ghrelin under current-clamp conditions without the injection of depolarizing current, and 7 out of 16 ^{TN}SST neurons were excited by ghrelin with current injection for increasing baseline firing (fig. S4, A to F). We further characterized the ^{TN}SST neurons by staining mRNA for ghrelin receptor (Ghsr), using fluorescence in situ hybridization (FISH); we found that 17.6% (120/682) of ^{TN}SST neurons were Ghsr-positive, with the most caudal TN containing fewer Ghsr-positive SST neurons (fig. S4, G and H). Ghsr-postive and Ghsr-negative ^{TN}SST neurons were similarly activated by overnight fasting (fig. S4, I and J), indicating that both populations were involved in feeding regulation.

We next injected Cre recombinase–inducible adeno-associated viruses (AAVs) expressing chemogenetic or optogenetic effectors into the TN of SST-Cre mice (Fig. 2) and analyzed their eating behavior (fig. S5). After the mice habituated in behavioral chambers for 4 days (fig. S6A), chemogenetic activation of ^{TN}SST neurons by expressing the excitatory DREADD (designer receptor exclusively activated by designer drug) hM3D and injection of CNO in the late morning (11 a.m.) dramatically promoted food consumption within the subsequent 3 hours and significantly enhanced eating time and frequency (Fig. 2, A to E). Similar results were found when CNO was injected at 5 p.m., when mice were more spontaneously active (fig. S6, B and C). No effect of CNO on eating behavior was observed in control mice with green fluorescent protein (GFP) expressed in ^{TN}SST neurons (Fig. 2, B to E, black traces). After expressing Cre-dependent channelrhodopsin (ChR2) in ^{TN}SST neurons, we characterized the optogenetic response of ^{TN}SST neurons in acute slices (fig. S7, A to F) and used a light intensity that can reliably excite ^{TN}SST neurons for in vivo experiments (*22*). In vivo unilateral optogenetic stimulation reliably and progressively promoted eating as stimulation frequency was increased (fig. S7, G and H). Moreover, repeated optogenetic stimulation (20 Hz for 1 hour) reliably enhanced eating frequency, which required the presence of chow (fig. S8A); in a control experiment, chemogenetic activation of ^{TN}SST neurons did not elicit gnawing of a wood stick (fig. S8B). As reported recently (*17*), we also found that chemogenetic activation of ^{Arc}SST promoted eating (fig. S6D). We further examined the necessity of ^{TN}SST neurons in homeostatic eating by expressing the inhibitory DREADD κ opioid receptor (KORD) in SST-Cre mice and injecting salvinorin B (SalB) to inhibit the activity of ^{TN}SST neurons (Fig. 2F) (*23*). Injecting SalB at 10 p.m., at the start of the peak of homeostatic eating, significantly reduced cumulative eating time and eating frequency, but not eating bout duration (Fig. 2, G to I), which did not correlate with eating frequency in homeostatic eating (fig. S5). SalB injection in GFP control animals did not produce a significant difference from vehicle-injected animals (Fig. 2, G to I, black traces). Inhibition of ^{TN}SST neurons by SalB also significantly reduced food consumption in refeeding after overnight fasting (Fig. 2J). Because injecting SalB at the peak of the animals' dark cycle may cause stress and interfere with homeostatic eating, we expressed Cre-dependent archaerhodopsin (ArchT) in the TN of SST-Cre mice

[1]Singapore Bioimaging Consortium, Agency for Science Technology and Research (A*STAR), Singapore 138667. [2]Discipline of Neuroscience and Department of Anatomy, Histology and Embryology, School of Medicine, Shanghai Jiao Tong University, Shanghai, China 200025. [3]Center for Brain Science, Key Laboratory of Magnetic Resonance in Biological Systems, Wuhan Institute of Physics and Mathematics, Chinese Academy of Sciences, Wuhan, China 430071. [4]Department of Physiology, Yong Loo Lin School of Medicine, National University of Singapore, Singapore 117597. [5]Institutes of Brain Science, State Key Laboratory of Medical Neurobiology, Fudan University, Shanghai, China 200032.
*These authors contributed equally to this work.
†Corresponding author. Email: fu_yu@sbic.a-star.edu.sg

and optogenetically inhibited these neurons by using light from 10 p.m. to 12 a.m., without disturbing the mice's activity (Fig. 2K). Again, optogenetic inhibition of ^{TN}SST neurons significantly reduced cumulative eating time and eating frequency, but not eating bout duration (Fig. 2, L to N). The same optogenetic protocol did not cause changes in eating behavior in GFP control mice (Fig. 2, L to N, black traces). To test whether ^{TN}SST neurons have long-term effects on energy homeostasis, we injected AAV-flex-taCasp3-TEVp to express caspase-3 and ablate ^{TN}SST neurons in SST-Cre mice (*24*) (fig. S9). Ablation of ^{TN}SST neurons reduced body weight gain by 56% over 10 weeks (Fig. 2O). We further studied the impact of ablating ^{TN}SST neurons by using another set of mice in metabolic chambers, 4 weeks after injecting viruses, when the

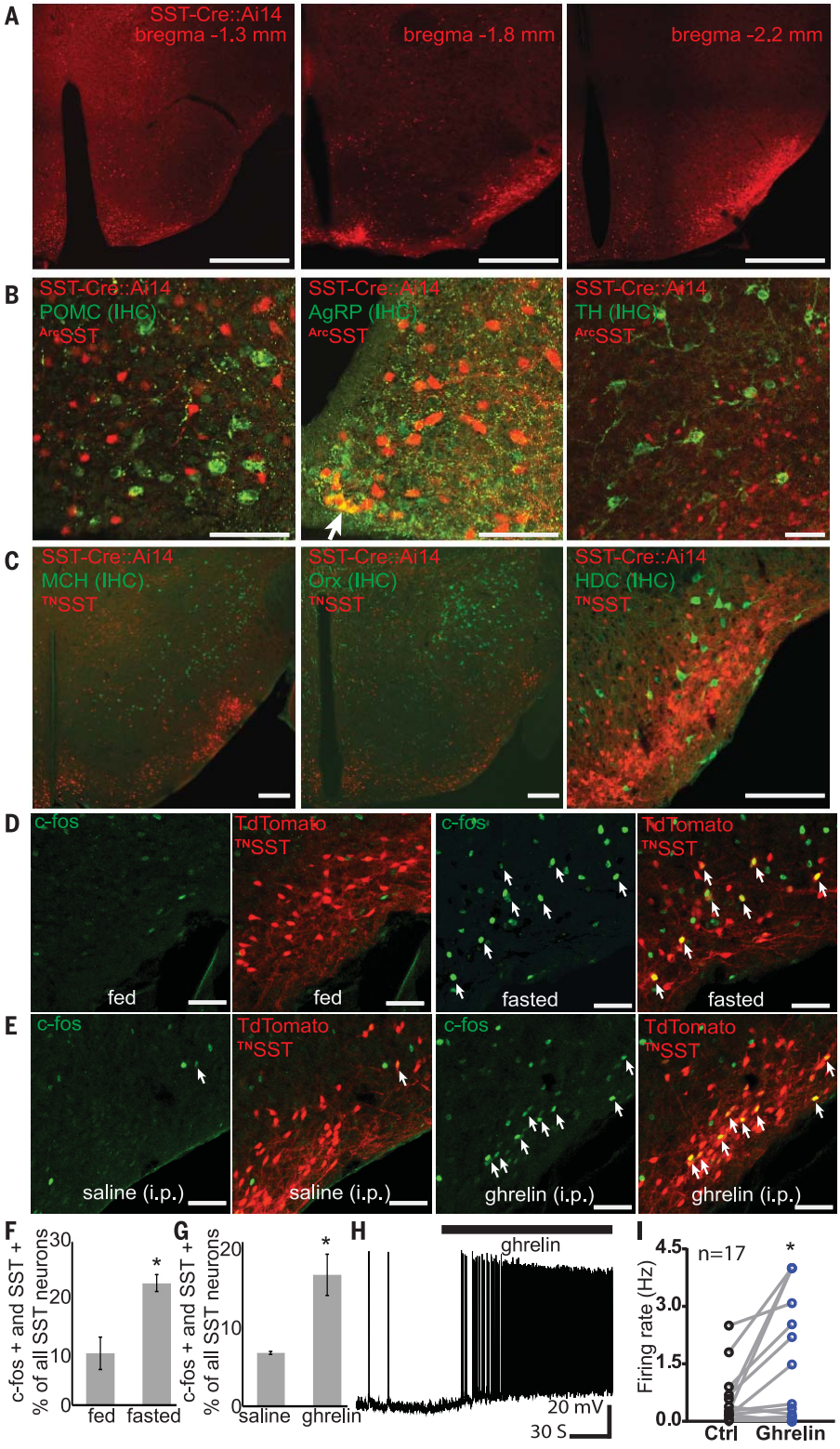

Fig. 1. The ventral hypothalamic SST neuron clusters. (**A**) Serial coronal sections of SST-Cre::Ai14 mice showing distinct SST neuron clusters in both the arcuate area and the tuberal nucleus of the hypothalamus. Scale bars, 500 μm. (**B**) Coronal sections of SST-Cre::Ai14 mice stained for POMC, AgRP, and TH (the white arrow indicates a SST neuron that is positive for AgRP). Scale bars, 100 μm. IHC, immunohistochemistry. (**C**) Coronal sections of SST-Cre::Ai14 mice stained for MCH, Orx (orexin), and HDC. Scale bars, 200 μm. (**D**) Coronal sections of SST-Cre::Ai14 mice that were (fasted) or were not (fed) subjected to overnight fasting and immunostained for c-Fos. White arrows indicate SST neurons that are c-Fos–positive. (**E**) Coronal sections of SST-Cre::Ai14 mice after i.p. injection of saline or ghrelin, immunostained for c-Fos. White arrows indicate SST neurons that are c-Fos–positive. Scale bars in (D) and (E), 100 μm. (**F**) Percentage of c-Fos–positive SST neurons under fed or fasted conditions (mean ± SEM, n = 3, unpaired t test, $^*P$ < 0.02). (**G**) Percentage of c-Fos–positive SST neurons after i.p. injection of saline or ghrelin (mean ± SEM, n = 3, unpaired t test, $^*P$ < 0.02). (**H**) Whole-cell patch recording trace showing the change in firing frequency after bath application of ghrelin (100 nM). (**I**) Firing rate before and after ghrelin application (n = 17, paired t test, $^*P$ < 0.05).

^{TN}SST-ablated mice did not show significant body weight differences from the control mice but gained body weight significantly more slowly (fig. S10). ^{TN}SST ablation resulted in mild but significantly reduced daily and dark-cycle food intake, reduced prandial drinking, mildly reduced respiratory exchange ratio, similar total energy expenditure, and mild changes in activity (fig. S10). Because both positive and negative valence mechanisms appear to play a role in controlling feeding (*25*–*28*), we explored the motivational valence of ^{TN}SST in mice. In the absence of food, chemogenetic activation of the ^{TN}SST neurons, paired with CNO injection, elicited a significant preference for the chamber (Fig. 2P).

To explore the circuit mechanisms of feeding regulation by ^{TN}SST neurons, we examined the projection pattern of ^{TN}SST neurons by injecting AAV-FLEX-GFP into the TN of SST-Cre mice (Fig. 3A). Similarly to AgRP neurons (*29*), ^{TN}SST neurons projected to various brain regions, including the paraventricular nucleus (PVN), the bed nucleus of the stria terminalis (BNST), the central amygdala (CeA), and the periaqueductal gray (PAG), with sparse projection to the paraventricular nucleus of the thalamus (PVT) and the parabrachial nuclei (PBN) (Fig. 3A). By injecting the retrograde tracers CTB488 and CTB647 into the BNST and PVN, respectively, in SST-Cre:Ai14 mice, we found that the majority (87.7%)

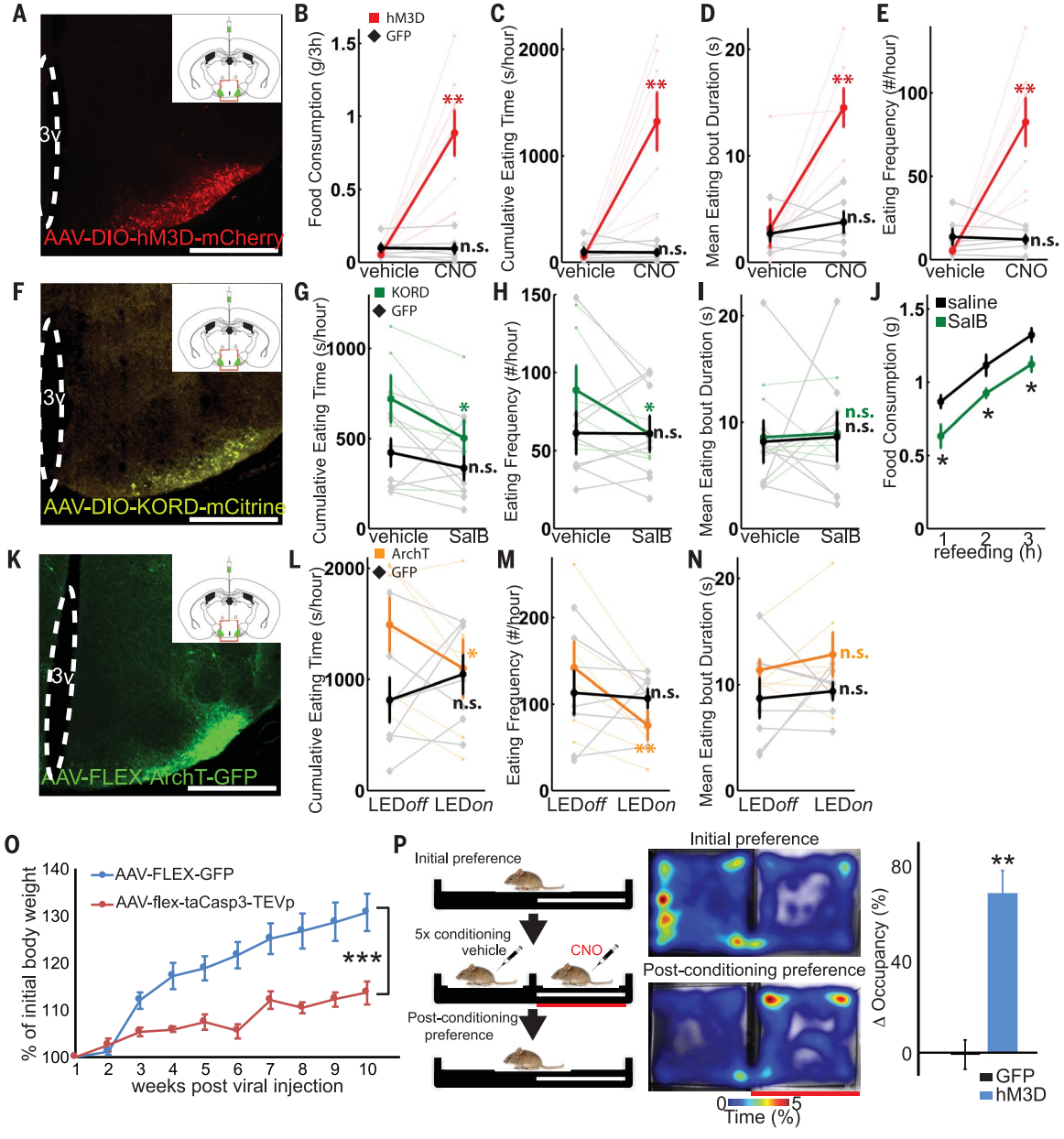

Fig. 2. The ^{TN}SST neurons regulate eating. (**A**) AAV-DIO-hM3D-mCherry was bilaterally injected into SST-Cre mice (DIO, double-floxed inverse orientation). (**B**) Food consumption, (**C**) cumulative eating time, (**D**) mean eating bout duration, and (**E**) eating frequency during the 3 hours after CNO injection at 11 a.m. (n = 7, $^{**}P$ < 0.01, paired two-tailed t test). SST-Cre mice were injected with AAV-FLEX-GFP as a control (n = 6, P > 0.5, paired two-tailed t test). n.s., not significant. (**F**) AAV-DIO-KORD-mCitrine was bilaterally injected into SST-Cre mice. (**G**) Cumulative eating time, (**H**) eating frequency, and (**I**) eating bout duration during the 3 hours after SalB injection (n = 6, $^{*}P$ < 0.05, paired two-tailed t test). SST-Cre mice were injected with AAV-FLEX-GFP as a control (n = 8, P > 0.5, paired two-tailed t test). (**J**) SST-Cre mice were injected with AAV-DIO-KORD-mCitrine, and food consumption after overnight fasting was measured [n = 7, $^{*}P$ < 0.05, one-way analysis of variance (ANOVA)]. (**K**) AAV-FLEX-ArchT-GFP was bilaterally injected into SST-Cre mice. (**L**) Cumulative eating time, (**M**) eating frequency, and (**N**) eating bout duration during 2 hours of yellow light illumination (n = 6, $^{*}P$ < 0.05, $^{**}P$ < 0.01, paired two-tailed t test). SST-Cre mice were injected with AAV-FLEX-GFP as a control (n = 7, P > 0.5, paired two-tailed t test). (**O**) Body weight gain on a normal chow diet for SST-Cre mice bilaterally injected in the TN with either AAV-FLEX-GFP as a control (n = 4) or AAV-flex-taCasp3-TEVp (n = 5) for ablating ^{TN}SST neurons (ablation versus control: repeated measures two-way ANOVA, F = 24.21, P < 0.001). (**P**) Experimental design of conditioned place preference with chemogenetic activation of ^{TN}SST neurons. A heat map shows the percent occupancy time before and after conditioning sessions. Red bar, chemogenetic activation side. The bar graph shows the change in occupancy time after conditioning sessions for SST-Cre mice injected bilaterally with AAV-DIO-hM3D-mCherry (n = 4) or AAV-FLEX-GFP (n = 3) ($^{**}P$ < 0.01, one-way ANOVA). Bold traces, means ± SEM; faint traces, individual mice. 3v, third ventricle. LED, light-emitting diode. Scale bars in (A), (F), and (K), 500 μm.

of PVN-projecting ^{TN}SST neurons projected to the BNST, and the majority (67.8%) of BNST-projecting ^{TN}SST neurons projected to the PVN (Fig. 3B). Using a similar method, we found that 36.1% of CeA-projecting ^{TN}SST neurons projected to the BNST, and 45.7% of BNST-projecting ^{TN}SST neurons projected to the CeA; 7.4% of BNST-projecting ^{TN}SST neurons projected to the PAG, and 30.5% of PAG-projecting ^{TN}SST neurons projected to the BNST; and, lastly, 13.8% of CeA-projecting ^{TN}SST neurons projected to the PAG, and 29.6% of PAG-projecting ^{TN}SST neurons projected to the CeA (Fig. 3, C to E, and fig. S11). Therefore, in contrast to AgRP neurons, different subpopulations of which project to different brain regions in a one-to-one pattern (*29*), the ^{TN}SST neurons showed a one-to-many projection pattern.

We then optogenetically stimulated ^{TN}SST axon terminals in different brain regions and examined their roles in feeding regulation. Stimulating the ^{TN}SST terminals in the PVN and BNST strongly promoted feeding, but stimulating the terminals in the CeA and PAG had no

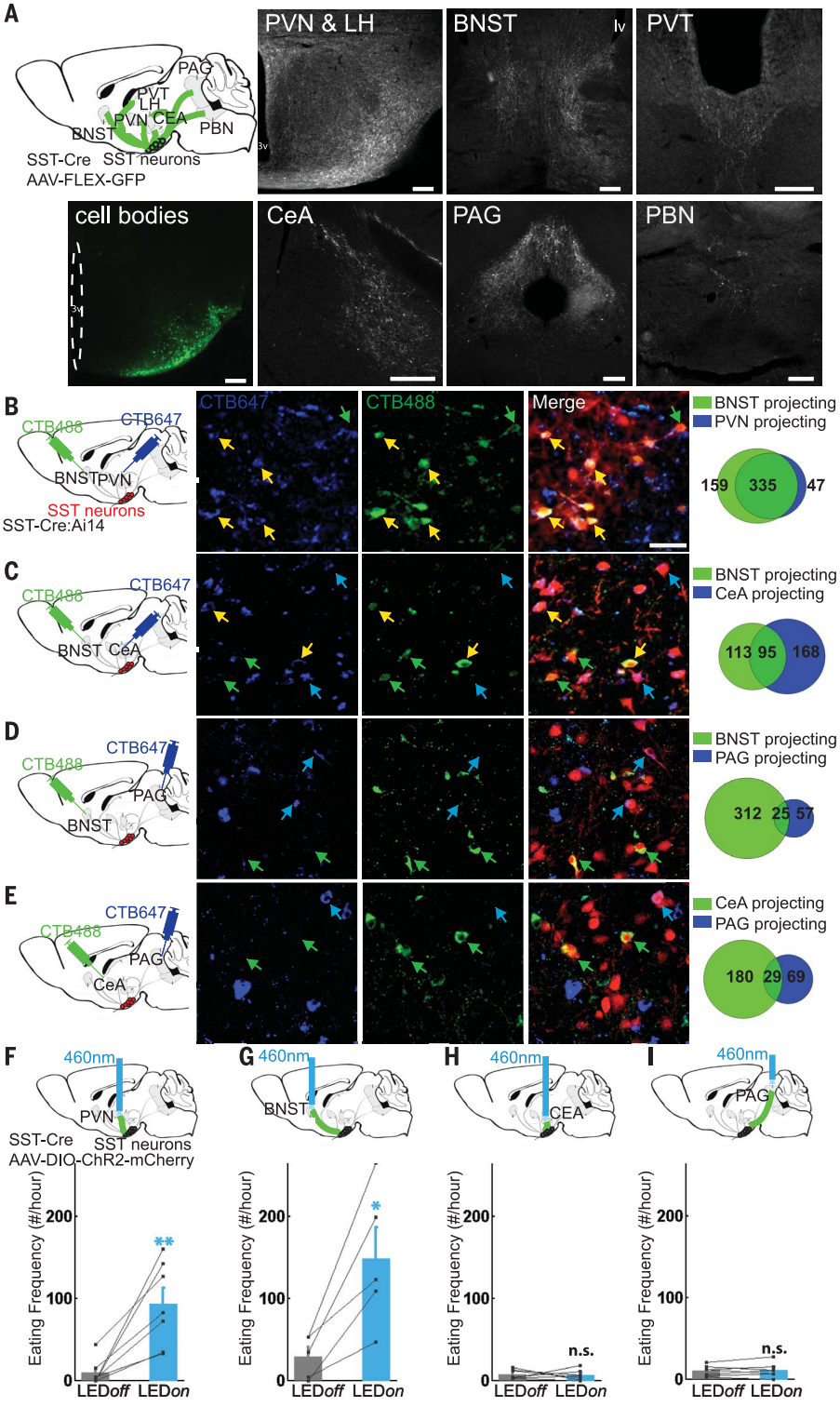

Fig. 3. The ^{TN}SST neurons regulate feeding through projections to the PVN and BNST. (**A**) Top left, diagram of a sagittal brain section summarizing the axonal projections of ^{TN}SST neurons of SST-Cre mice injected with AAV-FLEX-GFP. Other panels show GFP-expressing axon terminals in different brain regions. Scale bars, 200 μm. (**B** to **E**) Left, diagrams illustrating the injection of retrograde tracers in different brain regions of SST-Cre::Ai14 mice. Center, red ^{TN}SST neurons took up CTB647 or CTB488 injected in different projection sites. Yellow arrows indicate the ^{TN}SST neurons positive for both CTB647 and CTB488. Green arrows indicate the ^{TN}SST neurons positive only for CTB488. Blue arrows indicate the ^{TN}SST neurons positive only for CTB647. Scale bar, 50 μm. Right, Venn diagrams illustrate the quantifications from three mice. (**F** to **I**) Top, diagrams showing optogenetic stimulation of different axon terminals of ^{TN}SST neurons injected with AAV-DIO-ChR2-mCherry. Bottom, bar graphs showing the change in eating frequency after optogenetic stimulation (bars, means ± SEM; black lines, individual mice; $*P < 0.05$, $**P < 0.01$, paired two-tailed *t* test).

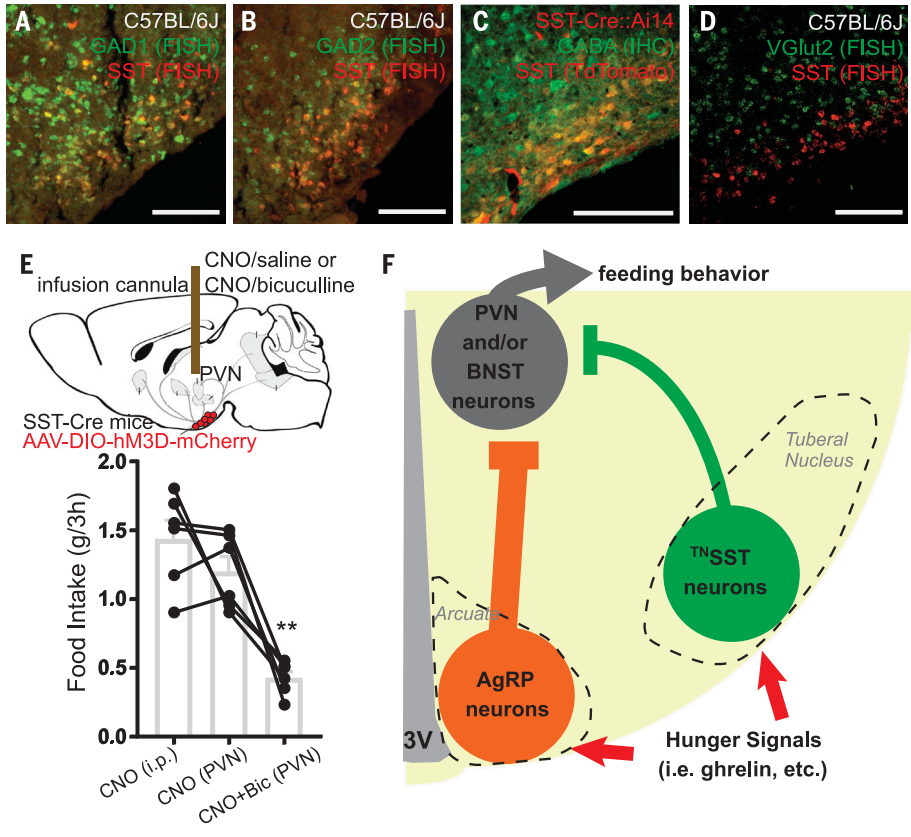

Fig. 4. The ^{TN}SST neurons are GABAergic. FISH for (**A**) SST and Gad1 or (**B**) SST and Gad2 in C57BL/6J mice. Scale bars, 200 μm. (**C**) Immunohistochemical staining for GABA in SST-Cre::Ai14 mice. Scale bars, 200 μm. (**D**) FISH for SST and VGlut2 in C57BL/6J mice. Scale bar, 200 μm. (**E**) SST-Cre mice were injected bilaterally with AAV-DIO-hM3D-mCherry in the TN, and CNO was injected either i.p. or by infusion cannula implanted over the PVN with or without bicuculline (Bic). The same animal was subjected to all three different injections on different days, and the amount of food consumption 3 hours after drug injection was analyzed (n = 6, $^{**}P < 0.01$, paired t test). Gray bars, means ± SEM; black lines, individual mice. (**F**) ^{TN}SST neurons in the mouse TN can be activated by hunger signals, including ghrelin. Activation of ^{TN}SST neurons stimulates feeding through inhibiting downstream neurons in the PVN and BNST, a mechanism similar to the activation of AgRP neurons in the arcuate area.

effect on feeding (Fig. 3, F to I, and fig. S12). To better understand the neural transmission between ^{TN}SST neurons and their downstream neurons, we performed FISH for SST and Gad1 or Gad2, the two major enzymes for producing γ-aminobutyric acid (GABA) (*30*). We found that 91.4% of ^{TN}SST neurons expressed Gad1, and 87.8% expressed Gad2 (Fig. 4, A and B). We further confirmed by immunohistochemistry that the majority of ^{TN}SST neurons produced GABA (Fig. 4C). Moreover, no ^{TN}SST neurons were positive for VGlut2 (Fig. 4D), the major glutamatergic neuron marker in the hypothalamus (*25*). To directly examine the contribution of GABA signaling on the effect of activating ^{TN}SST neurons, we locally injected CNO with or without the $GABA_A$ receptor antagonist bicuculline into the PVN of SST-Cre mice that had been injected with AAV-DIO-hM3D in the TN. Local injection of CNO into the PVN stimulated feeding similarly to i.p. injection of CNO (1.43 ± 0.14 g versus 1.20 ± 0.11 g chow; P = 0.27), but co-injecting bicuculline into the PVN dramatically reduced this effect (1.20 ± 0.11 g versus 0.43 ± 0.05 g; $P < 0.01$) (Fig. 4E). Therefore, ^{TN}SST neurons stimulated feeding through the inhibition of downstream neurons, a mechanism similar to that of AgRP neurons (*31*, *32*). Despite this similar effect in promoting feeding, ablating AgRP neurons leads to severe starvation (*33*), but we found that ablating ^{TN}SST neurons resulted in reduced body weight gain—an effect that is comparable to that of ablating lateral hypothalamic or zona incerta GABAergic neurons (*28*, *34*)—suggesting a functional differentiation between AgRP and other hypothalamic orexigenic neurons.

Our results show that, as in humans (*12*), the TN in mice is marked by SST-positive neurons. This fact provided us with genetic access to study the function of this previously enigmatic brain region. We found that ^{TN}SST neurons are required for maintaining normal body weight gain, and ^{TN}SST neurons project to various brain regions and promote feeding by inhibiting downstream neurons. Taken together, our results reveal an important role of the TN in energy homeostasis and point to a previously unknown circuit mechanism of feeding regulation that operates through orexigenic ^{TN}SST neurons (Fig. 4F). These findings promise a better understanding of the appetite and body weight changes.

REFERENCES AND NOTES

1. W. E. Le Gros Clark, J. Beattie, G. Riddoch, N. M. Dott, *The Hypothalamus: Morphological, Functional, Clinical and Surgical Aspects* (Oliver and Boyd, 1938).
2. D. F. Swaab, *Handb. Clin. Neurol.* **79**, xi–xii (2003).
3. H. P. Kremer, R. A. Roos, G. Dingjan, E. Marani, G. T. A. M. Bots, *J. Neuropathol. Exp. Neurol.* **49**, 371–382 (1990).
4. H. P. Kremer, *Prog. Brain Res.* **93**, 249–261 (1992).
5. J. A. van de Nes, W. Kamphorst, R. Ravid, D. F. Swaab, *Acta Neuropathol.* **96**, 129–138 (1998).
6. H. Braak, E. Braak, *Brain Res.* **802**, 119–124 (1998).
7. H. Braak, E. Braak, *Neuropathol. Appl. Neurobiol.* **15**, 13–26 (1989).
8. K. Kovacs, H. L. Sheehan, *Fertil. Steril.* **37**, 83–89 (1982).
9. L. E. White, R. F. Hain, *Arch. Pathol.* **68**, 275–281 (1959).
10. K. Lewin, D. Mattingly, R. R. Millis, *BMJ* **2**, 629–630 (1972).
11. N. Kamalian, R. E. Keesey, G. M. ZuRhein, *Neurology* **25**, 25–30 (1975).
12. H. J. Timmers, D. F. Swaab, J. A. van de Nes, H. P. Kremer, *Brain Res.* **728**, 141–148 (1996).
13. L. Madisen *et al.*, *Nat. Neurosci.* **13**, 133–140 (2010).
14. G. J. Morton, T. H. Meek, M. W. Schwartz, *Nat. Rev. Neurosci.* **15**, 367–378 (2014).
15. E. Gropp *et al.*, *Nat. Neurosci.* **8**, 1289–1291 (2005).
16. X. Zhang, A. N. van den Pol, *Nat. Neurosci.* **19**, 1341–1347 (2016).
17. J. N. Campbell *et al.*, *Nat. Neurosci.* **20**, 484–496 (2017).
18. T. Sakurai *et al.*, *Cell* **92**, 573–585 (1998).
19. B. B. Whiddon, R. D. Palmiter, *J. Neurosci.* **33**, 2009–2016 (2013).
20. H. Haas, P. Panula, *Nat. Rev. Neurosci.* **4**, 121–130 (2003).
21. M. Tschöp, D. L. Smiley, M. L. Heiman, *Nature* **407**, 908–913 (2000).
22. A. M. Aravanis *et al.*, *J. Neural Eng.* **4**, S143–S156 (2007).
23. E. Vardy *et al.*, *Neuron* **86**, 936–946 (2015).
24. C. F. Yang *et al.*, *Cell* **153**, 896–909 (2013).
25. J. H. Jennings, G. Rizzi, A. M. Stamatakis, R. L. Ung, G. D. Stuber, *Science* **341**, 1517–1521 (2013).
26. J. N. Betley *et al.*, *Nature* **521**, 180–185 (2015).
27. Y. Chen, Y. C. Lin, C. A. Zimmerman, R. A. Essner, Z. A. Knight, *eLife* **5**, e18640 (2016).
28. X. Zhang, A. N. van den Pol, *Science* **356**, 853–859 (2017).
29. J. N. Betley, Z. F. Cao, K. D. Ritola, S. M. Sternson, *Cell* **155**, 1337–1350 (2013).
30. M. G. Erlander, N. J. Tillakaratne, S. Feldblum, N. Patel, A. J. Tobin, *Neuron* **7**, 91–100 (1991).
31. D. Atasoy, J. N. Betley, H. H. Su, S. M. Sternson, *Nature* **488**, 172–177 (2012).
32. A. S. Garfield *et al.*, *Nat. Neurosci.* **18**, 863–871 (2015).
33. S. Luquet, F. A. Perez, T. S. Hnasko, R. D. Palmiter, *Science* **310**, 683–685 (2005).
34. J. H. Jennings *et al.*, *Cell* **160**, 516–527 (2015).

ACKNOWLEDGMENTS

We thank M. Stryker for critical reading of the manuscript. **Funding:** This work was supported by an A*STAR Investigatorship provided by the Biomedical Research Counsel (BMRC) of A*STAR

(1530700142 to Y.F.), intramural funding from A*STAR BMRC (to W.H.), the National Natural and Science Foundation of China (81771215 to J.H.), and National Medical Research Council Collaborative Research Grants (NMRC/CBRG/0099/2015 and NMRC-OFIRG-0037-2017 to K.K. and S.S.). **Author contributions:** Y.F. conceived of the project and wrote the manuscript. S.X.L., J.H., Q.L., and Y.F. designed and implemented the study. H.M. performed retrograde tracing and local CNO injection. C.-Y.L., K.K., and S.S. contributed electrophysiological recordings. A.M.-Y.K., Y.L.T., and M.H. performed immunohistochemical staining. J.Y.L., and H.L. performed the metabolic chamber study. J.S. helped with in vivo optogenetic stimulation. L.Y.Y. and J.G. performed magnetic resonance imaging. All authors discussed the results and commented on the manuscript. **Competing interests:** The authors declare no competing interests. **Data and materials availability:** All data deeded to evaluate the conclusions of the paper are present in the paper and the supplementary materials.

SUPPLEMENTARY MATERIALS

www.sciencemag.org/content/361/6397/76/suppl/DC1
Materials and Methods
Figs. S1 to S12
References (*35*–*37*)

18 November 2017; accepted 8 May 2018
10.1126/science.aar4983

DOMESTICATION

The evolutionary history of dogs in the Americas

Máire Ní Leathlobhair[1]*, Angela R. Perri[2,3]*, Evan K. Irving-Pease[4]*, Kelsey E. Witt[5]*, Anna Linderholm[4,6]*, James Haile[4,7], Ophelie Lebrasseur[4], Carly Ameen[8], Jeffrey Blick[9]†, Adam R. Boyko[10], Selina Brace[11], Yahaira Nunes Cortes[12], Susan J. Crockford[13], Alison Devault[14], Evangelos A. Dimopoulos[4], Morley Eldridge[15], Jacob Enk[14], Shyam Gopalakrishnan[7], Kevin Gori[1], Vaughan Grimes[16], Eric Guiry[17], Anders J. Hansen[7,18], Ardern Hulme-Beaman[4,8], John Johnson[19], Andrew Kitchen[20], Aleksei K. Kasparov[21], Young-Mi Kwon[1], Pavel A. Nikolskiy[21,22], Carlos Peraza Lope[23], Aurélie Manin[24,25], Terrance Martin[26], Michael Meyer[27], Kelsey Noack Myers[28], Mark Omura[29], Jean-Marie Rouillard[14,30], Elena Y. Pavlova[21,31], Paul Sciulli[32], Mikkel-Holger S. Sinding[7,18,33], Andrea Strakova[1], Varvara V. Ivanova[34], Christopher Widga[35], Eske Willerslev[7], Vladimir V. Pitulko[21], Ian Barnes[11], M. Thomas P. Gilbert[7,36], Keith M. Dobney[8,37], Ripan S. Malhi[38,39], Elizabeth P. Murchison[1]‡§, Greger Larson[4]‡§, Laurent A. F. Frantz[4,40]‡§

Dogs were present in the Americas before the arrival of European colonists, but the origin and fate of these precontact dogs are largely unknown. We sequenced 71 mitochondrial and 7 nuclear genomes from ancient North American and Siberian dogs from time frames spanning ~9000 years. Our analysis indicates that American dogs were not derived from North American wolves. Instead, American dogs form a monophyletic lineage that likely originated in Siberia and dispersed into the Americas alongside people. After the arrival of Europeans, native American dogs almost completely disappeared, leaving a minimal genetic legacy in modern dog populations. The closest detectable extant lineage to precontact American dogs is the canine transmissible venereal tumor, a contagious cancer clone derived from an individual dog that lived up to 8000 years ago.

The history of the global dispersal of dogs continues to be contentious (*1*). In North America, the earliest confirmed dog remains (from Koster, IL) have been radiocarbon dated to ~9900 calibrated years before the present (*2*, *3*), ~4500 years after the earliest unambiguous evidence of humans arriving in the Americas (*4*). Although these early dogs were most likely not domesticated in situ (*5*), the timing of their arrival and their geographic origins are unknown. Studies of the control region of mitochondrial DNA have suggested that the precontact American dog population was largely replaced following the arrival of European dogs after colonization and the introduction of Eurasian Arctic dogs (e.g., Siberian huskies) during the Alaskan gold rush (*5*–*7*). It remains possible, however, that some modern American dogs retain a degree of ancestry from the precontact population (*8*, *9*).

We sequenced complete mitochondrial genomes (mitogenomes) from 71 archaeological dog remains collected in North America and Siberia (Fig. 1A and table S1) and analyzed these with 145 mitogenomes derived from a global dataset of modern and ancient canids (*3*). A phylogenetic tree constructed from the mitogenomes indicated that all sampled precontact dogs (PCDs) (from time frames spanning ~9000 years) formed a monophyletic group within dog haplogroup A (Fig. 1B and figs. S3 and S6). This analysis indicated that the mitochondrial lineage most closely related to the PCD clade is that of the ~9000-year-old population of dogs from Zhokhov Island in Eastern Siberia (*3*) (Fig. 1B and figs. S3 and S6). In addition, molecular clock analyses suggest that all PCDs share a common ancestor that lived ~14,600 years ago [95% highest posterior density (HPD), 16,484 to 12,965 years ago] (Fig. 1B and fig. S6), which had diverged from an ancestor shared with the Zhokhov Island dogs ~1000 years earlier (95% HPD, 17,646 to 13,739 years ago) (Fig. 1B and fig. S6). These time frames are broadly coincident with early migrations into the Americas (*10*–*12*).

To further investigate the evolutionary history of PCDs, we generated low-coverage (~0.005 to 2.0×) nuclear genome sequences from seven PCDs sampled in six locations in North America from time frames spanning ~9000 years (table S1). We analyzed these nuclear data alongside publicly available datasets including 45 modern canid whole genomes sampled from Eurasia and the Americas (table S2) (*13*–*16*). A neighbor-joining tree constructed by using single-nucleotide polymorphisms (SNPs) revealed that, like the mitogenome phylogeny, PCDs clustered in a distinct monophyletic lineage that is more closely related to dogs than to either Eurasian or North American wolves (Fig. 1C). Furthermore, our nuclear genome analysis indicated that the closest-related sister clade to PCDs consists of modern Arctic dogs from the Americas (including Alaskan malamutes, Greenland dogs, and Alaskan huskies) and Eurasia (Siberian huskies) (Fig. 1C). Treemix (*3*) (Fig. 1D), outgroup *f3* statistics (fig. S13), and D statistics (figs. S14 and S15) also supported this phylogenetic structure. Combined, our mitochondrial and nuclear results indicate that PCDs were not domesticated in situ from North American wolves but were instead introduced by people into the Americas via Beringia from a population related to modern Arctic dogs.

Studies of nuclear genome data have identified two modern clades of global dogs: an East Asian clade (including dingoes) and a Western Eurasian clade (including European, Indian, and African dogs) (*9*, *14*, *16*). These analyses placed modern Arctic dogs with either Western Eurasian (*16*, *17*) or East Asian (*9*, *14*) dogs. Our analyses of nuclear genome data revealed a close relationship between Arctic dogs and PCDs, which together form

[1]Transmissible Cancer Group, Department of Veterinary Medicine, University of Cambridge, Cambridge, UK. [2]Department of Archaeology, Durham University, Durham, UK. [3]Department of Human Evolution, Max Planck Institute for Evolutionary Anthropology, Leipzig, Germany. [4]The Palaeogenomics and Bio-Archaeology Research Network, Research Laboratory for Archaeology and History of Art, University of Oxford, Oxford, UK. [5]School of Integrative Biology, University of Illinois at Urbana-Champaign, Urbana-Champaign, IL, USA. [6]Department of Anthropology, Texas A&M University, College Station, TX, USA. [7]Centre for GeoGenetics, Natural History Museum of Denmark, University of Copenhagen, Copenhagen, Denmark. [8]Department of Archaeology, Classics and Egyptology, University of Liverpool, Liverpool, UK. [9]Department of Government and Sociology, Georgia College and State University, Milledgeville, GA, USA. [10]Department of Biomedical Sciences, Cornell University, Ithaca, NY, USA. [11]Department of Earth Sciences, Natural History Museum, London, UK. [12]Department of Anthropology, University at Albany–SUNY, Albany, NY, USA. [13]Pacific Identifications, Victoria, Canada. [14]Arbor Biosciences, Ann Arbor, MI, USA. [15]Millennia Research, Victoria, Canada. [16]Department of Archaeology, Memorial University, Queen's College, St. John's, Canada. [17]Department of Anthropology, University of British Columbia, Vancouver, Canada. [18]The Qimmeq Project, University of Greenland, Nuussuaq, Greenland. [19]Department of Anthropology, Santa Barbara Museum of Natural History, Santa Barbara, CA, USA. [20]Department of Anthropology, University of Iowa, Iowa City, IA, USA. [21]Institute for the History of Material Culture, Russian Academy of Sciences, St. Petersburg, Russia. [22]Geological Institute, Russian Academy of Sciences, Moscow, Russia. [23]Centro INAH Yucatán, Mérida, Yucatán, México. [24]Department of Archaeology, BioArCh, University of York, York, UK. [25]UMR 7209, Archéozoologie, Archéobotanique, Muséum National d'Histoire Naturelle, Paris, France. [26]Research and Collections Center, Illinois State Museum, Springfield, IL, USA. [27]Touray & Meyer Veterinary Clinic, Serrekunda, Gambia. [28]Glenn A. Black Laboratory of Anthropology, Indiana University Bloomington, Bloomington, IN, USA. [29]Department of Mammalogy, Museum of Comparative Zoology, Harvard University, Cambridge, MA, USA. [30]Department of Chemical Engineering, University of Michigan, Ann Arbor, MI, USA. [31]Arctic & Antarctic Research Institute, St. Petersburg, Russia. [32]Department of Anthropology, Ohio State University, Columbus, OH, USA. [33]Natural History Museum, University of Oslo, Oslo, Norway. [34]VNIIOkeangeologia Research Institute, St. Petersburg, Russia. [35]Center of Excellence in Paleontology, East Tennessee State University, Gray, TN, USA. [36]Norwegian University of Science and Technology, University Museum, Trondheim, Norway. [37]Department of Archaeology, University of Aberdeen, Aberdeen, UK. [38]Department of Anthropology, University of Illinois at Urbana-Champaign, Urbana-Champaign, IL, USA. [39]Carl R. Woese Institute for Genomic Biology, University of Illinois at Urbana-Champaign, Urbana-Champaign, IL, USA. [40]School of Biological and Chemical Sciences, Queen Mary University of London, London, UK.
*These authors contributed equally to this work. †Deceased. ‡These authors cosupervised this work.
§Corresponding author. Email: laurent.frantz@qmul.ac.uk (L.A.F.F.); greger.larson@arch.ox.ac.uk (G.L.); epm27@cam.ac.uk (E.P.M.)

a clade (PCD/Arctic) that is basal to both Western Eurasian and East Asian dogs and suggests the existence of a third monophyletic clade of dogs (Fig. 1C). Although all three clades are well supported, the relationships between them are ambiguous. For example, outgroup f3 statistics analysis (fig. S13) indicated that the PCD/Arctic clade is basal to the two other Eurasian dog clades. However, when we excluded specific East Asian dogs that possess evidence of gene flow from European dogs (table S7) (*14*), East Asian dogs became the most basal clade in a neighbor-joining tree and the PCD/Arctic clade became the sister clade to Western Eurasian dogs (fig. S11). Conversely, admixture graphs (*3*) (fig. S25) and Treemix (*18*) (Fig. 1D) suggested that the PCD/Arctic clade is closest to East Asian dogs and that Western Eurasian dogs are the most basal. Conflicting phylogenies based on nuclear data have been reported on numerous occasions (*1*, *14*, *16*), and these inconsistent topologies could result either from substantial post-divergence gene flow among Eurasian dogs (Fig. 1C and fig. S25) (*3*, *14*) or from nearly simultaneous divergence of all three lineages.

Our nuclear genome data indicate that modern Arctic dogs sampled from both Siberia and North America cluster in a distinct phylogenetic group that forms a sister taxon to PCDs (Fig. 1C). This close phylogenetic relationship between modern American Arctic dogs (Alaskan malamutes, Alaskan huskies, and Greenland dogs) and modern Eurasian Arctic dogs (Siberian huskies) (Fig. 1C and figs. S11 and S13) suggests that PCDs are not the direct ancestor of modern American Arctic dogs. It is possible that modern American Arctic dogs are the descendants of dogs brought onto the continent by the Paleo-Eskimos (~6000 years ago) or by the Thule (~1000 years ago) (*19*). However, both mitogenomic and low-coverage nuclear data from a late Paleo-Eskimo dog from Kodiak Island, Alaska (Uyak site sample AL3198) (Fig. 1A

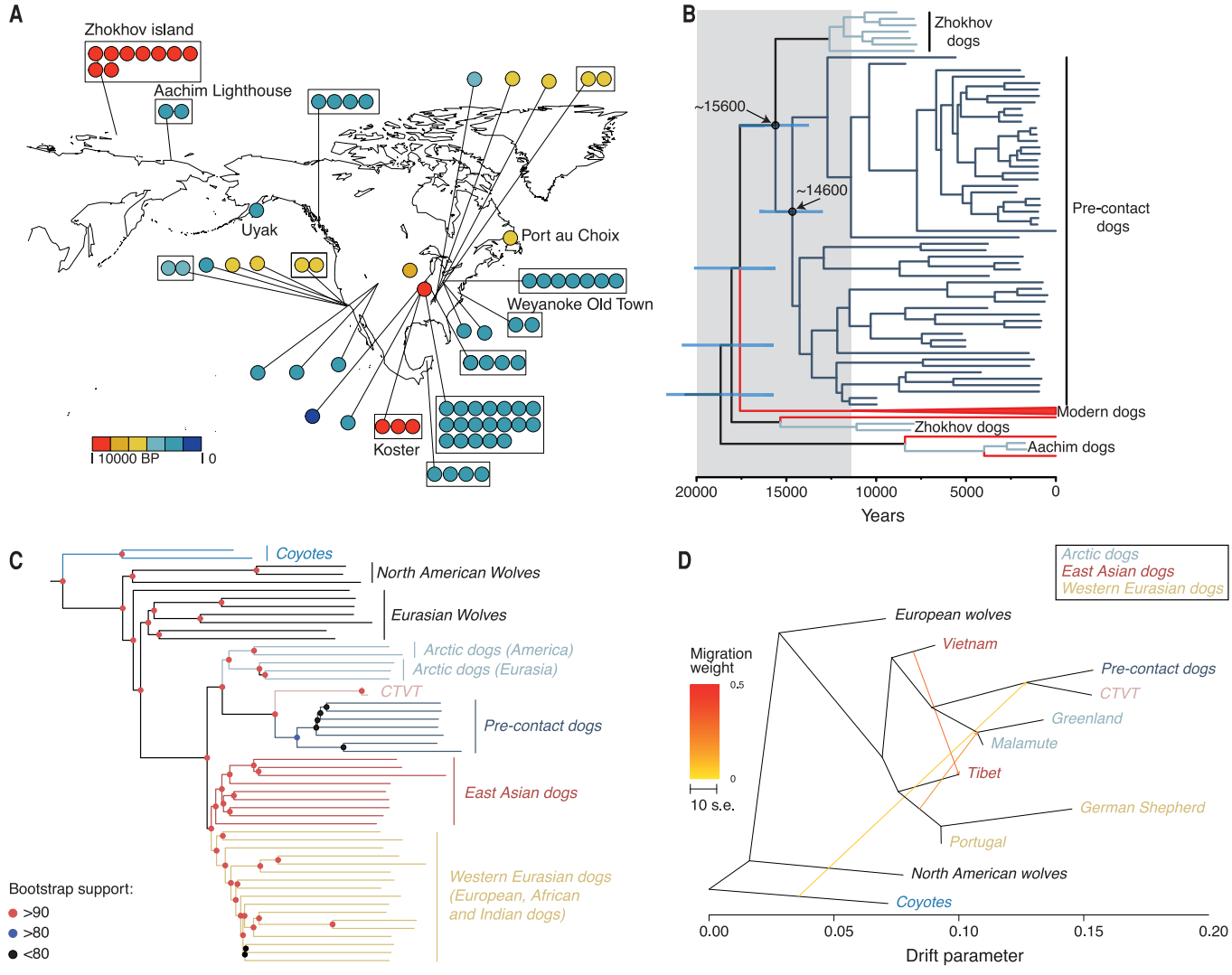

Fig. 1. Sample locations and ancestry of PCDs. (**A**) A map depicting the locations and ages of the archaeological remains analyzed in this study. Each dot represents a single sample, and multiple samples per archaeological site are grouped in boxes. Sites mentioned in the text are labeled. BP, before the present. (**B**) A tip-calibrated Bayesian mitochondrial phylogenetic tree of dogs within haplogroup A. This analysis was conducted with 66 novel ancient mitogenomes (all genomes with at least 10× coverage) together with 145 publicly available mitogenomes from both modern and ancient canids (*3*) (fig. S6). Red branches represent modern dogs, dark blue represents PCDs, and light blue denotes ancient DNA from Arctic dogs. Blue bars on nodes represent 95% HPD ages. The gray shaded area represents the time frame during which people likely entered the Americas based on the age of divergence between Native Americans and ancient Beringians (~20,000 years ago) (*12*) and the flooding of the Bering land bridge (~11,000 years ago) (*11*). (**C**) A neighbor-joining tree built with whole genomes (*3*). (**D**) An admixture graph constructed with Treemix (on the basis of transversions) (*3*, *18*) depicting the relationship between PCDs [including the Port au Choix (AL3194) and Weyanoke Old Town (AL3223) samples] and other dog, wolf, and CTVT populations. The scale bar shows 10 times the average standard error (s.e.) of the entries in the sample covariance matrix (*18*).

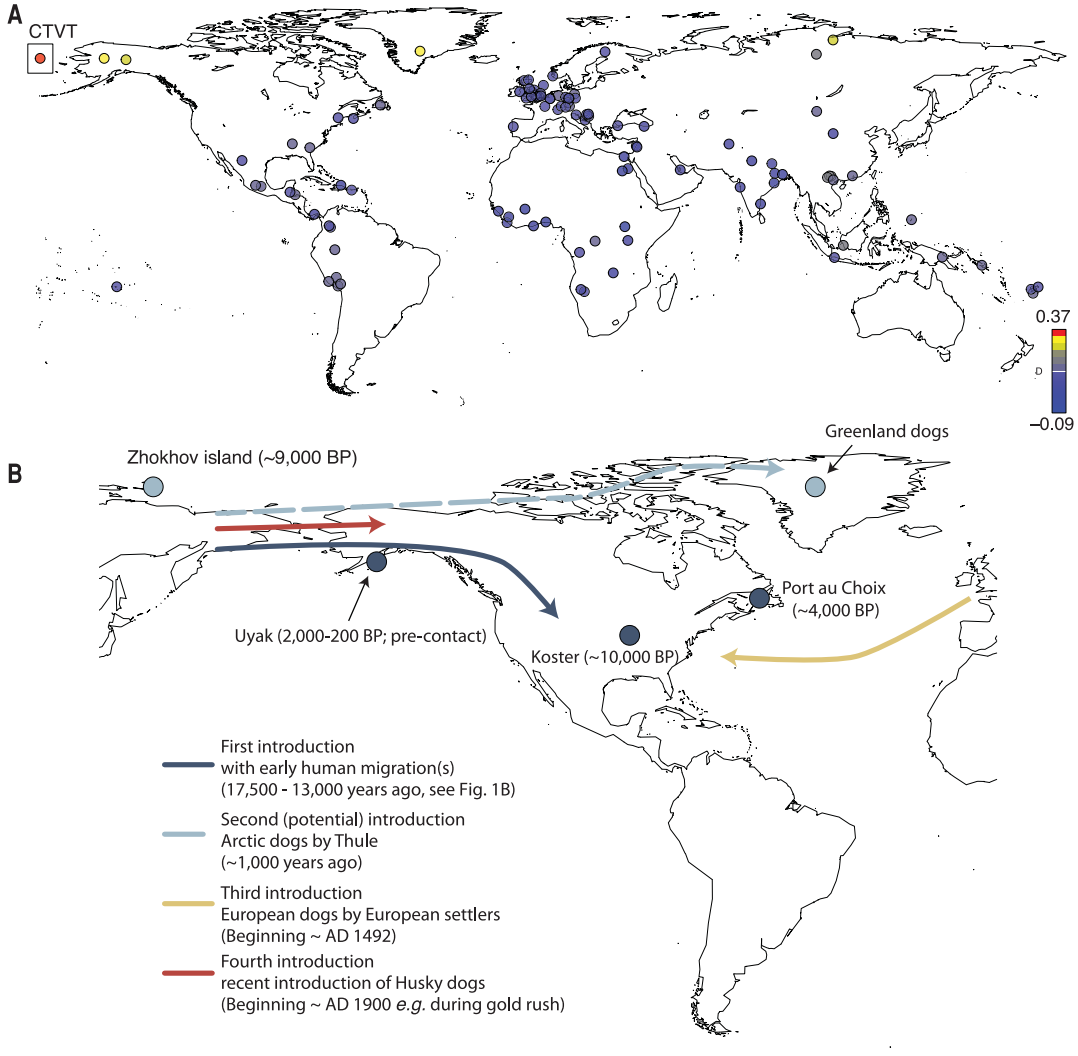

Fig. 2. Legacy of PCDs in modern American dogs. (**A**) A map showing the locations of dog populations obtained from (*9*) and their degrees of relatedness (D statistics) to the ~4000-year-old Port au Choix dog (AL3194) [see (*3*) and fig. S14]. Higher values (in red) represent closer relatedness. The location of the founder CTVT individual, labeled in the plot, is unknown. (**B**) A map depicting the multiple introductions of dogs into the Americas.

and table S1), indicate that this dog was more closely related to PCDs than to modern American Arctic dogs (figs. S4 and S10). This finding suggests that modern American Arctic dogs are not the descendants of Paleo-Eskimo dogs and that Paleo-Eskimos likely acquired local dogs in North America or brought Siberian dogs that were genetically indistinguishable from PCDs. Our sampling did not include dogs from sites associated with the Thule culture, so it is plausible that the modern American Arctic dogs included in our analysis, such as Alaskan malamutes and Greenland dogs, are the descendants of dogs introduced by the Thule. Alternatively, the modern American Arctic dogs that we sampled may be the descendants of recently introduced Eurasian Arctic dogs, many of which were introduced during the 19th-century Alaskan gold rush and as sled dog racing stock (*6*).

Previous genomic analyses of the canine transmissible venereal tumor (CTVT) genome indicated a close affinity with modern Arctic dogs (*20*). CTVT is a contagious cancer clone that manifests as genital tumors and spreads between dogs by the transfer of living cancer cells during mating. This clone first originated from the cells of an individual dog, the "CTVT founder dog," which lived several thousand years ago, and the clone still carries the genome of this individual (*20*). To investigate the relationship between the CTVT founder dog and PCDs, we analyzed two CTVT genomes alongside a panel of modern and ancient canid genomes.

Because CTVT is a cancer, and to limit the impact of somatic mutations, we confined our genotyping analysis to SNPs mapping to genomic regions that have retained both parental chromosomal copies in CTVT (*20*) and excluded singleton SNPs called exclusively in CTVT genomes and not found in any other canid genome. CTVT clustered with PCDs on neighbor-joining trees (Fig. 1C and figs. S10 and S11), a Bayesian tree (fig. S12), Treemix (Fig. 1D), and admixture graphs (fig. S25). This result is further supported by both outgroup f3 statistics (fig. S13) and D statistics (figs. S14 and S15). These findings indicate that the CTVT founder dog is more closely related to PCDs than to modern Arctic dogs. Multiple horizontal transfers of mitochondrial genomes from dog hosts to CTVT has led to the replacement of the founder dog's mitogenome (*21*, *22*); thus, we could not determine the mitochondrial haplogroup of the CTVT founder dog, and we limited our analyses to the nuclear genome.

To assess whether the CTVT founder dog lived before or after dogs entered North America, we re-estimated its temporal origin by sequencing the nuclear genomes of two CTVTs, 608T and 609T. 608T is a CTVT from the skin of a 10-month-old puppy and was likely engrafted from the mother's vaginal tumor (609T) during birth. We identified mutations generated by a clocklike mutational process that were present in 608T but not detectable in 609T and used these to derive a lower bound for a somatic mutation rate for CTVT (*3*). Applying this rate to the total burden of clocklike somatic mutations in the CTVT lineage (*3*), we estimated that the CTVT founder dog lived up to 8225 years ago (*3*). This time frame postdates the initial arrival of dogs into the Americas, raising the possibility that CTVT may have originated in a dog living in North America.

To further assess this scenario, we quantified the degree of introgression between canids endemic to North America (coyotes and North

American wolves), PCDs, modern Arctic dogs, and the CTVT founder dog. Our analyses indicated that, unlike Arctic dogs, PCDs share a number of derived alleles with coyotes and North American wolves, indicative of admixture (figs. S16 and S17). The CTVT founder dog also showed some weak evidence of coyote ancestry but did not appear to possess admixture with North American wolves (figs. S16 and S17). Because coyotes are restricted to North America, this finding suggests that CTVT may have originated there. As we did not ascertain the degree of coyote ancestry in ancient PCD-related dogs in Northern Siberia (such as the Zhokhov Island dogs) (Fig. 1), however, this analysis does not establish the location in which CTVT originated. Furthermore, studies that used somatic mutations to reconstruct the phylogeography of the CTVT clone indicated deep divergence in Asia and recent introduction to the Americas (*21*). Altogether, these results suggest a scenario in which CTVT originated in Asia from a dog that was closely related to PCDs, although we cannot exclude the possibility that the clone arose in America and then dispersed early into Asia before being reintroduced to America.

The legacy of PCDs in modern American canid populations is uncertain. It has been suggested that some North American wolves obtained a mutation leading to black coat color possibly via admixture with early American dogs (*23*). This allele was not present, however, in either of the two higher-coverage ancient PCDs in this study (*3*) or in CTVT (*20*). Additional ancient genomes are necessary to determine if this allele was present in the PCD population.

In addition, previous studies have argued that some modern American dog populations possess a genetic signature from indigenous American dogs (*8*, *9*, *24*). To test this hypothesis, we analyzed nuclear data obtained from more than 5000 modern dogs (including American village dogs) genotyped on a 180,000 SNP array (*9*). We found 7 to 20% PCD ancestry in modern American Arctic dogs (Alaskan huskies, Alaskan malamutes, and Greenland dogs) by using f4 ratios (tables S10 and S11) (*3*). This result, however, may reflect ancient population substructure in Arctic dogs rather than genuine admixture (*3*). Our f4 ratio analysis did not detect a significant admixture signal from PCDs in any modern American dogs of European ancestry (table S10).

Our admixture analysis detected varying degrees (0 to 33%) of PCD/Arctic ancestry in three individual Carolina dogs (fig. S20). This analysis, however, could not distinguish between PCD and Arctic ancestry, and we cannot rule out that this signal was a result of admixture from modern Arctic dogs and not from PCDs (*3*). The majority of modern American dog populations, including 138 village dogs from South America and multiple "native" breeds (e.g., hairless dogs and Catahoulas), possess no detectable traces of PCD ancestry (Fig. 2A, fig. S20, and table S10), though this analysis may suffer from ascertainment bias.

To further assess the contribution of PCDs to modern American dog populations, we also analyzed 590 additional modern dog mitogenomes, including those from 169 village and breed dogs that were sampled in North and South America (*21*). We identified two modern American dogs (a chihuahua and a mixed-breed dog from Nicaragua) that carried PCD mitochondrial haplotypes (fig. S5), consistent with a limited degree of PCD ancestry (<2%) in modern American dogs. We also identified three East Asian dogs that carried a PCD haplotype, possibly as a result of ancient population substructure or recent dog dispersal (fig. S5) (*3*). Although greater degrees of PCD ancestry may remain in American dogs that have not yet been sampled, our results suggest that European dogs almost completely replaced native American dog lineages. This near disappearance of PCDs likely resulted from the arrival of Europeans, which led to shifts in cultural preferences and the persecution of indigenous dogs (*25*). Introduced European dogs may also have brought infectious diseases to which PCDs were susceptible.

The first appearance of dogs in the North American archaeological record occurred ~4500 years after the earliest evidence of human activity on the continent (*4*, *11*). In addition, our molecular clock analysis indicates that the PCD lineage appeared ~6500 years after North American human lineages (Fig. 1B) (*10*). These discrepancies suggest that dogs may not have arrived into the Americas alongside the very first human migration but were instead potentially part of a later arrival (*12*) before the flooding of the Bering land bridge ~11,000 years ago (*11*). This timing is compatible with both the archaeological record and our PCD divergence time estimate and suggests a scenario in which dogs were brought to the Americas several thousand years after the first people arrived there.

This initial dog population entered North America and then dispersed throughout the Americas, where it remained isolated for at least 9000 years. Within the past 1000 years, however, at least three independent reintroductions of dogs have occurred. The first may have consisted of Arctic dogs that arrived with the Thule culture ~1000 years ago (*6*). Then, beginning in the 15th century, Europeans brought a second wave of dogs that appear to have almost completely replaced native dogs. Lastly, Siberian huskies were introduced to the American Arctic during the Alaskan gold rush (*25*). As a result of these more recent introductions, the modern American dog population is largely derived from Eurasian breeds, and the closest known extant vestige of the first American dogs now exists as a worldwide transmissible cancer.

REFERENCES AND NOTES

1. G. Larson *et al.*, *Proc. Natl. Acad. Sci. U.S.A.* **109**, 8878–8883 (2012).
2. A. Perri *et al.*, bioRxiv 343574 [Preprint]. 11 June 2018.
3. See supplementary materials.
4. T. Goebel, M. R. Waters, D. H. O'Rourke, *Science* **319**, 1497–1502 (2008).
5. J. A. Leonard *et al.*, *Science* **298**, 1613–1616 (2002).
6. S. K. Brown, C. M. Darwent, E. J. Wictum, B. N. Sacks, *Heredity* **115**, 488–495 (2015).
7. K. E. Witt *et al.*, *J. Hum. Evol.* **79**, 105–118 (2015).
8. B. van Asch *et al.*, *Proc. R. Soc. London Ser. B* **280**, 20131142 (2013).
9. L. M. Shannon *et al.*, *Proc. Natl. Acad. Sci. U.S.A.* **112**, 13639–13644 (2015).
10. M. Raghavan *et al.*, *Science* **349**, aab3884 (2015).
11. M. Jakobsson *et al.*, *Clim. Past* **13**, 991–1005 (2017).
12. J. V. Moreno-Mayar *et al.*, *Nature* **553**, 203–207 (2018).
13. Z. Fan *et al.*, *Genome Res.* **26**, 163–173 (2016).
14. G.-D. Wang *et al.*, *Cell Res.* **26**, 21–33 (2016).
15. A. H. Freedman *et al.*, *PLOS Genet.* **10**, e1004016 (2014).
16. L. A. F. Frantz *et al.*, *Science* **352**, 1228–1231 (2016).
17. B. M. vonHoldt *et al.*, *Nature* **464**, 898–902 (2010).
18. J. K. Pickrell, J. K. Pritchard, *PLOS Genet.* **8**, e1002967 (2012).
19. M. Raghavan *et al.*, *Science* **345**, 1255832 (2014).
20. E. P. Murchison *et al.*, *Science* **343**, 437–440 (2014).
21. A. Strakova *et al.*, *eLife* **5**, e14552 (2016).
22. C. A. Rebbeck, A. M. Leroi, A. Burt, *Science* **331**, 303 (2011).
23. T. M. Anderson *et al.*, *Science* **323**, 1339–1343 (2009).
24. H. G. Parker *et al.*, *Cell Rep.* **19**, 697–708 (2017).
25. M. Derr, *A Dog's History of America: How Our Best Friend Explored, Conquered, and Settled a Continent* (Farrar, Straus and Giroux, 2005).
26. M. Ní Leathlobhair *et al.*, The evolutionary history of dogs in the Americas, Dryad (2018); doi: 10.5061/dryad.s1k47j4.

ACKNOWLEDGMENTS

We thank L. Orlando, R. K. Wayne, and D. Meltzer for their valuable comments; B. M. Kemp, M. Masson, and J. Chupasko for support; and J. Southon (W. M. Keck Carbon Cycle Accelerator Mass Spectrometry Laboratory, University of California, Irvine) for the radiocarbon date on the Port au Choix dog. We acknowledge the University of Oxford Advanced Research Computing (ARC) facility for providing computing time. We thank the Illinois State Museum, the Illinois State Archaeological Survey, the Glenn A. Black Laboratory of Archaeology at Indiana University Bloomington, the Instituto Nacional de Antropologia e Historia, and the Ohio Historical Society for access to material. We thank The Rooms (Museum Division), the Board Executive, and the Government of Newfoundland and Labrador for permission to access and sample the Port au Choix material. We are grateful to M. Ptaszynska for useful information and to S. Zhang for assistance with samples. We thank the staff of the Danish National High-throughput Sequencing Centre for assistance in data generation. **Funding:** L.A.F.F. was supported by the Wellcome Trust (210119/Z/18/Z) and by Wolfson College (University of Oxford). L.A.F.F., J.H., A.L., A.H.-B., O.L., K.M.D., and G.L. were supported by a European Research Council grant (ERC-2013-StG-337574-UNDEAD) or Natural Environmental Research Council grants (NE/K005243/1 and NE/K003259/1) or both. M.N.L. and E.P.M. were supported by Wellcome (102942/Z/13/A) and a Philip Leverhulme Prize awarded by the Leverhulme Trust. A.R.P. was supported by the Max Planck Society. E.K.I.-P. was supported by a Clarendon Fund scholarship from the University of Oxford. M.T.P.G. was supported by a European Research Council grant (ERC-2015-CoG-681396–Extinction Genomics). A.M. was supported by the Muséum National d'Histoire Naturelle. K.E.W. and R.S.M. were supported by an NSF grant (BCS-1540336) and a Wenner-Gren grant. V.G. was supported by a Social Sciences and Humanities Research Council Insight grant. V.V.P., E.Y.P., and P.A.N. were supported by Russian Science Foundation project N16-18-10265-RNF. Y.-M.K. was supported by a Herchel Smith research fellowship. S.J.C. was supported by Millennia Research. J.J. was supported by the Santa Barbara Museum of Natural History. A.R.B. was supported by the American Kennel Club and the NIH. We thank the Illinois State Museum Society for funding. **Author contributions:** L.A.F.F., G.L., and E.P.M. conceived of the project and designed the research; A.R.P., K.M.D., and G.L. coordinated the archaeological analyses and sample collection efforts with input from R.S.M., C.A., A.H.-B., and K.E.W.; A.R.P., C.A., J.B., E.G., A.J.H., M.-H.S.S., S.J.C., M.E., Y.N.C., V.G., J.J., A.K.K., P.A.N., C.P.L., A.M., T.M., K.N.M., M.O., E.Y.P., P.S., V.V.I., C.W., and V.V.P. provided and/or collected samples; K.E.W., A.L., J.H., O.L., S.B., A.D., E.A.D., J.E., J.-M.R., and M.-H.S.S. conducted the ancient laboratory work with input from R.S.M., G.L., L.A.F.F., E.W., I.B., and M.T.P.G.; M.M., E.P.M., and A.S. provided and/or collected CTVT samples; M.N.L. and Y.-M.K. conducted the CTVT analyses with input from E.P.M., K.G., and L.A.F.F.; M.N.L., L.A.F.F., and E.K.I.-P. conducted the analyses of ancient data with input from S.G., A.K., A.R.B., and E.P.M.; and L.A.F.F., G.L., E.P.M., M.N.L., and A.R.P. wrote the paper with input from all other authors. **Competing interests:** A.D., J.E., and J.-M.R. are employees of Arbor Biosciences, which provided target enrichment kits used in this study. J.-M.R. is also a founder of Arbor Biosciences. A.R.B. is the founder and chief strategy

officer of Embark Veterinary. K.M.D. currently holds honorary professor positions in the departments of archaeology at both the University of Aberdeen and Simon Fraser University. **Data and materials availability:** The reads for the ancient data have been deposited at the European Nucleotide Archive (ENA) with project number PRJEB22026. Reads for new CTVT genomes were deposited at the European Nucleotide Archive (ENA) with project number PRJEB22148. Mitochondrial sequence alignments, genotype files (in plink format), and phylogenetic trees were deposited in Dryad (*26*).

SUPPLEMENTARY MATERIALS

www.sciencemag.org/content/361/6397/81/suppl/DC1
Materials and Methods
Figs. S1 to S27
Tables S1 to S16
References (*27*–*180*)

13 September 2017; resubmitted 26 December 2017
Accepted 10 May 2018
10.1126/science.aao4776

DOMESTICATION

Ancient goat genomes reveal mosaic domestication in the Fertile Crescent

Kevin G. Daly[1]*, Pierpaolo Maisano Delser[1,2]*, Victoria E. Mullin[1,3], Amelie Scheu[1,4], Valeria Mattiangeli[1], Matthew D. Teasdale[1,5], Andrew J. Hare[1], Joachim Burger[4], Marta Pereira Verdugo[1], Matthew J. Collins[5,6], Ron Kehati[7], Cevdet Merih Erek[8], Guy Bar-Oz[9], François Pompanon[10], Tristan Cumer[10], Canan Çakırlar[11], Azadeh Fatemeh Mohaseb[12,13], Delphine Decruyenaere[12], Hossein Davoudi[14,15], Özlem Çevik[16], Gary Rollefson[17], Jean-Denis Vigne[12], Roya Khazaeli[13], Homa Fathi[13], Sanaz Beizaee Doost[13], Roghayeh Rahimi Sorkhani[18], Ali Akbar Vahdati[19], Eberhard W. Sauer[20], Hossein Azizi Kharanaghi[21], Sepideh Maziar[22], Boris Gasparian[23], Ron Pinhasi[24], Louise Martin[25], David Orton[5], Benjamin S. Arbuckle[26], Norbert Benecke[27], Andrea Manica[2], Liora Kolska Horwitz[7], Marjan Mashkour[12,13,15], Daniel G. Bradley[1]†

Current genetic data are equivocal as to whether goat domestication occurred multiple times or was a singular process. We generated genomic data from 83 ancient goats (51 with genome-wide coverage) from Paleolithic to Medieval contexts throughout the Near East. Our findings demonstrate that multiple divergent ancient wild goat sources were domesticated in a dispersed process that resulted in genetically and geographically distinct Neolithic goat populations, echoing contemporaneous human divergence across the region. These early goat populations contributed differently to modern goats in Asia, Africa, and Europe. We also detect early selection for pigmentation, stature, reproduction, milking, and response to dietary change, providing 8000-year-old evidence for human agency in molding genome variation within a partner species.

The Fertile Crescent of Southwest Asia and adjacent areas were the location of transformative prehistoric innovations including the domestication of sheep, goats, cattle, and pigs (*1*–*3*). Archaeological evidence suggests local development of wild goat (bezoar) management strategies in different regions in the mid- to late 11th millennium before the present (BP) with domestic phenotypes emerging in the 10th millennium, first in the Anatolian region (*4*–*6*). A key question is whether these early patterns of exploitation are consistent with a geographically focused singular domestication process or whether domestic goats were recruited from separate populations, with parallel genetic consequences. Genetic evidence is inconclusive (*7*, *8*).

We generated ancient *Capra* genome data from Neolithic sites from western (Anatolia and the Balkans), eastern (Iran and Turkmenistan), and southern (Jordan and Israel) regions around the Fertile Crescent (tables S1 to S3). To maximize yields, we sampled mainly petrous bones; 51 such samples produced nuclear genome coverage ranging from 0.01× to 14.89× (median 1.05×) (tables S4 and S5). We enriched for mitochondrial DNA (mtDNA) in poorly preserved samples and obtained a total of 83 whole mitochondrial genomes (median 70.95×) (table S6 and figs. S1 and S2) (*9*).

The majority of our ancient domestic mitochondrial sequences fall within modern haplogroups A, B, C, D, and G (Fig. 1A, figs. S3 to S6, and tables S7 to S9). The Paleolithic wild goat samples fall exclusively in more divergent clades T [similar to the related wild caprid, the West Caucasian tur (*Capra caucasica*)] and F [previously reported in bezoar and a small number of Sicilian goats (*10*)]. Here, we found F in a >47,000 BP bezoar from Hovk-1 cave, Armenia; in a pre-domestic goat from Direkli Cave, Turkey; and in Levantine goats at 'Ain Ghazal, an early Neolithic village in Jordan, and Abu Ghosh, Israel.

A geographic plot of Neolithic samples illustrates that early domestic goat haplogroups are highly structured (Fig. 1B), with disjunct distributions in the western, eastern, and southern (Levantine) regions of the Near East (tables S10 and S11). In this early farming period, partitioning is significant; analysis of molecular variance (*9*) estimates that 81% of the mtDNA diversity stems from differences between the three regions (P = 0.028, permutation test) (tables S12 and S13). When we use an approximate Bayesian computation (ABC) framework on this mtDNA variation to investigate demographic history, a model suggesting a pre-domestic branching of the divergent Levant population (38,500 to 195,200 BP) is favored. This suggests multiple wild origins of Neolithic goat herds (tables S14 to S19) (*9*). In the later post-Neolithic samples,

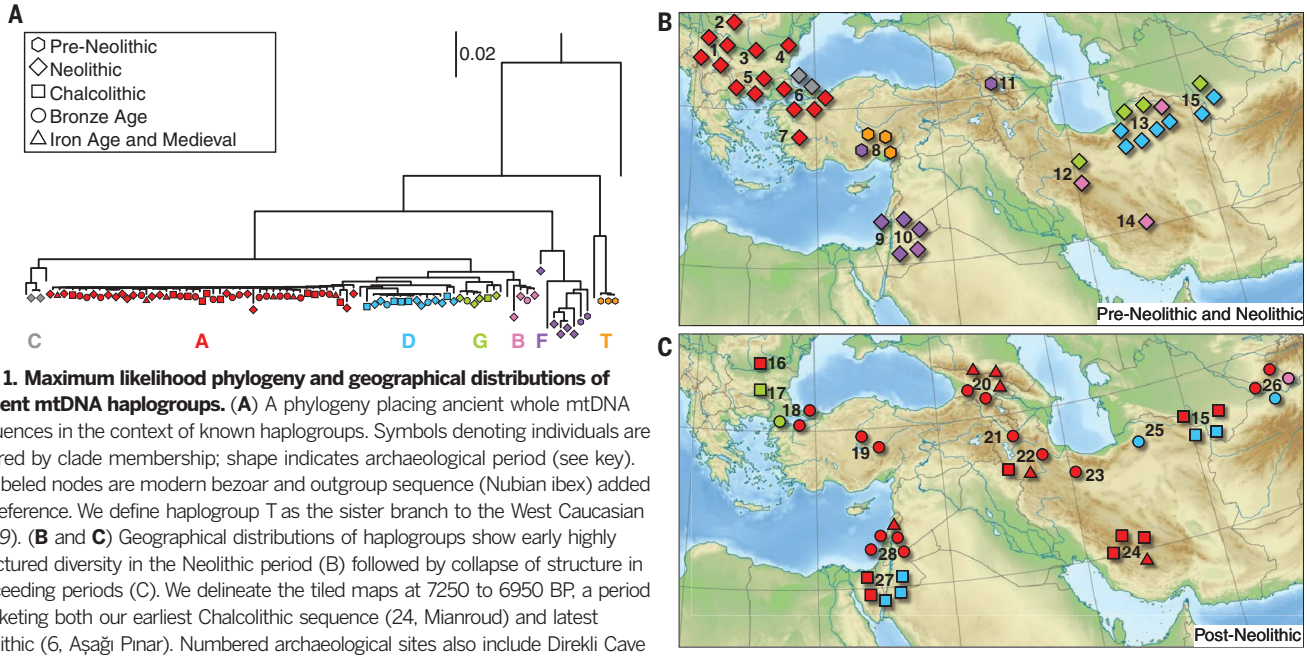

Fig. 1. Maximum likelihood phylogeny and geographical distributions of ancient mtDNA haplogroups. (**A**) A phylogeny placing ancient whole mtDNA sequences in the context of known haplogroups. Symbols denoting individuals are colored by clade membership; shape indicates archaeological period (see key). Unlabeled nodes are modern bezoar and outgroup sequence (Nubian ibex) added for reference. We define haplogroup T as the sister branch to the West Caucasian tur (*9*). (**B** and **C**) Geographical distributions of haplogroups show early highly structured diversity in the Neolithic period (B) followed by collapse of structure in succeeding periods (C). We delineate the tiled maps at 7250 to 6950 BP, a period bracketing both our earliest Chalcolithic sequence (24, Mianroud) and latest Neolithic (6, Aşağı Pınar). Numbered archaeological sites also include Direkli Cave (8), Abu Ghosh (9), 'Ain Ghazal (10), and Hovk-1 Cave (11) (table S1) (*9*).

this partitioning collapses to zero (Fig. 1C) and the ubiquitous modern haplogroup, A, becomes widespread.

Analyses of genome-wide variation also argue against a single common origin. Neolithic samples from the west, east, and Levant each cluster separately in principal components analysis (PCA; Fig. 2) and in phylogenetic reconstruction (figs. S7 to S10). *D* statistics show that these clusters have significantly different levels of allele sharing with two regional samples of pre-domestic wild goats: a ~13,000 BP population from Direkli cave (Southeast Anatolia) and a >47,000 BP bezoar from Hovk-1 cave (Armenia) (Fig. 3A) (*9*). These differences are consistent with qpGraph estimation of relationships (Fig. 3B, fig. S11, and table S20) where a primary ancestral divide between western and eastern genomes occurred more than 47,000 BP. The latter clade gave rise to the eastern Neolithic population. However, the western and Levant Neolithic goat derive ~50% and ~70% of their ancestry from a divergent source in the western clade that had affinity to the Anatolian wild population, in line with f_4 ratios and Treemix graphs (fig. S12 and table S21). These different proportions infer substantial local recruitment from different wild populations into early herds in regions proximal to each of the different vertices of the Fertile Crescent. ABC modeling of autosomal variation also rejects a single domestication origin scenario (figs. S13 to S15 and tables S11 and S22 to S25) (*9*).

Thus, our data favor a process of Near Eastern animal domestication that is dispersed in space and time, rather than radiating from a central core (*3*, *11*). This resonates with archaeozoological evidence for disparate early management strategies from early Anatolian, Iranian, and Levantine Neolithic sites (*12*, *13*). Interestingly, our finding of divergent goat genomes within the Neolithic echoes genetic investigation of early farmers. Northwestern Anatolian and Iranian human Neolithic genomes are also divergent (*14*–*16*), which suggests the sharing of techniques rather than large-scale migrations of populations across Southwest Asia in the period of early domestication. Several crop plants also show evidence of parallel domestication processes in the region (*17*).

PCA affinity (Fig. 2), supported by qpGraph and outgroup f_3 analyses, suggests that modern European goats derive from a source close to the western Neolithic; Far Eastern goats derive from

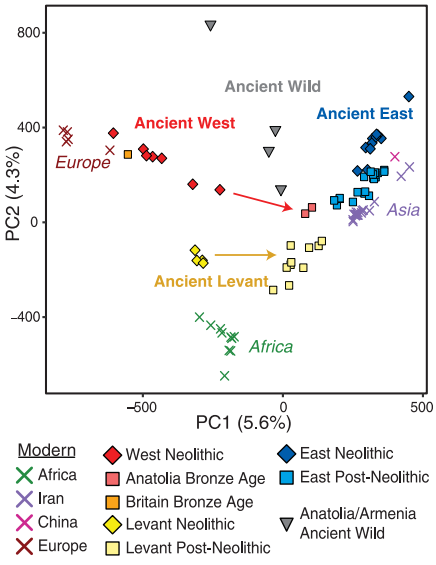

Fig. 2. Principal components analysis of ancient and modern goat genomes. Ancient goats cluster in three vertices: eastern (Iran, Uzbekistan, Turkmenistan, Georgia), western (Balkans, Anatolia), and southern or Levantine (Jordan, Israel) margins of the Near East. Modern European, Asian and, interestingly, African goats follow this pattern, but Bronze Age Anatolian (red arrow) and Chalcolithic/Bronze Age Israeli (yellow arrow) samples show shifts relative to earlier genomes from those regions, suggesting post-Neolithic admixture within the primary regions.

early eastern Neolithic domesticates; and African goats have a contribution from the Levant, but in this case with considerable admixture from the other sources (figs. S11, S16, and S17 and tables S26 and 27). The latter may be in part a result of admixture that is discernible in the same analyses extended to ancient genomes within the Fertile Crescent after the Neolithic (figs. S18 and S19 and tables S20, S27, and S31) when the spread of metallurgy and other developments likely resulted in an expansion of inter-regional trade networks and livestock movement.

Animal domestication likely involved adaptive pressures due to infection, changes in diet, translocation beyond natural habitat, and human selection (*18*). We thus took an outlier approach to identify loci that underwent selective sweeps in either six eastern Neolithic genomes or four western genome samples (minimum coverage 2×). We compared each population to 16 modern bezoar genomes (*19*) and identified 18 windows with both high divergence (highest 0.1% *Fst* values) and reduced diversity in Neolithic goats (lowest 5% θ ratio: Neolithic/wild; tables S28, S29, and S32).

The pigmentation loci, *KIT* and *KITLG*, are the only shared signals in both Neolithic populations. Both are common signals in modern livestock analyses (*19*, *20*). We thus examined *Fst* values for previously reported coloration genes and identified *ASIP* and *MITF* as also showing high values (Fig. 4, A and B, fig. S20, and table S30). Whereas modern breeds are defined in part by color pattern, the driver of the ~8000-year-old selection observed in the Neolithic for pigmentation may be less obvious. *KIT* is involved in the piebald trait in mammals (*21*) and may have been favored as a means of distinguishing individuals and maintaining ownership within shared herds as well as for aesthetic value. Pigmentation change has also been proposed as a pleiotropic effect of selection for tameness (*22*). Intriguingly, selective sweeps around the *KIT* locus were clearly independent in the eastern and western Neolithic goat sampled genomes, as the resulting locus genotypes are distinct and contribute differently to modern eastern and western populations (Fig. 4C).

Trait mapping in cattle, the most studied ungulate, offers interpretation of three other caprine signals identified here. *SIRT1* (identified in the western Neolithic) has variants affecting stature (*23*), and a reduction in size is a widespread signal of early domestication. *EPGN* (eastern Neolithic) is linked to calving interval; increase in reproductive frequency is another general feature of domestication. *STAT1* (eastern Neolithic) is involved in mammary gland development and has been linked to milk production (*24*). The second most extreme eastern signal maps to a homolog of human *CYP2C19*, which (like other cytochrome P450 products) contributes to metabolism of xenobiotics including enniatin B, a toxic product of fungal strains that contaminate cereals and grains. This selection signal has been hypothesized as a response to early agriculture in humans (*25*). Early recycling of agricultural by-products as animal fodder has been suggested as a motivation for the origins of husbandry (*3*), and fungal toxins may have been a challenge to early domestic goats as well as their agriculturist owners.

Our results imply a domestication process carried out by humans in dispersed, divergent,

[1]Smurfit Institute of Genetics, Trinity College Dublin, Dublin 2, Ireland. [2]Department of Zoology, University of Cambridge, Cambridge CB2 3EJ, UK. [3]Department of Earth Sciences, Natural History Museum, London SW7 5BD, UK. [4]Palaeogenetics Group, Institute of Organismic and Molecular Evolution (iOME), Johannes Gutenberg University Mainz, 55099 Mainz, Germany. [5]BioArCh, University of York, York YO10 5DD, UK. [6]Museum of Natural History, University of Copenhagen, Copenhagen, Denmark. [7]National Natural History Collections, Faculty of Life Sciences, The Hebrew University, Jerusalem, Israel. [8]Gazi University, Ankara 06500, Turkey. [9]Zinman Institute of Archaeology, University of Haifa, Mount Carmel, Haifa, Israel. [10]Université Grenoble Alpes, Univ. Savoie Mont Blanc, CNRS, LECA, F-38000 Grenoble, France. [11]Groningen Institute of Archaeology, Groningen University, Groningen, Netherlands. [12]Archéozoologie, Archéobotanique (UMR 7209), CNRS, MNHN, UPMC, Sorbonne Universités, Paris, France. [13]Archaeozoology section, Archaeometry Laboratory, University of Tehran, Tehran, Iran. [14]Department of Archaeology, Faculty of Humanities, Tarbiat Modares University, Tehran, Iran. [15]Osteology Department, National Museum of Iran, Tehran, Iran. [16]Trakya Universitesi, Edebiyat Fakültesi, Arkeoloi Bölümü, Edirne, Turkey. [17]Department of Anthropology, Whitman College, Walla Walla, WA 99362, USA. [18]Faculty of Cultural Heritage, Handicrafts and Tourism, University of Mazandaran, Noshahr, Iran. [19]Provincial Office of the Iranian Center for Cultural Heritage, Handicrafts and Tourism Organisation, North Khorassan, Bojnord, Iran. [20]School of History, Classics and Archaeology, University of Edinburgh, William Robertson Wing, Old Medical School, Edinburgh EH8 9AG, UK. [21]Prehistory Department, National Museum of Iran, Tehran, Iran. [22]Institut für Archäologische Wissenschaften, Goethe Universität, Frankfurt am Main, Germany. [23]Institute of Archaeology and Ethnology, National Academy of Sciences of the Republic of Armenia, Yerevan 0025, Republic of Armenia. [24]Department of Anthropology, University of Vienna, 1090 Vienna, Austria. [25]Institute of Archeology, University College London, London, UK. [26]Department of Anthropology, University of North Carolina, Chapel Hill, NC, USA. [27]Department of Natural Sciences, German Archaeological Institute, 14195 Berlin, Germany.
*These authors contributed equally to this work.
†Corresponding author. Email: dbradley@tcd.ie

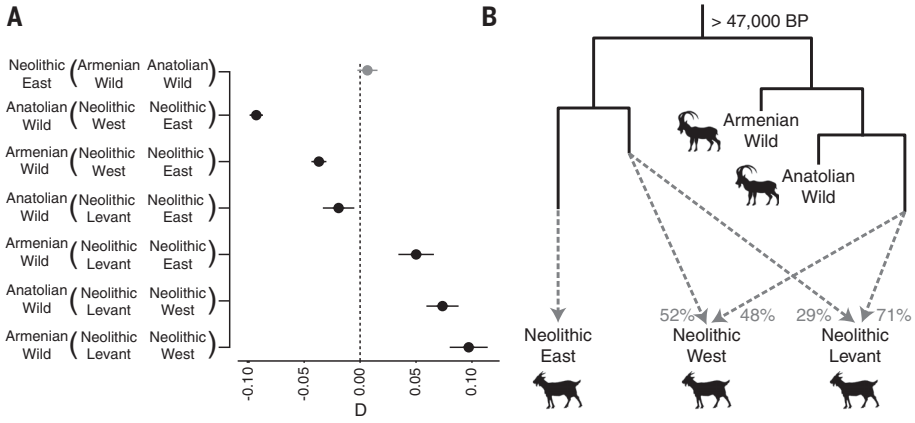

Fig. 3. *D* statistics and admixture graph of ancient and modern goats. (**A**) In the test *X*(*Y*, *Z*), positive or negative *D* values indicate a greater number of derived alleles between *X* and *Z* or *X* and *Y*, respectively; yak is used as an outgroup. *D* values for each test are presented with error bars of 3 SE; a nonsignificant test is shown in gray. These show that regional pre-domestic wild goats relate asymmetrically to Neolithic domestic populations, ruling out a singular origin. (**B**) Admixture graph reconstructing the population history of pre-Neolithic and Neolithic goats. Relative inputs from divergent sources into early domestic herds are represented by gray dashed arrows (drawn from fig. S11F) (*9*).

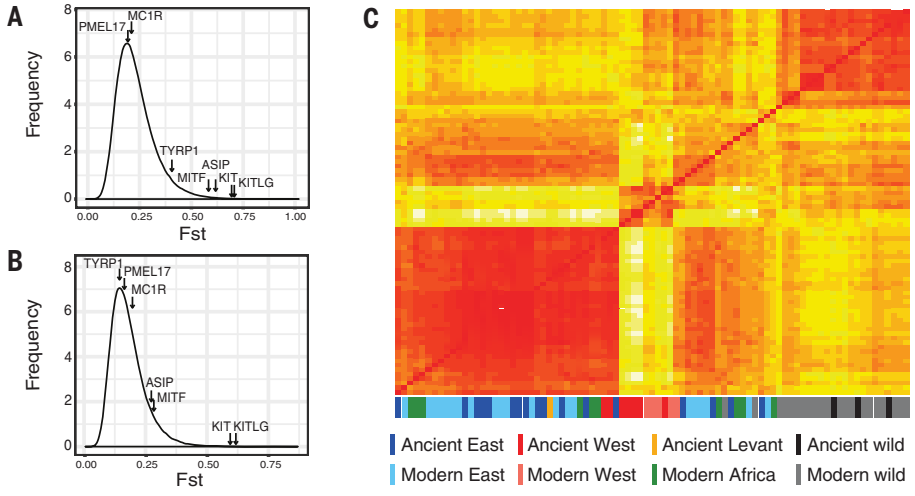

Fig. 4. *Fst* distributions between modern bezoar and Neolithic western and eastern populations, and a heat map of allele sharing between modern and domestic goats at the *KIT* locus. (**A** and **B**) The highest *Fst* values for 50-kb windows overlapping seven pigmentation loci showing evidence of selection in modern goat, sheep, or cattle studies are indicated for western (A) and eastern (B) populations (tables S30 and S32). (**C**) The pigmentation locus, *KIT*, shows evidence of selection in both western and eastern Neolithic samples, but allele sharing distances (illustrated as a heat map) suggest that selection acted on divergent standing variation in parallel but separate processes. Five of the seven ancient western samples are from Neolithic contexts and cluster with modern western haplogroups. The two remaining western ancients (red) falling in the eastern cluster (mainly blue) are Bronze Age Anatolian samples with indications of secondary admixture (Fig. 2).

but communicating communities across the Fertile Crescent who selected animals in early millennia, including for pigmentation, the most visible of domestic traits.

REFERENCES AND NOTES

1. J. Peters, A. von den Driesch, D. Helmer, in *The First Steps of Animal Domestication: New Archaeological Approaches*, J. D. Vigne, J. Peters, D. Helmer, Eds. (Oxbow, 2005), pp. 96–123.
2. M. A. Zeder, *J. Anthropol. Res.* **68**, 161–190 (2012).
3. J.-D. Vigne, L. Gourichon, D. Helmer, L. Martin, J. Peters, in *Quaternary in the Levant*, Y. Enzel, O. Bar Yosef, Eds. (Cambridge Univ. Press, 2017), pp. 753–760.
4. M. A. Zeder, B. Hesse, *Science* **287**, 2254–2257 (2000).
5. D. Helmer, L. Gourichon, in *Archaeozoology of the Near East, vol. 9*, M. Mashkour, M. Beech, Eds. (Oxbow, 2017), pp. 23–40.
6. B. Moradi *et al.*, in *The Neolithic of the Iranian Plateau*, K. Roustaei, M. Mashkour, Eds. (Ex Oriente, 2016), pp. 1–14.
7. S. Naderi *et al.*, *Proc. Natl. Acad. Sci. U.S.A.* **105**, 17659–17664 (2008).
8. P. Gerbault *et al.*, in *Population Dynamics in Prehistory and Early History: New Approaches Using Stable Isotopes and Genetics*, E. Kaiser, J. Burger, W. Schier, Eds. (De Gruyter, 2012), pp. 17–30.
9. See supplementary materials.
10. M. T. Sardina *et al.*, *Anim. Genet.* **37**, 376–378 (2006).
11. M. A. Zeder, *Curr. Anthropol.* **52**, S221–S235 (2011).
12. L. K. Horwitz *et al.*, *Paléorient* **25**, 63–80 (1999).
13. B. S. Arbuckle, L. Atici, *Levant* **45**, 219–235 (2013).
14. F. Broushaki *et al.*, *Science* **353**, 499–503 (2016).
15. I. Lazaridis *et al.*, *Nature* **536**, 419–424 (2016).
16. M. Gallego-Llorente *et al.*, *Sci. Rep.* **6**, 31326 (2016).
17. D. Q. Fuller, G. Willcox, R. G. Allaby, *World Archaeol.* **43**, 628–652 (2011).
18. M. A. Zeder, *Interface Focus* **7**, 20160133 (2017).
19. F. J. Alberto *et al.*, *Nat. Commun.* **9**, 813 (2018).
20. J. W. Kijas *et al.*, *PLOS Biol.* **10**, e1001258 (2012).
21. N. Reinsch *et al.*, *J. Hered.* **90**, 629–634 (1999).
22. L. Trut, I. Oskina, A. Kharlamova, *BioEssays* **31**, 349–360 (2009).
23. M. Li *et al.*, *Mol. Cell. Probes* **27**, 215–220 (2013).
24. O. Cobanoglu, I. Zaitoun, Y. M. Chang, G. E. Shook, H. Khatib, *J. Dairy Sci.* **89**, 4433–4437 (2006).
25. R. E. Janha *et al.*, *BMC Evol. Biol.* **14**, 71 (2014).

ACKNOWLEDGMENTS

We thank L. Cassidy, E. Jones, L. Frantz, G. Larson, and M. Zeder for critical reading of the text; the Israel Antiquities Authority for permitting sampling of the Israeli sites (under permit); excavators, archaeozoologists, and museums who permitted sampling from their excavations and collections without which this project would not have been possible, including T. Levy, C. Grigson, A. Maeir, S. Gitin, P. de Miroschedji, S. Davis, and A. Ben-Tor; the Iranian Cultural Heritage Handicraft and Tourism organization and the National Museum of Iran (NMI) and J. Nokandeh, director, and F. Biglari, cultural deputy; H. Laleh and A. Aliyari, Directors of the Archaeometry Laboratory of the University of Tehran. The ATM Project of MNHN supported sampling of several sites as well as the LIA HAOMA CNRS project. We are grateful for assistance from J. Vuković, J. Bulatović, I. Stojanović, H. Greenfield, Wiltshire Museum, L. Brown, and Trinseq. The authors wish to acknowledge the DJEI/DES/SFI/HEA Irish Centre for High-End Computing (ICHEC) for the provision of computational facilities and support. **Funding:** Supported by ERC Investigator grant 295729-CodeX. Additional support from Science Foundation Ireland Award 12/ERC/B2227. P.M.D. was supported by the HERA Joint Research Programme "Uses of the Past" (CitiGen); and the European Union's Horizon 2020 research and innovation program under grant agreement no. 649307. A.M. was supported by ERC Consolidator grant 647787-LocalAdaptation. M.D.T. was supported by the Marie Skłodowska-Curie Individual Fellowship SCRIBE H2020-MSCA-IF-2016 747424. Author contributions: D.G.B. conceived of the project and designed the research, with input from J.B. and M.C.; C.C., R.P., L.M., D.O., B.S.A., N.B., L.K.H., M.M., R.Ke., C.M.E., G.B.O., F.P., T.C., J.D.V., A.F.M., D.D., H.D., Ö.C., R.Kh., H.F., S.B., R.R.S., A.A.V., E.W.S., H.A.K., and S.M. provided samples and data; K.G.D., V.E.M., V.M., A.S., A.J.H., and M.D.T. performed genomics laboratory work; P.M.D. performed ABC analyses, with input from A.M., K.G.D., and D.G.B.; K.G.D. performed the computational analyses with input from D.G.B., V.E.M., M.P.V., and M.D.T.; D.G.B. and K.G.D. wrote the paper, with input from all other co-authors; K.G.D. and P.M.D. wrote the supplementary information, with input from all other authors. **Competing interests:** The authors declare that they have no competing interests. **Data and materials availability:** Raw reads and mitochondrial sequences have been deposited at the European Nucleotide Archive (ENA) with project number: PRJEB26011. Mitochondrial phylogenies are available at https://osf.io/g5c8k/.

SUPPLEMENTARY MATERIALS

www.sciencemag.org/content/361/6397/85/suppl/DC1
Materials and Methods
Figs. S1 to S20
Tables S1 to S32
References (*26*–*187*)

11 January 2018; resubmitted 13 February 2018
Accepted 4 June 2018
10.1126/science.aas9411

HUMAN GENOMICS

The prehistoric peopling of Southeast Asia

Hugh McColl[1]*, Fernando Racimo[1]*, Lasse Vinner[1]*, Fabrice Demeter[1,2]*, Takashi Gakuhari[3,4], J. Víctor Moreno-Mayar[1], George van Driem[5,6], Uffe Gram Wilken[1], Andaine Seguin-Orlando[1,7], Constanza de la Fuente Castro[1], Sally Wasef[8], Rasmi Shoocongdej[9], Viengkeo Souksavatdy[10], Thongsa Sayavongkhamdy[10], Mohd Mokhtar Saidin[11], Morten E. Allentoft[1], Takehiro Sato[12], Anna-Sapfo Malaspinas[13], Farhang A. Aghakhanian[14], Thorfinn Korneliussen[1], Ana Prohaska[15], Ashot Margaryan[1,16], Peter de Barros Damgaard[1], Supannee Kaewsutthi[17], Patcharee Lertrit[17], Thi Mai Huong Nguyen[18], Hsiao-chun Hung[19], Thi Minh Tran[18], Huu Nghia Truong[18], Giang Hai Nguyen[18], Shaiful Shahidan[11], Ketut Wiradnyana[20], Hiromi Matsumae[4], Nobuo Shigehara[21], Minoru Yoneda[22], Hajime Ishida[23], Tadayuki Masuyama[24], Yasuhiro Yamada[25], Atsushi Tajima[12], Hiroki Shibata[26], Atsushi Toyoda[27], Tsunehiko Hanihara[4], Shigeki Nakagome[28], Thibaut Deviese[29], Anne-Marie Bacon[30], Philippe Duringer[31,32], Jean-Luc Ponche[33], Laura Shackelford[34], Elise Patole-Edoumba[35], Anh Tuan Nguyen[18], Bérénice Bellina-Pryce[36], Jean-Christophe Galipaud[37], Rebecca Kinaston[38,39], Hallie Buckley[38], Christophe Pottier[40], Simon Rasmussen[41], Tom Higham[29], Robert A. Foley[42], Marta Mirazón Lahr[42], Ludovic Orlando[1,7], Martin Sikora[1], Maude E. Phipps[14], Hiroki Oota[4], Charles Higham[43,44], David M. Lambert[8], Eske Willerslev[1,15,45]†

The human occupation history of Southeast Asia (SEA) remains heavily debated. Current evidence suggests that SEA was occupied by Hòabìnhian hunter-gatherers until ~4000 years ago, when farming economies developed and expanded, restricting foraging groups to remote habitats. Some argue that agricultural development was indigenous; others favor the "two-layer" hypothesis that posits a southward expansion of farmers giving rise to present-day Southeast Asian genetic diversity. By sequencing 26 ancient human genomes (25 from SEA, 1 Japanese Jōmon), we show that neither interpretation fits the complexity of Southeast Asian history: Both Hòabìnhian hunter-gatherers and East Asian farmers contributed to current Southeast Asian diversity, with further migrations affecting island SEA and Vietnam. Our results help resolve one of the long-standing controversies in Southeast Asian prehistory.

Anatomically modern humans expanded into Southeast Asia (SEA) at least 65 thousand years (ka) ago (*1*, *2*), leading to the formation of the Hòabìnhian hunter-gatherer tradition first recognized by ~44 ka ago (*3*, *4*). Though Hòabìnhian foragers are considered the ancestors of present-day hunter-gatherers from mainland Southeast Asia (MSEA) (*5*), the East Asian phenotypic affinities of the majority of present-day Southeast Asian populations suggest that diversity was influenced by later migrations involving rice and millet farmers from the north (*4*). These observations have generated two competing hypotheses: One states that the Hòabìnhian hunter-gatherers adopted agriculture without substantial external gene flow (*6*, *7*), and the other (the "two-layer" hypothesis) states that farmers from East Asia (EA) replaced the indigenous Hòabìnhian inhabitants ~4 ka ago (*8*, *9*). Studies of present-day populations have not resolved the extent to which migrations from EA affected the genetic makeup of SEA.

Obtaining ancient DNA evidence from SEA is challenging because of poor preservation conditions (*10*). We thus tested different whole-human-genome capture approaches and found that a modified version of MYbaits Enrichment performed best (*11*). We applied this method together with standard shotgun sequencing to DNA extracted from human skeletal material from Malaysia, Thailand, the Philippines, Vietnam, Indonesia, Laos, and Japan dating between 0.2 and 8 ka ago (*11*). We obtained 26 low-coverage ancient whole genomes, including those of a Japanese Ikawazu Jōmon individual and Hòabìnhian hunter-gatherers from Malaysia and Laos, as well as Late Neolithic, Bronze Age, and Iron Age farmers from across SEA (Fig. 1 and table S1) (*11*). We also sequenced mitochondrial DNA from 16 additional ancient individuals and high-coverage whole genomes from two present-day Jehai individuals from Northern Parak state, West Malaysia (table S3). All samples showed damage patterns typical of ancient DNA and minimal amounts of contamination (table S3) (*11*).

We performed a principal component analysis (PCA) of worldwide present-day populations (*12*, *13*) to find the strongest axes of genetic variation in our data and projected the ancient individuals onto the first two principal components. The two oldest samples—Hòabìnhians from Pha Faen, Laos [La368; 7950 with 7795 calendar years before the present (cal B.P.)] and Gua Cha, Malaysia (Ma911; 4415 to 4160 cal B.P.)—henceforth labeled "group 1," cluster most closely with present-day Önge from the Andaman Islands and away from other East Asian and Southeast Asian populations (Fig. 2), a pattern that differentiates them from all other ancient samples. We used ADMIXTURE (*14*) and fastNGSadmix (*15*) to model ancient genomes as mixtures of latent ancestry components (*11*). Group

[1]Centre for GeoGenetics, Natural History Museum of Denmark, Copenhagen, Denmark. [2]National Museum of Natural History, Ecoanthropology and Ethnobiology, Musée de l'Homme, Paris, France. [3]Center for Cultural Resource Studies, Kanazawa University, Kanazawa, Japan. [4]Kitasato University School of Medicine, Sagamihara, Kanagawa, Japan. [5]Institut für Sprachwissenschaft, Universität Bern, Bern, Switzerland. [6]University of New England, Armidale, NSW, Australia. [7]Laboratoire AMIS, Université Paul Sabatier (UPS), Toulouse, France. [8]Australian Research Centre for Human Evolution, Griffith University, Nathan, QLD, Australia. [9]Department of Archaeology, Faculty of Archaeology, Silpakorn University, Bangkok, Thailand. [10]Department of Heritage, Ministry of Information, Culture and Tourism, Vientiane, Lao People's Democratic Republic. [11]Centre for Global Archaeological Research, Universiti Sains Malaysia, Penang, Malaysia. [12]Department of Bioinformatics and Genomics, Graduate School of Advanced Preventive Medical Sciences, Kanazawa University, Kanazawa, Japan. [13]Department of Computational Biology, University of Lausanne and SIB Swiss Institute of Bioinformatics, Lausanne, Switzerland. [14]Jeffrey Cheah School of Medicine & Health Sciences, Monash University Malaysia, Jalan Lagoon Selatan, Sunway City, Selangor, Malaysia. [15]Department of Zoology, University of Cambridge, Cambridge, UK. [16]Institute of Molecular Biology, National Academy of Sciences, Yerevan, Armenia. [17]Department of Biochemistry, Faculty of Medicine Siriraj Hospital, Mahidol University, Bangkok, Thailand. [18]Anthropological and Paleoenvironmental Department, Institute of Archaeology, Hanoi, Vietnam. [19]Department of Archaeology and Natural History, Australian National University, Canberra, ACT, Australia. [20]Balai Archeology, Medan, Indonesia. [21]Nara National Research Institute for Cultural Properties, Nara, Japan. [22]University Museum, University of Tokyo, Tokyo, Japan. [23]Graduate School of Medicine, University of the Ryukyus, Nishihara, Okinawa, Japan. [24]Educational Committee of Tahara City, Tahara, Japan. [25]National Museum of Japanese History, Sakura, Chiba, Japan. [26]Division of Genomics, Medical Institute of Bioregulation, Kyushu University, Fukuoka, Japan. [27]Center for Information Biology, National Institute of Genetics, Mishima, Japan. [28]School of Medicine, Trinity College Dublin, University of Dublin, Dublin, Ireland. [29]Oxford Radiocarbon Accelerator Unit (ORAU), University of Oxford, Oxford, UK. [30]Laboratoire AMIS, Université Paris Descartes, Faculté de Chirurgie Dentaire, Montrouge, France. [31]École et Observatoire des Sciences de la Terre, Université de Strasbourg, Strasbourg, France. [32]Institut de Physique du Globe de Strasbourg (IPGS) (CNRS/UDS UMR 7516), Strasbourg, France. [33]Laboratory "Image Ville et Environnement LIVE," UMR7362, CNRS and Université de Strasbourg, Strasbourg, France. [34]Department of Anthropology, University of Illinois at Urbana-Champaign, Champaign, IL, USA. [35]Natural History Museum of La Rochelle, La Rochelle, France. [36]CNRS, UMR7055 "Préhistoire et Technologie," Maison Archéologie et Ethnologie, Nanterre, France. [37]Research Institute for Development, National Museum of Natural History, UMR Paloc, Paris, France. [38]Department of Anatomy, School of Biomedical Sciences, University of Otago, Dunedin, New Zealand. [39]Department of Archaeogenetics, Max Planck Institute for the Science of Human History, Jena, Germany. [40]École Française d'Extrême-Orient, Paris, France. [41]Department of Bio and Health Informatics, Technical University of Denmark, Kongens Lyngby, Denmark. [42]Leverhulme Centre for Human Evolutionary Studies, Department of Archaeology, University of Cambridge, Cambridge, UK. [43]Department of Anthropology and Archaeology, University of Otago, Dunedin, New Zealand. [44]St. Catharine's College, University of Cambridge, Cambridge, UK. [45]Wellcome Trust Sanger Institute, Hinxton, UK.

*These authors contributed equally to this work.

†Corresponding author. Email: ewillerslev@snm.ku.dk

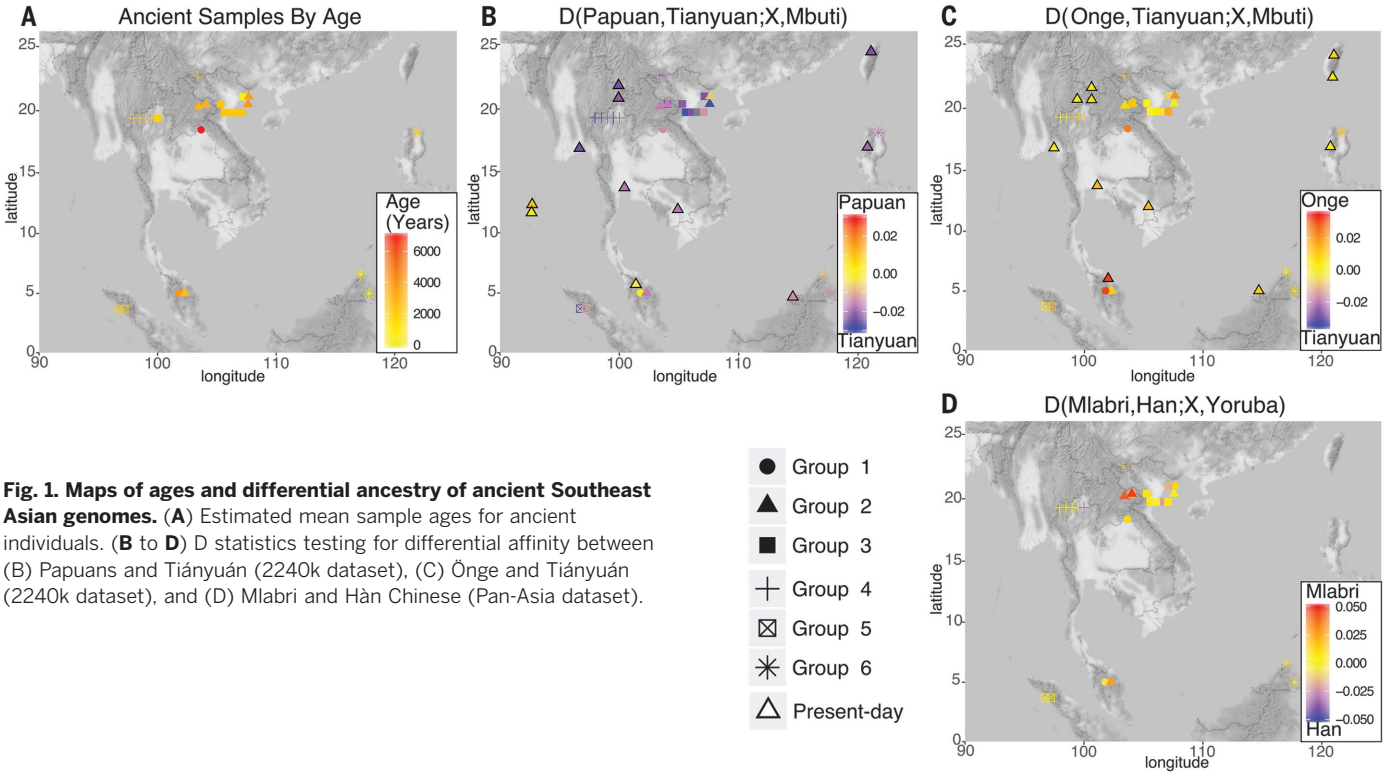

Fig. 1. Maps of ages and differential ancestry of ancient Southeast Asian genomes. (**A**) Estimated mean sample ages for ancient individuals. (**B** to **D**) D statistics testing for differential affinity between (B) Papuans and Tiányuán (2240k dataset), (C) Önge and Tiányuán (2240k dataset), and (D) Mlabri and Hàn Chinese (Pan-Asia dataset).

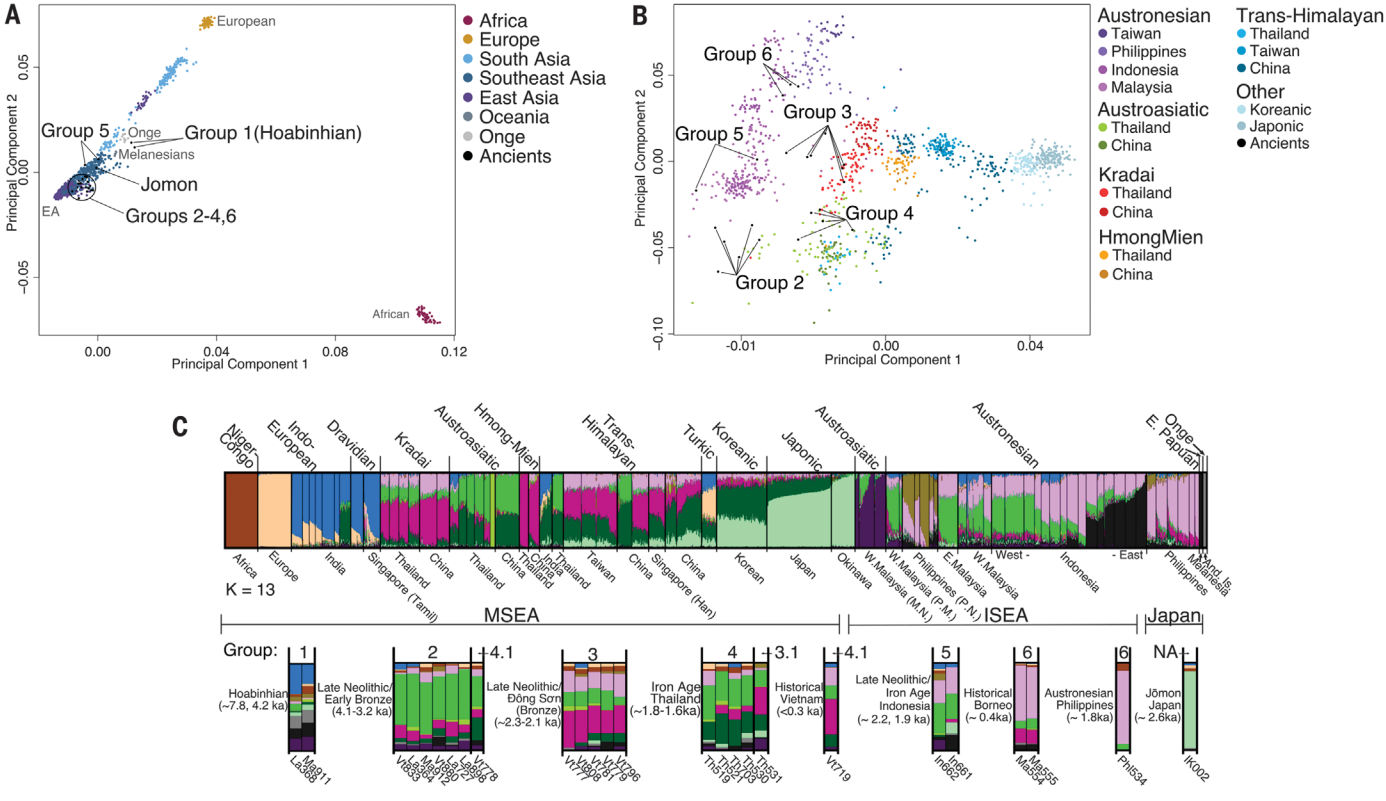

Fig. 2. Exploratory analyses of relationships of ancient Southeast Asian genomes to those of present-day populations. Ancient samples are projected on the first two components of PCAs for (**A**) worldwide populations and (**B**) a subset of populations from EA and SEA. (**C**) fastNGSadmix plot at $K = 13$ (*11*). We refer to the following present-day language-speaking groups in relation to our ancient samples: Austroasiatic (bright green), Austronesian (pink), and Hmong-Mien (dark pink), along with a broad East Asian component (dark green). P.M., proto-Malay; M.N., Malaysian negrito; P.N., Philippines negrito; And. Is., Andaman Islands; NA, not applicable.

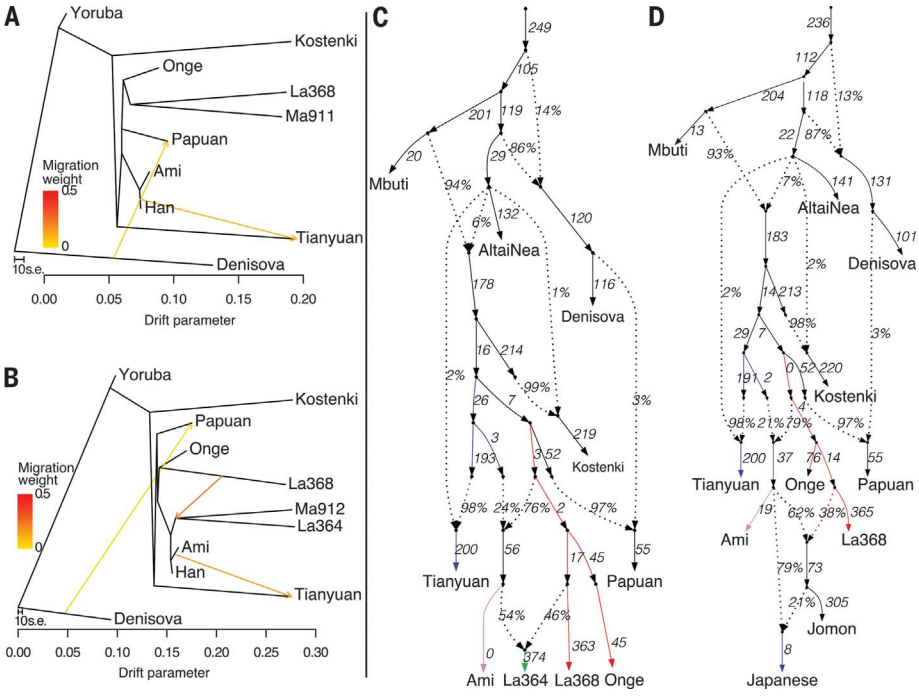

Fig. 3. Admixture graphs fitting ancient Southeast Asian genomes. TreeMix and qpGraph admixture graphs combining present-day populations and selected ancient samples with high single-nucleotide polymorphism coverage (*11*). (**A**) A graph including group 1 samples (Ma911 and La368) fits them as sister groups to present-day Önge. (**B**) A graph including the highest-coverage group 1 (La368) and group 2 (La364, Ma912) samples shows that group 2 receives ancestry from both group 1 and the East Asian branch. (**C**) Using qpGraph, we modeled present-day East Asians (represented by Amis) as a mixture of an Önge-like population and a population related to the Tiányuán individual. (**D**) The Jōmon individual is modeled as a mix of Hòabìnhian (La368) and East Asian ancestry.

1 individuals differ from the other Southeast Asian ancient samples in containing components shared with the supposed descendants of the Hòabìnhians: the Önge and the Jehai (Peninsular Malaysia), along with groups from India and Papua New Guinea.

We also find a distinctive relationship between the group 1 samples and the Ikawazu Jōmon of Japan (IK002). Outgroup f_3 statistics (*11*, *16*) show that group 1 shares the most genetic drift with all ancient mainland samples and Jōmon (fig. S12 and table S4). All other ancient genomes share more drift with present-day East Asian and Southeast Asian populations than with Jōmon (figs. S13 to S19 and tables S4 to S11). This is apparent in the fastNGSadmix analysis when assuming six ancestral components (K = 6) (fig. S11), where the Jōmon sample contains East Asian components and components found in group 1. To detect populations with genetic affinities to Jōmon, relative to present-day Japanese, we computed D statistics of the form D(Japanese, Jōmon; X, Mbuti), setting X to be different present-day and ancient Southeast Asian individuals (table S22). The strongest signal is seen when X = Ma911 and La368 (group 1 individuals), showing a marginally nonsignificant affinity to Jōmon (*11*). This signal is not observed with X = Papuans or Önge, suggesting that the Jōmon and Hòabìnhians may share group 1 ancestry (*11*).

D-statistics of the form D(Papuan, Tiányuán; Y, Mbuti), where Y is a test population, are consistent with present-day East Asian populations and most populations of ancient and present-day SEA being more closely related to Tiányuán [a 40-ka-old East Asian individual (*17*)] than to Papuans (Fig. 1) (*11*, *18*). However, this D statistic is not significantly different from 0 for Y = Jehai, Önge, Jarawa or group 1 (the ancient Hòabìnhians) (table S12). D statistics of the form D(Önge, Tiányuán; X, Mbuti), where X is Jarawa, Jehai, or group 1, show that these populations share more ancestry with Önge than with Tiányuán (Fig. 1) (*11*). Using TreeMix and qpGraph (*16*, *19*) to explore admixture graphs that could potentially fit our data, we find that group 1 individuals are best modeled as a sister group to present-day Önge (Fig. 3, and figs. S21 to S23 and S35 to S37). Finally, the Jōmon individual is best-modeled as a mix between a population related to group 1/Önge and a population related to East Asians (Amis), whereas present-day Japanese can be modeled as a mixture of Jōmon and an additional East Asian component (Fig. 3 and fig. S29).

The remaining ancient individuals are modeled in fastNGSadmix as containing East Asian and Southeast Asian components present in high proportions in present-day Austroasiatic, Austronesian, and Hmong-Mien speakers, along with a broad East Asian component. A PCA including only East Asian and Southeast Asian populations that did not show considerable Papuan or Önge-like ancestry (fig. S11) separates the present-day speakers of ancestral language families in the region: Trans-Himalayan (formerly Sino-Tibetan), Austroasiatic, and Austronesian/Kradai (*20*). The ancient individuals form five slightly differentiated clusters (groups 2 to 6) (Fig. 1B), in concordance with fastNGSadmix and f_3 results (Fig. 2 and figs. S12 to S19) (*11*).

Group 2 contains late Neolithic and early Bronze Age individuals (4291 to 2184 cal B.P.), from Vietnam, Laos, and the Malay Peninsula who are closely related to present-day Austroasiatic language speakers such as the Mlabri and Htin (Fig. 1) (*11*). Compared with groups 3 to 6, group 2 individuals lack a broad East Asian ancestry component that is at its highest proportion in northern EA in fastNGSadmix. TreeMix analyses suggest that the two individuals with the highest coverage in group 2 (La364 and Ma912) form a clade resulting from admixture between the ancestors of East Asians and of La368 (Fig. 3 and figs. S24 to S27). This pattern of complex, localized admixture is also evident in the Jehai, fitted as an admixed population between group 2 (Ma912) and the branch leading to present-day Önge and La368 (fig. S28). Consistent with these results, La364 is best modeled as a mixture of a population ancestral to Amis and the group 1/Önge-like population (Fig. 3). The best model for present-day Dai populations is a mixture of group 2 individuals and a pulse of admixture from East Asians (fig. S39).

Group 6 individuals (1880 to 299 cal B.P.) originate from Malaysia and the Philippines and cluster with present-day Austronesians (*11*) (Fig. 2). Group 6 also contains Ma554, having the highest amounts of Denisovan-like ancestry relative to the other ancient samples, although we observe little variation in this archaic ancestry in our samples from MSEA (*11*).

Group 5 (2304 to 1818 cal B.P.) contains two individuals from Indonesia, modeled by fastNGSadmix as a mix of Austronesian- and Austroasiatic-like ancestry, similar to present-day western Indonesians, a finding consistent with their position in the PCA (Fig. 2) (*11*). Indeed, after Mlabri and Htin, the present-day populations sharing the most drift with group 2 are western Indonesian samples from Bali and Java previously identified as having mainland Southeast Asian ancestry (*21*) (fig. S13). Treemix models the group 5 individuals as an admixed population receiving ancestry related to group 2 (figs. S30 and S31) and Amis. Despite the clear relationship with the mainland group 2 seen in all analyses, the small ancestry components in group 5 related to Jehai and Papuans visible in fastNGSadmix may be remnants of ancient Sundaland ancestry. These results suggest that group 2 and group 5 are related to a

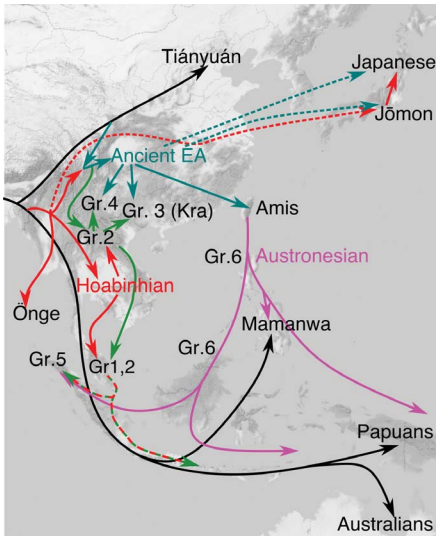

Fig. 4. Model for plausible migration routes into SEA. This schematic is based on ancestry patterns observed in the ancient genomes. Because we do not have ancient samples to accurately resolve how the ancestors of Jōmon and Japanese populations entered the Japanese archipelago, these migrations are represented by dashed arrows. A mainland component in Indonesia is depicted by the dashed red-green line. Gr, group; Kra, Kradai.

mainland migration that expanded southward across MSEA by 4 ka ago and into island Southeast Asia (ISEA) by 2 ka ago (*22*–*24*). A similar pattern is detected for Ma555 (fig. S33) in Borneo (505 to 326 cal B.P., group 6), although this may be a result of recent gene flow.

Group 3 is composed of several ancient individuals from northern Vietnam (2378 to 2041 cal B.P.) and one individual from Long Long Rak (LLR), Thailand (1691 to 1537 cal B.P.). They cluster in the PCA with the Dai, Amis, and Kradai speakers from Thailand, consistent with an Austro-Tai linguistic phylum, comprising both the Kradai and Austronesian language families (*20*, *25*). Group 4 contains the remaining ancient individuals from LLR in Thailand (1570 to 1815 cal B.P.), and Vt778 from inland Vietnam (2750 to 2500 cal B.P.). These samples cluster with present-day Austroasiatic speakers from Thailand and China, in support of a South China origin for LLR (*26*). The genetic distinction between Austroasiatic and Kradai speakers is discussed further in (*11*).

Present-day Southeast Asian populations derive ancestry from at least four ancient populations (Fig. 4). The oldest layer consists of mainland Hòabìnhians (group 1), who share ancestry with present-day Andamanese Önge, Malaysian Jehai, and the ancient Japanese Ikawazu Jōmon. Consistent with the two-layer hypothesis in MSEA, we observe a change in ancestry by ~4 ka ago, supporting a demographic expansion from EA into SEA during the Neolithic transition to farming. However, despite changes in genetic structure coinciding with this transition, evidence of admixture indicates that migrations from EA did not simply replace the previous occupants. Additionally, late Neolithic farmers share ancestry with present-day Austroasiatic-speaking hill tribes, in agreement with the hypotheses of an early Austroasiatic farmer expansion (*20*). By 2 ka ago, Southeast Asian individuals carried additional East Asian ancestry components absent in the late Neolithic samples, much like present-day populations. One component likely represents the introduction of ancestral Kradai languages in MSEA (*11*), and another the Austronesian expansion into ISEA reaching Indonesia by 2.1 ka ago and the Philippines by 1.8 ka ago. The evidence described here favors a complex model including a demographic transition in which the original Hòabìnhians admixed with multiple incoming waves of East Asian migration associated with the Austroasiatic, Kradai, and Austronesian language speakers.

REFERENCES AND NOTES

1. F. Demeter *et al*., *Curr. Anthropol.* **58** (suppl. 17), S527–S538 (2017).
2. K. E. Westaway *et al*., *Nature* **548**, 322–325 (2017).
3. X. Ji *et al*., *Quat. Int.* **400**, 166–174 (2016).
4. C. Higham, *Early Mainland Southeast Asia: From First Humans to Angkor* (River Books, 2014).
5. F. Aghakhanian *et al*., *Genome Biol. Evol.* **7**, 1206–1215 (2015).
6. T. Hanihara, in *Bioarchaeology of Southeast Asia*, M. O. Oxenham, N. Tayles, Eds. (Cambridge Univ. Press, 2006), pp. 91–111.
7. M. Pietrusewsky, in *The Peopling of East Asia: Putting Together Archaeology, Linguistics and Genetics*, L. Sagart, R. Blench, A. Sanchez-Mazas, Eds. (Routledge, 2005), pp. 201–229.
8. H. Matsumura, M. Oxenham, in *Bioarchaeology of East Asia*, K. Pechenkina, M. Oxenham, Eds. (Univ. Press of Florida, 2013), pp. 179–209.
9. T. A. Jinam *et al*., *Genome Biol. Evol.* **9**, 2013–2022 (2017).
10. R. D. Harter, "Acid soils of the tropics" (ECHO Technical Note, ECHO 2007).
11. See supplementary text.
12. G. Abraham, M. Inouye, *PLOS ONE* **9**, e93766 (2014).
13. M. A. Abdulla *et al*., *Science* **326**, 1541–1545 (2009).
14. D. H. Alexander, J. Novembre, K. Lange, *Genome Res.* **19**, 1655–1664 (2009).
15. E. Jørsboe, K. Hanghøj, A. Albrechtsen, *Bioinformatics* **33**, 3148–3150 (2017).
16. N. Patterson *et al*., *Genetics* **192**, 1065–1093 (2012).
17. M. A. Yang *et al*., *Curr. Biol.* **27**, 3202–3208.e9 (2017).
18. S. Mallick *et al*., *Nature* **538**, 201–206 (2016).
19. J. K. Pickrell, J. K. Pritchard, *PLOS Genet.* **8**, e1002967 (2012).
20. G. L. van Driem, in *Language Dispersal Beyond Farming*, M. Robbeets, A. Savelyev, Eds. (John Benjamins Publishing Company, 2017), pp. 183–214.
21. G. Hudjashov *et al*., *Mol. Biol. Evol.* **34**, 2439–2452 (2017).
22. M. Lipson *et al*., *Nat. Commun.* **5**, 4689 (2014).
23. T. Simanjuntak, in *New Perspectives in Southeast Asian and Pacific Prehistory*, P. J. Piper, H. Matsumura, D. Bullock, Eds. (ANU Press, 2017), pp. 201–211.
24. R. A. Blust, *The Austronesian Languages* (Asia-Pacific Linguistics, Australian National University, 2009).
25. W. Ostapirat, in *The Peopling of East Asia: Putting Together Archaeology, Linguistics and Genetics*, L. Saguaro, R. Blench, A. Sanchez-Mazas, Eds. (Routledge Curzon, 2005), pp. 107–131.
26. R. Shoocondej, *Coffin Culture of Thailand in Southeast Asian Context* (Charansanitwonge Press, 2017).

ACKNOWLEDGMENTS

We thank the National High-throughput DNA Sequencing Centre (Copenhagen Denmark) for advice and sequencing of samples, the Duckworth laboratory, University of Cambridge, for access to materials, K. Gregersen for making casts of teeth before sampling, and P. Tacon, ARCHE, Griffith University for assistance with sample transfer. E.W. thanks St. John's College, University of Cambridge, for providing an inspiring environment for scientific thought. **Funding:** This work was supported by the Lundbeck Foundation, the Danish National Research Foundation, and the KU2016 program. H.Mc. is supported by the University of Adelaide's George Murray Scholarship. R.S. thanks the Thailand Research Fund (TRF) for support (grants RTA6080001 and RDG55H0006). The excavation of the Jōmon individual was supported by a Grant-in-Aid for Scientific Research (B) (25284157) to Y.Y. The Jōmon genome project was organized by H.I.; as well as T.H. and H.O., who were supported by MEXT KAKENHI grants 16H06408 and 17H05132; and a Grants-in-Aid for Challenging Exploratory Research (23657167) and for Scientific Research (B) (17H03738). The Jōmon genome sequencing was supported by JSPS KAKENHI grant 16H06279 to A.T. and partly supported by the CHOZEN project in Kanazawa University and the Cooperative Research Project Program of the Medical Institute of Bioregulation, Kyushu University. Computations for the Jōmon genome were partially performed on the NIG supercomputer at ROIS National Institute of Genetics. M.M.L. is supported by the ERC award 295907. D.M.L. was supported by ARC grants LP120200144, LP150100583, and DP170101313. A.P. is supported by Leverhulme Project Research grant RPG-2016-235. M.E.P. acknowledges the Cardio-Metabolic research cluster at Jeffrey Cheah School of Medicine & Health Sciences, TMB research platform, Monash University Malaysia, and MOSTI Malaysia for research grant 100-RM1/BIOTEK 16/6/2B. A.S.M. was financed by the European Research Council (starting grant) and the Swiss National Science Foundation. **Author contributions:** E.W. initiated and led the study. E.W., D.M.L., L.V., M.E.A., H.O., M.E.D., A.S.M., L.O., H.Mc., and F.D. designed the study. E.W. and D.M.L. supervised the overall project, and L.V., F.D., F.R., V.S., T.S., M.M.S., R.S., T.M.H.N., C.H., K.W., E.P.E., J.C.G., R.K., H.B., C.P., H.I., T.H., M.E.D., F.A.A., A.S.M., and H.O. supervised specific aspects of the project. H.Mc., L.V., F.D., U.G.W., C.D., M.E.A., V.S., T.S., M.M.S., R.S., S.K., P.L., T.M.H.N., H.C.H., T.M.T., T.H.N., S.S., G.H.N., K.W., N.S., T.M., Y.Y., A.M.B., P.D., J.L.P., L.S., E.P.E., N.A.T., B.B.P., J.C.G., R.K., H.B., M.E.D., F.A.A., and C.P. excavated, curated, sampled, and/or described samples. H.Mc., L.V., T.G., A.S.O., S.W., P.B.D., M.Y., A.Ta., H.S., A.To., S.R., T.D., M.E.D., F.A.A., A.S.M., and T.H. produced data for analysis. H.Mc., F.R., L.V., T.G., J.V.M.M., C.D., T.K, T.S., H.Ma., S.N., S.W., A.M., A.S.M., M.E.D., L.O., and M.S. analyzed or assisted in the analysis of data. H.Mc., F.R., L.V., F.D., T.G., A.M., L.O., M.S., C.H., D.M.L., and E.W. interpreted the results. H.Mc., F.R., L.V., F.D., T.G., H.O., M.M.L., R.A.F., C.H., D.M.L., and E.W. wrote the manuscript with considerable input from J.V.M.M., C.D., S.W., G.V.D., A.P., V.S., T.S., M.M.S., R.S., T.M.H.N., H.C.H., T.H.N., K.W., T.H., S.N., and M.S. All authors discussed the results and contributed to the final manuscript. **Competing interests:** The authors declare no competing interests. **Data and materials availability:** This study has been evaluated by the Danish Bioethical Committee (H-16018872) and the Department of Orang Asli Affairs, Malaysia [JHEOA.PP.30.052 Iss.5 (17)]. MoU's exist with local institutions where the sampling took place. Genomic data are available for download at the ENA (European Nucleotide Archive) with accession number PRJEB26721.

SUPPLEMENTARY MATERIALS

www.sciencemag.org/content/361/6397/88/suppl/DC1
Supplementary Text
Figs. S1 to S43
Tables S1 to S25
References (*27*–*111*)

21 February 2018; accepted 29 May 2018
10.1126/science.aat3628

HUMAN GENOMICS

Ancient genomes document multiple waves of migration in Southeast Asian prehistory

Mark Lipson[1]*, Olivia Cheronet[2,3,4], Swapan Mallick[1,5], Nadin Rohland[1], Marc Oxenham[6], Michael Pietrusewsky[7], Thomas Oliver Pryce[8,9,10], Anna Willis[11], Hirofumi Matsumura[12], Hallie Buckley[13], Kate Domett[14], Giang Hai Nguyen[15], Hoang Hiep Trinh[15], Aung Aung Kyaw[16], Tin Tin Win[16], Baptiste Pradier[9], Nasreen Broomandkhoshbacht[1,17], Francesca Candilio[18,19], Piya Changmai[20], Daniel Fernandes[2,3,21], Matthew Ferry[1,17], Beatriz Gamarra[3,4], Eadaoin Harney[1,17], Jatupol Kampuansai[22,23], Wibhu Kutanan[24], Megan Michel[1,17], Mario Novak[3,25], Jonas Oppenheimer[1,17], Kendra Sirak[3,26], Kristin Stewardson[1,17], Zhao Zhang[1], Pavel Flegontov[20,27]†, Ron Pinhasi[2,3]*‡, David Reich[1,5,17]*‡

Southeast Asia is home to rich human genetic and linguistic diversity, but the details of past population movements in the region are not well known. Here, we report genome-wide ancient DNA data from 18 Southeast Asian individuals spanning from the Neolithic period through the Iron Age (4100 to 1700 years ago). Early farmers from Man Bac in Vietnam exhibit a mixture of East Asian (southern Chinese agriculturalist) and deeply diverged eastern Eurasian (hunter-gatherer) ancestry characteristic of Austroasiatic speakers, with similar ancestry as far south as Indonesia providing evidence for an expansive initial spread of Austroasiatic languages. By the Bronze Age, in a parallel pattern to Europe, sites in Vietnam and Myanmar show close connections to present-day majority groups, reflecting substantial additional influxes of migrants.

The archaeological record of Southeast Asia documents a complex history of human occupation, with the first archaic hominins arriving at least 1.6 million years before the present (yr B.P.) and anatomically modern humans becoming widely established by 50,000 yr B.P. (*1*–*3*). Particularly profound changes in human culture were propelled by the spread of agriculture. Rice farming began in the region ~4500 to 4000 yr B.P. and was accompanied by a relatively uniform and widespread suite of tools and pottery styles displaying connections to southern China (*4*–*7*). It has been hypothesized that this cultural transition was effected by a migration of people who were not closely related to the indigenous hunter-gatherers of Southeast Asia (*5*, *7*–*10*) and who may have spoken Austroasiatic languages, which today have a wide, but fragmented, distribution in the region (*4*, *5*, *11*–*14*). In this scenario, the languages spoken by the majority of present-day people in Southeast Asia (e.g., Thai, Lao, Myanmar, Malay) reflect later population movements. However, no genetic study has resolved the extent to which the spread of agriculture into the region and subsequent cultural and technological shifts were achieved by movement of people or ideas.

Here we analyze samples from five ancient sites (Table 1 and Fig. 1A): Man Bac (Vietnam, Neolithic; 4100 to 3600 yr B.P.), Nui Nap (Vietnam, Bronze Age; 2100 to 1900 yr B.P.), Oakaie 1 [Myanmar, Late Neolithic/Bronze Age; 3200 to 2700 yr B.P. (*15*)], Ban Chiang [Thailand, Late Neolithic through Iron Age; 3500 to 2400 yr B.P. (*16*)], and Vat Komnou [Cambodia, Iron Age; 1900 to 1700 yr B.P. (*17*)]. We initially screened a total of 350 next-generation sequencing libraries generated from petrous bone samples [specifically the high-yield cochlear region (*18*)] from 146 distinct individuals. For libraries with evidence of authentic ancient DNA, we generated genome-wide data using in-solution enrichment, yielding sequences from 18 individuals (Table 1 and table S1) (*19*). Because of poor preservation conditions in tropical environments, we observed both a low rate of conversion of screened samples to working data and also limited depth of coverage per sample, and thus we created multiple libraries per individual (102 in total in our final dataset).

We initially analyzed the data by performing principal component analysis (PCA) using two different sets of present-day populations (*19*). First, compared to a set of diverse non-Africans (East and Southeast Asians, Australasians, Central Americans, and Europeans), the ancient individuals fall close to present-day Chinese and Vietnamese when projected onto the first two axes, with Man Bac, Ban Chiang, and Vat Komnou shifted slightly in the direction of Onge (Andaman Islanders) and Papuan (fig. S1). To focus on East and Southeast Asian diversity, we then used a panel of 16 present-day populations from the region, with three primary directions in the first two dimensions represented by Han Chinese, Austroasiatic-speaking groups (Mlabri and Htin from Thailand, Nicobarese, and Cambodian, but not Kinh), and aboriginal (Austronesian-speaking) Taiwanese [right, left, and top, respectively; Fig. 1B; compare (*20*)]. Man Bac, Ban Chiang (all periods), and Vat Komnou cluster with Austroasiatic speakers, whereas Nui Nap projects close to present-day Vietnamese and Dai near the center, and Oakaie projects close to present-day Myanmar and other Sino-Tibetan speakers. Present-day Lao are intermediate between Austroasiatic speakers and Dai, and western Indonesians (Semende from southern Sumatra and Barito from southeastern Borneo) fall intermediate between Austroasiatic speakers and aboriginal Taiwanese.

We measured levels of allele sharing between populations via outgroup f_3-statistics and obtained results consistent with those from PCA (table S2). Nominally, the top sharing for each ancient population is provided by another ancient population, but this pattern may be an artifact due to correlated genotype biases between different ancient samples (table S3). Restricting to present-day comparisons, Man Bac, Ban Chiang, and Vat Komnou share the most alleles with Austroasiatic-speaking groups (as Austroasiatic-speaking groups do with each other); Nui Nap with Austronesian speakers, Dai, and Kinh; and Oakaie with Sino-Tibetan-speaking groups. We

[1]Department of Genetics, Harvard Medical School, Boston, MA 02115, USA. [2]Department of Anthropology, University of Vienna, 1090 Vienna, Austria. [3]Earth Institute, University College Dublin, Dublin 4, Ireland. [4]School of Archaeology, University College Dublin, Dublin 4, Ireland. [5]Medical and Population Genetics Program, Broad Institute of MIT and Harvard, Cambridge, MA 02142, USA. [6]School of Archaeology and Anthropology, Australian National University, Canberra, ACT 0200, Australia. [7]Department of Anthropology, University of Hawai'i at Mānoa, Honolulu, Hawai'i 96822, USA. [8]Centre National de la Recherche Scientifique, 75016 Paris, France. [9]UMR 7055 Préhistoire et Technologie, Université Paris Nanterre, 92023 Nanterre, France. [10]CEA/CNRS UMR 3685 NIMBE, 91191 Gif-sur-Yvette, France. [11]College of Arts, Society and Education, James Cook University, Townsville, Queensland 4811, Australia. [12]School of Health Science, Sapporo Medical University, Sapporo 060-8556, Japan. [13]Department of Anatomy, University of Otago, Dunedin 9054, New Zealand. [14]Division of Tropical Health and Medicine, College of Medicine and Dentistry, James Cook University, Townsville, Queensland 4811, Australia. [15]Department of Prehistoric Archaeology, Vietnam Institute of Archaeology, Hanoi, Vietnam. [16]Department of Archaeology, Ministry of Religious Affairs and Culture, Mandalay, Myanmar. [17]Howard Hughes Medical Institute, Harvard Medical School, Boston, MA 02115, USA. [18]Soprintendenza Archeologia Belle Arti e Paesaggio per la Città Metropolitana di Cagliari e per le Province di Oristano e Sud Sardegna, 09124 Cagliari, Italy. [19]Physical Anthropology Section, University of Pennsylvania Museum of Archaeology and Anthropology, Philadelphia, PA 19104, USA. [20]Department of Biology and Ecology, Faculty of Science, University of Ostrava, 70103 Ostrava, Czech Republic. [21]CIAS, Department of Life Sciences, University of Coimbra, Coimbra 3000-456, Portugal. [22]Department of Biology, Faculty of Science, Chiang Mai University, Chiang Mai 50200, Thailand. [23]Center of Excellence in Bioresources for Agriculture, Industry and Medicine, Chiang Mai University, Chiang Mai 50200, Thailand. [24]Department of Biology, Faculty of Science, Khon Kaen University, Khon Kaen, 40002, Thailand. [25]Institute for Anthropological Research, 10000 Zagreb, Croatia. [26]Department of Anthropology, Emory University, Atlanta, GA 30322, USA. [27]Institute of Parasitology, Biology Centre, Czech Academy of Sciences, 37005 České Budějovice, Czech Republic.
***Corresponding author. Email: mlipson@genetics.med.harvard.edu (M.L.); ron.pinhasi@univie.ac.at (R.P.); reich@genetics.med.harvard.edu (D.R.)** †P.F. holds part-time positions as a research assistant at the Faculty of Science, University of South Bohemia, Ceske Budejovice, Czech Republic and at the Institute for Information Transmission Problems, Russian Academy of Sciences, Moscow, Russia. ‡These authors contributed equally to this work.

also computed statistics $f_4(X, \text{Kinh}; \text{Australasian}, \text{Han})$, where "Australasian" is a union of Papuan and Onge, to search for signals of admixture from outside the East Asian clade in test populations X (increasingly positive values for increasing proportions of deeply splitting ancestry). Present-day Myanmar, Lao, western Indonesians, and Austroasiatic speakers all yield significantly positive values, as do the majority of the ancient samples, with approximately equal results for Mlabri, Nicobarese, and Man Bac (Fig. 2). The Man Bac individuals are additionally mostly similar to each other, except for one, VN29, which is significantly higher than the population mean [Bonferroni-corrected Z-test, $p < 0.02$ (*19*)]. Vat Komnou and Ban Chiang also yield high positive values, while Oakaie is modestly positive, and Nui Nap is close to zero ($Z = 1.1$).

Next, we built admixture graph models to test the relationships between the Vietnam Neolithic samples and present-day Southeast Asians in a phylogenetic framework. We began with a scaffold model containing the Upper Paleolithic Siberian Ust'-Ishim individual (*21*) as an outgroup and present-day Mixe, Onge, and Atayal, to which we added Man Bac, Nicobarese, and Mlabri. The latter three were inferred to have ancestry from a Southeast Asian farmer–related source (~70%, forming a clade with Atayal) and a deeply diverging eastern Eurasian source [~30%, sharing a small amount of drift with Onge; f-statistics indicate that this source is also not closely related to Papuans, South Asians, or the 40,000 yr B.P. Tianyuan individual (*22*); table S3]. The allele sharing demonstrated by outgroup f_3-statistics can be accommodated along the farmer lineage,

Table 1. Sample information. Calibrated radiocarbon dates are shown in bold (95.4% confidence interval, rounded to nearest 5 years); dates in plain text are estimated from archaeological context. Lib., number of sequencing libraries; Cov., average coverage level for 1.2 million genome-wide SNP (single-nucleotide polymorphism) targets; N, Neolithic; LN, Late Neolithic; BA, Bronze Age; IA, Iron Age.

ID	Lib.	Date (yr B.P.)	Site	Country/period	Lat.	Long.	Sex	Mt Hap	Y Hap	Cov.
VN22	6	**3835–3695**	Man Bac	Vietnam N	20.1	106.0	F	M13b	..	0.048
VN29	9	3900–3600	Man Bac	Vietnam N	20.1	106.0	F	M7b1a1	..	0.049
VN31	1	3900–3600	Man Bac	Vietnam N	20.1	106.0	M	No call	No call	0.005
VN33	2	3900–3600	Man Bac	Vietnam N	20.1	106.0	M	B5a1a	O2a	0.028
VN34	10	**4080–3845**	Man Bac	Vietnam N	20.1	106.0	F	M7b1a1	..	0.106
VN37	4	**3825–3635**	Man Bac	Vietnam N	20.1	106.0	M	M7b1a1	CT	0.019
VN39	11	**3830–3695**	Man Bac	Vietnam N	20.1	106.0	M	M7b1a1	O2a1c1b1a	0.102
VN40	6	**3820–3615**	Man Bac	Vietnam N	20.1	106.0	M	M74b	O1b1a	0.041
VN41	5	2100–1900	Nui Nap	Vietnam BA	19.8	105.8	F	C7a	..	0.373
VN42	6	**1995–1900**	Nui Nap	Vietnam BA	19.8	105.8	M	M8a2a	F	0.042
OAI1/S28	20	3200–2700	Oakaie 1	Myanmar LN/BA	22.4	95.0	F	D4q	..	0.178
OAI1/S29	4	3200–2700	Oakaie 1	Myanmar LN/BA	22.4	95.0	F	D4h1c	..	0.011
BCES B67	1	3500–3200	Ban Chiang	Thailand LN/BA	17.4	103.2	F	F1f	..	0.005
BCES B38	1	3200–3000	Ban Chiang	Thailand BA	17.4	103.2	F	B5a1a	..	0.017
BCES B54	1	3200–3000	Ban Chiang	Thailand BA	17.4	103.2	M	B5a1c	CT	0.010
BCES B27	7	3000–2800	Ban Chiang	Thailand BA	17.4	103.2	F	M74b2	..	0.030
BCES B16	1	2600–2400	Ban Chiang	Thailand IA	17.4	103.2	M	M72a	F	0.017
AB40	7	**1890–1730**	Vat Komnou	Cambodia IA	11.0	105.0	M	B5a1a	O	0.047

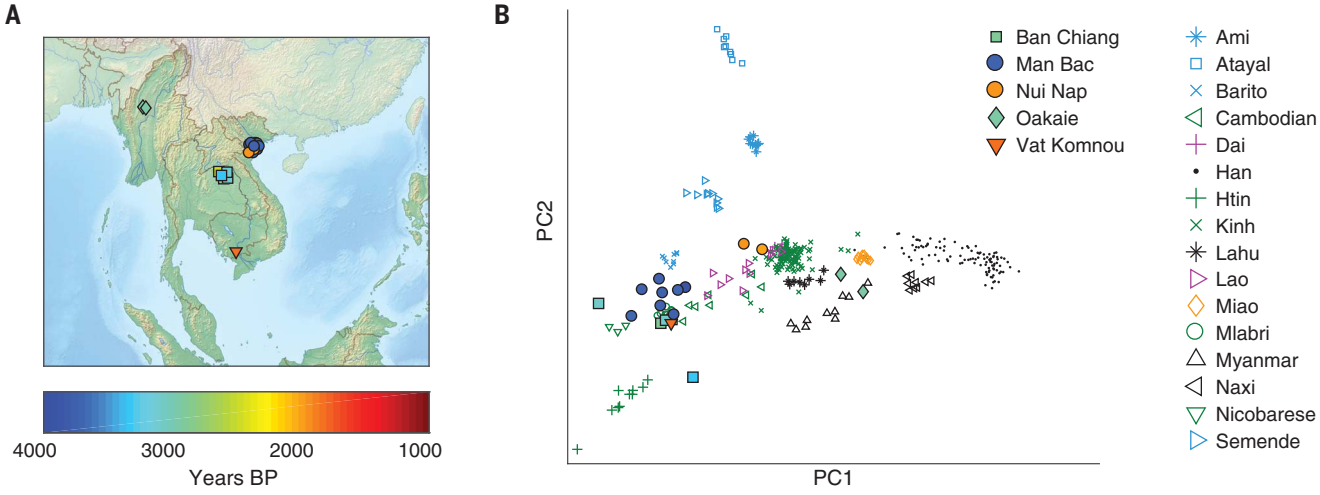

Fig. 1. Overview of samples. (**A**) Locations and dates of ancient individuals. Overlapping positions are shifted slightly for visibility. (**B**) PCA with East and Southeast Asians. We projected the ancient samples onto axes computed using the present-day populations (with the exception of Mlabri, who were projected instead owing to their large population-specific drift). Present-day colors indicate language family affiliation: green, Austroasiatic; blue, Austronesian; orange, Hmong-Mien; black, Sino-Tibetan; magenta, Tai-Kadai. Map data from www.freeworldmaps.net/asia/southeastasia/physical.html.

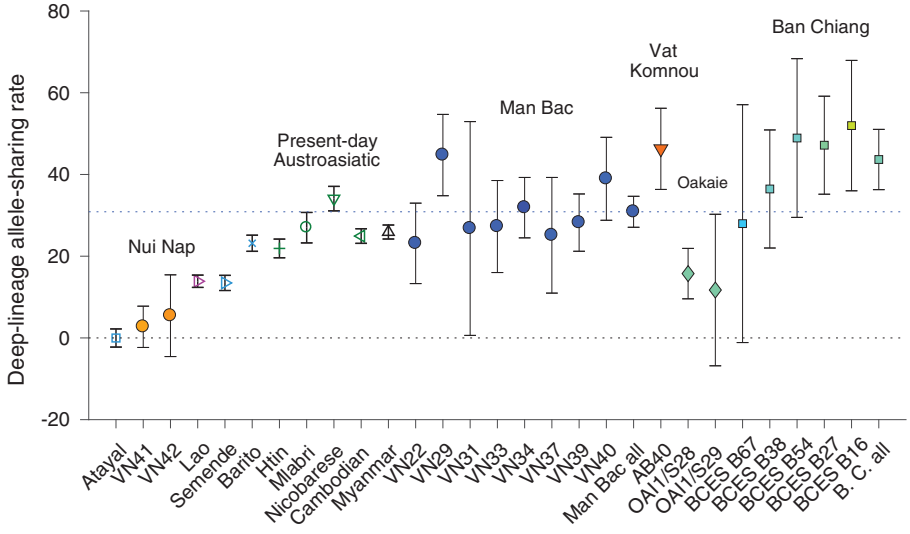

Fig. 2. Relative amounts of deeply diverged ancestry. The *y* axis shows $f_4(X$, Kinh; Australasian, Han) (multiplied by 10^4) for populations *X* listed on the *x* axis (present-day as aggregate; ancient samples individually, except for points labeled "all"). Symbols are as in Fig. 1. Bars give two standard errors in each direction; dotted lines indicate the levels in Man Bac (top, blue) and Kinh (zero, black). B. C., Ban Chiang.

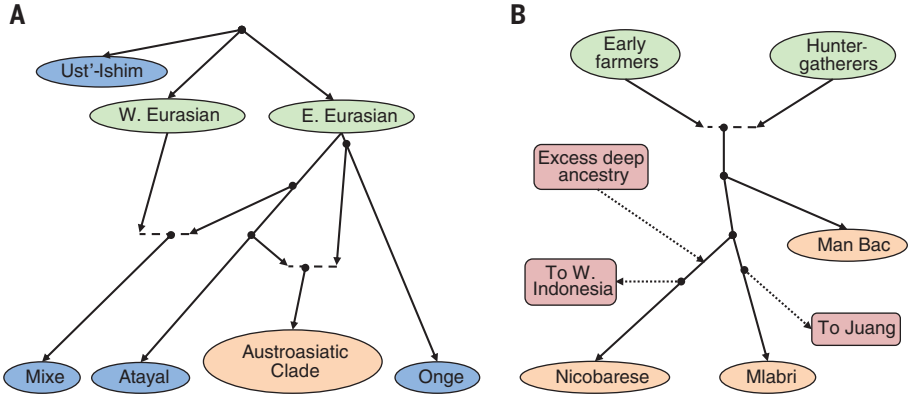

Fig. 3. Schematics of admixture graph results. (**A**) Wider phylogenetic context. (**B**) Details of the Austroasiatic clade. Branch lengths are not to scale, and the order of the two events on the Nicobarese lineage in (B) is not well determined (*19*).

the deeply splitting lineage, or a combination of the two, but given the closeness of the mixture proportions among the three groups, we found that the most parsimonious model (Fig. 3 and fig. S2) involved a shared ancestral admixture event (29% deep ancestry; 28% omitting VN29), followed by divergence of Man Bac from the present-day Austroasiatic speakers, and lastly, a second pulse of deep ancestry (5%) into Nicobarese (*19*).

Finally, to assess the relationships among additional present-day populations, we fit two extended admixture graphs (figs. S3 and S4), with the first including Dai, Semende, Barito, Lebbo (from east-central Borneo), and Juang (an Austroasiatic-speaking group from India), and the second including Dai, Semende, Barito, and Lao. The western Indonesians could be fit well with three (but not two) sources of ancestry: Austronesian-related, Austroasiatic-related, and Papuan-related (table S3), in respective proportions of ~67, 29, and 4% (Semende); ~37, 60, and 2% (Barito); and ~55, 23, and 22% (Lebbo) (*19*). The Austroasiatic-associated component was inferred to be closer to Nicobarese than to Mlabri or Man Bac, forming a "southern" Austroasiatic subclade (Fig. 3B). For Juang, we also obtained a good fit with three ancestry components: one western Eurasian, one deep eastern Eurasian (interpreted as an indigenous South Asian lineage), and one from the Austroasiatic clade (fig. S3). The Austroasiatic source for Juang (proportion 35%) was inferred to be closest to Mlabri, as supported by statistics f_4(Juang, Palliyar; Mlabri, *X*) > 0 for *X* = Atayal, Man Bac, or Nicobarese (Z = 5.1, 2.8, 2.3), creating a "northern" Austroasiatic subclade. Separately, we found that Lao also possesses ancestry from the Austroasiatic clade (47%; fig. S4) but cannot be fit as a simple mixture of the same two components found in Nicobarese and Mlabri (residual statistic Z = 3.4 without a source to explain distantly shared ancestry between Lao and Mixe) (*19*).

Our results provide genetic support for the hypothesis that agriculture was first practiced in mainland Southeast Asia by (proto-) Austroasiatic-speaking migrants from southern China (*4*–*6*, *11*–*13*). We find that all eight of our sampled individuals from Man Bac (as well as individuals from Ban Chiang and Vat Komnou) are closely related to present-day Austroasiatic speakers, including a shared pattern of admixture, with one, VN29, exhibiting significantly elevated indigenous ancestry. By comparison, studies of cranial and dental morphology have placed Man Bac either close to present-day East and Southeast Asians ("Neolithic"), intermediate between East Asians and a cluster containing more ancient hunter-gatherers from the region plus present-day Onge and Papuan ("indigenous"), or split between the two clusters (*7*, *8*, *23*). The simplest explanation for our results is that the majority of our Man Bac samples represent a homogeneous Neolithic cluster, with recent local contact between farmers and hunter-gatherers leading to additional hunter-gatherer ancestry in VN29 and perhaps VN40 (*7*, *8*). This model would imply that the incoming farmers had already acquired 25 to 30% hunter-gatherer ancestry, either in China or Southeast Asia, establishing the characteristic Austroasiatic-affiliated genetic profile seen in multiple populations today. The wide distribution of this profile across Southeast Asia (in some cases in admixed form) also supports a coherent migration with early shared admixture. The symmetric position of aboriginal Taiwanese and the majority East Asian ancestral lineage in Man Bac (and Austroasiatic speakers) with respect to Native Americans points to an origin for the farming migration specifically in southern China [contrasting with $f_4(X$, Atayal; Mixe, Dinka) > 0 for northern East Asians; *X* = Han, Japanese, or Korean, Z > 4.5). Conversely, the signal of allele sharing between Lao and Native Americans points to admixture in Lao from a population affected by Han Chinese migrations, with a plausible explanation for our results being a mixture between resident Austroasiatic speakers and incoming Tai speakers within historical times (*5*).

Our findings also have implications for genetic transformations linked to later cultural and linguistic shifts in Southeast Asia and beyond. We observe substantial genetic turnover between the Neolithic period and Bronze Age in Vietnam, likely reflecting a new influx of migrants from China (*24*). Late Neolithic to Bronze Age Myanmar individuals from Oakaie also do not possess an Austroasiatic genetic signature, in their case being closer to populations speaking Sino-Tibetan languages (including present-day Myanmar), pointing to an independent East Asian origin. Outside of mainland Southeast Asia, we document admixture events involving Austroasiatic-related lineages in India (where Austroasiatic languages

continue to be spoken) and in Borneo and Sumatra (where all languages today are Austronesian). In the latter case, the shared ancestry with Nicobarese (in addition to separate Papuan-related and Austronesian-associated components) supports previous genetic results and archaeological hints of an early Austroasiatic-associated Neolithic expansion to western Indonesia (*25*, *26*). Overall, Southeast Asia shares common themes with Europe, Oceania, and sub-Saharan Africa, where ancient DNA studies of farming expansions and language shifts have revealed similar instances of genetic turnover associated with archaeologically attested transitions in culture.

REFERENCES AND NOTES

1. C. Higham, *Hum. Biol.* **85**, 21–43 (2013).
2. M. Oxenham, H. R. Buckley, The population history of mainland and island Southeast Asia, in *The Routledge Handbook of Bioarchaeology in Southeast Asia and the Pacific Islands*, M. Oxenham, H. R. Buckley, Eds. (Routledge, 2016), pp. 9–23.
3. C. J. Bae, K. Douka, M. D. Petraglia, *Curr. Anthropol.* **58**, S373–S382 (2017).
4. C. Higham, Languages and farming dispersals: Austroasiatic languages and rice cultivation, in *Examining the Farming/Language Dispersal Hypothesis*, P. Bellwood, C. Renfrew, Eds. (McDonald Institute for Archaeological Research, 2002), pp. 223–232.
5. P. Bellwood, *First Farmers: The Origins of Agricultural Societies* (Blackwell, Oxford, 2005).
6. Z. Chi, H.-C. Hung, *Antiquity* **84**, 11–25 (2010).
7. M. F. Oxenham, H. Matsumura, K. D. Nguyen, *Man Bac: The Excavation of a Neolithic Site in Northern Vietnam* (ANU Press, 2011).
8. H. Matsumura *et al.*, *Anthropol. Sci.* **116**, 135–148 (2008).
9. Z. Chi, H.-C. Hung, *Antiquity* **86**, 11–29 (2012).
10. H. Matsumura, M. F. Oxenham, *Am. J. Phys. Anthropol.* **155**, 45–65 (2014).
11. C. F. Higham, Archaeology, linguistics and the expansion of the East and Southeast Asian Neolithic, in *Archaeology and Language II: Correlating Archaeological and Linguistic Hypotheses*, R. Blench, M. Spriggs, Eds. (Routledge, 1998), pp. 103–114.
12. I. Pejros, V. Shnirelman, Rice in Southeast Asia: A regional interdisciplinary approach, in *Archaeology and Language II: Correlating Archaeological and Linguistic Hypotheses*, R. Blench, M. Spriggs, Eds. (Routledge, 1998), pp. 379–389.
13. P. Bellwood *et al.*, *Asian Perspect.* **50**, 144–175 (2011).
14. P. Sidwell, R. Blench, The Austroasiatic Urheimat: The southeastern riverine hypothesis, in *Dynamics of Human Diversity: The Case of Mainland Southeast Asia*, N. J. Enfield, Ed. (Pacific Linguistics, 2011), pp. 317–345.
15. T. O. Pryce *et al.*, *J. Indo-Pacific Arch.* **39**, 38–49 (2015).
16. M. Pietrusewsky, M. T. Douglas, *Ban Chiang, a Prehistoric Village Site in Northeast Thailand, Volume 1, The Human Skeletal Remains* (Univ. of Pennsylvania Museum of Archaeology and Anthropology, 2002).
17. R. M. Ikehara-Quebral *et al.*, *Asian Perspect.* **56**, 191–236 (2017).
18. R. Pinhasi *et al.*, *PLOS ONE* **10**, e0129102 (2015).
19. Materials and methods are available as supplementary materials.
20. M. A. Abdulla *et al.*, *Science* **326**, 1541–1545 (2009).
21. Q. Fu *et al.*, *Nature* **514**, 445–449 (2014).
22. M. A. Yang *et al.*, *Curr. Biol.* **27**, 3202–3208.e9 (2017).
23. J. Corny *et al.*, *J. Hum. Evol.* **112**, 41–56 (2017).
24. M. F. Oxenham, *Bioarchaeology of Ancient Vietnam* (BAR International Series 2781, Hadrian, 2016).
25. M. Lipson *et al.*, *Nat. Commun.* **5**, 4689 (2014).
26. T. Simanjuntak, The western route migration: A second probable Neolithic diffusion to Indonesia, in *New Perspectives in Southeast Asian and Pacific Prehistory*, P. J. Piper, H. Matsumura, D. Bulbeck, Eds. (ANU Press, 2017), pp. 201–212.

ACKNOWLEDGMENTS

We thank I. Lazaridis, V. Narasimhan, I. Olalde, and N. Patterson for technical assistance; N. Adamski and A.-M. Lawson for aiding with lab work; and T. T. Minh, R. Ikehara-Quebral, M. Stark, M. Toomay Douglas, and J. White for help with archaeological samples. **Funding:** This work was supported by the French Ministry for Europe and Foreign Affairs (T.O.P.), Japan Society for the Promotion of Science (grant 16H02527; H.M.), Statutory City of Ostrava (grant 0924/2016/ŠaS; P.C.), Moravian-Silesian Region (grant 01211/2016/RRC; P.C.), Irish Research Council (grant GOIPG/2013/36; D.F.), Thailand Research Fund (grant MRG5980146; W.K.), University of Ostrava (IRP projects; P.F. and P.C.), Czech Ministry of Education, Youth and Sports (project OPVVV 16_019/0000759; P.F. and P.C.), National Science Foundation (HOMINID grant BCS-1032255; D.R.), National Institutes of Health (NIGMS grant GM100233; D.R.), an Allen Discovery Center of the Paul Allen Foundation (D.R.), and the Howard Hughes Medical Institute (D.R.). **Author contributions:** N.R., P.F., R.P., and D.R. supervised the study. M.O., M.P., T.O.P., A.W., H.M., H.B., K.D., N.G.H., T.H.H., A.A.K., T.T.W., B.P., and R.P. provided samples and assembled archaeological and anthropological information. M.L., O.C., S.M., N.R., N.B., F.C., D.F., M.F., B.G., E.H., M.M., M.N., J.O., K.Si., K.St., Z.Z., R.P., and D.R. performed ancient DNA laboratory and data processing work. P.C., J.K., W.K., and P.F. provided present-day data. M.L., S.M., and D.R. analyzed genetic data. M.L., R.P., and D.R. wrote the manuscript with input from all coauthors. **Competing interests:** The authors declare no competing interests. **Data and materials availability:** The aligned sequences are available through the European Nucleotide Archive under accession number PRJEB24939. Genotype datasets used in analysis are available at https://reich.hms.harvard.edu/datasets. All the skeletons for which we newly report ancient DNA data are curated by coauthors of this paper, who affirm that the sampling of the skeleton was performed with appropriate permissions.

SUPPLEMENTARY MATERIALS

www.sciencemag.org/content/361/6397/92/suppl/DC1
Materials and Methods
Figs. S1 to S4
Tables S1 to S3
References (*27*–*70*)

13 February 2018; accepted 3 May 2018
Published online 17 May 2018
10.1126/science.aat3188

THE NORWEGIAN ACADEMY OF SCIENCE AND LETTERS

ANNOUNCES THE 2018 WINNERS OF

THE KAVLI PRIZE℠

THE KAVLI PRIZE IN ASTROPHYSICS

EWINE VAN DISHOECK
Leiden University,
The Netherlands

"for her combined contributions to observational, theoretical and laboratory astrochemistry, elucidating the life cycle of interstellar clouds and the formation of stars and planets."

THE KAVLI PRIZE IN NANOSCIENCE

EMMANUELLE CHARPENTIER
Max Planck Institute for Infection Biology,
Berlin, Germany

JENNIFER A. DOUDNA
University of California,
Berkeley, USA

VIRGINIJUS ŠIKŠNYS
Vilnius University,
Lithuania

"for the invention of CRISPR-Cas9, a precise nanotool for editing DNA, causing a revolution in biology, agriculture and medicine."

THE KAVLI PRIZE IN NEUROSCIENCE

A. JAMES HUDSPETH
Rockefeller University,
New York, USA

ROBERT FETTIPLACE
University of Wisconsin-Madison,
Wisconsin, USA

CHRISTINE PETIT
Collège de France/Pasteur Institute,
Paris, France

"for their pioneering work on the molecular and neural mechanisms of hearing."

The Kavli Prize is a partnership between The Kavli Foundation (USA),
The Norwegian Academy of Science and Letters
and The Norwegian Ministry of Education and Research.

www.kavliprize.org

10 YEARS OF PRIZES FOR THE FUTURE · THE KAVLI PRIZE 2008-2018 ·

HOW FAR WILL YOUR ESSAY TAKE YOU?

Apply for the *Science* & SciLifeLab Prize for Young Scientists — an annual prize awarded to early-career scientists. The prize is presented in four categories: Cell and Molecular Biology, Genomics and Proteomics, Ecology and Environment, and Translational Medicine.

The winners will have their essays published by *Science*, win up to USD 30,000 and be invited to a week in Sweden to attend the award ceremony. Get ready for a life-changing moment in your scientific career.

SCIENCEPRIZE.SCILIFELAB.SE

Science & SciLifeLab PRIZE For Young Scientists

Knut och Alice Wallenbergs Stiftelse

Science AAAS

SciLifeLab

Publish your research in *Science Immunology*

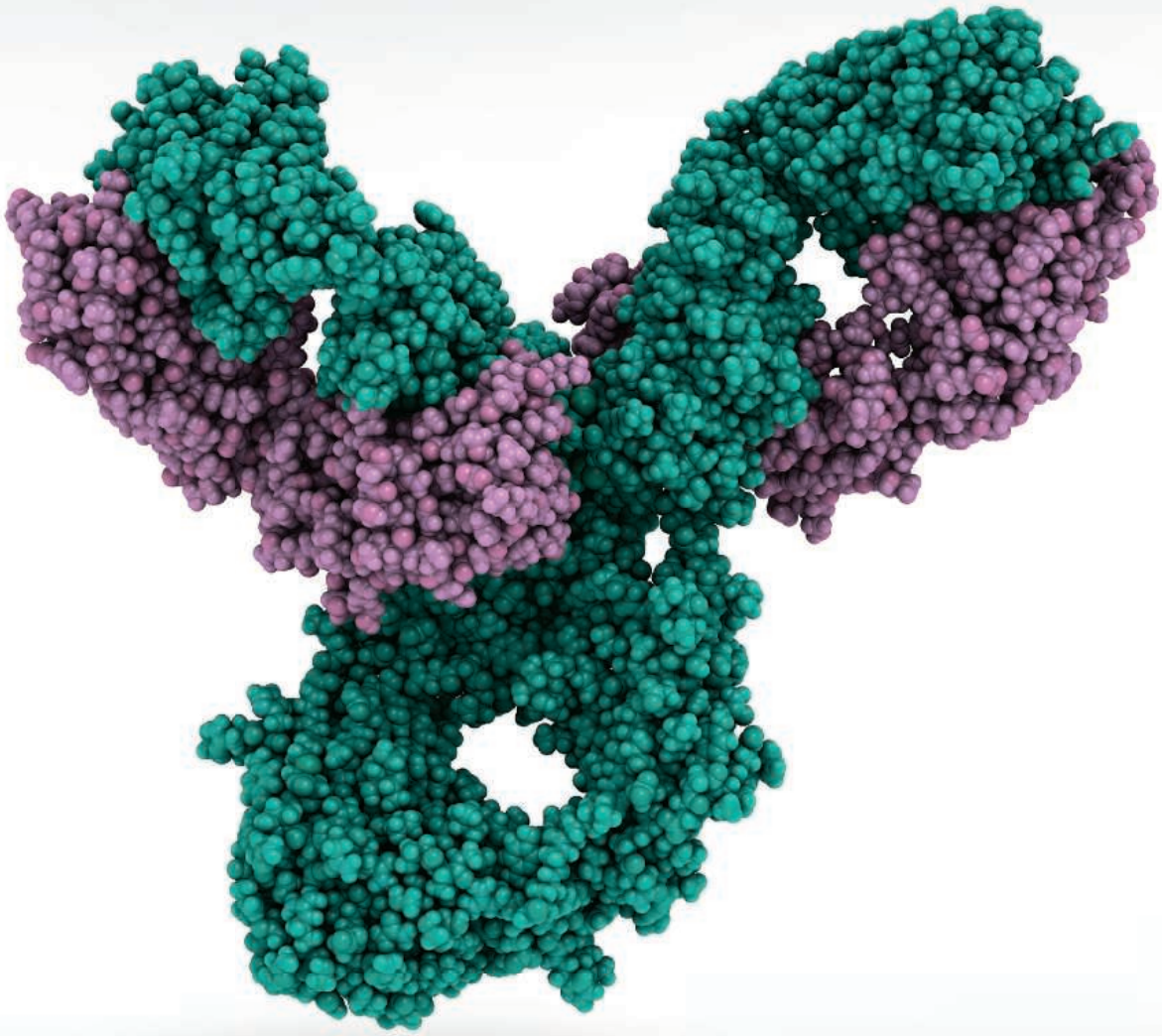

Science Immunology publishes original, peer-reviewed, science-based research articles that report critical advances in all areas of immunological research, including important new tools and techniques.

For more information: **ScienceImmunology.org**

Science Immunology

AAAS

Spectrophotometers

Get the most from your requirements for routine and high-throughput ultraviolet-visible (UV-Vis)/Vis measurements. Built for demanding real-world applications, Thermo Scientific's rugged, compact GENESYS spectrophotometers are ideal for walk-up measurements, high-throughput QC/QA testing, research labs, or the classroom. Choose from UV-Vis or Vis configurations for single cuvette/test tube applications, quantitative analysis, multiple-cell changers, temperature control, remote sampling, double-beam reference cell design, or preprogrammed life science methods. All instruments feature superior performance, sampling convenience, and user-friendly operation and are built to withstand heavy use. A new line of accessories, including automated cell changers, a Peltier thermostatted cell holder, a disposable microcell holder, a sipper, and fiber optic probes, is designed to simplify sampling and accommodate high-throughput and temperature-control needs.

Thermo Fisher Scientific
For info: 866-356-0354
www.thermofisher.com

Filtered Hood

Latitude Series C Filtered Hoods from Mystaire provide biotechnology and pharmaceutical companies with an important safety solution when handling potentially harmful chemicals in particulate and/or liquid forms. Latitude maximizes user accessibility and incorporates redundant filtration for added safety and easy maintenance. Its design pulls potentially harmful particulate away from the operator's breathing zone in an even, horizontal airflow path, increasing particulate and vapor capture. The hood incorporates the Saf-T-Zone filtration system, which isolates the prefilter and main high-efficiency particulate air (HEPA) filter during filter change out. The EverSafe microprocessor controller is standard on every hood, constantly monitoring your safety with advanced electronic sensors and removing any guesswork about whether the hood is protecting you.

Mystaire
For info: 877-328-3912
www.mystaire.com

Tube and Cuvette Racks

Eppendorf Tube and Cuvette Racks ensure user-friendly, efficient handling of clearly arranged samples. Their wavelike design supports clear visibility and allocation of vessels even when they are placed in different rows. All racks are stackable to save lab space when not in use. They are also UV-resistant, fully autoclavable, and have labeling surfaces to assist identification. Six different formats offer the optimal solution and perfect fit for all tubes and cuvettes commonly used in laboratories. These racks are ideal for sample processing and short- or medium-term sample storage. Able to withstand temperatures as low as –80°C, they can also be stored in a freezer.

Eppendorf
For info: 800-645-3050
www.eppendorf.com

Microplate Support Mats and Deep-Well Plates

Designed to fit into the skirt of our deep-well plates, silicone impact support mats allow plates to be used in a centrifuge without risking plate distortion, cracking, or breaking that can result in well leakage and loss of valuable samples. Mats are now available for Porvair Sciences' square deep-well plates (2 mL, 1 mL, and 350 µL), round-well plates (2 mL and 1 mL), and range of large-volume deep-well plates. We offer a range of high-quality polypropylene deep-well plates for applications in cell biology, molecular biology, drug discovery, combinatorial chemistry, screening, and genomics. Manufactured under Class 10,000 conditions from ultrapure grade polypropylene, Porvair deep-well plates contain no contaminants that may leach out and affect stored samples or bacterial or cell growth. For sensitive biological applications, Porvair also offers a selection of 96-well deep-well plates that are available certified as RNase/DNase free.

Porvair Sciences
For info: +44-(0)-1978-666222
www.porvair-sciences.com

Drug Screening Software

PerkinElmer Signals Screening solution is an intuitive, configurable, and flexible drug screening workflow using TIBCO Spotfire data visualization and analysis software. Signals Screening is an instrument-independent, image- and data-analysis, management, and aggregation platform offering "out-of-the-box" support for a complete screening workflow. Built on application program interfaces (APIs) and customizable workflows, the toolset allows R&D organizations to conduct data analysis, review, and reporting as well as compare data from different assay types and multiple platforms—all from a central location. Signals Screening quickly handles most instrument outputs, performs advanced data analysis in minutes, and processes data at the key stages of assay development, protocol execution, and automation, while offering integration with public or private data repositories and electronic lab notebooks.

PerkinElmer
For info: 800-762-4000
www.perkinelmer.com/product/signals-screening-signalss

Acoustic Sample Management System

The Access Dual-Robot System (DRS) and the Echo 655T Liquid Handler are key components of a new acoustic sample management solution that will support the next generation of pharmaceutical drug discovery, which demands faster, high-throughput screens while requiring less sample. Acoustic liquid handling, pioneered by Labcyte, has been adopted across pharmaceutical sample management and screening programs for the dispensing of reagents in a wide variety of molecular and cellular assays. It uses the gentle energy of sound waves to move liquids in nanoliter increments with extremely high precision and accuracy. The technology is contactless, avoiding risks of sample carryover or cross-contamination, and reduces sample volume needs, leading to improved data quality, higher throughput, and lower assay costs.

Labcyte
For info: 408-542-7855
www.labcyte.com

Electronically submit your new product description or product literature information! Go to www.sciencemag.org/about/new-products-section for more information.

Newly offered instrumentation, apparatus, and laboratory materials of interest to researchers in all disciplines in academic, industrial, and governmental organizations are featured in this space. Emphasis is given to purpose, chief characteristics, and availability of products and materials. Endorsement by *Science* or AAAS of any products or materials mentioned is not implied. Additional information may be obtained from the manufacturer or supplier.

Present your work to the world

Are you a representative of the upcoming generation of thought leaders in your field? Together we look forward to your application for the new Sartorius & *Science* Prize for Regenerative Medicine & Cell Therapy.

Apply now!

www.passionforscience.com/prize

The Sartorius & *Science* Prize for Regenerative Medicine & Cell Therapy

Awarded by sartorius Science

Science Careers

SCIENCE CAREERS ADVERTISING

For full advertising details, go to ScienceCareers.org and click For Employers, or call one of our representatives.

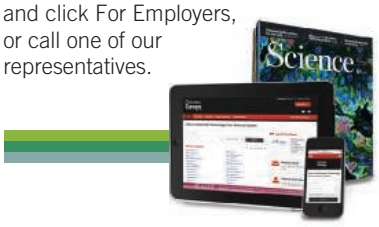

AMERICAS

+1 202 326-6577
+1 202 326-6578
advertise@sciencecareers.org

EUROPE, INDIA, AUSTRALIA, NEW ZEALAND, REST OF WORLD

+44 (0) 1223 326527
advertise@sciencecareers.org

CHINA, KOREA, SINGAPORE, TAIWAN, THAILAND

+86 131 4114 0012
advertise@sciencecareers.org

JAPAN

+81 3-6459-4174
advertise@sciencecareers.org

CUSTOMER SERVICE

AMERICAS

+1 202 326-6577

REST OF WORLD

+44 (0) 1223 326528

advertise@sciencecareers.org

All ads submitted for publication must comply with applicable U.S. and non-U.S. laws. *Science* reserves the right to refuse any advertisement at its sole discretion for any reason, including without limitation for offensive language or inappropriate content, and all advertising is subject to publisher approval. *Science* encourages our readers to alert us to any ads that they feel may be discriminatory or offensive.

ScienceCareers
FROM THE JOURNAL SCIENCE AAAS

ScienceCareers.org

TEMPLE UNIVERSITY

Full / Associate Professor of Chemistry

FALL 2019

The Department of Chemistry at Temple University invites applications and nominations for an outstanding senior hire in areas including Biochemistry, Bioorganic Chemistry, and Chemical Biology. Applicants who have demonstrated leadership in biology-related chemistry through publications, grant support, invited talks, and awards are particularly encouraged to apply. Applications should include a CV, statement of teaching, proposed research plan, references, and selected reprints.

Application materials should be submitted electronically at **https://academicjobsonline.org/ajo/jobs/11280**. Applications submitted by **October 31, 2018** will receive full consideration. There is a strong commitment to diversity at Temple and applications from women and chemists from underrepresented groups are encouraged.

Temple University is an Equal Opportunity, Equal Access, Affirmative Action Employer committed to achieving a diverse community (AA,EOE,M/F/D/V).

The College of Agriculture and Life Sciences and Texas A&M AgriLife Research at Texas A&M University seek applicants for a **tenure-track Assistant Professor** position in Biophotonics; 9-month College, 1-month AgriLife Research appointment in department most relevant to expertise.

Applicant with potential to (1) establish program in sensor development, optical spectroscopy, Raman spectroscopy and/or cyber-physical systems, (2) function in an interdisciplinary team to translate quantum physics and spectroscopic techniques into functional systems for agricultural/industrial needs, (3) publish, direct graduate students, develop intellectual property/patents, attract extramural funding. Teaching will fit departmental needs and individual's expertise. Service expected to institution and professional societies. Ph.D. required in appropriate discipline, engineering or physics; licensed or ability to license as professional engineer.

Apply: **https://tamus.wd1.myworkdayjobs.com/TAMU_External/job/College-Station-AL-RSCH/Assistant-Professor-Biophotonics_R-008096**. Upload: (1) Letter of application with interests, qualifications, unique skills, perspectives, and how contribute to a culturally diverse educational environment, (2) current curriculum vitae; (3) list five most significant publications with impact in the field, (4) names and contact information of five references. Review of applications begin July 31, 2018, and date of hire September 1, 2018 or until a suitable applicant is hired.

Texas A&M University, the College, and AgriLife Research are Equal Opportunity/ Affirmative Action/Veterans/ Disability Employers. Applications from women, minorities, individuals with disabilities, and covered veterans encouraged. Info: David Reed 979-458-0710 or dwreed@tamu.edu.

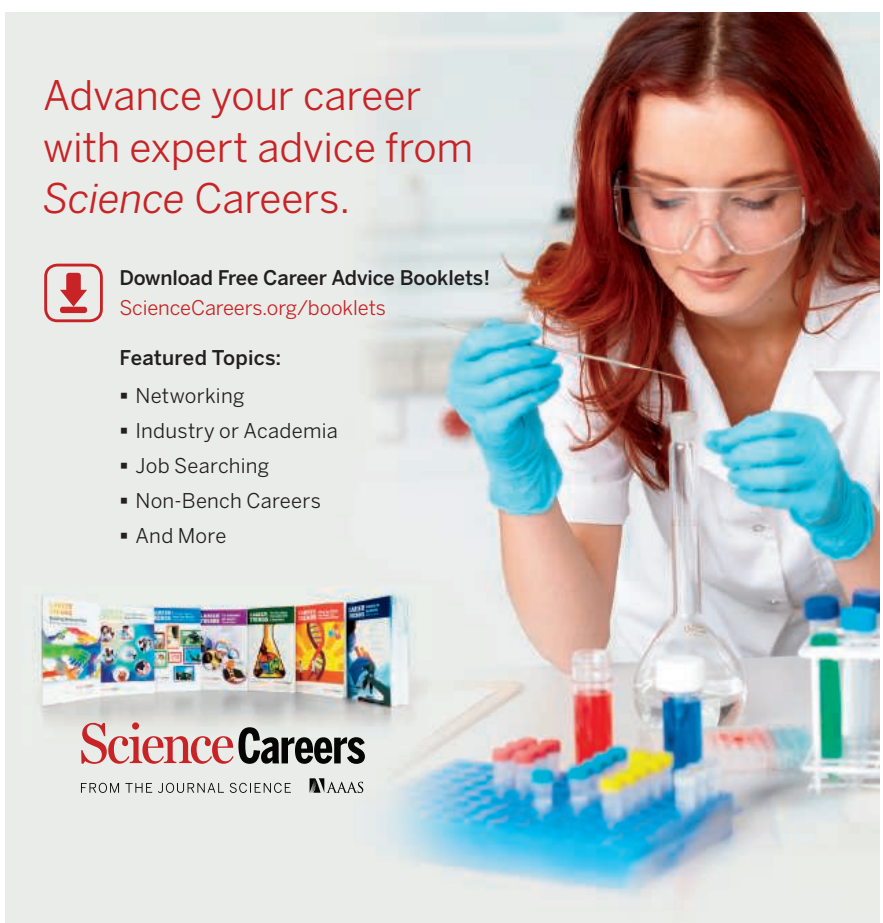

Qingdao International Academician Park

—— QIAP is committed to creating the world's first Academician Community.

Situated in core urban district of Qingdao, a coastal city in eastern China, next to the site of the World Horticultural Exposition 2014 and surrounded by Ocean University of China, Shandong University (Qingdao), and Qingdao National Laboratory of Marine Science and Technology, Qingdao International Academician Park (QIAP) aims to create an advanced platform for technology innovation and commercialization, distinctively characterized by rallying the brainpower of international academicians.

Operating with a global vision and by international standards and focusing on information technology, life science, design and development engineering, high-end equipment manufacturing, alternative energy and new material, QIAP introduces globally academicians to conduct scientific researches and commercialization of state-of-the-art technology. Within 3 years, it hopes to attract 10 world's top scientists and 100 renowned academicians from home and abroad to build a world-class and unique powerhouse for creation, innovation, entrepreneurship and funding for academicians.

Goal and problem-solving oriented and relying on new and innovative system & mechanism, we aim to promote the integration of the strengths of academies of sciences and academies of engineering, the communication between system & mechanism for scientific research in the West and China, the coordinated development of and seamless transition between R & D and commercialization, so as to set in motion the flow of institutions, human resource, facilities, capital and projects, to initiate a new phase of system innovation, integrated innovation and coordinated innovation.

Looking ahead, QIAP will uphold its motto of 'facing up to problems, conquering difficulties, being creative, keeping ahead and remaining top-notch' and march firmly forward, doing all it can to realize its dream by building a base camp for academicians to scale new heights in science and technology as well as an ecosystem for creation and innovation that boasts both great originality and considerable scales of industry.

Research Project: Vaccines for Plants

Definition

Vaccines for plants increase the plant's resistance to disease and tolerance for adversity by activating its immune system and regulating its (especially vegetable and fruit) metabolism. These vaccines fall into two categories, plant immunity inducer (such as protein, oligose, and glycoprotein biometabolites or bioactive molecules) and bacteria that induce immunity, such as Trichoderma and bacillus.

Technology goal

Aiming at tapping the global demand for vaccines for plants, to research in and develop vaccines for plants that are adaptive to different plant, soil and climate, which removes the global constrains on research and commercialization in the field.

1. Study in techniques in comprehensive biological pest control, generating fungal and viral strain resources and in genetically modifying strains.
2. Harmlessly mass-produce microbial metabolites through fermentation of engineered bacteria.
3. Manufacture synthesized or modified natural compounds that are friendly to the environment and non-toxic to animal and human.
4. Mass-produce or develop versatile vaccines for plants, which resist disease, promote growth, increase production and improve quality for crops.

QIAP cordially invites academicians globally to join us in the research and commercialization of vaccines for plants.

Contacts: Wang Junxian & Luo Luqiao
Tel: 0532-8467 0756, 0532-8467 0736
E-mail: wjx@qdiap.com, llq@qdiap.com
Website: http://www.qdiap.com/
Address: 171 Jinshui Road, Licang District, Qingdao, Shandong.

Rat der Eidgenössischen Technischen Hochschulen ETH-Rat

Conseil des écoles polytechniques fédérales CEPF

Consiglio dei politecnici federali CPF

Board of the Swiss Federal Institutes of Technology ETH Board

The Swiss Federal Institute of Technology Zurich (ETH Zurich) stands for excellent teaching, pioneering basic research, creativity and innovation – and the application of the results for the benefit of society. Together with EPFL and the four federal research institutes PSI, WSL, Empa and Eawag, ETH Zurich is part of the ETH Domain, whose strategic management and supervisory body is the ETH Board. The ETH Board is advertising the position of

President of the Swiss Federal Institute of Technology Zurich (ETH Zurich)

under its mandate of submitting to the Swiss Federal Council a proposal for a successor.

ETH Zurich was established in 1855 and is one of the internationally leading universities in the field of technical and natural sciences, and as such provides researchers with an inspiring environment and their students with a thorough education. Currently, more than 28,000 people are studying, working and carrying out research at ETH Zurich.

Requirements
Your record in exact, natural or engineering sciences has been internationally recognised. You are able to identify and foster out-standing potentials and visionary ideas, specify strategic guidelines and raise issues in current scientific, technological and societal areas. As an experienced executive in a big organisation, preferably in the field of science or in trade and industry, you have provided evidence of your integrative leadership skills. You have good networks inside and outside the scientific community, and you are prepared to develop ETH Zurich's future and to lend an active hand in shaping the entire ETH Domain with great dedication.

Your personality is characterised by a high degree of social competence, assertiveness and the ability to deal with conflict, also in a participative management culture like that of ETH Zurich. You possess a high degree of communication competence, which you would use both inside and outside the university, and you understand Switzerland's political structures, legislative processes and cultural diversity. Finally, you have a good command of German and English, and preferably a knowledge of French. You are willing to hold office for at least two terms of office (i. e. eight years). Ideally the starting date would be at the beginning of 2019.

Applications
Please send your complete application to ethzurich@egonzehnder.com. Egon Zehnder is assisting the ETH Board in its preparations for the selection process. The President of the ETH Board, Dr. iur. Fritz Schiesser, ETH-Rat, Häldeliweg 15, 8092 Zurich, Switzerland, will be pleased to provide further information (phone +41 44 632 20 01, schiesser@ethrat.ch). All applications received by August 13th 2018 will be considered for the selection process. Your data will be treated in strict confidence. They will be used only in connection with your application and in accordance with Swiss data protection law. By submitting your application, you give us your consent to process your data for this purpose and to exchange it with the above-mentioned company.

Applications from women are particularly welcome.

Tenure-track faculty positions

The Department of Otolaryngology – Head and Neck Surgery at The Ohio State University and Ohio State's Comprehensive Cancer Center – James Cancer Hospital and Solove Research Institute in Columbus, Ohio, are seeking new tenure-track faculty at the assistant-, associate- or full-professor level to join a program that supports the highest quality basic and translational research with a view toward its application in head and neck cancer.

The program seeks several accomplished scientists within the fields of cancer, cell biology, cancer genomics and immunology, including one at a senior level and others at a junior or senior level. Scientists with experience in tumor immunology, cancer stem cells, tumor lineage, single-cell analysis, DNA repair pathways and epigenetics will be strongly considered. Applicants with funded programs or strong evidence of funding potential will receive the highest priority and will be offered highly competitive start-up packages. Applicants should have a PhD and/or MD degree and will be expected to maintain an independent basic research effort while helping the department build strong interdisciplinary research and training programs.

Applicants should send a cover letter describing their interest in the department, along with their CV and a brief description of their research interests, as a single PDF document addressed to **Professor James W. Rocco, MD, PhD, Chair, Department of Otolaryngology — Head and Neck Surgery, at James.Rocco@osumc.edu.**

Review of applications will continue until the positions are filled.

The Ohio State University is an equal opportunity employer. All qualified applicants will receive consideration for employment without regard to race, color, religion, sex, sexual orientation, gender identity, national origin, disability status or protected veteran status.

The James
The Ohio State University
Wexner Medical Center
cancer.osu.edu

Lecturer/ Senior Lecturer/ Associate Professor/ Professor/ Clinical Academic

We are seeking academic staff with the ambition to match ours. Whether you are an internationally renowned professor seeking a Professorial Gillings fellowship or are an exceptionally talented early career researcher, Lecturer, Senior Lecturer, Associate Professor or Professor we have exciting opportunities for you. We are growing our team and invite applications from talented researchers, educators and clinical academics. Join Exeter and you'll join a team whose research quality is ranked in the top 30 world-wide while establishing a tenured career located in a beautiful part of the country.

We are particularly interested in:

- Individuals who will contribute to our main areas of research which are: diabetes and associate conditions, brain health and mental health, ageing, health services research, primary care, public health and the environment and human health.
- Individuals with a passion for teaching and educational strengths in anatomy, assessment, student support, fitness to practice or fundamental science.

We will offer generous set up packages for candidates that transfer significant research grants to the University.

Interested? Full details are available at medicine.exeter.ac.uk/about/joinus
Or to apply now, please go to exeter.ac.uk/jobs and key word search P01148

University of Exeter | Medical School

Athena SWAN Silver Award

WORKING LIFE

By **Allison Perrigo**

The road less traveled

I peered sidelong into my laptop's keyboard. If I was careless with the mangosteen and papaya in my little tropical island bungalow, the ants were sure to invade—and end up squashed among the keys as I pushed out the morning's emails. I would often end up singing "the ants go marching one by one" while trying to reroute them out the door with sticky trails of decoy papaya juice. ("Hurrah! Hurrah!") This was not a problem I expected to encounter as part of running my scientific editing business. But it was the price—a small one—of my life as a digital nomad.

I've always been a travel junkie. Vacations never cut it, so during my Ph.D. and postdoc in biogeography, I traveled for work anytime I could. But eventually, even the rare desk days became too much. After a visit to the Paris herbarium, where I was sorting through 150-year-old dried tree ferns for my postdoc research, I decided it was time. I needed to be somewhere lush and green, among living ferns.

Just a week later, a professor in my department insisted on paying me for my work editing his manuscripts. I had helped many colleagues and friends with this type of work over the years. I enjoyed writing and helping out. But the professor's offer triggered a realization: I could make a living with this work. Even better, all I would need was a computer and an internet connection fast enough to email Word documents and support the occasional Skype call. The adventurer in me saw an opportunity. My postdoc ended 6 months later, and many of my colleagues said they would consider hiring me to edit their manuscripts or books. I was ready to take the leap.

"All I would need was a computer and an internet connection."

Work was slow at first. When I emailed my network to let people know I was officially in business, many expressed interest but didn't have projects ready for me. I had expected this, so—despite fleeting doubts about the course I had chosen—I remained patient. Every day the work emails failed to show up was another chance to explore and find my nomadic rhythm. I trained to be a divemaster in the fast-moving waters between the islands of Bali and Lombok, the famous division that separates Asian and Australian faunas. I loved diving at Bali's Manta Point, where reef manta rays twice my size glided around me. I watched the sun rise over pagodas in Myanmar, saw ash spewing from Volcán de Fuego in Guatemala, ate schnitzel in the Austrian Alps, and felt the earth shake in New Zealand. When people asked how long I was traveling, I responded, "As long as I want," feeling impossibly lucky.

Yet in the beginning, while I was only getting work sporadically, I sometimes wondered what I was doing. Was I really an editor, or was I just a vagabond with a computer? I began reflecting on what defines a profession. Was it working 40 (or more) hours a week? Making ends meet? Was it enough to have a business plan and a passion? For a while, I tried to figure out the "right" way to do it. But as I met other digital nomads, I found that each had a unique story and there was no single right way. So I just kept doing it my way. Eventually, as the stamps in my passport piled up, my business grew. The impostor syndrome melted away. In its place I felt a contentment I never found during my years of research.

After two and a half years working and exploring in 18 different countries, I had just finished a major book project and felt that I could call my business a success. However, the now long hours meant I could no longer explore as much as I once had. When I found out that a colleague back in Sweden was creating a biodiversity center, I couldn't help but get excited about working to start it up. The job would involve some travel, which I embraced. I would get work-free vacations, too—a luxury I had come to miss. The time felt right to have a hint of stability again.

But I haven't forgotten my time of adventure. Every now and then, I come across early-career researchers thinking of trying a nontraditional path. I'm happy to give them a push away from routine and into the deep end. After all, there might be mantas down there. ■

Allison Perrigo is the coordinator of the Gothenburg Global Biodiversity Centre in Sweden. Send your career story to SciCareerEditor@aaas.org.

ILLUSTRATION: ROBERT NEUBECKER